

*A humanized mouse melanoma model for  
liposomal drug delivery*

Dissertation  
zur Erlangung des Grades  
„Doktor der Naturwissenschaften“  
im Promotionsfach Pharmazie

am Fachbereich 09 - Chemie, Pharmazie,  
Geographie und Geowissenschaften  
der Johannes Gutenberg-Universität Mainz

Jonathan Schupp  
geboren am 21.05.1989 in Wiesbaden

Mainz, den 01.12.2021



JOHANNES GUTENBERG  
UNIVERSITÄT MAINZ

Dekanin: [REDACTED]  
1. Berichterstatter: [REDACTED]  
2. Berichterstatterin: [REDACTED]

Tag der mündlichen Prüfung: 03.03.2022

Prüfungskommission der mündlichen Prüfung:

1. Prüfer: [REDACTED]  
2. Prüferin: [REDACTED]  
3. Prüfer: [REDACTED]  
4. Prüfer: [REDACTED]

This dissertation has been composed at the Department of Dermatology of the University Medical Center of the Johannes Gutenberg-University Mainz under supervision of [REDACTED] and [REDACTED], Institute of Pharmaceutical and Biomedical Sciences of the Johannes Gutenberg-University Mainz, in the time between April 2015 and December 2020.

*Die vorliegende Dissertation wurde an der Hautklinik der Universitätsmedizin der Johannes Gutenberg-Universität Mainz unter der Betreuung von [REDACTED] und [REDACTED], Institut für Pharmazeutische und Biomedizinische Wissenschaften der Johannes Gutenberg-Universität Mainz, in der Zeit von April 2015 bis Dezember 2020 verfasst.*

I hereby certify in accordance with § 10 para. 3d of the doctoral regulations of 24.07.2007:

I have prepared the work now presented as a dissertation myself and have indicated all the aids used (literature, apparatus, material) in the work.

I had neither submitted the work now presented as a dissertation nor parts of it to another faculty or department as a dissertation.

*Hiermit versichere ich gemäß § 10 Abs. 3d der Promotionsordnung vom 24.07.2007:*

*Ich habe die jetzt als Dissertation vorgelegte Arbeit selbst angefertigt und alle benutzten Hilfsmittel (Literatur, Apparaturen, Material) in der Arbeit angegeben.*

*Ich hatte weder die jetzt als Dissertation vorgelegte Arbeit noch Teile davon bei einer anderen Fakultät bzw. einem anderen Fachbereich als Dissertation eingereicht.*

---

Date

*Datum*

Place

*Ort*

---

Signature

*Unterschrift*

“THE QUICKEST WAY OF ENDING A  
WAR IS TO LOSE IT.”

GEORGE ORWELL

# Content

|       |  |    |
|-------|--|----|
| 1     | Abstract.....  | 1  |
| 1.1   | Deutsch .....  | 1  |
| 1.2   | Englisch .....   | 2  |
| 2     | Introduction.....  | 3  |
| 2.1   | Melanoma.....  | 3  |
| 2.1.1 | Epidemiology .....   | 3  |
| 2.1.2 | Diagnosis and Pathology .....  | 4  |
| 2.1.3 | Tumor microenvironment .....   | 5  |
| 2.1.4 | Novel therapeutic strategies .....                                     | 8  |
| 2.1.5 | Tasquinimod.....   | 10 |
| 2.1.6 | Doxorubicin .....  | 11 |
| 2.2   | Humanized mice .....   | 12 |
| 2.3   | Highplex analysis of the tumor microenvironment in humanized mice..... | 14 |
| 2.4   | GARP as potential target for melanoma immunotherapy.....               | 16 |
| 2.5   | Rationale .....  | 18 |
| 3     | Materials and Methods.....   | 19 |
| 3.1   | Human PMBC Isolation .....   | 19 |
| 3.2   | Cell counting.....   | 19 |
| 3.3   | Cell culture macrophages .....   | 19 |
| 3.4   | Generation of human plasma .....                                       | 19 |
| 3.5   | Cell culture cell lines .....  | 20 |
| 3.6   | Flow cytometry.....  | 20 |
| 3.7   | Confocal microscopy.....   | 21 |
| 3.8   | Seahorse analyzer .....  | 22 |
| 3.9   | qPCR .....   | 23 |
| 3.10  | ImageStream .....  | 24 |
| 3.11  | NanoString.....  | 25 |
| 3.12  | Liposome preparation .....   | 25 |
| 3.13  | Animal experiments.....  | 28 |
| 3.14  | chipcytometry .....  | 29 |
| 3.15  | Immunohistochemistry .....   | 31 |
| 3.16  | Quantification of Doxorubicin content in liposomes .....               | 31 |
| 3.17  | Targeting of biotin liposomes.....                                     | 31 |
| 3.18  | Anchor stability experiments .....                                     | 32 |
| 3.19  | siRNA transfection.....  | 32 |
| 3.20  | siRNA transfection with liposomes .....                                | 32 |
| 3.21  | Tasquinimod effect on human PBMC.....                                  | 32 |
| 3.22  | Tasquinimod effect on human melanoma cell lines .....                  | 33 |
| 3.23  | Tasquinimod effect on human monocyte-derived macrophages .....         | 33 |
| 3.24  | Statistics .....   | 33 |
| 4     | Results and Discussion .....   | 34 |
| 4.1   | <i>in vitro</i> macrophage culture M0/M1/M2 .....                      | 34 |
| 4.2   | siRNA knockdown in macrophages.....                                    | 39 |
| 4.3   | Tasquinimod as siRNA alternative.....                                  | 44 |
| 4.4   | Analysis of human melanoma metastases .....                            | 51 |
| 4.5   | Development of liposomes as drug carrier .....                         | 53 |
| 4.5.1 | Rationale .....  | 53 |
| 4.5.2 | Liposomes at the edge of stability .....                               | 55 |
| 4.5.3 | Doxorubicin as model cargo for release assays .....                    | 58 |
| 4.5.4 | Novel screening method for Doxorubicin release .....                   | 65 |
| 4.5.5 | Screening of liposomes with modifications: biotin and PEG .....        | 68 |

|       |   |     |
|-------|---|-----|
| 4.5.6 | Stability of liposomal membrane anchors .....                                   | 71  |
| 4.5.7 | Targeting of biotin liposomes.....  | 75  |
| 4.6   | <i>In vivo</i> melanoma model in humanized mice.....                            | 82  |
| 4.6.1 | Rationale .....   | 82  |
| 4.6.2 | TME analysis by immunohistochemistry and flow cytometry.....                    | 87  |
| 4.6.3 | Transcriptome analysis by NanoString Sprint Profiler.....                       | 90  |
| 4.7   | Analysis of the tumor microenvironment comparing low- and highplex methods..... | 93  |
| 4.8   | GARP (LRRC32) as target molecule .....  | 98  |
| 5     | Conclusion .....  | 102 |
| 6     | Outlook.....  | 106 |
| 7     | Literature.....   | 108 |
| 8     | Supplemental.....   | 122 |
| 9     | Acknowledgments.....  | 124 |
| 10    | List of figures.....  | 125 |
| 11    | Curriculum Vitae .....  | 129 |
| 12    | List of publications.....   | 130 |

## 1 Abstract

### 1.1 Deutsch

Ziel dieser Arbeit war die Entwicklung effektiver Immunotherapien auf Basis von Nanopartikeln ausgerichtet sind, aufgeteilt auf drei Teile: Die Entwicklung eines humanisierten *in vivo* Systems (i) zur Ansprache und Beeinflussung von tolerogenen Immunzellen in der Tumormikroumgebung (ii) mit gründlich charakterisierten Nano-Transportern (iii).

Um Immunantworten möglichst nah an der Situation im Menschen zu untersuchen, haben wir ein humanes Melanommodell in immundefizienten Mäusen entwickelt, die mit humanen Immunzellen aus humanen peripheren mononukleären Blutzellen (PBMC) besiedelt sind ("humanisierte Mäuse"). In diesem System werden NOD.Cg-Mcph1<sup>Tg(HLA-A2.1)</sup>1<sup>Enge</sup> Prkdc<sup>scid</sup>/DvsJ-Mäuse ("NOD-Scid") als Empfängermause verwendet. Diesen Mäusen fehlt ein adaptives Immunsystem, wodurch sie in der Lage sind, xenogene Transplantate von Tumoren und menschlichen Immunzellen zu akzeptieren. Das System der humanisierten Maus ermöglicht die Modulation von menschlichen Immunzellen in der Tumormikroumgebung von menschlichen Tumoren, wie dem Melanom in diesem Zusammenhang, zu untersuchen. Die Etablierung des Tiermodells beinhaltete die Analyse der Tumormikroumgebung mittels Durchflusszytometrie, Immunhistochemie und der neuartigen Multiplexmethode Chipzytometrie.

Tumorassoziierte Makrophagen sind wichtige Zielzellen für die Manipulation der Immunsuppression, da sie Schlüsselspieler in der Tumormikroumgebung sind. Die Manipulation von tumorunterstützenden immunsuppressiven Makrophagen, die die Immunantwort gegen Krebszellen unterstützen, wird im zweiten Teil dieser Arbeit untersucht. Zu diesem Zweck wurden primäre humane monozytäre Makrophagen in ihren beiden polarisiertesten Zuständen als M1- und M2-Makrophagen hinsichtlich ihrer Gen- und Oberflächenmarkerexpression, sowie ihrer Reaktion auf die Behandlung mit einem Immunmodulator und der siRNA-Transfektion analysiert. Hierbei wurden moderne Methoden wie Durchflusszytometrie, qPCR und konfokale Fluoreszenzmikroskopie zur Untersuchung der Markerexpression und/oder des Phänotyps der Makrophagen eingesetzt. Es wurden auch Studien zur Aufnahme verschiedener Nanopartikeltypen durchgeführt.

Die auf die Mikroumgebung des Tumors begrenzte Manipulation von Immunzellen erfordert Vehikel, die in der Lage sind, bestimmte Immunzellen anzusprechen bzw. zu adressieren, die Fracht/Wirkstoffe abgeschirmt von äußeren Einflüssen zu transportieren sowie eine vorzeitige Freisetzung und ein Eindringen aus dem Blutkreislauf in das Tumorgewebe zu verhindern. Dieses umfangreiche Design und die Entwicklung von geeigneten Nanopartikeln in Zusammenarbeit mit Instituten aus der Chemie und Pharmazie, eingebettet in den Sonderforschungsbereich 1066: "Nanodimensionale Polymertherapeutika für die Tumorthherapie", ist der dritte Teil dieser Studie. Wirkstoffe wie Ribonukleinsäuren (RNS) und niedermolekulare Wirkstoffe wurden *in vitro* und teilweise *in vivo* getestet. Für die Anwendung dieser Systeme in biologischen Experimenten ist die Definition von Beladungseffizienz, Stabilität und Freisetzung von entscheidender Bedeutung. Für lange Lagerfähigkeit bei 4 °C und physiologischen pH-Wert und gleichzeitig guten Freisetzungseigenschaften bei 37°C und pH 5 wurden Liposome entworfen, die am Rande der Stabilität liegen. Um im nächsten Schritt die Kopplung von Antikörpern an bestimmte Immunzell-Subpopulationen zu ermöglichen und unspezifische Bindungen zu reduzieren, wurden Lipide mit PEG-Ketten und Biotin am ungebundenen Ende in die liposomale Membran eingeführt. In zukünftigen Studien könnte Streptavidin als Brücke verwendet werden, um Biotin-markierte Antikörper an die Liposomenoberfläche zu koppeln. Die Studien mit Nanopartikeln waren nicht auf Liposomen beschränkt, aber diese Partikelklasse lieferte die vielversprechendsten Ergebnisse und bietet gleichzeitig eine hohe Flexibilität bei der Zusammensetzung und Beladung mit Medikamenten.

# *Abstract*

## **1.2 English**

This work has three major parts pointing all towards a more effective immune therapy based on nanoparticles: The development of a humanized *in vivo* system (i) to address and influence tolerogenic immune cells in the tumor microenvironment (ii) with thoroughly characterized nanocarriers (iii).

In order to investigate immune response in a human setting we developed a human melanoma model in immunodeficient mice populated with human immune cells originating from human Peripheral blood mononuclear cells (PBMC) (“humanized mice”). This system uses NOD.Cg-Mcph1<sup>Tg(HLA-A2.1)</sup>1<sup>Enge</sup> Prkdc<sup>scid</sup>/DvsJ mice (“NOD-Scid”) as recipient mice. Those mice lack an adaptive immune system, which enables them to accept xenograft tumors and human immune cells. This system makes it possible to study modulation of human immune cells in the tumor microenvironment of human tumors like melanoma in this context. The establishment of the animal model included analysis of the tumor microenvironment using flow cytometry, immunohistochemistry and the novel multiplex method chipcytometry.

Tumor associated macrophages are important target cells for manipulation of the immune suppression, as they are key players in the tumor microenvironment. Their manipulation from tumor supporting immune suppressive macrophages into macrophages supporting the immune response towards cancer cells is the second part of this thesis. Consequently, primary human monocyte-derived macrophages in their two most polarized states as M1 and M2 macrophages were analyzed regarding their gene and surface marker expression as well as their response towards immunomodulator treatment and the feasibility to transfect them with siRNA to change their polarization. State of the art methods like flow cytometry, qPCR and confocal fluorescence microscopy were used to investigate marker expression and/or phenotypes of macrophages. Uptake studies of different nanoparticle types were also conducted.

Immune cell manipulation limited to the tumor microenvironment requires vehicles capable of targeting certain immune cells, transporting cargo shielded from external influences as well as preventing premature release and penetrating from the blood stream into the tumor tissue. This extensive design and development of suitable nanoparticles in cooperation with the chemistry and pharmacy department embedded into the *Collaborative Research Center 1066: “Nanodimensional polymer therapeutics for tumor therapy”* is the third part of this study. Cargo substances like ribonucleic acid (RNA) and small molecules were tested *in vitro* and, partly, *in vivo*. Defining loading efficacy, stability and release are paramount for applying those systems in biological experiments. Liposomes were designed at the edge of stability, meaning a compromise between stability in shelf storage at 4°C and pH7 and release capability at 37°C and pH5. To enable antibody coupling to target immune cell subpopulations and reduce unspecific binding, lipids carrying PEG chains with biotin at the unbound end were introduced into the liposomal formula. In future studies streptavidin could be used as bridge to couple biotin-labeled antibodies to the liposome surface. Nanoparticle studies were not limited to liposomes, but this particle class generated the most promising results while offering high flexibility in composition and loading with drugs.



# 2 Introduction

## 2.1 Melanoma

### 2.1.1 Epidemiology

Malignant melanoma is a type of skin cancer originating from melanocytes, the melanin-producing cells located mostly but not only in the stratum basale of the epidermis. Since melanocytes are not exclusively located in the epidermis, but also in the uveal layer of the eye, the meninges, hair follicles and in mucosal tissue, melanoma development is not confined to the skin. In order to distinguish between melanomas with different sites of origin and more important their disparity in genetic profiles and clinical treatment guidelines, melanoma is categorized in cutaneous (skin), mucosal and uveal. <sup>1,2</sup>

This study is focused on cell lines originating from cutaneous melanoma. In 2018 it had an incidence of 2,6 / 20,4 per 100 000 (both sexes, ages 0-74, World / Germany) and an estimated 5-year prevalence of 722 031 / 85 032 (both sexes, ages 0-74, World / Germany) and is the most deadly type of skin cancer due to its high rate of metastasis. Despite a growing incidence in Germany, melanoma mortality stays at constant low levels on account of the vast majority being resectable stage I tumors without metastases. The introduction of skin cancer screening in Germany in 2008 boosted numbers of melanoma detected at the early stage. Although dangerous, it is not the most common type of skin cancer. Basal-cell skin cancer (BCC), squamos-cell skin cancer and a few very rare types of skin cancer are grouped as non-melanoma skin cancer (NMSC). BCC is the most common skin cancer. <sup>3</sup>

One common risk factor is DNA damage caused by ultraviolet irradiation. Australia serves as an example of a country with a high UV index which applied already in the 1980's public campaigns ("Slip, Slop, Slap!", nowadays "Slip Slop Slap Seek Slide") stating the most important measures of prevention like wearing protective clothing, applying sunscreen, covering head and face, minimizing sun exposure and using sunglasses. Australia also banned commercial solariums in most of its territories.

Clear evidence of other possible risk factors is the appearance of melanoma in sun-protected sites and the existence of genetic predisposition of developing melanoma and the density of pre-existing naevi influencing melanoma occurrence. <sup>4,5</sup>

# *Introduction*

## **2.1.2 Diagnosis and Pathology**

Pigmented skin anomalies suspected of being cutaneous melanoma are identified using the “ABCD” rule. <sup>6</sup> It stands for Asymmetry, Border irregularities, Color heterogeneity and Dynamics in color, size or elevation. A dermatologist using a dermatoscope does this classification. Today, this work can be optimized using sequential video documentation of suspicious lesions or even whole-body images or machine learning approaches in visually identifying melanoma. <sup>7-9</sup> In the near future validated health apps using smartphone cameras could provide guidance for patients especially in regions with suboptimal health systems. <sup>10</sup> Melanoma do not exclusively originate from naevi. The progression from naevi towards (invasive) melanoma is a possible route for melanocytes, although melanoma development can also skip steps and develop via intermediate neoplasms directly from pathogenic melanocytes. The root cause for melanocytes to become melanoma is complex. Pre-existing or acquired genetic predisposition combined with UV irradiation contribute to melanoma formation. It is worth to mention, that also benign naevi can arise through UV irradiation and harbor BRAF mutations but somehow their proliferation rate and invasiveness is held in place mostly lifelong or until they vanish. <sup>11</sup>

Tumor biopsies are necessary to stage according to the American Joint Committee on Cancer (AJCC) TNM (tumor, node and metastasis) classification which is the standard in Germany and many other countries. <sup>12,13</sup> *T* describes the primary tumor and its thickness, ranging from T0 / Tis without measurable thickness to T4 with more than 4,0 mm. *N* describes the status of the regional lymphatic system counting the metastases and *M* the distant metastases from no metastases (M0) to metastases in different compartments M1a-d like skin, lung or the central nervous system. TNM staging categories are summarized in anatomic stage groupings ranging from 0 to IV. Stage 0 to II are tumors without metastases with growing thickness from Tis (0) to T4 (II). Stage III tumors have regional metastases at the tumor site or the draining lymph nodes whereas stage IV tumors have distant metastases.

Genetically cutaneous melanoma has four subtypes: mutant *BRAF* (mostly V600E), mutant *RAS*, mutant *NF1* and triple wild-type. <sup>14</sup> Since those mutated genes are proto-oncogenes or regulators thereof (*NF1*), it is no surprise to find this high mutational load. However, the availability of targeted drugs (inhibitors) makes it important to test the genetic profile to treat metastatic melanoma (see 2.1.4).

# *Introduction*

## **2.1.3 Tumor microenvironment**

The term “tumor microenvironment” (TME) describes the complex interplay between tumor cells and their surrounding tissue including immune cells. It has become evident, that despite the high proliferation capacity of tumor cells hallmarks of cancer have to include tissue modification for nutrient supply or metastasis and immune modulation to evade anti-tumor responses by the immune system in order to survive.<sup>15</sup> In the past cancer therapy focused on direct targeting of the tumor cells by using chemotherapeutics to target fast replicating cells or by inhibitors of specific or upregulated signal pathways. With the introduction of the checkpoint inhibitors, this focus shifted towards the immune system (see 2.1.4). In order to estimate treatment response or to understand occurring resistance, knowledge about the tumor microenvironment is paramount.

Since this work is concentrated on modifying macrophages in the TME to overcome immune suppression, this section is focused on the function of those. Myeloid cells like dendritic cells, macrophages and myeloid derived suppressor cells (MDSC) as well as T-cells and neutrophils build a network inside the tumor with mutual influence (see **Figure 1**).<sup>16,17</sup> Macrophages do arise from embryonic precursor cells, being later only replenished by monocytes in special situations like inflammation or cancer.<sup>18</sup>

Our immune system defends our body against pathogens like bacteria, viruses and fungi. It is also able to selectively kill cells in the body, which become abnormal, and to recognize those cells via expression of neo-antigens or an altered surface maker expression profile. Supporting tumor growth is obviously the contrary and leads to death. Mechanisms normally responsible for tissue homeostasis, wound repair, prevention of autoimmunity and angiogenesis are hijacked by the tumor cells via secretion of immunosuppressive cytokines and expression of surface antigens, the so-called tumor escape mechanisms.

Macrophages are a very versatile cell type, capable of fighting pathogens by phagocytosis and bridging innate and adaptive immunity as professional antigen-presenting cells as well as supporting angiogenesis and tissue remodeling. They can be found in almost every tissue type and organs, giving rise to a lot of different names like Kupffer cells (liver), microglia (brain) or osteoclasts (bones). In *in vitro* research, macrophages are often used in their two most polarized phenotypes, M1 and M2 macrophages. Lipopolysaccharide, IFN- $\gamma$ , GM-CSF or a combination of them can shift macrophages towards the activated, pro-inflammatory M1 phenotype, whereas IL-4, IL-13 and IL-10 are used for the rather tolerogenic, tumor-promoting M2 macrophages. It is possible to influence/modulate macrophages with a lot of different substances like dexamethasone or iron, making clear rules for nomenclature necessary. Macrophages sense the surrounding environment on cellular and soluble level via receptors and adapt their phenotype in a broad spectrum, with M1 and M2 only being the poles.<sup>19</sup> *In vivo* it is more important to analyze and classify macrophages by their function. Therefore, the term “tumor associated macrophages (TAM)” is rather a functional and spatial description, than defining one special phenotype. TAM phenotype is determined by integrating information (soluble proteins and cell-cell-contact) of the TME. Inflammation or pathogen clearance is driven by secretion of TNF- $\alpha$ , IL-12, IL-1, IFN- $\gamma$ , IL-6, IL-23 and CXCL-10 and the expression of inducible nitric oxide synthases. On the other hand, immune suppression and tissue remodeling by secretion of TGF- $\beta$ , IL-10, IL-1RA, CCL22, CXCL12, VEGFA and MMP-9. L-arginine and tryptophan depletion by arginase and 2,3-dioxygenase also act suppressive on T cells. However, the M1 and M2 model does not give clear answers in cancers since cells have depending on the tumor mixed phenotypes and chronic inflammation is one major risk factor for cancer.<sup>20,21</sup> Tumors depend strongly on the support of macrophages to develop and grow, that’s why macrophages are abundant in the TME of most tumors. Of course, tumor cells

## *Introduction*

manipulate macrophages to suppress immune responses and to support the formation of new blood vessels. These mimics normal processes in wound healing or developmental processes. They do so by secreting cytokines, interacting through cell-cell contact and by creating hypoxic conditions. TAM respond by secreting cytokines like IL-6, IL-8, IL-10 and CCL2 to create a chronic inflammation, dampen T cell responses and recruiting more monocytes from the blood stream.<sup>22</sup> Even at one local tumor site, there are many different TAM phenotypes, depending on their local cell interactions, cytokine milieu and their origin. TAM might stem from resident macrophages or recruited monocytes. This is called ontogeny.<sup>23</sup> A combination of different methods is necessary to decipher the TME and its cellular components with their phenotype. TAM rely on oxidative phosphorylation for energy supply, in contrast to proinflammatory M1 macrophages fighting pathogens, which depend more on glycolysis.<sup>24,25</sup>

T cells are a very versatile cell type existing in many subtypes. They play an ambiguous role in the TME. On the one hand, regulatory T cells (Treg) are responsible for immunosuppression, like TAM, but on the other hand, CD8<sup>+</sup> cytotoxic T lymphocytes (CTL) are the most important cells to kill tumor cells directly and the key effector cells of immune therapies.<sup>26,27</sup> Treg belong to the subgroup of CD4<sup>+</sup> T cells and are in physiologic situation tasked with maintaining the steady state of the immune system to prevent auto immunity against self-antigens. After development in the bone marrow, they are “educated” in the thymus. Only T cells weakly recognizing self-antigens are selected to become Treg and are released afterwards. Alternatively, T cells can be activated in the periphery to become induced Treg (iTreg) by contact with foreign antigens without proper stimulation.<sup>28</sup> Despite having the transcription factor FOXP3 as hallmark for Treg function, it does not serve as marker for T cells since it is not exclusive making Treg identification and research difficult. FOXP3 is also expressed in activated CD4<sup>+</sup> T cells, a subset of CD8<sup>+</sup> T cells, natural killer T cells and even tumor cells. Exactly those two T cell subtypes are intertwined and determine the outcome of immune checkpoint inhibitor therapies (see 2.1.4).<sup>29,30</sup> Initially it was thought that the first checkpoint inhibitor, an anti-CTLA-4 antibody, blocks the negative feedback loop between CTLA-4 on T cells and CD80/CD86 on antigen presenting cells after T cell activation. This removal of negative feedback should then boost existing anti-tumor responses of CTL. In contrast, studies showed that this antibody therapy depletes Treg, which also express CTLA-4, through antibody-dependent cellular cytotoxicity (ADCC). Accordingly, anti-tumor effects would be the result of a lifted immunosuppression. Another immune checkpoint therapy uses an anti-PD-1 antibody to target PD-1 on T cells. PD-1 is another receptor on T cells responsible for downregulation of immune responses after binding to its ligands PD-L1 and PD-L2., yet non-redundant to CTLA-4. Prevention of binding between receptor and ligand, leads to a boost of exhausted CTL. This binding can also be abrogated by blocking PD-L1. For that reason, anti-PD-L1 antibodies are approved as immune checkpoint inhibitors, too. Primary resistance - no response to treatment - to immune checkpoint inhibitors can be attributed towards to two key factors. The heterogeneous tumor cells themselves and the composition and activation state of the TME. A high number of neoantigens due to a high mutational burden and PD-L1 expression serve as positive prognostic marker on the level of the tumor cells. Interaction of the immune system with the tumor is described in the expression hot or cold tumor.<sup>31</sup> Hot tumors show signs of inflammation and a high infiltration of the tumor mass with immune cells. “Hot” tumors show a higher response rate towards immunotherapy than cold tumors. Of note, correct assessment of a hot or cold immune signature is not trivial, has to incorporate not only T cells and has to consider their spatial information.

# Introduction

In contrast to enhancers of naturally occurring immune cells, introduction of genetically modified T or natural killer (NK) cells into the TME to attack tumor cells and modify the TME by cytokine secretion. <sup>32,33</sup> Those cells carry a modular artificial antigen-receptor called chimeric antigen receptor (CAR). Key structures are a variable extracellular antigen binding domain, a transmembrane domain to anchor it in the cell membrane and an intracellular signaling domain to activate the cell upon ligand binding. CAR T cells specific for CD19 have been approved for treatment of B-cell acute lymphoblastic leukemia, while it is not yet a treatment option for solid tumors with a tumor microenvironment. <sup>34,35</sup>

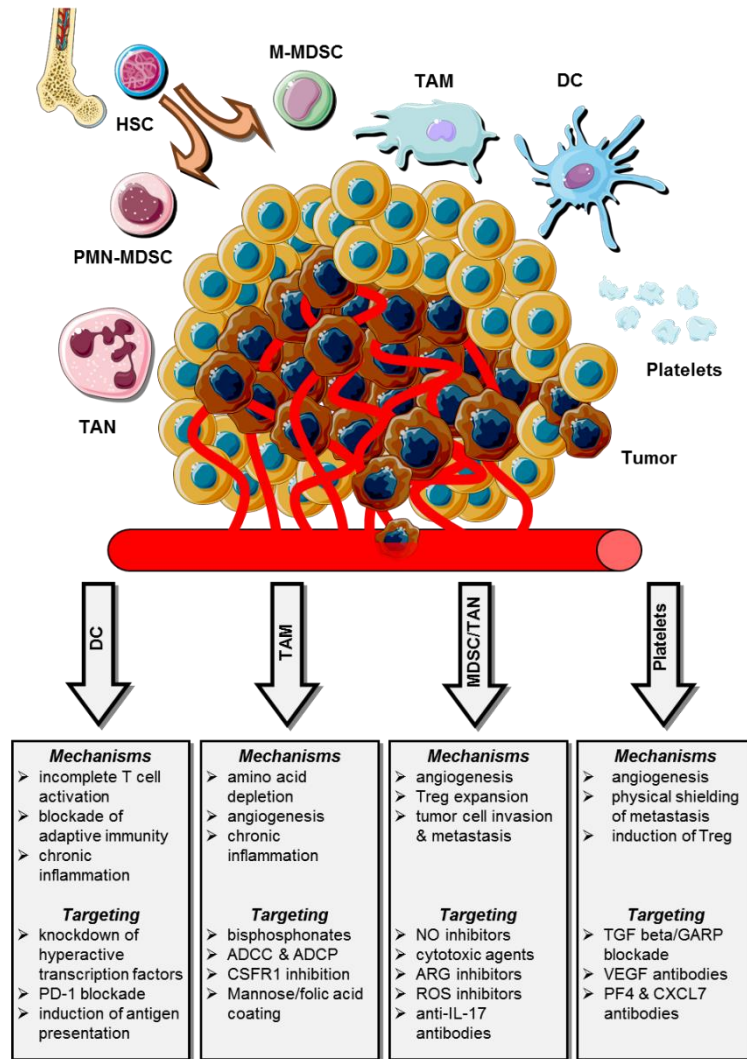


**Figure 1:** Myeloid cells of the tumor microenvironment, their key effector functions and strategies to target them. <sup>16</sup>

# *Introduction*

## **2.1.4 Novel therapeutic strategies**

Resectable tumors without metastases are curable. Tumor thickness directly correlates with mortality.<sup>12</sup> Until the last decade melanoma stages III and IV had a high mortality, since the only available treatment options were chemotherapy and radiotherapy, both having severe adverse side effects. Those treatments do not eradicate every single tumor cell in the body, making relapses almost inevitable.

Revolution came from two different directions almost simultaneously. Targeted therapy with inhibitors of mutated and dysregulated tumor driver genes like BRAF and checkpoint inhibitors.<sup>36,37</sup>

*BRAF* inhibitor therapy targets the V600 mutation in B-Raf quite common in melanoma.<sup>38</sup> It can be combined with *MEK* inhibitors, a target further downstream in the RAS-RAF-MEK-ERK pathway. This pathway is activated by mitogens like EGF upon their binding to the corresponding receptor (EGFR).<sup>39</sup> Ligand-bound receptor leads through phosphorylation steps to GTP for GDP exchange at the small GTPase Ras and its subsequent activation. A cascade of phosphorylation follows, from Raf (a mitogen activated kinase kinase kinase / MAP3K), to MEK (MAP2K), MAPK and MNK, which phosphorylates as last kinase in the cascade transcription factors to alter gene expression. There are numerous different mitogen activated kinases creating a signaling network enabling the cell to sense and regulate its reaction to external factors like growth factors and cytokines. Mutated B-Raf has elevated kinase activity independent of external signals boosting cell proliferation.<sup>40</sup> Vemurafenib and Dabrafenib are *BRAF* inhibitors, which have been combined in clinical trials with Cobimetinib and Trametinib, both *MEK* inhibitors. Combination therapy of inhibitor and chemotherapeutic agent (Dacarbazine or Paclitaxel) has also been tested.<sup>13</sup> Those studies showed that combination therapy is superior to single inhibitor therapy, but overall survival and progression free survival is mostly calculated in months, not years. Relapses after acquired therapy resistance, upregulation of alternative signaling pathways and severe side effects are the major obstacles in this therapy approach. *BRAF* and *MEK* inhibitor treatment remains an option for tumors with detected *BRAF* mutations.<sup>7,13</sup>

Immense improvement for patients arrived with the introduction of checkpoint inhibitors into the clinic, starting with Ipilimumab, which received its FDA approval for melanoma treatment in 2011. Ipilimumab is a human antibody against the protein cytotoxic T-lymphocyte-associated protein 4 (CTLA-4), which is involved in the negative feedback loop of activated T-cells. CTLA-4 is upregulated upon activation of T cells and its binding to CD80 and CD86 on antigen-presenting cells or tumor cells and acts as deactivating signal, although the exact mechanism of downregulation remains controversial as well as the immune response against the tumor in detail.<sup>41</sup> Binding of Ipilimumab to CTLA-4 blocks this receptor. This inhibition of negative feedback results in a boost of T-cell responses in general. The enhanced proliferation of CD8<sup>+</sup> T-cells reactive against tumor antigens is the major beneficial effect for tumor patients. It is evident, that autoimmunity is a common severe side effect, because autoreactive T-cells are boosted, too.<sup>42</sup>

The second immune checkpoint inhibitors introduced in the clinic were Nivolumab (2014) and Pembrolizumab (2014), both humanized antibodies against programmed cell death protein 1 (PD-1). PD-1 is expressed on T-cells and bind to its ligands PD-L1 and PD-L2, which are expressed on various cell types including myeloid immune cells. Some tumors also express those ligands, albeit they are not suitable as biomarkers.<sup>43</sup> PD-1 blockade primarily induces expansion of exhausted-like tumor-infiltrating CD8<sup>+</sup> T-cells.<sup>41</sup> Exhaustion of T cells describes the change in responsiveness to external factors during chronic antigen stimulation, like in tumors. The lack of expression of transcription factor *HNF1 homeobox A* (*HNF1A* / *TCF1*) and epigenetic changes seem to determine an exhausted state.<sup>44</sup> Since monotherapy with

## *Introduction*

anti-PD-1 antibodies or combination therapy with anti-CTLA-4 and anti-PD-1 antibodies is superior to monotherapy with Ipilimumab, they serve as first-line-treatment for patients with inoperable melanoma stage III to IV in Europe and Germany.<sup>45,43</sup> Overall survival rates of around 50% (all patients) to 60% (patients with BRAF mutation) for patients receiving combination therapy after a follow-up time of 5 years (“long-term survivors”) justify using the term “revolution”. On the other hand, half of the patients does not respond to checkpoint blockade directly (“primary resistance”) or acquire resistance during therapy.<sup>30</sup> Underlying mechanism include inadequate T-cell infiltration, T-cell exclusion, Interferon gamma resistance or loss of T-cell function or antigen presentation.<sup>46</sup> Of note, although one would assume PD-L1 expression on tumor cells to be a valid prognostic marker, patients with PD-L1<sup>+</sup> tumors do have a better outcome, but patients with PD-L1<sup>-</sup> tumors still profit more from anti-PD-L1 therapy than from anti-CTLA-4 therapy, making the former standard for systemic treatment of irresectable grade IV melanoma regardless of PD-L1 expression.<sup>47,48</sup>

Nowadays clinical trials are investigating possible benefits of combining checkpoint inhibitors with BRAF and MEK inhibitors for tumors positive for BRAF<sup>V600E/K</sup>.<sup>49,50</sup> Another hope for patients, who do not benefit from checkpoint inhibitors, are cancer vaccines. Vaccinations against infectious diseases caused by pathogens like bacteria or viruses, cancer vaccinations aim to use the immune system and cause a cellular and humoral immune response against the tumor. Unfortunately, tumors do not express foreign antigens which would be recognized by the immune system. On the contrary, tumors just overexpress genes belonging to the organism or deregulates pathways to grow uncontrollable. Targeting by vaccination antigens overexpressed by the tumor might cause auto-immunity and the rapid loss of expression by the tumor due to selection pressure. Therefore, this old concept failed always if only single antigens are targeted.<sup>51</sup> But tumor cells do differ from normal tissue. They have a higher mutational burden and tumors arise through mutations in key tumor suppressor genes. Neoepitopes, alterations of epitopes / proteins known to the immune system, emerge from these mutations and pose a point of attack since no tolerance towards them exists, nor are those neoepitopes expressed by non-tumor cells. Modern approaches hence analyze the mutome of each patient designing exclusive vaccines against developed neoepitopes (“personalized medicine”)<sup>52-54</sup> or combine several antigens associated with the tumor. At least some patients profit from mRNA based liposomal tumor vaccination, even after failed anti-PD-1 therapy.<sup>55</sup>

As addition new checkpoint inhibitors targeting other signaling pathways are currently investigated as treatment option when treatments with anti-CTLA-4 or anti-PD-1 antibodies fail. Two inhibitory receptors on T (and NK) cells, T-cell immunoglobulin and mucin domain 3 (Tim-3) and T cell immunoglobulin and ITIM domain (TIGIT) are hot candidates.<sup>56,57</sup>

Novel therapies also include the use of nano-scaled technologies. Gene therapy can include vectors for mRNA, siRNA or plasmids based on polymers or liposomes. Up to now, several obstacles hinder the broad application in the clinic.<sup>58</sup> Doxil® being an exemption (see 2.1.6). Nanocarriers encounter high concentrations of proteins in biological fluids like blood, forming a protein corona thereby altering the properties of the nanocarriers.<sup>59</sup> Targeting of tumor tissue is a further ongoing issue, since the enhanced permeability and retention (EPR) effect caused by newly formed leaky vasculature in the tumor is not usable in every tumor entity and is very heterogeneous.<sup>60</sup> This effect was thought to enable passive targeting of tumors.<sup>61</sup> Nano-sized drugs would only be able to penetrate the ring of endothelial cells in capillaries in tumors, but not in blood vessel of healthy tissue. Liposomal vaccination, as mentioned before, is one of the most promising approach.

# *Introduction*

## **2.1.5 Tasquinimod**

The immunomodulator Tasquinimod was developed as a modification of the drug Roquinimex in a screening approach.<sup>62</sup> Due to promising results *in vitro* and *in vivo* using animal models in mice and rats, the drug was tested in several clinical trials. Its main field of use was patients with (metastatic) castration-resistant prostate cancer (mCRPC)<sup>63</sup>, but also other tumor entities like hepatocellular, ovarian, renal cell and gastric cancers have been assessed in trials.<sup>64</sup> Although a meta-analysis revealed, that Tasquinimod is associated with enhanced radiologic progression-free survival in metastatic castration-resistant prostate cancer, Tasquinimod failed to show clinical activity in the other entities.<sup>64,65</sup> Serious adverse effects appeared in 26-35% of patients.

Tasquinimod has been shown to act as immunomodulator by binding to S100 calcium-binding protein A9 (S100A9) and thereby reduce infiltration and function of myeloid cells.<sup>66</sup> As a dimer with S100A8 it is a very abundant protein in neutrophils and macrophages, which can sequester iron, manganese and zinc. If it is released during infection it serves as ligand for toll-like receptor 4.<sup>67</sup> Especially it repolarizes tumor associated macrophages to pro-inflammatory M1 macrophages.<sup>68</sup> Although it is under debate if those effects are causally linked to effects by inhibition of S100A9.<sup>69</sup> The anti-tumor effect of Tasquinimod can be enhanced by PD-L1 blockade in animal models of bladder cancer.<sup>70</sup> Furthermore, it reduces angiogenesis in tumors through allosteric modulation of Histone deacetylase 4 (HDAC4), influencing epigenetic regulation.<sup>71</sup> Evidence in human prostate cancer xenografts in mice shows, that blocking of angiogenesis is most effective at early time points in growing tumors and not in well-established tumors and metastases. This might explain the lack of efficacy in clinical trials with heavily pre-treated patients. Those HDAC4 mediated effects of Tasquinimod have been shown to suppress tumor growth of nasopharyngeal carcinoma in mice.<sup>72</sup> Exhaustion of regulatory T cells and MDSC by Tasquinimod seems also to enhance bacterial clearance during tuberculosis in mice, indicating that its effects are not limited to myeloid cells.<sup>73</sup>



# ***Introduction***

## **2.1.6 Doxorubicin**

Doxorubicin (DOX) is an anthracycline antibiotic, a natural compound produced by *Streptomyces* bacterium strains, used to treat a variety of tumors like leukemia, ovarian cancer, AIDS-related Kaposi's Sarcoma and Multiple Myeloma. Being the most widely used anthracycline and a very potent chemotherapeutic, DOX is listed on the WHO List of Essential Medicines.<sup>74,75</sup> Since it is water-insoluble, the water-soluble Doxorubicin hydrochloride salt (DOX HCl) is used in formulations for the clinic. In 1974, DOX (Adriamycin®) was approved by the FDA as a solution of DOX HCl.<sup>76</sup> Almost 20 years later, 1995, DOX (Doxil®) premiered as first FDA-approved nano-drug, being encapsulated into nano-sized liposomes featuring PEG chains on the surface (PEGylation).<sup>77</sup> 2000 (Myocet®) and 2002 (Lipo-Dox®), two non-PEGylated alternatives, saw their market approval.

DOX unfolds its anti-cancer effect by directly intercalating into the DNA, arresting DNA synthesis by stabilizing the topoisomerase II-DNA complex causing double strand breaks, and by generating iron-mediated free radicals.<sup>75,76</sup> A newly described mechanism of DOX, aside from DNA damage response and apoptosis, is histone eviction.<sup>78</sup> DOX and other anthracyclines disrupt binding of several histones to DNA. The free histones stay in the nucleoplasm or get degraded. Thereby DOX influences epigenetic gene regulation.

Those strong effects against cancer do not come without collateral damage: One of its deadliest adverse effects is cardiotoxicity.<sup>79</sup> This can be explained as cardiomyocytes rely heavily on oxidative metabolism and mitochondria are attacked by DOX, because they contain DNA, their membrane contains the negatively charged cardiolipin and they are sensitive to oxidative stress.

In order to minimize adverse effects and enhance delivery to the tumor as target tissue, several strategies are tested in research or are evaluated in clinical trials. As a continuation to the proven strategy of Doxil®, an approach of encapsulating Doxorubicin into (murine) red blood cells (RBC) and subsequent DOX therapy with those carriers compared to free DOX in a human colorectal adenocarcinoma xenograft model. Enhanced anti-tumor effects, reduced cardiac toxicity and decreased myelosuppression could be shown.<sup>80</sup> A more elegant and easier to transfer into the clinic as the former approach is the use of liposomes synthesized with parts of leucocyte membranes (and their membrane proteins), so called "leukosomes".<sup>81</sup> In murine in vivo models of breast cancer and melanoma DOX-loaded leukosomes showed superior effects compared to free DOX. Further studies are targeted at the interplay between DOX chemotherapy and immune therapy<sup>82,83</sup> and the co-delivery of DOX with ceramide.<sup>84</sup> It remains an open question if classical chemotherapy with compounds like Doxorubicin will be displaced by immunotherapy or may act synergistic to overcome immunosuppression.

# Introduction

## 2.2 Humanized mice

Malignancies or mutations remodeled in animals like mice and rats are the pillar of basic research. Genetic homology of laboratory strains and a high number of biological replicates allow for significant results. But when it comes to therapy or molecular mechanisms, animal models of disease often lack transferability into the clinical setting due to differences between laboratory animals and humans.<sup>85,86</sup> One prominent example is the transcription factor FoxP3, which serves as exclusive marker for murine Treg, but not for human Treg.<sup>87</sup>

To overcome these limitations of animal models, the idea of humanized mice was developed.<sup>88-90</sup> Basically, those animals provide some sort of biological reactor. In the best case, every kind of cells connected to the disease should be of human origin, whereas the remaining mouse tissue and organs provide perfusion, nutrients and a framework of extracellular matrices, something even 3D *in vitro* culture cannot mimic perfectly. In case of tumor models, researchers developed models with human tumor cells, derived either from cell lines or patient derived xenografts<sup>91</sup>, and human immune cells. These models serve to investigate interactions in the tumor microenvironment and tumor response to treatment. The source of human immune cells can be either human PBMC from adult donors or patients as an easy T cell based model or human hematopoietic stem cells.

Humanized mice development achieved some major milestones, each targeted at higher engraftment of human cells and better development of human immune cells. It started with the transplantation of human cells into athymic *nude* mice, carrying a mutation in the *FOXN1* gene. Those mice only lack T cells and enable tumor cell engraftment due to absence of cytotoxic T cells. Around 20 years later the autosomal recessive *scid* mutation was discovered.<sup>92</sup> A loss of function mutation in the *PRKDC* gene coding for DNA-dependent protein kinase, catalytic subunit leads to disrupted B and T cell receptor formation and therefore to the absence of both cell types. This mutation has been shown to have some “leakiness” meaning, that some B and T cells do arise in this model. Mutations in the recombination activating genes (RAG) 1<sup>93</sup> and 2<sup>94</sup> don’t show this phenomenon. Crossing of NOD (non-obese diabetic) mice with *scid* mice resulted in NOD-*scid* offspring with reduced murine myeloid and NK cell function and signal regulatory protein alpha receptor (SIRP $\alpha$ ) similar to the human variant.<sup>95</sup> This combined leads to higher engraftment rates. Nevertheless, all those three models suffer from the existence of murine NK cells. This obstacle was eliminated with the introduction of a loss of function mutation or just a signaling deficient variant of interleukin 2 receptor, gamma chain leading to NSG<sup>TM</sup><sup>96</sup> or NOG<sup>97</sup> mice. Modern developments of those strains are the NSG-SGM3<sup>98</sup>, with transgenic expression of human IL-3, GM-CSF and SCF, or MISTRG mice<sup>99</sup> with expression of human M-CSF, IL-3, GM-CSF, Thrombopoietin and human SIRP $\alpha$ .

Despite those achievements, there are limitations and the disease model has to fit the humanized mouse strain. Even the latest developments like NSG-SGM3 or MISTRG have drawbacks. The efficient development of human monocytes and macrophages combined with poor erythropoiesis causes anemia in MISTRG mice and cell engraftment in NSG-SGM3 mice is limited to 5 months. Even if cells develop in the mouse, they find themselves in a foreign environment. As there is no human thymus and no human MHC molecules, T cells are educated to murine MHC molecules (H2). Lymphoid tissue development in immunodeficient mice is impaired, impeding adaptive immunity, too. There are sophisticated models to avoid this H2 restriction, which transplant human fetal liver and thymus under the highly vascularized kidney capsule and transplant HSCs from the same donor.<sup>100</sup> This model has human T cells educated on human MHC of the donor and population of mucosal tissue by human immune cells. Pitfalls are legal

## ***Introduction***

situation regarding human fetal tissue and graft versus host disease (GvHD) since T cells show reactivity against murine MHC molecules.

GvHD is a common problem in humanized mice, since CD8<sup>+</sup> cytotoxic T cells, which are not selected in murine thymus, can show reactivity to xenogenous MHC molecules. It is most common in models with mature T cells, e.g. injected PBMC or educated T cells in transplanted human tissue. One way to prolong available time for experiments before GvHD occurs is the transgenic expression of human HLA like HLA-A2.1 and the use of matched donors for PBMC or HSC.

As this work is focused on anti-tumor therapy, other disease models in humanized mice are not further elucidated here. In cancer research humanized mice serve as carrier of patient-derived xenografts <sup>91</sup> or human cancer cell lines and enable the investigation of immune therapies <sup>101</sup>, CAR T cells <sup>102</sup> and the tumor microenvironment in general <sup>103</sup>.

## ***Introduction***

### **2.3 Highplex analysis of the tumor microenvironment in humanized mice**

As described in chapter 2.1.3, the tumor microenvironment (TME) consists of a complex interplay between many different cell types like cancer cells, immune cells (herein regulatory and effector cells), stroma cells and endothelial cells. In order to understand mechanism regulating cancer growth, it is mandatory to thoroughly characterize the cells and to retain their spatial information to find localization patterns and interaction partners of those cells. <sup>104</sup> Furthermore, the tumor itself is very heterogeneous, interpersonal, intrapersonal and even intratumoral making it hard to find the right treatment option. <sup>105</sup> This results in two demands for state-of-the-art analysis of the TME: First, a high number of (protein) markers are necessary to identify the cells correctly. This is especially true for immune cells with their many subpopulations. Those markers can not only identify the correct cell type, moreover it can also give hints to their phenotype and activation status, something that is much more important than a mere cell classification. Second, as spatial information is the key to understand underlying mechanisms, it must not be lost. Therefore, analysis methods which rely on single cell suspensions, like flow cytometry, are of limited use in the investigation of solid tumors, although they offer the needed highplex analysis of markers in systems with up to 40 detection channels. <sup>106,107</sup> Likewise, classical IHC-P staining with DAB or as 2-marker method offers spatial information, but insufficient information about the cells (1-2 markers). None of the two methods offer comprehensive information.

Immunofluorescence, using antibodies labeled with fluorophores, is a common method to stain frozen or formalin-fixed and paraffin-embedded (FFPE) samples. Fluorophores are excited by lasers or by filtered light of a continuous light source and emit light in a characteristic spectrum. This emitted light can be detected by photomultiplier tubes or CCD cameras equipped with filters. Limitations in simultaneous detection of markers arise from the fact, that fluorophores absorb and emit in spectra and not discrete bands. This results in crosstalk between different fluorophores during excitation and emission, limiting detection to 3 – 5 markers / colors depending on the laser and detector setup. Special equipment allows detection not only of discrete wavelength areas through filters but complete emission spectra. This multispectral detection enables staining up to 9 markers in one run. <sup>108</sup> Several multi-plex methods using immunofluorescence circumvent this limitation by applying cycles of staining and detection. <sup>109,110</sup> A definite number of fluorophores (mostly bound to antibodies) is used in a staining cycle. After image acquisition the bound antibody-fluorophore conjugates are either removed by buffer exchange and heat or the fluorophores are bleached by a light source and remain bound to their antigen. A new staining cycle starts by incubation of the tissue sample with new antibody-fluorophore conjugates. These repetitive cycles allow for an unlimited number of markers to be stained theoretically. But practically besides consumption of resources for panel development, some markers are sensitive towards heat treatment in antibody removal steps, making bleaching a better alternative.

Chipcytometry is a technique based on repetitive staining cycles combined with bleaching. It has been developed at the Hannover Medical School and commercialized by the biotech company Zellkraftwerk GmbH which is now part of Bruker Corporation. <sup>111</sup>

## ***Introduction***

Technical application of the staining cycles themselves is only one part of the highplex analysis. Data acquisition and data processing, including recording high dynamic range images to level out high and low expressed markers, cell recognition by algorithms and connecting this information into single cell data dot plots like in flow cytometry, are the other part of such analysis. Besides, tissue and cells are recorded on special coated slides and can be stored up to two years for later (re)analysis, which is not possible for single cell suspensions in flow cytometry or stained tissue slides for fluorescence microscopy.

So far, this method has been used on fluid samples like circulating tumor cells, cerebrospinal fluid cells and mesenchymal stromal cells, as well as tissue samples from colon, lung and brain.<sup>112-117</sup> Applying this method to tumor samples from humanized mice has not been tried so far and poses new obstacles like the mixed human/murine tissue requiring human specificity of all antibodies used.

## *Introduction*

### **2.4 GARP as potential target for melanoma immunotherapy**

Cancer immunotherapy with checkpoint inhibitors is one of the successful novel approaches to fight cancer using the bodies' own immune system as described in chapter 2.1.4. Depending on the targeted molecule, mainly CTLA-4 or PD-1, more than half of the patients profit only temporarily or not at all from this new therapy. One factor is the targeted tumor entity. Some tumor types are less responsive towards immunotherapy like glioblastoma.<sup>118</sup> But even in melanoma, the target of the first checkpoint inhibitor therapies, more than 50% of the patients do not respond permanently or at all.

One identified factor influencing the tumor and its surrounding tumor microenvironment is the TGF- $\beta$  signaling axis. Among the three known TGF- $\beta$  subtypes, 1-3, TGF- $\beta$ 1 is immunosuppressive and linked to immunotherapy evasion of tumors.<sup>119-121</sup> TGF- $\beta$ 2 was primarily thought to play only a role in embryogenesis, but recent reports showed TGF- $\beta$ 2 to participate in autophagy regulation in gliomas, being a prognostic marker in colorectal cancer and metabolism.<sup>122-124</sup> TGF- $\beta$ 3 is important during embryogenesis and wound healing.<sup>125</sup>

Closely linked to TGF- $\beta$  is glycoprotein-A repetitions predominant (GARP). Inactive TGF- $\beta$ 1 is bound on the cell surface non-covalently attached to latency associated peptide (LAP) which is in turn anchored to the cell surface by disulfide bonds to GARP (see **Figure 2**).<sup>126</sup> Release requires physical force by integrins  $\alpha$ V $\beta$ 6 or  $\alpha$ V $\beta$ 8. Anchoring GARP and with it TGF- $\beta$ 1 to the cell membrane is one option, the other one is to tether GARP to the extracellular matrix (ECM) via a class of proteins called latent TGF- $\beta$  binding proteins (LTBPs). GARP exists also in a cleaved soluble form whose function is still not clear. It has been shown to modulate human CD4<sup>+</sup> T cells towards induced Tregs and it might regulate the bioavailability of TGF- $\beta$ 1 by forming a non-covalent complex in the ECM and blood with it.<sup>127,128</sup> GARP, and with it the potency to act as TGF- $\beta$ 1 carrier, has been detected on regulatory T cells (Treg), platelets and several cancers *in vivo* and *in vitro*.<sup>129-133</sup> This renders GARP suitable as target for lifting the immunosuppression in the tumor microenvironment.<sup>132</sup> Targeting TGF- $\beta$ 1 or its receptors directly poses the danger of producing off-target effects by interfering with pathways outside of the intended cancer, since it is a pleiotropic cytokine.<sup>134</sup> The effect of TGF- $\beta$ 1 mediated immunosuppression might be partly responsible for resistance towards PD-1 checkpoint blockade.<sup>135</sup> Platelets, expressing GARP and TGF- $\beta$ 1, have been shown to liberate TGF- $\beta$ 1 by proteolysis of GARP by thrombin which is stored in platelets and released upon activation.<sup>136</sup> Preventing liberation of TGF- $\beta$ 1 from GARP using the thrombin inhibitor Dabigatran restored and enhanced responsiveness towards anti-PD-1 therapy in preclinical animal models. The same strategy of blocking TGF- $\beta$ 1 release from GARP, but facilitated with an anti-GARP:TGF- $\beta$ 1 murine antibody, enhanced anti-PD-1 therapy in a murine model of subcutaneous CT26 colon carcinoma tumors.<sup>137</sup> New findings indicate that TGF- $\beta$ 1 can be activated and exert its signaling function without release from the latent TGF- $\beta$ 1 complex.<sup>138</sup>

## Introduction

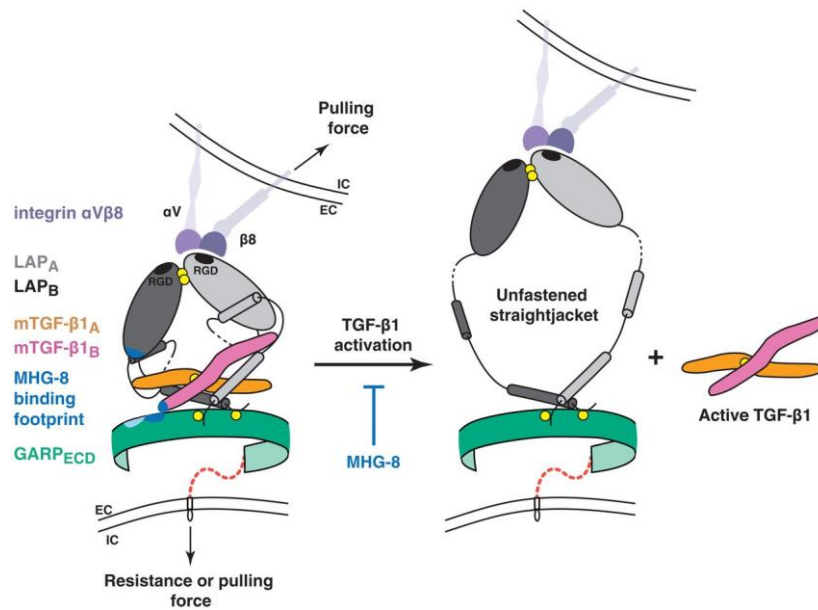


**Figure 2:** Proposed model for TGF-β1 in a complex with two LAP and GARP in its inactive form. Physical pulling force exerted by integrins ( $\alpha V\beta 8$ ) on a second cell might change conformation of both LAPs and the subsequent release of active TGF-β1. GARP is depicted as mere cell membrane anchor and chaperone for the protein. The monoclonal antibody MHG-8 stabilizes this conformation and thereby prevents TGF-β1 release.<sup>126</sup>

Recent findings underline that many aspects of GARP function and influence on processes in the immune system remain nebulous. B cells also express GARP but only after stimulation of some of their Toll-like receptors and it inhibits proliferation, induces IgA class switching and confers immune tolerance by B cells.<sup>139,140</sup> Moreover, in our group strong indication of nuclear localization of GARP has been detected (see **Figure 51** and **Figure 54**). It is still unknown how GARP is transported into the nucleus and what functions it has in this compartment. Further studies will clarify if GARP acts as transcription factor or is able to control transcription indirectly. Besides, it would be beneficial to avoid unforeseen negative effects by GARP blockade in patients caused by TGF-β1 independent functions of GARP.

# *Introduction*

## **2.5 Rationale**

The last years saw a massive rise in cancer treatments modulating the immune system to use the bodies' own weapons to fight cancer (see 2.1.4). Depending on the tumor entity, those therapies were quite effective, resulting in long term survivors of previously deadly tumors. Despite this great success it is not yet the ultimate weapon against cancer. Immunotherapy with checkpoint inhibitors is not effective in every kind of cancer and even if it shows effectiveness, only up to every second patient can be saved. Deciphering the immune evasion of tumors, which renders immune therapy futile and finding ways to surpass it will be the key to rescue the other half of patients. Checkpoint inhibitors are a rather unspecific way to activate the T cell based immune response by blocking negative feedback loops. This lack in specificity results also in side effects. Finding tools to address and modify certain pro-tolerogenic immune cells is a promising route towards more effective manipulation of the immune system (see 2.1.3). Like in vaccinations, the body's own immune system is the best option in regards of specificity and rate of side effects in fighting pathogens or tumor cells revolting against their own host.

The boosting of immune therapies by reducing the suppression of the immune response against the tumor with drugs encapsulated in nanocarriers delivering the drugs mainly to the immune cells responsible for suppression is the long-term goal of this work and the *Collaborative Research Center 1066* itself.

Translational immune therapy must be developed in a system mimicking the situation in human cancer patients as closely as possible. The same holds true for nanocarriers, which should have the purpose to be translated into the clinic. They have to prove their eligibility in terms of stability, targeting and release in an *in vivo* system. Due to ethical, financial and time-related limitations, animal models are not well suited for larger screening experiments to find the best material and cargo for nanoparticle immune therapies. It was essential to develop an *in vitro* test system to screen potential nanocarriers to be used *in vivo*. Key readouts of this test system for translational applications are release kinetics to determine the effective dose of drugs encapsulated in nanoparticles like liposomes. Since drug release is linked to uptake and subsequent degradation of its carrier, this test system should be carried out with the intended target cells, in this case human macrophages and melanoma tumor cells. The latter are available as cell lines whereas the former can be generated from human monocytes extracted from blood. Doxorubicin (hydrochloride) was chosen as hydrophilic test drug because it is easy to detect via its fluorescence in the nuclei.

Side by side with pharmacokinetic readouts, the *in vitro* system should also serve as platform to analyze effects on phenotypes of immune cells and tumor cells by treatment with immunomodulatory drugs to the limited amount possible. A variety of methods must be employed to fully decipher the phenotype of a (immune) cell at the levels of mRNA, protein and function.

Completing the *in vitro* test system, a major part of this thesis was to develop a (human) melanoma model in humanized mice to cover the *in vivo* validation of the nanocarriers that have been selected based on *in vitro* results. Previous studies already established a xenograft tumor model in the same immunodeficient mouse strain.<sup>141</sup> This model had to be refined because it was based on the epidermoid carcinoma cell line A431 and used repetitive injections of PBMC gained from one single HLA-A2.1<sup>+</sup> donor in a large donation of white blood cells (leukapheresis). Those immune cells were injected intraperitoneally (i.p.) only and not at the tumor site resulting in very low immune cell counts in the tumor.



### **3 Materials and Methods**

#### **3.1 Human PMBC Isolation**

Buffy coats were obtained from healthy volunteers, with approval by the local ethical committee (Landesärztekammer Rhineland Palatine No. 837.019.10 (7028), approved on 4 March 2010). Peripheral blood mononuclear cells (PBMC) were isolated using density gradient centrifugation with Biocoll Separating Solution (#L6115, Merck, Darmstadt, Germany) at 800 g, 30 min and room temperature. After removal of the layer of PBMC at the interphase, the PBMC were washed two to three times with cold DPBS (#14190-094, Thermo Fisher Scientific, Waltham, USA) containing 1 mM EDTA (#A3553, AppliChem, Darmstadt, Germany) by centrifugation at 350 g, 7 min and 4°C. Cells were then suspended in DPBS containing 1 mM EDTA, counted (see 3.2) and stored at 4°C.

#### **3.2 Cell counting**

Leukocytes and tumor cells were counted by dilution (dilution factor in formula) with trypan blue solution (#T8154, Merck, Darmstadt, Germany), to exclude dead cells, in a Neubauer Improved bright line counting chamber (#612-5713, VWR International, Radnor, USA).  $x$  is the number of cells counted in one large quadrant which has a volume of  $0,1 \text{ mm}^3$  (=  $0,1 \mu\text{L}$ ). To calculate a concentration of cells per mL [ $1/\text{mL}$ ] the following formula has to be used:

$$\text{cell concentration} = \frac{x * \text{dilution factor}}{0,1 \mu\text{L}} = x * \text{dilution factor} * 10000 \frac{1}{\text{mL}}$$

#### **3.3 Cell culture macrophages**

$200 * 10^6$  human PBMC were seeded on 10 cm Cell Culture Dishes (#430167, Corning, New York, USA) in RPMI-1640 medium (#32404014, Thermo Fisher Scientific, Waltham, USA) supplemented with 1% GlutaMAX™ (#35050038, Thermo Fisher Scientific, Waltham, USA), 0.1% primocin (#ant-pm-2, InvivoGen, San Diego, USA) and 50 ng/mL human macrophage colony-stimulating factor (M-CSF) (#11343115, Immunotools, Friesoythe, Germany) and incubated for 1 hour at 37°C and 5% CO<sub>2</sub>. Non-adherent cells were flushed with prewarmed DPBS (#14190-094, Thermo Fisher Scientific, Waltham, USA). Adherent cells were cultured in the medium mentioned beforehand with additional 1% human plasma (see 3.4). After 5-7 days cells were harvested using Accutase for 1 hour at 4°C (#00-4555-56, Thermo Fisher Scientific, Waltham, USA). For polarization macrophages were treated with 100 ng/mL LPS (#tlrl-ebllps, InvivoGen, San Diego, USA) and 20 ng/mL human IFN- $\gamma$  (#11343536, Immunotools, Friesoythe, Germany) for the M1 phenotype or 20 ng/mL human IL-4 (#11340045, Immunotools, Friesoythe, Germany) for the M2 phenotype. All polarization steps were carried out for 24-48 hours with 50 ng/mL human M-CSF in the medium. Cells were harvested again with Accutase if needed.

#### **3.4 Generation of human plasma**

Buffy coats from up to 10 healthy individuals were centrifuged for 15 min at 400 g and room temperature without a density gradient. The supernatant was subjected to a second and third centrifugation step for 15 minutes at 800 g and 1000 g respectively at room temperature to further reduce the cellular content. Plasma from at least 5 different donors was pooled and incubated at 56°C for 20 minutes to deactivate the complement system. Insoluble denatured protein was removed by centrifugation at 3000 g for 15 minutes at room temperature. Human plasma was stored at -20°C until use in the culture of human primary cells (see 3.3).

# ***Materials and Methods***

## **3.5 Cell culture cell lines**

The UKRV-Mel-15 cell line originates from a lymph node biopsy of stage IV nodular melanoma from a 48-year-old female patient, harbors a *NRAS* Q61R mutation and is *BRAF* wild type. The Ma-Mel-19 cell line originates from a (sub)cutaneous biopsy of stage IV superficial spreading melanoma from a 62-year-old female patient, harbors a B-Raf V600E mutation and is N-Ras wild type.<sup>142,143</sup>

The MaMel-19 and UKRV-Mel-15a human melanoma cell lines were cultured with RPMI-1640 medium (#31870, Thermo Fisher Scientific, Waltham, USA) supplemented with 10% fetal bovine serum (FBS) (#10500064, Thermo Fisher Scientific, Waltham, USA), 1% GlutaMAX™ (#35050038, Thermo Fisher Scientific, Waltham, USA) and 0.1% primocin (#ant-pm-2, InvivoGen, San Diego, USA). Cells were detached via incubation with Trypsin-EDTA (#T3924, Merck, Darmstadt, Germany) for 5 min at 37°C every 3 to 4 days. Cell lines were regularly authenticated at Eurofins Genomics (Ebersberg, Germany), last time in April 2021. The resulting STR profiles were matched with the online databases of the German collection of microorganisms and cell cultures (DSMZ) (Available online: <http://www.dsmz.de/de/service/services-human-and-animal-cell>) and Cellosaurus database (Available online: <https://web.expasy.org/cellosaurus/>) references.

## **3.6 Flow cytometry**

Tissue samples were digested by incubation with Accumax (#00-4666-56, Thermo Fisher Scientific, Waltham, USA) for 1 hour at room temperature followed by manual disruption and passage through a 40 µm Cell strainer (#732-2757, VWR International, Radnor, USA). Cells cultured *in vitro* were harvested with Trypsin-EDTA (#T3924, Merck, Darmstadt, Germany) for 5 min at 37°C (cell lines) or with Accutase for 1 hour at 4°C (#00-4555-56, Thermo Fisher Scientific, Waltham, USA). Single cell suspension was treated either with Foxp3/Transcription Factor Staining Buffer Kit (#00-5523-00, Thermo Fisher Scientific, Waltham, USA) (T cell panel) or fixed with 1% PFA (#0335.1, Carl Roth, Karlsruhe, Germany) in DPBS (#14190-094, Thermo Fisher Scientific, Waltham, USA) and stained in FACS buffer containing 0.5% HSA (#10530a/96, CSL Behring, Marburg, Germany), 1 mM EDTA (#A3553, AppliChem, Darmstadt, Germany), 10 µg/mL human IgG (#EU/1/08/446/001, CSL Behring GmbH, Marburg, Germany) in DPBS (#14190-094, Thermo Fisher Scientific, Waltham, USA).

## Materials and Methods

**Table 1.** Antibodies for flow cytometry.

| Marker                | Clone  | Catalog number | Fluorophore | Vendor                   | Dilution |
|-----------------------|--------|----------------|-------------|--------------------------|----------|
| CD45                  | 5B1    | 130-113-122    | VioBlue     | Miltenyi Biotec          | 20x      |
| CD3                   | SK7    | 344840         | APC-Fire750 | BioLegend                | 20x      |
| CD4                   | REA623 | 130-113-227    | PE-Vio770   | Miltenyi Biotec          | 20x      |
| CD8                   | SK1    | 344734         | BV711       | BioLegend                | 20x      |
| CD206                 | DCN228 | 130-100-152    | PE-Vio770   | Miltenyi Biotec          | 20x      |
| CD163                 | GHI/61 | A15792         | PE          | Thermo Fisher Scientific | 20x      |
| CD36                  | AC106  | 130-095-480    | PerCP       | Miltenyi Biotec          | 20x      |
| CD14                  | MEM-15 | 21279143       | FITC        | Immunotools              | 20x      |
| HLA-DR                | L243   | 307650         | BV650       | BioLegend                | 40x      |
| CD68                  | Y1/82A | 565594         | BV711       | BD Biosciences           | 20x      |
| MS4A4A                | 818112 | FAB7797R       | AF647       | R&D Systems              | 20x      |
| CD3                   | UCHT-1 | 21270036       | APC         | Immunotools              | 20x      |
| CD4                   | RPA-T4 | 555347         | PE          | BD Biosciences           | 20x      |
| Ki67                  | REA183 | 130-120-416    | APC         | Miltenyi Biotec          | 20x      |
| Fixable Viability Dye | ---    | 65-0866-18     | eFluor506   | Thermo Fisher Scientific | 200x     |
| Fixable Viability Dye | ---    | 65-0865-18     | eFluor780   | Thermo Fisher Scientific | 200x     |

Flow cytometry was performed on a LSRII flow cytometer (BD Biosciences, Franklin Lakes, USA) and data was analyzed using Cytobank.<sup>144</sup>

### 3.7 Confocal microscopy

Confocal microscopy is a modification of brightfield fluorescence microscopy, which uses a pinhole to detect only light, which is emitted only from one horizontal plane, by photomultiplier tubes after excitation via lasers. Although magnification remains unchanged in comparison to brightfield microscopy, scattered light from above and below the focused horizontal plane is greatly reduced thereby creating sharp images from one focus plane (z-plane). Images from

## ***Materials and Methods***

consecutive z-planes can be combined to 3D object by special software. This technique is ideal to image cells, thin tissue slices and spheroids. Penetration depth is limited because the laser light can be scattered or absorbed on its way through the sample.

For the confocal imaging, the Leica SP8 with HyD Detector (Wetzlar, Germany) was used. Melanoma cell line Ma-Mel-19 were cultured for 24 h in ibidi  $\mu$ -slides 18 well or 8 well (#81816 or #80826, Ibidi, Gräfelfing, Germany), 15 000 cells/well each in 300  $\mu$ L medium. Macrophages were seeded at a density of 75 000 cells/well in 300  $\mu$ L medium.

For Doxorubicin detection cells were fixed with 1% PFA (#0335.1, Carl Roth, Karlsruhe, Germany) in DPBS (#14190-094, Thermo Fisher Scientific, Waltham, USA) for 20 min at room temperature. DNA was stained by 10  $\mu$ M Hoechst 33342 (#PK-CA707-40046, PromoCell, Heidelberg, Germany).

For GARP detection cells were checked for adherence and then fixed and permeabilized with a Foxp3/Transcription Factor Staining Buffer Kit (eBioscience, San Diego, CA, USA). For analysis of intracellular localization, cells were stained with anti-GARP rabbit polyclonal antibody (#AP17415PU-N, OriGene, Rockville, USA) for 20 min at RT in a 100-fold dilution as primary antibody and goat anti-Rabbit IgG (H+L), Superclonal™ Recombinant Secondary Antibody Alexa Fluor 555 (#A27039, Thermo Fisher Scientific, Waltham, USA) for 20 min at RT in a 100fold dilution as secondary antibody. Additionally, DNA was stained by 10  $\mu$ M Hoechst 33342 (#PK-CA707-40046, PromoCell, Heidelberg, Germany) and the membrane by NeuroDio (#PK-CA707-30021, PromoCell, Heidelberg, Germany) for 30 min at room temperature each.

For detection of binding of biotinylated liposomes to streptavidin or bovine serum albumin coated silica beads, liposomes and silica beads were incubated in 0,5 mL reaction tubes (#AM12350, Thermo Fisher Scientific, Waltham, USA) in 200  $\mu$ L DPBS (#14190-094, Thermo Fisher Scientific, Waltham, USA) for 30 min at room temperature. Afterwards, suspension was centrifuged at 400 g for 5 min at room temperature. Silica beads and liposomes were resuspended in 200  $\mu$ L DPBS and transferred to a 8 well ibidi  $\mu$ -slide and imaged at the same day.

For data analysis, Fiji was used.<sup>145</sup>

### **3.8 Seahorse analyzer**

Cellular metabolism was analyzed using the Cell Mito Stress Test Kit (#103010-100, Agilent, Santa Clara, USA) on an Agilent Seahorse XFp Analyzer according to the manufacturer's instructions. Oxygen consumption rate (OCR) and extracellular acidification rate (ECAR) is measured by solid state sensor probes in special cell culture plates resulting in conclusions about mitochondrial respiration and glycolysis of the (pure) living cell sample.

In brief, 20 000 human primary macrophages were seeded into cell culture miniplates (#103025-100, Agilent, Santa Clara, USA) the day before the measurement and polarized to M1 and M2 macrophages (see 3.3). Cell culture medium was replaced twice by Seahorse XF RPMI Medium pH 7,4 (#103576-100, Agilent, Santa Clara, USA) with 1% (v/v) added supplements glucose, pyruvate and glutamine (#103577-100, #103578-100, #103579-100, Agilent, Santa Clara, USA) and Cytokines (see 3.3) one hour and directly before the measurement. During the assay, the following concentrations were used: 1,5  $\mu$ M Oligomycin, 2  $\mu$ M carbonyl cyanide-4-(trifluoromethoxy)phenylhydrazone (FCCP) and 0,5  $\mu$ M Rotenone / Antimycin A. Cells were treated with 100  $\mu$ M Tasquinimod (#A12616, Adooq Bioscience, Irvine, USA) or with an equal amount of the solvent 3,3  $\mu$ L DMSO (#D2650, Merck, Darmstadt, Germany) as control.

# Materials and Methods

## 3.9 qPCR

qPCR or real-time polymerase chain reaction measures gene expression by quantifying the abundance of mRNA molecules in relation to so called housekeeping genes with a stable expression.

RNA from cells was extracted by lysis with chaotropic buffer containing guanidinium thiocyanate and purification with silica spin columns. The peqlab Micro RNA Kit (S-Line) (#732-2757, VWR International, Radnor, USA) was used according to the manufacturer's instructions without further DNA digestion.

After elution in RNase free water included in the kit, the RNA concentration was determined by absorption at 260 nm detected with a NanoDrop 2000 (Thermo Fisher Scientific, Waltham, USA) instrument. Long-time storage was at -80°C.

RNA was converted to cDNA by using iScript™ cDNA Synthesis Kit (#1708891, Bio-Rad Laboratories, Hercules, USA) according to the manufacturer's instructions. 100 ng of RNA was transcribed in a 20 µL reaction. If the RNA was too diluted to reach 100 ng, the maximum amount of RNA solution per reaction (15 µL) was used.

Targets amplified in real-time polymerase chain reaction (PCR) were detected by intercalation of the DNA dye SYBR Green I into the DNA helix. The reaction was performed in a 2x SYBR Green qPCR Master Mix (#B21203, bimake.com, Houston, USA) with high ROX on a 7300 Real-Time PCR System (Thermo Fisher Scientific, Waltham, USA) or no ROX on a Rotor-Gene Q (Qiagen, Hilden, Germany). Primer concentration in the final reaction mix was 100 nM.

**Table 2.** Primer sequences for qPCR.

| Target        | Sequence (5' → 3')     |
|---------------|------------------------|
| huSTAT6_s_1   | CAGATGAGCCTGCCCTTTGA   |
| huSTAT6_as_1  | CACCAATCCAAGTGCCCTGA   |
| huL4R_s_1     | ATTGTCATCCTGGCCGTCTG   |
| huL4R_as_1    | CACTGTGACCCCTGAGCATC   |
| huIDO1_s_1    | TGGCCAGCTTCGAGAAAGAG   |
| huIDO1_as_1   | TGGCAAGACCTTACGGACATC  |
| huCD206_s_1   | CGATCCGACCCTTCCTTGAC   |
| huCD206_as_1  | TGTCTCCGCTTCATGCCATT   |
| huCD163_s_1   | GTGATTTGCTCAAAGGGAGCAG |
| huCD163_as_1  | GCGTTAACTCGACCAATGGC   |
| huSNRPD3_s_1  | AAAGTAGGCCAGAGCCGAAC   |
| huSNRPD3_as_1 | TGGACATCTGGCAGTTCATGT  |
| huGAPDH_s_1   | TCCAAAATCAAGTGGGGCGA   |
| huGAPDH_as_1  | CAAATGAGCCCCAGCCTTCT   |

## Materials and Methods

|               |                        |
|---------------|------------------------|
| huYKL-40_s_1  | TCCAGTGCTGCTCTGCATAC   |
| huYKL-40_as_1 | CCAGGTGTCGATGTGATCGT   |
| huNOR1_s_1    | ACAGCACTCAAAGCCCACTG   |
| huNOR1_as_1   | GTATCTTGCGCGCTGAATGG   |
| huCD36_s_1    | AAAATGGGCTGTGACCGGAA   |
| huCD36_as_1   | TCTTCGAGGACAACCTTGCTTT |
| MS4A4A_s_1    | TCTGCTGCCATGACAACCAT   |
| MS4A4A_as_1   | TGCACAACCCCAAGGACTTT   |
| huL4R_2_s     | CCTACCTAGAACCCTCCCTCC  |
| huL4R_2_as    | CCTGTAGGAGTTGTGCCACTT  |
| huL4R_3_s     | CCAAGTGGCACAACCTCCTACA |
| huL4R_3_as    | GCTGACATAGCACAAACAGGC  |
| huPPARG_2_s   | TGCGAAAGCCTTTTGGTGAC   |
| huPPARG_2_as  | GGGCGGTCTCCACTGAGAATA  |
| huLMNA_s      | TCAACTCCACTGGGGAAGAAG  |
| huLMNA_as     | GTCGTCCTCAACCACAGTCA   |
| huPD-L1_s     | TCCTGAGGAAAACCATACAGC  |
| huPD-L1_as    | GCCAGAGGTAGTTCTGGGATG  |
| huPD-L2_s     | CAGTGCTATCTGAACCTGTGGT |
| huPD-L2_as    | GCCAGGTGTTGGCTAGTCTT   |
| huL1RN_s      | GGAGGGAAGATGTGCCTGTC   |
| huL1RN_as     | TCAGTGATGTAACTGCCTCCA  |
| HIF1alpha_s   | CACAGAAATGGCCTTGTGAA   |
| HIF1alpha_as  | CCAAGCAGGTCATAGGTGGT   |

### 3.10 ImageStream<sup>1</sup>

The Amnis® ImageStream®<sup>X</sup> Mk II (Luminex, Austin, USA) is an imaging flow cytometer which functions like a conventional flow cytometer, but it records the cell's fluorescence by taking images with fluorescence microscopes instead of detecting signals by photomultiplier tubes. Those multichannel images permit to resolve the cellular location

<sup>1</sup> Data acquisition and analysis was carried out by [REDACTED], research group of [REDACTED] at the Dermatology of the University Medical Center Mainz.

## ***Materials and Methods***

of the fluorescence signal rather than recording whole cell fluorescence like in conventional instruments. Furthermore, cells can be analyzed for morphological features and for cell-cell-contacts, if sample preparation has been gentle enough.

UKRV-Mel-15a cells were cultured in 24 well plates at a density of  $2.5 \cdot 10^5$  cells per well in 1 mL of their cell culture medium (see 3.5) for 2 days. Cells were treated with different Doxorubicin (#D1515, Merck, Darmstadt, Germany) containing liposome species or with the free substance as control for 30 minutes and 4 hours. Both time points ended simultaneously. After the treatment, cells were harvested with Accutase (#00-4555-56, Thermo Fisher Scientific, Waltham, USA) for 15 minutes at 4°C, sedimented by centrifugation at 400 g, 5 minutes, 4°C and stained with Hoechst 33342 (#PK-CA707-40046, PromoCell, Heidelberg, Germany) for 30 minutes at 4°C as DNA stain. Fixation was done with 4% paraformaldehyde (#0964.1, Carl Roth, Karlsruhe, Germany) containing DPBS for 15 minutes at 4°C. Storage of cells was in DPBS at 4°C. Shortly before measurement, cells were centrifuged in 5 mL polystyrene round-bottom tubes with cell-strainer caps (#352235, Corning, New York, USA) to remove aggregates.

Cells were analyzed on an Amnis® ImageStream<sup>®</sup>X Mk II using AMNIS IDEAS Software (Luminex, Austin, USA). Debris and dead cells were excluded from analysis. Due to staining of the cell nuclei by Hoechst 33342, it was possible to distinguish fluorescence originating from the cytoplasm or nucleus.

### **3.11 NanoString**

The NanoString nCounter® SPRINT Profiler (NanoString Technologies, Seattle, USA) directly detects up to 800 RNA sequences via capture and reporter probes, the latter carrying a molecular fluorescence barcode. After hybridization, the complex of the RNA molecule and both probes is immobilized on a glass slide of a microfluidic cartridge and detected by a built-in fluorescence microscope. The number of RNA targets is counted directly and normalized using a combination of housekeeping genes.

Extracted RNA from tumor samples (see 3.9 for extraction and 3.13 for mouse experiments) were analyzed on a nCounter® SPRINT Profiler using the PanCancer IO 360™ Panel (NanoString Technologies, Seattle, USA). 50 ng of total RNA was used per lane of the cartridge. Data analysis was performed on the ROSALIND™ online platform (OnRamp Bioinformatics, San Diego, USA).

### **3.12 Liposome preparation<sup>¶</sup>**

Lipids dissolved in organic solvents were first combined in a PCR tube (#G001 F, Kisker Biotech, Steinfurt, Germany) in proportion to their mol-% ratio (see **table 2**) and then solvents were removed using a SpeedVac vacuum concentrator (Thermo Fisher Scientific, Waltham, USA). For complete drying, they were freeze-dried at -80°C on an Alpha 2-4 LD (Martin Christ Gefriertrocknungsanlagen, Osterode am Harz, Germany). For complete separation of DMSO (#D2650, Merck, Darmstadt, Germany), purified water (#Direct-Q® 5, Merck, Darmstadt, Germany) was added to lipid tasquinimod mixture and lyophilized again. This step was repeated several times and afterwards lipids were stored at -20°C until use.

---

<sup>¶</sup> This part was carried out by ██████████, research group of ██████████ at the Institute of Pharmacy and Biochemistry of the Johannes Gutenberg University Mainz.

## ***Materials and Methods***

To prepare liposomes by dual centrifugation, 9.3  $\mu$ L DPBS (#14190-094, Thermo Fisher Scientific, Waltham, USA) and 325 mg beads (#96035, Typ ZY-S 0,3 – 0,4 mm, Sigmund Lindner, Warmensteinach, Germany) were added to 5 mmol dry lipids and incubated for 10 min at room temperature. The mixture was mixed for 20 min at 2500 rpm and 4°C using a Zentrifuge 380 R (Andreas Hettich, Tuttlingen, Germany). 77,2  $\mu$ L DPBS (#14190-094, Thermo Fisher Scientific, Waltham, USA) were added to the resulting phospholipid gel and homogenized twice for 2 min at 2500 rpm and 4°C again.

After dual centrifugation, 100  $\mu$ L of liposome suspension was injected into Agilent 1100 HPLC (Agilent, Santa Clara, USA) system at 1 mL / min DPBS flow rate of and a BioRAD UNO Q1 column (Bio Rad Laboratories, Hercules, USA) filled with 2 mL Sephacryl S500-HR (#GE17-0613-01, Merck, Darmstadt, Germany) was used as size exclusion column to separate unconfined tasquinimod. The purified liposomes were automatically collected in 2.0 mL vials (#XC84.1 Carl Roth, Karlsruhe, Germany) by a fraction collector.

Physicochemical properties (diameter, PDI & zeta potential) of liposomes were determined by dynamic light scattering (DLS) on a Malvern Zetasizer (Malvern Panalytical, Malvern, United Kingdom). 2  $\mu$ L liposome emulsion or 10  $\mu$ L of purified liposome dispersion were measured in 1 mL DPBS (#14190-094, Thermo Fisher Scientific, Waltham, USA).

For quantification of tasquinimod, 10  $\mu$ L liposome suspension was purified by HPLC using size exclusion chromatography and 1 mL / min water flow rate. A fraction collector automatically collected the purified particles. The liposome fraction was rapidly cooled with liquid nitrogen to 196°C and then thawed for 15 min in an ultrasonic bath (Sonorex Super RK 52, Bandelin electronic, Berlin, Germany) to break up the particles.

The determination of the drug concentration was performed by LC-MS/MS (Q-ToF Premier™ Micromass MS Technologies, Waters, Milford, USA). Samples were eluted with 0.35 mL / min 0.1% aqueous formic acid (#09676-100 mL, Honeywell, Morristown, USA) and acetonitrile (#34147-2 2.5L, Honeywell, Morristown, USA) (60 vol-% : 40 vol-%) over a Synergi 4  $\mu$ m Fusion-RP 80 Å column (Phenomenex, Aschaffenburg, Germany), at 20°C column temperature, 20 eV collision energy and negative electron spray ionization. The mean Tasquinimod concentration in liposomes was 69,12  $\mu$ g/mL.



# Materials and Methods

**Table 3.** Liposome compositions in mol%.

|                                 | EPC    | Chol  | DOPG  | DOPC  | DODAP | DOTAP | DMPC  | CHEMS | Biotin-PEG-DSPG | MPEG-DSPE 2000 | DOPE-Biotin | DOPE | DiD  |
|---------------------------------|--------|-------|-------|-------|-------|-------|-------|-------|-----------------|----------------|-------------|------|------|
| L0                              | 54,9%  | 45,0% |       |       |       |       |       |       |                 |                |             |      | 0,1% |
| C83                             |        |       | 66,4% |       |       | 28,5% |       | 5,0%  |                 |                |             |      | 0,1% |
| C73                             |        |       |       |       | 28,5% |       | 66,4% | 5,0%  |                 |                |             |      | 0,1% |
| C63                             |        |       |       | 62,9% | 27,0% |       |       | 10,0% |                 |                |             |      | 0,1% |
| GB10 (C83 + 5% Biotin)          |        |       | 61,4% |       |       | 28,5% |       | 5,0%  | 5,0%            |                |             |      | 0,1% |
| GB11 (C83 + 5% PEG-2000)        |        |       | 61,4% |       |       | 28,5% |       | 5,0%  |                 | 5,0%           |             |      | 0,1% |
| GB12 (L0 + 5% Biotin)           | 52,2%  | 42,8% |       |       |       |       |       |       | 5,0%            |                |             |      | 0,1% |
| GB13 (L0 + 5% PEG-2000)         | 52,2%  | 42,8% |       |       |       |       |       |       |                 | 5,0%           |             |      | 0,1% |
| GB14 (C83 + 10% Biotin)         |        |       | 59,8% |       |       | 25,7% |       | 4,5%  | 10,0%           |                |             |      | 0,1% |
| GB15 (C83 + 10% PEG-2000)       |        |       | 59,8% |       |       | 25,7% |       | 4,5%  |                 | 10,0%          |             |      | 0,1% |
| GB16 (L0 + 10% Biotin)          | 49,4%  | 40,5% |       |       |       |       |       |       | 10,0%           |                |             |      | 0,1% |
| GB17 (L0 + 10% PEG-2000)        | 49,4%  | 40,5% |       |       |       |       |       |       |                 | 10,0%          |             |      | 0,1% |
| GB18 (C83 + 5% DOPE-Biotin)     |        |       | 61,4% |       |       | 28,5% |       | 5,0%  |                 |                | 5,0%        |      | 0,1% |
| GB19 (C83 + 5% DOPE)            |        |       | 61,4% |       |       | 28,5% |       | 5,0%  |                 |                |             | 5,0% | 0,1% |
| GB20 (L0 + 5% DOPE-Biotin)      | 52,2%  | 42,8% |       |       |       |       |       |       |                 |                | 5%          |      | 0,1% |
| GB21 (L0 + 5% DOPE)             | 52,2%  | 42,8% |       |       |       |       |       |       |                 |                |             | 5%   | 0,1% |
| GB30 (L0 + 0.5% DOPE-Biotin)    | 54,4%  | 44,9% |       |       |       |       |       |       |                 |                | 0,5%        |      | 0,1% |
| GB31 (L0 + 0.5% DOPE)           | 54,4%  | 44,9% |       |       |       |       |       |       |                 |                |             | 0,5% | 0,1% |
| GB32 (L0 + 0.1% DOPE-Biotin)    | 54,8%  | 45,0% |       |       |       |       |       |       |                 |                | 0,1%        |      | 0,1% |
| GB33 (L0 + 0.1% DOPE)           | 54,8%  | 45,0% |       |       |       |       |       |       |                 |                |             | 0,1% | 0,1% |
| GB34 (C83 + 0.5% DOPE-Biotin)   |        |       | 66,1% |       |       | 28,4% |       | 4,9%  |                 |                | 0,5%        |      | 0,1% |
| GB35 (C83 + 0.5% DOPE)          |        |       | 66,1% |       |       | 28,4% |       | 4,9%  |                 |                |             | 0,5% | 0,1% |
| GB36 (C83 + 0.1% DOPE-Biotin)   |        |       | 66,3% |       |       | 28,5% |       | 5,0%  |                 |                | 0,1%        |      | 0,1% |
| GB37 (C83 + 0.1% DOPE)          |        |       | 66,3% |       |       | 28,5% |       | 5,0%  |                 |                |             | 0,1% | 0,1% |
| GB38 (L0 + 1% PEG-Biotin)       | 53,9%  | 45,0% |       |       |       |       |       |       | 1,00%           |                |             |      | 0,1% |
| GB39 (L0 + 0.05% PEG-Biotin)    | 54,85% | 45,0% |       |       |       |       |       |       | 0,05%           |                |             |      | 0,1% |
| GB40 (L0 + 0.25% PEG-Biotin)    | 54,65% | 45,0% |       |       |       |       |       |       | 0,25%           |                |             |      | 0,1% |
| GB52 (C63 + 1 mol-% PEG-Biotin) |        |       |       | 61,9% | 27,0  |       | 10,0% |       | 1,0%            |                |             |      | 0,1% |
| GB53 (C73 + 1 mol-% PEG-Biotin) |        |       |       |       | 28,5% |       | 65,4% | 5,0%  | 1,0%            |                |             |      | 0,1% |
| GB54 (C63 + 1 mol-% PEG)        |        |       |       | 61,9% | 27,0  |       | 10,0% |       |                 | 1,0%           |             |      | 0,1% |
| GB55 (C73 + 1 mol-% PEG)        |        |       |       |       | 28,5% |       | 65,4% | 5,0%  |                 | 1,0%           |             |      | 0,1% |
| L0 anchor experiments*          | 50%    | 45%   |       |       |       |       |       |       |                 |                |             |      | 0,0% |

\*+ 5% alkyne lipid<sup>146</sup>

## Materials and Methods

| Abbreviation   | Full name   |
|----------------|---|
| EPC            | L- $\alpha$ -phosphatidylcholine (Egg, Chicken),  |
| Chol           | cholesterol   |
| DOPG           | 9-octadecenoic acid (9Z)-1,1'-[(1R)-1-[[[(2,3-dihydroxypropoxy)hydroxyphosphinyl]oxy]methyl]-1,2-ethanediyl] ester, monosodium salt                                     |
| DOPC           | 1,2-dioleoyl-sn-glycero-3-phosphatidylcholine   |
| DODAP          | 9Z-octadecenoic acid, 1,1'-[1-[(dimethylamino)methyl]-1,2-ethanediyl] ester   |
| DOTAP          | 1,2-dioleoyl-3-trimethylammoniumpropane, monochloride   |
| DMPC           | 1,2-dimyristoyl-sn-glycero-3-phosphatidylcholine  |
| CHEMS          | cholesteryl hemisuccinate   |
| MPEG-DSPE 2000 | $\alpha$ -[6-hydroxy-6-oxido-1,12-dioxo-9-[(1-oxooctadecyl)oxy]-5,7,11-trioxa-2-aza-6-phosphanonacos-1-yl]- $\omega$ -methoxy-poly(oxy-1,2-ethanediyl), monosodium salt |
| DOPE           | 1,2-dioleoyl-sn-glycero-3-phosphoethanolamine   |
| DiD            | 2-[5-(1,3-dihydro-3,3-dimethyl-1-octadecyl-2H-indol-2-ylidene)-1,3-pentadien-1-yl]-3,3-dimethyl-1-octadecyl-3H-indolium, monoperchlorate                                |
| DSPG           | 1,2-Distearoyl-sn-glycero-3-phosphoglycerol   |

### 3.13 Animal experiments

Animal experiments were approved by local authorities (G 15-1-070, Landesuntersuchungsamt Rheinland-Pfalz, Germany). NOD.Cg-Mcph1Tg(HLA-A2.1)1Enge Prkdcscid/DvsJ mice (#006609) acquired from The Jackson Laboratory (Bar Harbor, USA) were injected subcutaneously (s.c.) with  $2 \times 10^6$  Ma-Mel-19 melanoma cells at an age older than 8 weeks. Tumor volume was measured using a caliper and the formula  $V = \frac{length}{2} * width^2$ . After randomization  $20 \times 10^6$  human PBMC were injected s.c. and i.p. each. Tasquinimod (#S7617, Selleckchem, Munich, Germany) was applied at doses of 5 mg/kg and 1 mg/kg weekly s.c. at the tumor site in a 1:4 mixture of DMSO (#D2650, Merck, Darmstadt, Germany) and sodium chloride solution (0,9%) (#3200910, B. Braun, Melsungen, Germany). Control group received the mixture without the compound. After 3 weeks of treatment the animals were sacrificed and *ex vivo* analysis of the tumors and the spleen was performed. All animals were housed under specific pathogen-free conditions in the central animal facility of the Johannes Gutenberg-University in Mainz, and experiments were performed in accordance with relevant laws and institutional guidelines.

## *Materials and Methods*

### **3.14 chipcytometry<sup>III</sup>**

Chipcytometry is a form of iterative imaging cytometry, imaging cells or tissue with a fluorescence microscope on special chips. Antibodies labeled with fluorophores are used to stain protein antigens. Due to iterative staining cycles with new antibody cocktails and bleaching of the fluorophores from the previous cycle, theoretically an unlimited number of markers could be stained.

Tissue sections with 7 µm thickness were prepared at a standard cryostat and mounted on glass coverslips. The sections were fixed by immersion in ice-cold 100% acetone (#9372.1, Carl Roth, Karlsruhe, Germany) for 5 minutes, followed by serial immersion in 90% ethanol (#5054.1, Carl Roth, Karlsruhe, Germany), 70% ethanol and PBS for 3 minutes at 4°C, respectively. The glass coverslips with the fixed tissue samples were loaded onto ZellSafe™ Tissue Chips (#28050606/02-010, Zellkraftwerk, Leipzig, Germany), chips were filled up with storage buffer (Zellkraftwerk, Leipzig, Germany) and stored at 4°C until and in between staining cycles.

Chipcytometry analysis was performed on a ZellScanner One® instrument (Zellkraftwerk, Leipzig, Germany). Each of the 3 tissue samples was stained and imaged with an iterative multiplex staining assay summarized in table 1. Tissue chips were rinsed with 5 ml of wash buffer before starting an imaging cycle consisting of photobleaching for 40 sec per scanned position, followed by imaging of tissue autofluorescence and subsequently antibody staining and imaging of fluorescence signal. Staining was performed by diluting the antibodies in storage buffer and pipetting the working solution into the chip flow chamber. After incubation for 15 minutes at room temperature, the chip was rinsed thoroughly with wash buffer before imaging. This process was repeated until all biomarkers were stained and imaged. In one of the cycles the cell nuclei were stained by incubating with 0.05 µg/µl Hoechst 33342 (#H3570, Thermo Fisher Scientific, Waltham, USA) in storage buffer for 5 min at room temperature.

---

<sup>III</sup>This part was carried out by the company Zellkraftwerk GmbH (now Bruker Corporation).

# Materials and Methods

**Table 4.** Multiplex staining Chipcytometry.

| No. | Cycle | Marker | Clone        | Catalog number | Fluorophore  | Vendor                   |
|-----|-------|--------|--------------|----------------|--------------|--------------------------|
| 1   | 1     | CD25   | M-A251       | 555432         | PE           | BD Biosciences           |
| 2   | 2     | FOXP3  | 236A/E7      | 12-4777-42     | PE           | Thermo Fisher Scientific |
| 3   | 3     | CD3    | UCHT1        | 563546         | BUV395       | BD Biosciences           |
| 4   | 3     | CD4    | RPA-T4       | 300530         | PerCP-Cy5.5  | Biolegend                |
| 5   | 3     | CD8    | RPA-T8       | 301008         | PE           | Biolegend                |
| 6   | 4     | CD14   | HCD14        | 325622         | PerCP-Cy5.5  | Biolegend                |
| 7   | 4     | CD56   | AF12-7H3     | 130-113-307    | PE           | Miltenyi Biotech         |
| 8   | 4     | CD68   | KP1          | sc-20060       | AF488        | Santa Cruz               |
| 9   | 5     | CD45   | HI30         | 304028         | PerCP-Cy5.5  | Biolegend                |
| 10  | 5     | CD45RO | REA611       | 130-113-559    | PE           | Miltenyi Biotech         |
| 11  | 5     | CD45RA | HI100        | 740298         | BUV395       | BD Biosciences           |
| 12  | 6     | DNA    | ---          | H3570          | BUV395+BV421 | Thermo Fisher Scientific |
| 13  | 7     | HLA-DR | L243         | 307606         | PE           | Biolegend                |
| 14  | 8     | CD279  | EH12.1       | 560795         | PE           | BD Biosciences           |
| 15  | 9     | CD86   | 2331 (FUN-1) | 555658         | PE           | BD Biosciences           |
| 16  | 10    | CD105  | 43A3         | 323206         | PE           | Biolegend                |
| 17  | 11    | CD366  | 7D3          | 563422         | PE           | BD Biosciences           |

Resulting images were analyzed with ZellExplorer data analysis software (Zellkraftwerk, Leipzig, Germany). Net-fluorescence images were generated by subtracting the autofluorescence from the staining fluorescence image for each cycle and position. Cell segmentation was performed based on the nuclear DNA stain and for each segmented cell the fluorescence values for each marker stained in the multiplex assay were calculated, resulting in a single cell resolution quantitative data set. This data set was then analyzed by employing a gating strategy to identify cell populations of interest based on biomarker expression.

## ***Materials and Methods***

### **3.15 Immunohistochemistry<sup>IV</sup>**

Tumor specimens were immunohistochemically analyzed for infiltration with CD45<sup>+</sup>, CD4<sup>+</sup> and CD8<sup>+</sup> immune cells. Tumor sections (4 µm) were prepared from formalin-fixed, paraffin-embedded tissue. After deparaffinization and rehydration, slides were boiled. For CD45 stains, slides were boiled in Target Retrieval Solution, Low pH (#K800521-2, Agilent, Santa Clara, USA). For CD4 and CD8 stains, slides were boiled in Target Retrieval Solution, High pH (#K800421-2, Agilent, Santa Clara, USA). Endogenous peroxidase activity was blocked by Peroxidase-Blocking Solution (#S2023, Agilent, Santa Clara, USA) for 5 min. Sections were blocked with Normal Horse Serum Blocking Solution (#S-2000-2, Vector Laboratories, Burlingame, USA). Anti-human CD45 (clone M0701, Agilent, Santa Clara, USA), anti-human CD8 (clone M7103, Agilent, Santa Clara, USA) and anti-human CD4 (#104R-26, Merck, Darmstadt, Germany) were applied as primary mAb. For CD45 slides were incubated with a secondary biotinylated Horse Anti Mouse IgG Antibody (#BA 2000 1.5, Vector Laboratories, Burlingame, USA). The antigen detection by a color reaction with 3,3'-diaminobenzidine (#K346711 2, DAB+, Agilent, Santa Clara, USA) catalyzed by VECTASTAIN® Elite ABC-HRP Reagent, Peroxidase, R.T.U. (#PK 2000-2, Vector Laboratories, Burlingame, USA). For CD4 and CD8 samples were stained with EnVision Detection Systems Peroxidase/DAB, Rabbit/Mouse (#K5007, Agilent, Santa Clara, USA). Both methods were counterstained with Mayer's hemalum solution (#109249, Merck, Darmstadt, Germany).

Tissue samples were imaged by the tissue bank of the University Medical Center Mainz using a Hamamatsu NanoZoomer 2.0HT. IHC data was analyzed using QuPath.<sup>147</sup>

Human melanoma metastasis were stained by the tissue bank of the University Medical Center Mainz using: anti-human PU.1 (#2258, Cell Signaling Technology, Danvers, USA), anti-human CD296 (#MAB25341, Bio-Techne, Minneapolis, USA), anti-human PPARγ (#sc-7273, Santa Cruz Biotechnology, Dallas, USA) and anti-human CD68 (#GA61361-2, Agilent, Santa Clara, USA).

### **3.16 Quantification of Doxorubicin content in liposomes**

Liposomes were cracked by incubation in DPBS containing 5% (v/v) Triton® X 100 (#3051.3, Carl Roth, Karlsruhe, Germany) at room temperature for 15 minutes in a 96-well microtiter plate (#781662, BRAND, Wertheim, Germany). Absorbance was recorded at 488 nm wavelength on a Sense Beta Plus microplate reader (Hidex Oy, Turku, Finland). Doxorubicin content was calculated by comparing absorbance of the liposome dispersion to a standard curve of Doxorubicin Hydrochloride (#D1515, Merck, Darmstadt, Germany) solved in DPBS. Top standard concentration was 1,725 mM.

### **3.17 Targeting of biotin liposomes**

Non-fluorescent bovine serum albumin (BSA) and red-fluorescent streptavidin (SA) silica particles (#43-21-503 & #40-19-503, micromod Partikeltechnologie GmbH, Rostock, Germany) with a diameter of 5 µm were incubated in 96-well plates (#781602, BRAND, Weinheim, Germany) in 200 µL DPBS (#14190-094, Thermo Fisher Scientific, Waltham, USA) at a concentration of 156,25 µg/mL (each particle) with biotin and control liposomes (DiD labeled) at 2,5% (v/v) for 20 min at room temperature. Particles were washed through centrifugation at 400 g for 5 min and resuspended in 200 µL

---

<sup>IV</sup> Formalin-fixed tissue was processed and stained (CD45, CD4, CD8 and GARP) the core facility histology of the Research Center for Immunotherapy (FZI), of the Johannes Gutenberg University Mainz.

## ***Materials and Methods***

DPBS. Binding of liposomes to silica particles was quantified by their DiD fluorescence via flow cytometry. Due to their size forward and sideward scatter signals of silica particles could be analyzed in a flow cytometer (see 3.6). BSA and SA silica particles were distinguished by the red-fluorescent (PE channel) labeling of the latter.

### **3.18 Anchor stability experiments**

L0 liposomes (see 3.12) were modified with the fluorescent dye atto 488-azide (#AD 488-101, Atto-Tec, Siegen, Germany).<sup>146</sup>

Melanoma cells were cultured as described in 3.5. For analysis of anchor stability UKRV-Mel-15a were seeded at a density of  $10^5$  cells per well of a 24 well plate (#3524, Corning, Corning, USA) in 1 mL of cell culture medium and incubated with liposomes at a concentration of 1% or 5% (v/v) for 4 or 24 hours at 37°C and 5% CO<sub>2</sub>. For flow cytometric analysis cells were harvested by removing the supernatant, adding Trypsin-EDTA (#T3924, Merck, Darmstadt, Germany) for 5 minutes at 37°C. Cells were stained with Fixable Viability Dye eFluor™ 780 and fixed with 4% formaldehyde solution (see 3.6).

### **3.19 siRNA transfection**

For screening of transfection efficacy  $5 \cdot 10^4$  pre-polarized M2 macrophages per well (see 3.3) were seeded in 96 well cell culture plates in 100 µL macrophage medium. 10 µL transfection mix consisting of 0,2 µL Viromer BLUE (Lipocalyx, Halle, Germany), 7,3 µL buffer BLUE (Lipocalyx, Halle, Germany) and 2,5 µL siRNA Stock ( $c = 1 \mu\text{M}$ ). Final siRNA concentration during the assay was 25 nM and cells were transfected for 48 h. IL-4 (20 ng/mL) was added during culture. Knockdown was analyzed using qPCR (see 3.9) and effects on marker expression using flow cytometry (see 3.6).

siRNA: IL4R, PPARG, NR4A3, STAT6 (all siGENOME smart-pool, Horizon Discovery LTD, Cambridge, United Kingdom) & siGENOME Non-Targeting siRNA Pool #2 (#D-001206-14-20, Horizon Discovery LTD, Cambridge, United Kingdom).

### **3.20 siRNA transfection with liposomes**

Human monocyte-derived macrophages (see 3.3) were seeded into 24 well plates (#3524, Corning, Corning, USA) at a density of  $2,5 \cdot 10^5$  cells per well in 1 mL culture medium. Cells were incubated with 1,1% (v/v) siRNA-loaded liposomes, 50 nM Viromer BLUE (see 3.19) or 50 nM free siRNA for 24 hours. After medium change cells were cultured for further 24 hours (48 hours in total). siRNA content in liposomes was determined by fluorescence: L0 PPARG (579,1 nM), L0 Neg. Control (871,0 nM), C83 PPARG (2477,7 nM) and C83 Neg. Control (2926,4 nM). Transfection efficacy was analyzed by qPCR (see 3.9).

### **3.21 Tasquinimod effect on human PBMC**

Human PBMC were isolated as described in 3.1. 24 well plates (#3524, Corning, Corning, USA) were pre-coated with mouse anti-human CD3 antibody (#566685, BD Biosciences, Franklin Lakes, USA) at a concentration of 1 µg/mL in 200 µL/well DPBS (#14190-094, Thermo Fisher Scientific, Waltham, USA) for 1 hour at 37°C. For analysis of cell proliferation cells were labeled with 1 µM CFSE (#65-0850-84, Thermo Fisher Scientific, Waltham, USA) staining solution for 20 min at 37°C. Cells were washed with cell culture medium and centrifuged for 5 min at 400 g.  $3 \cdot 10^6$  cells

## ***Materials and Methods***

per well of a 24 well plate were seeded in 1 mL of X-VIVO™ 15 medium (#BE02-060F, Lonza Group, Basel, Switzerland) supplemented with 0,5 µg/mL anti-human CD28 antibody (#555725, BD Biosciences, Franklin Lakes, USA) and incubated with 10 µM or 100 µM Tasquinimod (#A12616, Adooq Bioscience, Irvine, USA) for 3 days at 37°C and 5% CO<sub>2</sub>. For flow cytometric analysis cells were harvested by removing the supernatant, sedimented by centrifugation at 400 g, 5 minutes, 4°C and stained with Fixable Viability Dye eFluor™ 780, anti-human CD3-APC, anti-human CD4-PE and anti-human CD8-BV711 (see 3.6).

### **3.22 Tasquinimod effect on human melanoma cell lines**

Melanoma cells were cultured as described in 3.5. For analysis of cell proliferation cells were labeled with 1 µM CFSE (#65-0850-84, Thermo Fisher Scientific, Waltham, USA) staining solution for 20 min at 37°C. Cells were washed with cell culture medium and centrifuged for 5 min at 400 g. 10<sup>5</sup> cells per well of a 24 well plate (#3524, Corning, Corning, USA) were seeded in 1 mL of cell culture medium and incubated with 10 µM or 100 µM Tasquinimod (#A12616, Adooq Bioscience, Irvine, USA) for 3 days at 37°C and 5% CO<sub>2</sub>. For flow cytometric analysis cells were harvested by removing the supernatant, adding 200 µL Accutase for 1 hour at 4°C (#00-4555-56, Thermo Fisher Scientific, Waltham, USA) for 15 minutes at 4°C and sedimented by centrifugation at 400 g, 5 minutes, 4°C and stained with Fixable Viability Dye eFluor™ 780 and anti-human Ki67-APC using the Foxp3 / Transcription Factor Staining Buffer Set (#00-5523-00, Thermo Fisher Scientific, Waltham, USA) (see 3.6).

### **3.23 Tasquinimod effect on human monocyte-derived macrophages**

Human monocyte-derived macrophages were cultured as described in 3.3. 2,5\*10<sup>5</sup> cells per well of a 24 well plate (#174899, Thermo Fisher Scientific, Waltham, USA) were seeded in 1 mL of cell culture medium and polarized for 48h in total at 37°C and 5% CO<sub>2</sub>. 24h after addition of cytokines Tasquinimod (10 µM or 100 µM) (#A12616, Adooq Bioscience, Irvine, USA) was added. For flow cytometric analysis cells were harvested by removing the supernatant, adding 200 µL Accutase for 1 hour at 4°C (#00-4555-56, Thermo Fisher Scientific, Waltham, USA) for 15 minutes at 4°C and sedimented by centrifugation at 400 g, 5 minutes, 4°C and stained with Fixable Viability Dye eFluor™ 506 anti-human CD14, anti-human CD163, anti-human CD36, anti-human CD206, anti-human MS4A4A, anti-human HLA-DR and anti-human CD68 (see 3.6).

### **3.24 Statistics**

Statistical tests were performed by GraphPad Prism 9 (GraphPad Inc., San Diego, USA). The test method and the conditions are stated in the figure caption.

# 4 Results and Discussion

## 4.1 *in vitro* macrophage culture M0/M1/M2

Tumor associated macrophages (TAM) are important regulators of tolerance in the tumor microenvironment and can prevent an effective anti-tumor immune response (see 2.1.3). Targeting those TAM with nanocarriers containing immunomodulators is a promising strategy to overcome this immunosuppression and enable responses against the tumor *in vivo*. Therefore, *in vitro* generated macrophages, polarized to their to most extreme states of polarization M1 (IFN- $\gamma$  and LPS) and M2 (IL-4), are an excellent test system for siRNA transfection, repolarization through immunomodulators like Tasquinimod and particle uptake and toxicity in general.

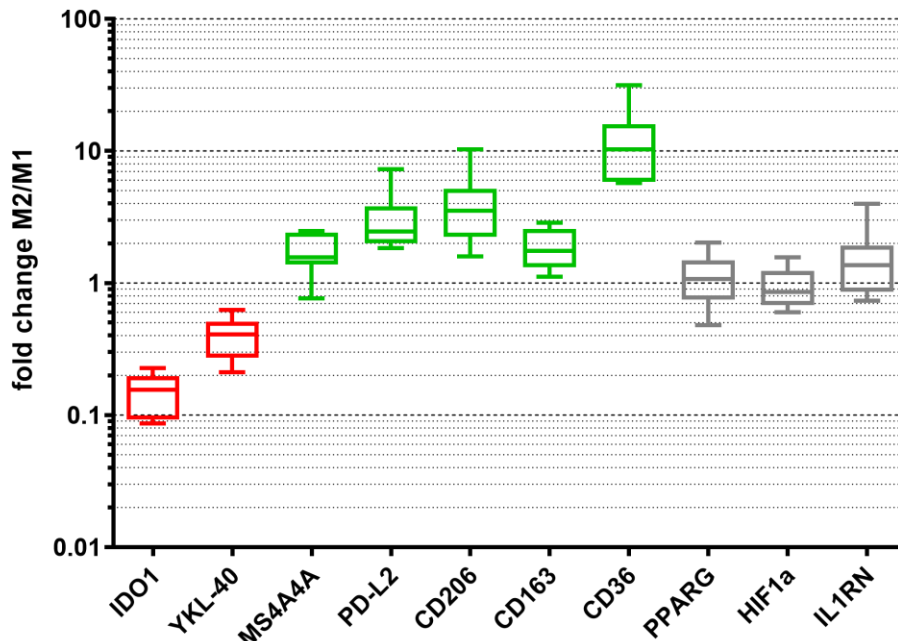
Macrophages were generated by culturing monocytes from the peripheral blood of human blood donors for around 7 days in the presence of M-CSF, a well-established strategy.<sup>148,149</sup> Although well-established, it is an absolute necessity to characterize these macrophages very thoroughly to be able to recognize repolarization and to overcome interindividual variations which cannot be avoided in human primary cells. Human macrophage-like cell lines like the THP-1 cell line would not show these variations but differ from primary macrophages in the body and require stimulation with 12-O-Tetradecanoylphorbol-13-acetate (PMA) to be adherent and “macrophage-like”.<sup>150</sup> However, TAM directly isolated from human melanoma biopsies on the other hand would be the best test objects but are hard to be obtained for research in sufficient quantities.

Monocytes isolated out of blood samples via Biocoll-gradient centrifugation and subsequent plastic adherence were cultured for 7 days in RPMI1640 containing M-CSF as growth factor and 1% human plasma pooled from several donors (see 3.3). Afterwards cells were harvested with Accutase due to their strong adherence to the cell culture plate and reseeded in cell culture plates. Polarization can be achieved with 24h to 48h incubation in the cell culture medium mentioned above plus IFN- $\gamma$  and LPS to have M1 macrophages and IL-4 to have M2 macrophages.

To characterize the phenotype of macrophages polarized in this *in vitro* system, gene expression was measured via qPCR (see **Figure 3**) as a ratio between M2 and M1 to even out donor variations in baseline expression of those markers or ability to respond to polarization. It revealed that M2 macrophages have a higher expression of *MS4A4*, *PD-L2*, *CD206* and *CD36* compared to their M1 counterparts, whereas M1 macrophages show a higher expression of *IDO1* and *YKL-40*. Further investigated targets like *PPARG*, *HIF1 $\alpha$*  and *IL1RN* are equally expressed in M1 and M2 macrophages.



Gene expression profile in human M1 and M2 macrophages



|                      | IDO1    | YKL-40  | MS4A4A | PD-L2  | CD206  | CD163  | CD36   | PPARG  | HIF1a  | IL1RN  |
|----------------------|---------|---------|--------|--------|--------|--------|--------|--------|--------|--------|
| P value (two tailed) | <0.0001 | <0.0001 | 0.0052 | 0.0050 | 0.0090 | 0.0030 | 0.0033 | 0.4226 | 0.7828 | 0.1168 |

**Figure 3:** Human monocyte-derived macrophages (M-CSF) were polarized for 48h towards M1 (IFN- $\gamma$  & LPS) and M2 (IL-4) phenotype and their gene expression was analyzed by qPCR with GAPDH as the housekeeping gene. Genes higher expressed in M2 macrophages are shown in green (values > 1), those lower expressed in M2 are shown in red (values < 1). Data is displayed as fold change and normalized to M1 macrophages. N = 9. Statistical significance was determined using the two tailed t-test.

As gene expression analysis does not necessarily equal with protein translation and surface marker expression at a given timepoint<sup>151</sup>, flow cytometry was used to stain and detect surface markers with fluorescence-labeled antibodies (see **Figure 4**). Dead cells and debris were excluded using a viability stain. Higher expression of CD206 and CD36 in M2 macrophages was verified by flow cytometry. CD163 protein on the cell surface is lower in M2 macrophages compared to M1 macrophages, although its mRNA is prevalent in M2 macrophages. Since the flow cytometry panel was optimized for animal experiments with the addition of CD3, CD45 and MHC-II to gate on macrophages, not every marker investigated in qPCR could be included in flow cytometry. CD14, not included in the qPCR panel, has a higher expression in M1 macrophages *in vitro*.

## Surface marker expression profile in human M1 and M2 macrophages

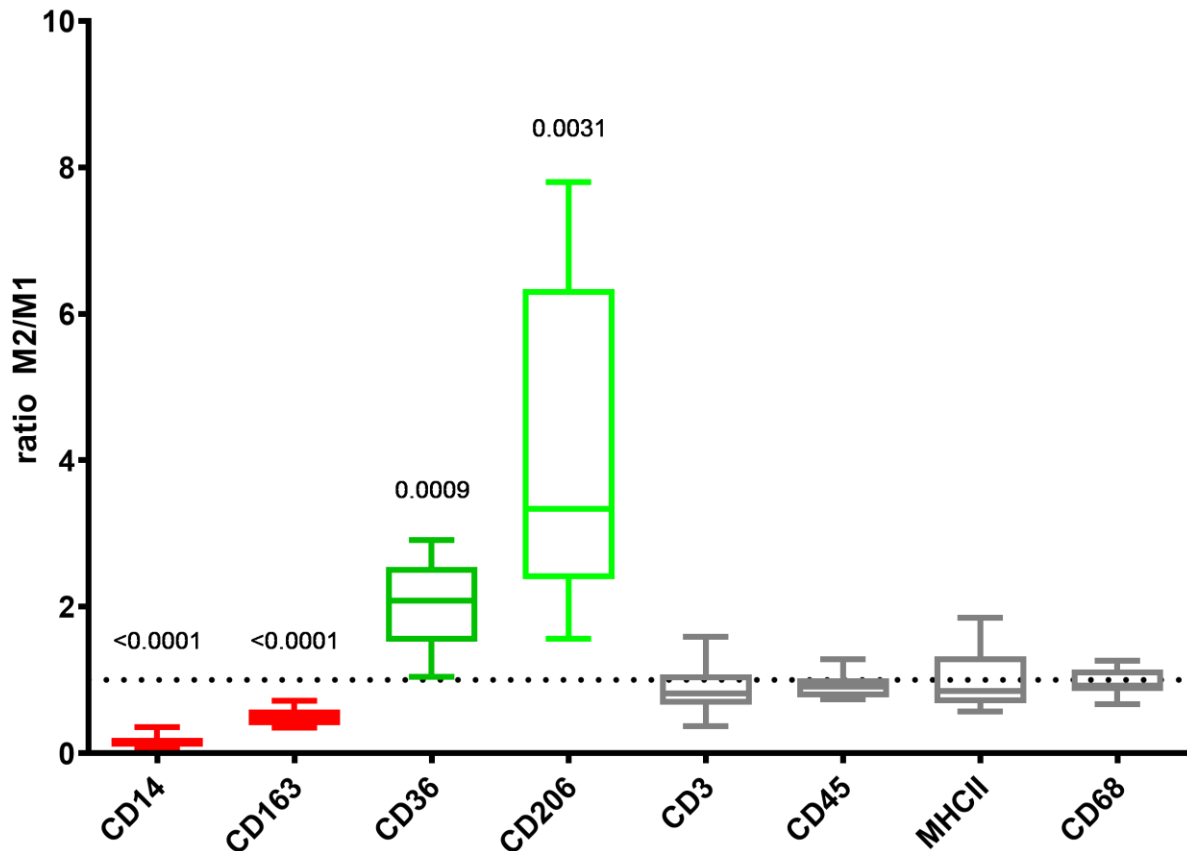


**Figure 4:** Human monocyte-derived macrophages (M-CSF) were polarized for 48h towards M1 (IFN- $\gamma$  & LPS) and M2 (IL-4) phenotype and their surface marker expression was analyzed by flow cytometry. Markers higher expressed in M2 macrophages are shown in green (values > 1), those lower expressed in M2 are shown in red (values < 1). Data is displayed as fold change of mean fluorescence intensity of the stained antigen and normalized to M1 macrophages. N = 9. Statistical significance was determined using the two tailed t-test.

The investigated markers have been described in the literature as associated with macrophages in different tumor entities. It is important to mention, that an *in vitro* polarization with IFN- $\gamma$ /LPS or IL-4 can only serve as test system for genes which are relevant in macrophage polarization and have been detected *in vivo*. CD163, described as M2 marker (see below), showed a lower expression in IL-4 treated M2 macrophages compared to M1 macrophages on the protein level. Differences in mRNA and protein level point to posttranslational regulatory processes.

Mannose receptor (CD206), a pattern recognition receptor of the innate immune system, is often used as “classical” M2 marker, whereas CD68 serves as general macrophage marker.<sup>152</sup> Despite being highly expressed on inhibitory TAM, binding and activation of CD206 by a synthetic peptide RP-182 led to a polarization of M2-like TAM to M1-like TAM in syngeneic murine melanoma and colon cancer models as well as in xenograft tumors of pancreatic cancer in immunodeficient mice resulting in longer survival times.<sup>153</sup> The same effect was observed in murine fibrosis models.

## Results and Discussion

Both effects would indicate, that in physiological settings there are no or different binding partners for CD206 in the TME or that it will not be activated.

A novel marker for TAM is MS4A4A, a cell membrane protein belonging to the same family as the B cell marker CD20.<sup>154</sup> Little is known about its function or its expression in the human body, in line with the whole family of membrane-spanning 4-domain proteins consisting of 18 proteins.<sup>155</sup> MS4A4A has been detected in monocytes, macrophages, immature dendritic cells and in plasma cells.<sup>154</sup> *In vitro* IL-4 polarized macrophages showed MS4A4A expression, whereas their M1 (IFN- $\gamma$ /LPS) counterparts did not, in line with our mRNA data showing higher levels in M2 macrophages (see **Figure 3**). Lifting the veil regarding its function, it was shown recently that it colocalizes with the  $\beta$ -glucan receptor dectin-1.<sup>156</sup> In MS4A4A knock out mice macrophages could not recognize N-glycan structures on B16F1 melanoma cells via dectin-1. Consequently, those macrophages failed to recruit NK cells for killing of melanoma cells. This effect was only important in prevention of metastasis, as primary tumor growth was unaltered. Melanoma cells without glycan structures recognized by dectin-1 (B16F10) had comparable number of metastases in wild type and knockout mice.

The scavenger receptor CD36 cannot serve as macrophage marker, since it is also expressed on tumor cells, but it plays an important role in cancer progression, metastasis and immune tolerance.<sup>157–159</sup> Ligands for CD36 are diverse, mostly negatively charged phospholipids, fatty acids, ox-LDL and also protein ligands like thrombosponin-I or other membrane proteins like integrins. Despite fueling mitochondria by binding fatty acids and translocating them into the cell, CD36 can influence gene expression via P59 and caspase-3-like proteases. In immune cells, changes in metabolism have a crucial effect on the phenotype. TAM have high levels of CD36 and switch to fatty acid oxidation instead of glycolysis. CD36 can also promote uptake of tumor micro vesicles during metastasis. Therefore, CD36 expression gives a hint at macrophage phenotype but not at macrophage identity.

Another scavenger receptor, CD163, is often cited as M2 macrophage marker. Nevertheless, as already mentioned, the heterogeneity of macrophages is hard to decipher. Often markers like CD163 are used as M2 marker in single-plex staining of tissue samples to generate conclusions of TAM function.<sup>160–162</sup> Markers are only valid to use in conjunction with several other markers and – even better – functional data. Multiplex immunohistochemistry allowed the detection of several M2-like subsets of TAM, with and without CD163 expression, in connection with spatial information in gastric cancer.<sup>163</sup> High numbers of CD68<sup>++</sup>CD163<sup>+</sup> TAM enhanced overall survival and relapse-free survival in patients. CD68 and CD206 expression seems to be regulated inversely, as CD206<sup>+</sup> TAM, prevalent in the tumor stroma, show low expression of CD68 and vice versa. CD163 knockout in mice slowed down growth of murine sarcoma cell lines *in vivo* and CD163 siRNA mediated knockdown had the same effect for human sarcoma cell lines *in vitro*.<sup>164</sup> Treatment with IL-4 led to a lower expression of CD163 in M2 macrophages compared to LPS and IFN- $\gamma$  treated M1 macrophages. To add complexity, both, CD163 and CD206, do exist in a soluble form (sCD163 and sCD206), whose function is not clear yet.<sup>165</sup> CD163 should be seen as macrophage activation marker.

Chitinase-3-like protein 1 (CHI3L1 or YKL-40) is an inflammatory signal molecule secreted by immune and cancer cells.<sup>166</sup> It has lost its chitinase activity unlike Chitinase 1 and Chitinase acidic, the two functional human chitinases used to degrade the biopolymer chitin from fungi or insects. YKL-40 acts as growth factor by regulating several signaling pathways like IGF-1 and Erk/Map-kinases and promotes angiogenesis. However, receptor or mechanism regarding how CHI3L1 remains unknown. Many studies investigated, if secreted YKL-40 in blood of cancer patients can serve as prognostic marker. A meta-analysis of 41 publications indicates that in many tumors it does may serve as new biomarker since its levels are elevated in many (solid) cancers, excluding breast cancer.<sup>167</sup> As it is a secreted marker it was only included in the qPCR panel of the primary human macrophages and in line with literature it was reduced in

## ***Results and Discussion***

M2 macrophages compared to M1. Of note, chitin and chitosan (deacetylated chitin), are used as biomaterials but they activate the inflammasome in macrophages. <sup>168</sup>

Indoleamine-pyrrole 2,3-dioxygenase (IDO1) catalyzes the oxidation of L-tryptophan to N-formylkynurenine. <sup>169</sup> Depletion of the essential amino acid L-tryptophan dampens pathogens but also T cell responses. The physiological immunosuppression happens in tissues where overshooting immune responses would be dangerous: mucosa, placenta, eye and pancreas. IDO1 expression has been reported in immune cells like macrophages and cancer cells. They hijack the mechanism of immune suppression mediated by tryptophan depletion. IDO2 and tryptophan 2,3-dioxygenase (TDO) are able to catalyze the oxidation of tryptophan, too. Their physiological roles are different, but all three enzymes have been detected in tumors and are investigated as druggable targets. Inhibitors as single therapy or in combination with immune checkpoint inhibitors against CTLA-4 or PD-1 are evaluated. <sup>170,171</sup> Unfortunately, a major drawback was the failing of a phase 3 IDO1 inhibitor study in advanced melanoma in conjunction with pembrolizumab (anti PD-1 antibody) since there were no benefits from IDO1 inhibition. <sup>172</sup> *In vitro* M2 macrophages show a strong down regulation of IDO1 in comparison to M1 macrophages. This might be because inflammatory M1 macrophages employ IDO1 as defense mechanism or it can be explained as *in vitro* artefact, because of the lower tryptophan concentration in cell culture medium (24,5  $\mu$ M) compared to normal blood concentrations (~70  $\mu$ M). <sup>173,174</sup>

## Results and Discussion

### 4.2 siRNA knockdown in macrophages

In order to influence gene expression, gene knockdown strategies are a common approach.<sup>175,176</sup> TAM should be repolarized towards pro-inflammatory M1 macrophages to overcome immune suppression in the tumor microenvironment. By switching off genes necessary for M2 function and phenotype, this repolarization could be achieved. To avoid off target effects, uptake of nanocarriers should be mostly limited to the target TAM and the targeted gene should be relatively exclusive for TAM. RNA interference by transfecting cells with small interfering RNA (siRNA) is one of several ways to lower gene expression by targeted degradation of the gene's mRNA. The IL-4 signaling axis via STAT6 or the nuclear receptor 4A3 (NR4A3) (nuclear receptor subfamily 4, group A, member 3) have been shown as promising targets to alter M2 polarization of macrophages.<sup>177,178</sup>

As a first milestone to achieve this therapy in melanoma, siRNA mediated knockdown in human macrophages *in vitro* needs to be validated (see **Figure 5**). After preliminary experiments with THP-1 cells (not shown), human monocyte-derived macrophages were transfected using VIROMER® BLUE, a polymer-based transfection reagent, with several pre-designed siRNA in a pool-of-4 format (see 3.19). Negative-control siRNA was used to normalize gene expression and to include effects stemming from the transfection itself. Significant reduction of the target genes could be achieved, ranging from 54% (LMNA) to 17% (NR4A3) expression compared to control cells at a final siRNA concentration of 25 nM and a duration of 48h.

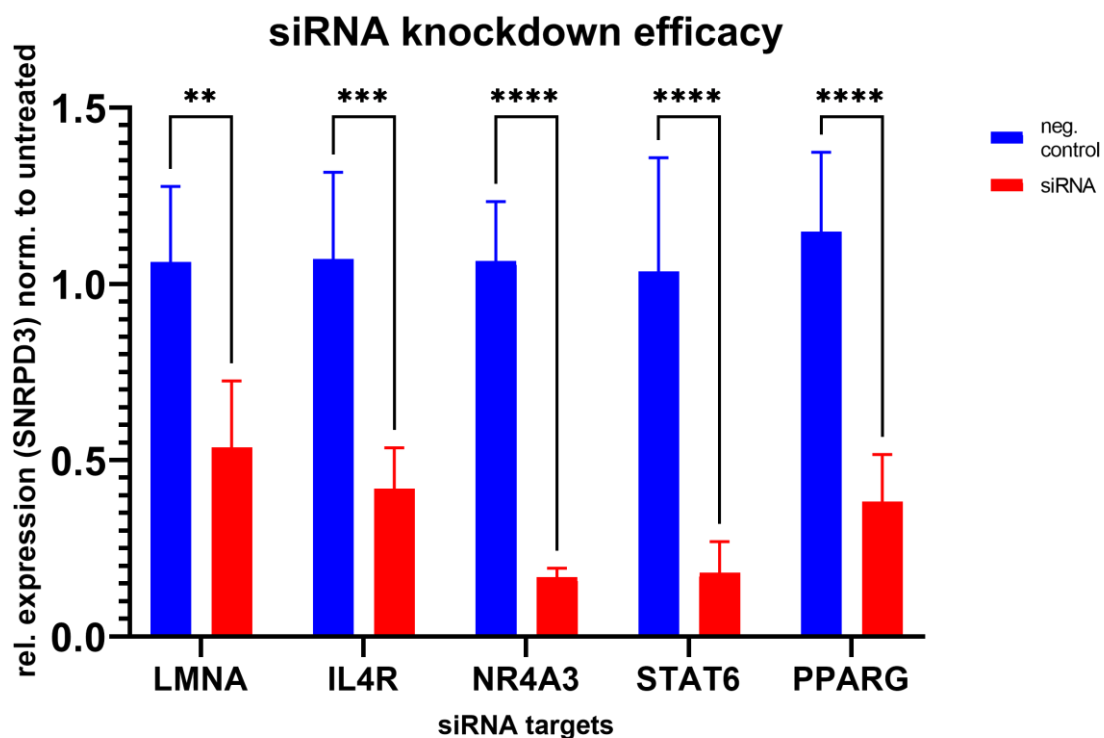


**Figure 5:** siRNA mediated knockdown of LMNA, IL4R, NR4A3, STAT6 and PPARG in human monocyte-derived macrophages using Viromer BLUE as transfection reagent for 48h. Transfection efficacy was determined using qPCR to measure gene expression. Data is shown as relative expression normalized to untreated samples and the housekeeping gene SNRPD3. N = 3. Statistical significance was determined using the Two-Way ANOVA with Fisher's LSD test. Ns = not significant, \*  $p < 0,05$ , \*\*  $p < 0,01$ , \*\*\*  $p < 0,001$ , \*\*\*\*  $p < 0,0001$ .

## ***Results and Discussion***

After verification of siRNA knockdown by qPCR, for two targets (*IL4R* & *PPARG*) its effects on the cell phenotype of M2 macrophages were assessed by analyzing cellular markers on the surface via flow cytometry and gene expression via qPCR after 48h of transfection (see **Figure 6**). Knockdown of *interleukin 4 receptor (IL4R, A)* enhances expression of *Chitinase-3-like protein 1 (CHI3L1 or YKL-40)* and *Matrix metalloproteinase 9 (MMP-9)*. All other investigated targets were not significantly changed by *IL4R* knockdown. The second investigated knockdown was of *Peroxisome proliferator-activated receptor gamma (PPARG, B)*. In this case only the expression of *interleukin-1 receptor antagonist (IL-1RN)* differs between untreated and transfected cells, but there is no difference between cells transfected with negative-control siRNA and target siRNA. Of course, since siRNA against PPARG was used, its expression level is around 50%. As the red bars, representing the expression in untreated cells, are not always around 1, this shows clearly, that the transfection itself influences marker expression in macrophages.

## Results and Discussion

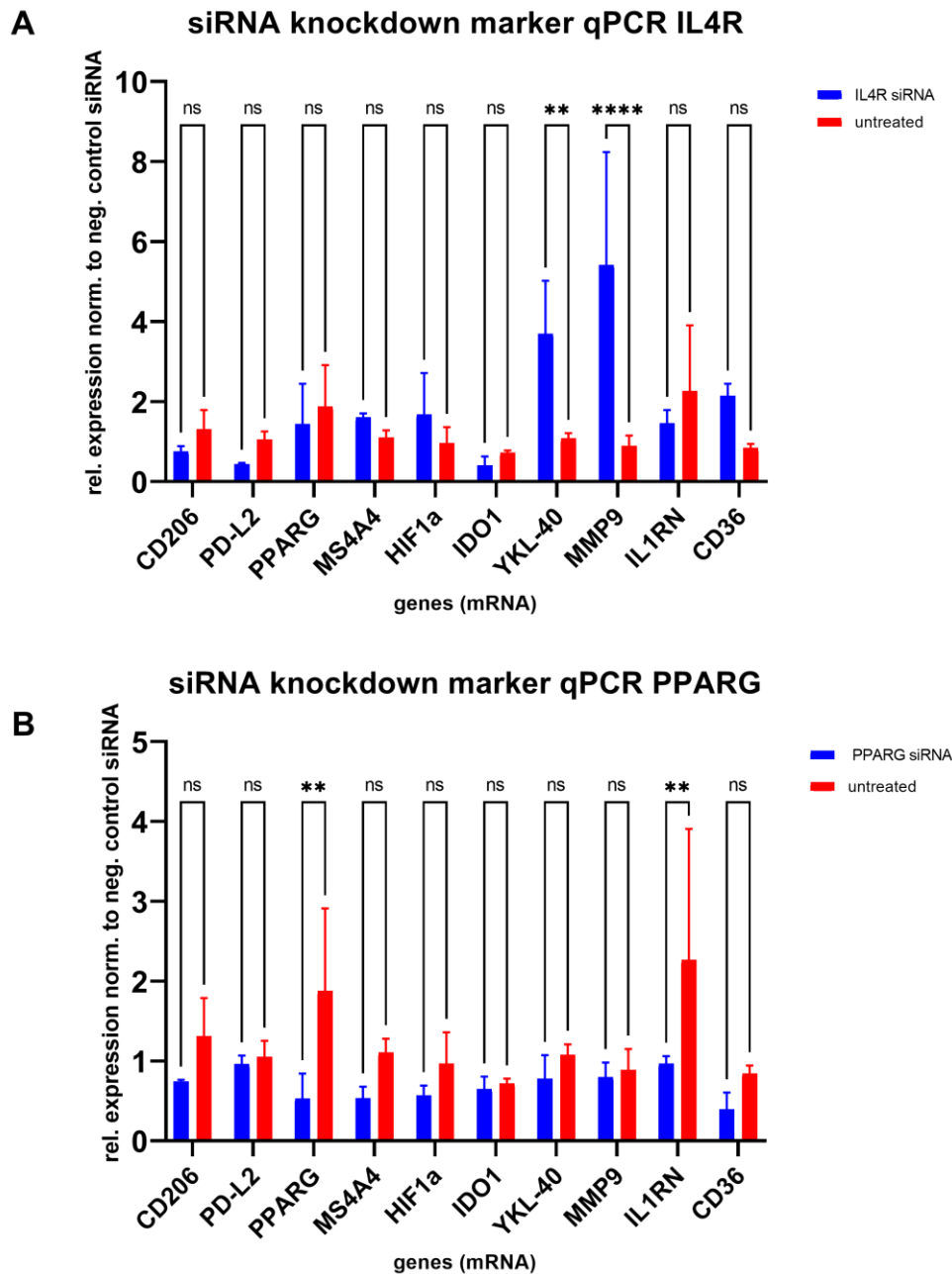


**Figure 6:** Human monocyte-derived and M2 polarized macrophages were transfected with siRNA against *IL4R* (upper chart) and *PPARG* (lower chart) and gene expression after 48h was analyzed using qPCR. Data is shown as relative expression normalized to samples transfected with negative control siRNA and the housekeeping gene *GAPDH*.  $N = 3$ . Statistical significance was determined using the Two-Way ANOVA with Fisher's LSD test. *Ns* = not significant, \*  $p < 0,05$ , \*\*  $p < 0,01$ , \*\*\*  $p < 0,001$ , \*\*\*\*  $p < 0,0001$ .

Phenotyping of transfected M2 macrophages was also done by flow cytometry and expanded to more knockdown targets (see **Figure 7**). In this case, siRNA against *STAT6* and *NR4A3* was included. Knockdown of *IL4R* serves as internal control, since IL-4 is included in the culture medium and drives the macrophages towards the M2 phenotype. Hence, *IL4R* knockdown is expected to show consequences. PD-L1 and PD-L2 are reduced, whereas CD206 and CD36, two M2 markers, are slightly upregulated. Knockdown of *STAT6*, downstream in the IL-4 signaling cascade, shows only

## Results and Discussion

significant downregulation of PD-L1. Interference with the nuclear receptor *PPARG* leads to upregulation of both ligands of PD-1, PD-L1 and PD-L2, and downregulation of CD36. *NR4A3*, another nuclear receptor, was also targeted. Reduction of its mRNA lead to upregulation of two M2 markers, CD206 and CD36.

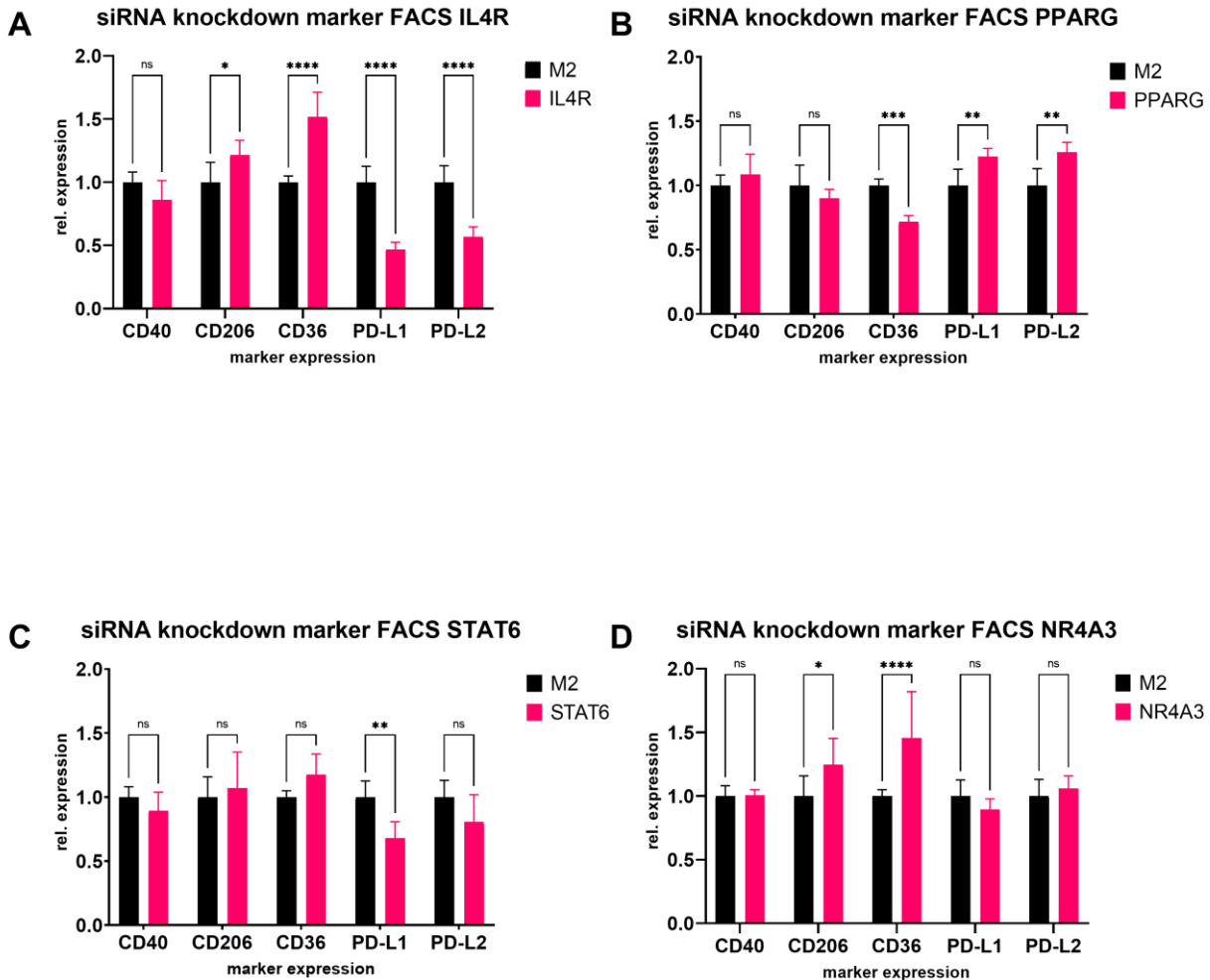


**Figure 7:** Human monocyte-derived and M2 polarized macrophages were transfected with siRNA against *IL4R* (A), *PPARG* (B), *STAT6* (C) and *NR4A3* (D) and surface marker expression after 48h was analyzed using flow cytometry. Data is shown as relative expression normalized to untreated (M2) samples.  $N = 3$ . Statistical significance was determined using the Two-Way ANOVA with Fisher's Uncorrected LSD test. Ns = not significant, \*  $p < 0,05$ , \*\*  $p < 0,01$ , \*\*\*  $p < 0,001$ , \*\*\*\*  $p < 0,0001$ .

Although transfection with siRNA-lipoplexes formed *in situ* in primary human macrophages was achieved using Viromer BLUE, a former commercially available transfection agent, it was not possible to transfect macrophages or other cell types with engineered nanocarriers. Exemplarily, one experiment using siRNA loaded liposomes (see 4.5 for more information on liposome design) to transfect human monocyte derived macrophages is shown in **Figure 8**. siRNA concentration in the Viromer BLUE samples was 50 nM, whereas with liposomes only 6 - 29 nM final siRNA concentration was achieved. After negative transfection assays with liposomes and other nanoparticle species focus was moved to small molecules to influence macrophage polarization.



## Results and Discussion

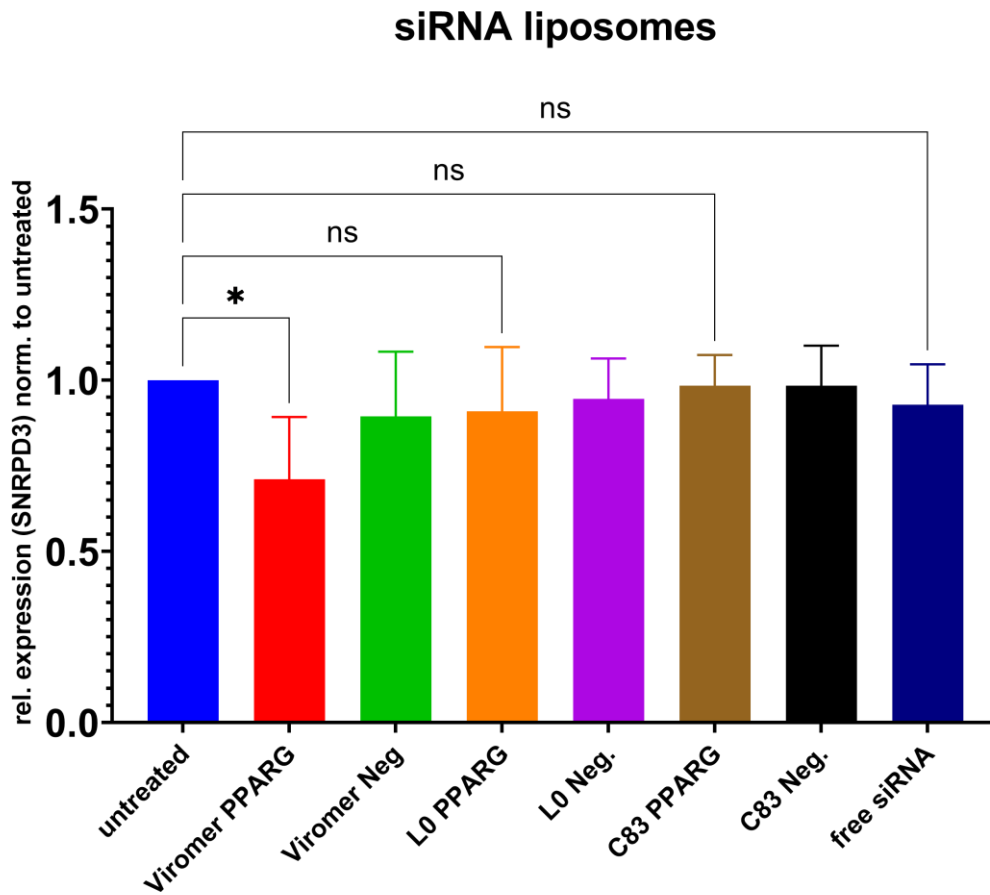


**Figure 8:** siRNA mediated knockdown of PPARG in human monocyte-derived macrophages using siRNA loaded L0 and C83 liposomes as transfection reagent for 48h. Transfection efficacy was determined using qPCR to measure gene expression. Data is shown as relative expression normalized to untreated samples and the housekeeping gene SNRPD3. N = 3. Statistical significance was determined using the Ordinary One-Way ANOVA with Fisher's LSD test. Ns = not significant, \*  $p < 0,05$ , \*\*  $p < 0,01$ , \*\*\*  $p < 0,001$ , \*\*\*\*  $p < 0,0001$ .

## Results and Discussion

### 4.3 Tasquinimod as siRNA alternative

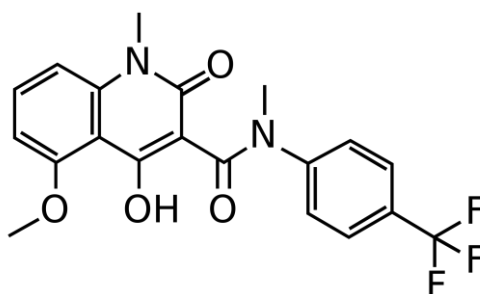


**Figure 9:** Chemical structure of Tasquinimod.

As a second strategy to repolarize macrophages, independent of RNA interference, the immunomodulator Tasquinimod (see 2.1.5 and **Figure 9**) was tested on human macrophages, human T cells and human melanoma cells *in vitro*. The aim of those studies was to clarify if Tasquinimod can influence macrophage marker expression and cell metabolism, T cell and melanoma cell proliferation. This way, pure toxicity effects on immune cells or tumor cells should be excluded. Later, we tested its ability to suppress tumor growth in our melanoma model in humanized mice (see 2.2 and 3.13).

When Tasquinimod was added in two concentrations (10  $\mu$ M & 100  $\mu$ M) for 24h to human macrophages *in vitro*, which were already polarized towards M1 and M2 macrophages, there was almost no significant effect on marker expression (see **Figure 10**). Only CD68 expression of M0 macrophages was reduced to half by both concentrations. This experiment was focused on the effects of Tasquinimod alone on both macrophage phenotypes.

## Results and Discussion

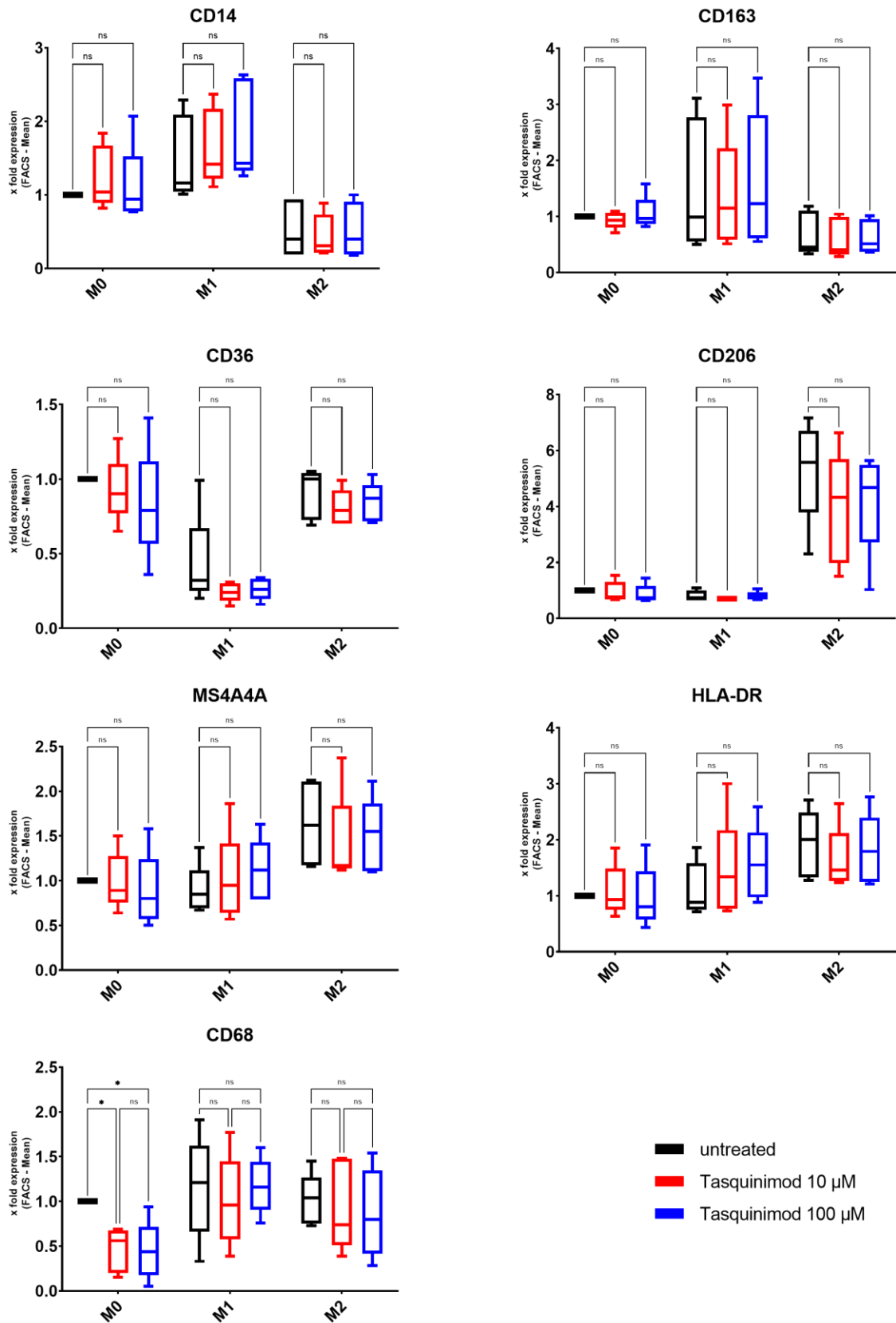


**Figure 10:** Human monocyte-derived macrophages were pre-polarized for 24h and incubated afterwards for 24h with Tasquinimod in two different concentrations (10 µM & 100 µM). Marker expression was analyzed via flow cytometry.  $N = 5$ . Statistical significance was determined using the Two-Way ANOVA with Fisher's Uncorrected LSD test. *Ns* = not significant, \*  $p < 0,05$ , \*\*  $p < 0,01$ , \*\*\*  $p < 0,001$ , \*\*\*\*  $p < 0,0001$ .

## ***Results and Discussion***

Since cell metabolism plays an important role in determining the cell phenotype<sup>24,25,179</sup>, influence of Tasquinimod on macrophage metabolism was investigated with the Seahorse Analyzer system, which can measure the oxygen consumption rate (OCR) and extracellular acidification rate (ECAR) (see 3.8). Human macrophages were polarized for 24h and then incubated with Tasquinimod (100  $\mu$ M) for 1h prior to measurement of the cell metabolism (see **Figure 11**). Untreated M1 and M2 macrophages served as control cells. Due to high donor to donor variations, the first value of the OCR was normalized to 1. For the Seahorse XF Cell Mito Stress Test Kit measurement, Oligomycin was added between measurement 3 and 4, FCCP between 6 and 7, and rotenone and antimycin A between 9 and 10 according to the manufacturing manual. Through those additions of inhibitors of the electron transport chain in the mitochondria and FCCP as uncoupling reagent, it is possible to measure basal respiration, ATP production, proton leak, maximal respiration, spare capacity and non-mitochondrial oxygen consumption.

M1 macrophages show a higher basal respiration, maximal respiration and ATP production, which is enhanced after Tasquinimod treatment, compared to M2 macrophages (see **Figure 12**). Those treated M1 macrophages show a even higher basal respiration and ATP production compared to both Tasquinimod treated and untreated M2 macrophages. The spare respiratory capacity is elevated in treated and untreated M1 macrophages compared to their M2 counterpart, although this difference is not significant. Basal respiration describes the oxygen consumption without any inhibitor added. Oligomycin blocks influx of protons through complex V of the electron transport chain. Remaining mitochondrial respiration occurs because of proton leakage, increasing with damaged membranes. The M2 macrophages have a higher non-mitochondrial respiration stemming from oxygen-consuming enzymes outside the mitochondria. Tasquinimod might lead to a minimal shift of M2 towards M1 macrophages and to a boost of the M1 phenotype, but longer incubation times and/or a higher number of different donors would be needed to clarify this yet minimal shift. *In vitro* M1 macrophages seem to be in a higher state of activation leading to more energy consumption. In contrast to literature, they display higher levels of oxidative phosphorylation instead of shifting towards glycolysis.

24

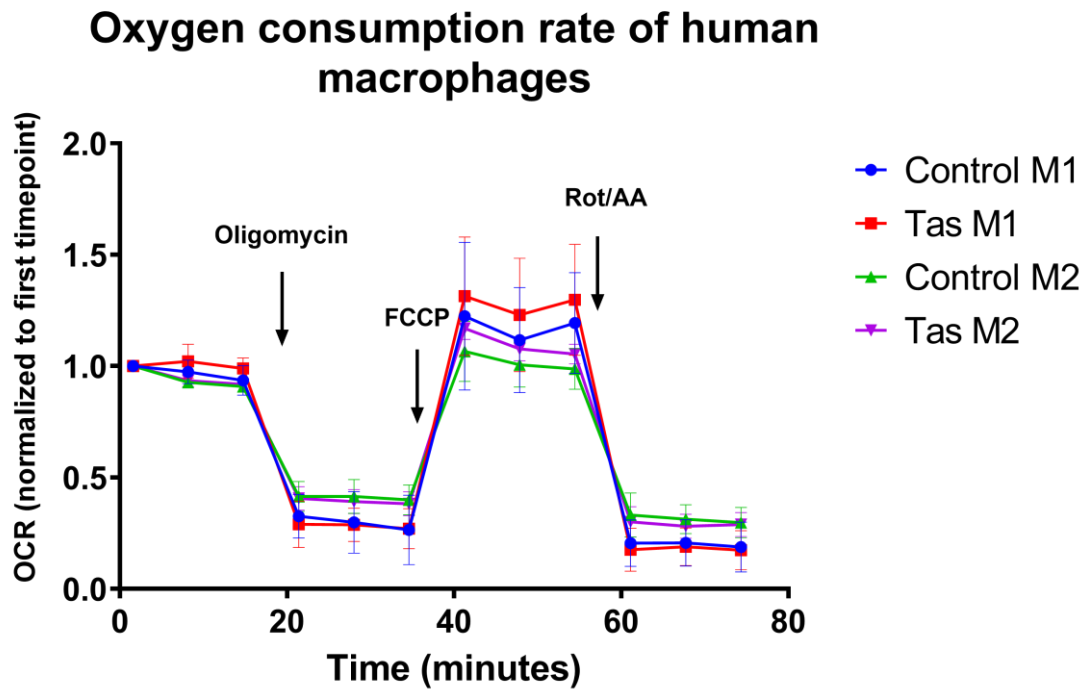


**Figure 11:** The effects of Tasquinimod on the energy metabolism of polarized human monocyte-derived macrophages has been investigated by measuring the oxygen consumption rate (OCR) and extracellular acidification rate (ECAR) with an Agilent Seahorse XFp Analyzer. Because of donor variations the first value was normalized to 1. Due to the addition of oligomycin (between data point 3-4), FCCP (between data point 6-7) and rotenone/antimycin A (between data point 9-10), basal, maximum and spare capacity respiration as well as proton leakage and ATP production can be calculated (see **Figure 12**). Macrophages were polarized for 24h and Tasquinimod was added at 100  $\mu$ M after polarization but 1h before the assay.

## Results and Discussion

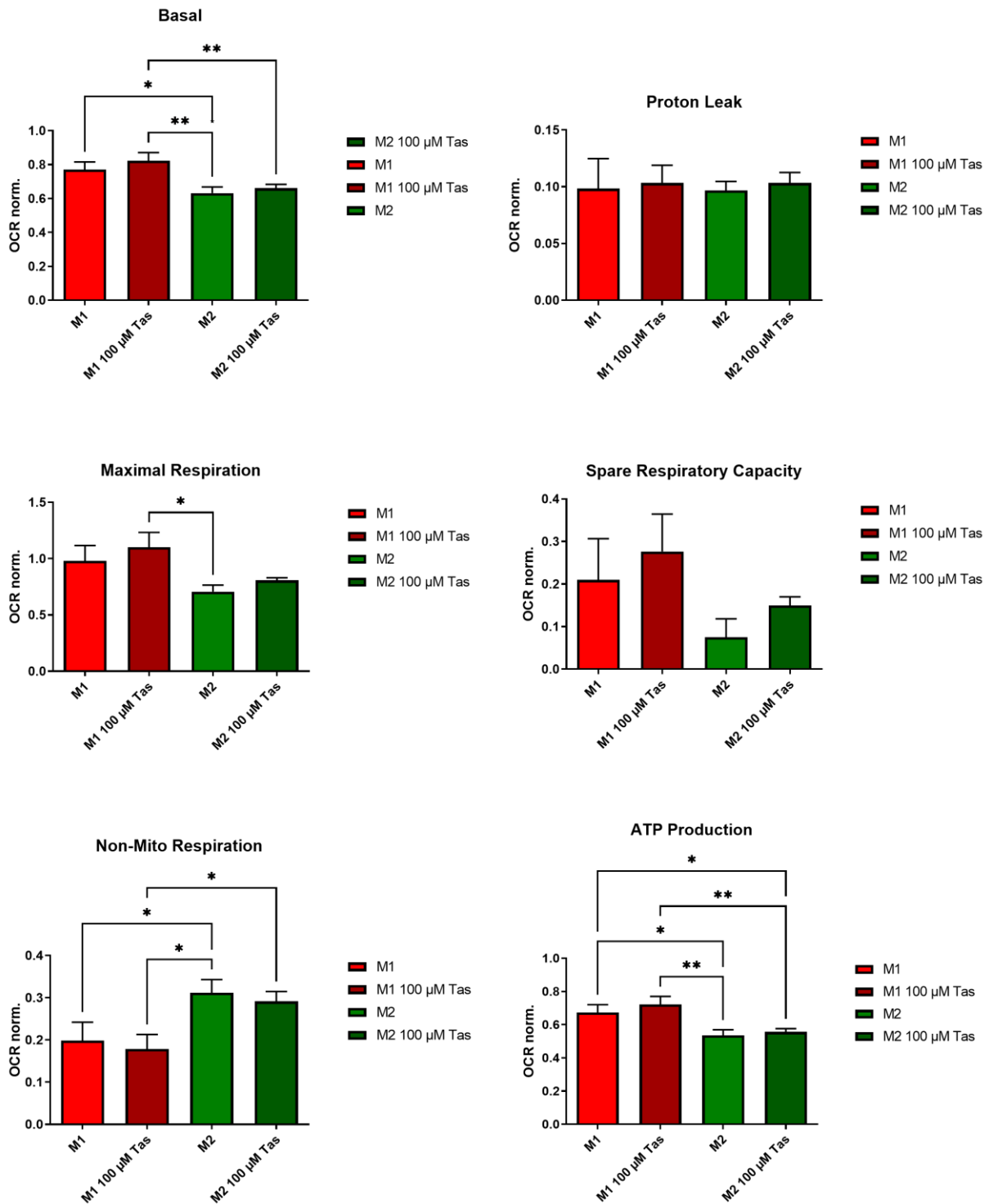


**Figure 12:** The effects of Tasquinimod on the energy metabolism of polarized human monocyte-derived macrophages has been investigated by measuring the oxygen consumption rate (OCR) and extracellular acidification rate (ECAR) with an Agilent Seahorse XFp Analyzer (see also **Figure 11**). Statistical significance was determined using the Ordinary One-Way ANOVA with Fisher's LSD test.  $N = 6$ . *Ns* = not significant (not shown), \*  $p < 0,05$ , \*\*  $p < 0,01$ , \*\*\*  $p < 0,001$ , \*\*\*\*  $p < 0,0001$ .

## Results and Discussion

To gain further insight on possible routes of Tasquinimod to influence the tumor microenvironment, we expanded analysis to two other major cell types of the tumor microenvironment: T cells and the cancer cells itself.

When T cells are stimulated *in vitro* by plate-bound anti-CD3 and soluble anti-CD-28 antibody<sup>128</sup>, they proliferate polyclonally. Human peripheral blood mononuclear cells consist mostly of CD4<sup>+</sup> and CD8<sup>+</sup> T cells, B cells, NK cells, monocytes, very few dendritic cells and – depending on the isolation protocol – granulocytes. Isolated T cells as well as not isolated T cells in PBMC from buffy coats can both be stimulated polyclonally. Cell type specific proliferation can be determined afterwards using flow cytometry and distinguish cells by their markers (CD3, CD4 and CD8). To measure proliferation cells were labeled with CFSE (see 3.21). The proliferation capacity of untreated cells was set to 100%. Tasquinimod presence at 10  $\mu$ M during three days of proliferation shows no effect, whereas a higher concentration of 100  $\mu$ M Tasquinimod lowers slightly, but significantly the proliferation of both CD4<sup>+</sup> and CD8<sup>+</sup> T cells to values of 83,2% ( $\pm$ 6,2%) and 82,7% ( $\pm$ 3,7%) (see **Figure 13**).

### Effects of Tasquinimod on human PBMC stimulated with $\alpha$ -CD3 ab

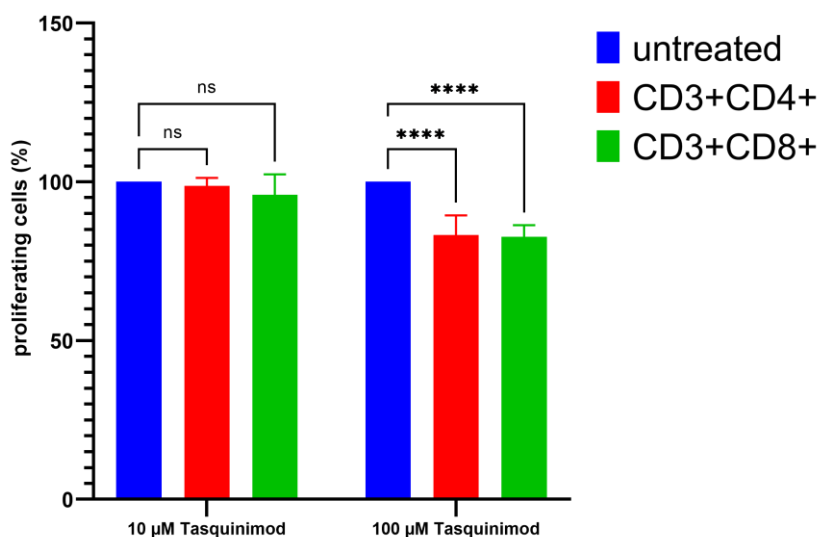


**Figure 13:** Human peripheral blood mononuclear cells were labeled with CFSE and cultured for 3 days in wells coated with anti-CD3 antibody in the presence of Tasquinimod at two different concentrations (10  $\mu$ M & 100  $\mu$ M). Afterwards their proliferation was measured using flow cytometry. Shown is the percentage of living proliferated CD4<sup>+</sup> and CD8<sup>+</sup> T cells normalized to untreated.  $N = 5$ . Statistical significance was determined using the Two-Way ANOVA with Fisher's LSD test.  $Ns =$  not significant, \*  $p < 0,05$ , \*\*  $p < 0,01$ , \*\*\*  $p < 0,001$ , \*\*\*\*  $p < 0,0001$ .

Since anti-tumor effects can arise from direct toxicity of the compound against the tumor cells, the influence of Tasquinimod on melanoma cell proliferation was tested on Ma-Mel-19, which were used in the animal model, and UKRV-Mel-15a cells. Labeling with CFSE enabled tracking of proliferation, just like in the T cell proliferation assay. In case of tumor cells, no discrete gating on only the proliferating cells is possible since every cell is dividing endlessly. The whole cell population will decrease their CFSE signal with every cell division by half. T cells on the other hand do not proliferate homogeneously and it is possible to divide between non-proliferating T cells and proliferating T cells, which can be further subdivided due to their number of divisions. Because of this fact, melanoma cell proliferation is

## Results and Discussion

displayed as % of initial CFSE signal (labeled cells measured directly after labeling). A high rate of proliferation will result in a low value of initial CFSE signal, because of a high number of cell divisions and therefore a high reduction of CFSE fluorescence. Untreated cells should show the highest reduction of CFSE signal.

Ma-Mel-19 and UKRV-Mel-15a cell proliferation were not disturbed by Tasquinimod up to 100  $\mu\text{M}$  (see **Figure 14**) at an assay duration of 3 days. In this assay, due to a higher general robustness of cancer cell lines, a concentration of 200  $\mu\text{M}$  Tasquinimod was added. At this higher concentration, Ma-Mel-19 proliferation begins to be significantly reduced compared to untreated cells, whereas there is only a not significant trend for UKRV-Mel-15a in the same direction.

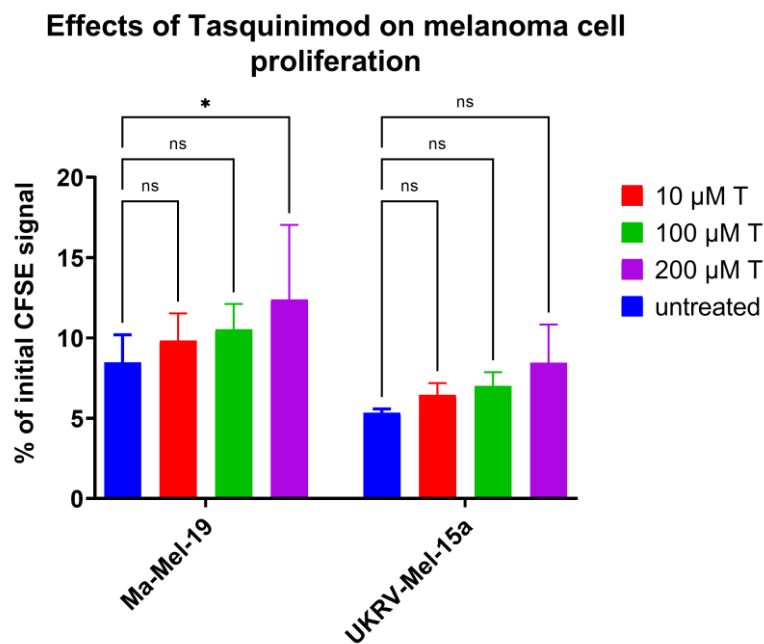


**Figure 14:** Human melanoma cell lines Ma-Mel-19 and UKRV-Mel-15 were labeled with CFSE and cultured for 3 days in the presence of Tasquinimod at three different concentrations (10  $\mu\text{M}$ , 100  $\mu\text{M}$  & 200  $\mu\text{M}$ ). Afterwards their proliferation was measured using flow cytometry. Shown is the percentage of living proliferated  $\text{CD4}^+$  and  $\text{CD8}^+$  T cells.  $N = 3$ . Statistical significance was determined using the Two-Way ANOVA with Fisher's LSD test. *Ns* = not significant, \*  $p < 0,05$ , \*\*  $p < 0,01$ , \*\*\*  $p < 0,001$ , \*\*\*\*  $p < 0,0001$ .



## *Results and Discussion*

### **4.4 Analysis of human melanoma metastases**

Since findings in cell culture might differ from the situation in melanoma patients, biopsies from different entities were stained and analyzed for expression of macrophages markers inside the tumor mass (see **Figure 15**). In this pilot study not every marker out of the planned panel of CD68, CD206, PU.1, PPARG and NOS2 could be stained in every sample. In some cases, the staining was unspecific or negative. Since no immune cell can be described by one marker only, duplex staining was planned but could not be established successfully. Intense DAB staining impeded detection of antigens stained with a red dye as second color. Focus was shifted to multiplex methods like flow cytometry and Chipcytometry for analyzing the tumor microenvironment in the animal experiments.

One conclusion which nevertheless can be drawn, is that macrophages classified by their marker CD68 are present in high numbers in those biopsies. Not only in the surroundings of the tumor but also distributed through the whole tumor mass, signifying their importance for tumor growth. Single marker analysis provided no information on their phenotype. M2 marker CD206 was detected in every sample, but it would be necessary to know the percentage of CD206<sup>+</sup> macrophages and/or the expression level of CD206. Transcription factor PU.1 was also detected in every sample. In most samples to higher levels than CD206 but to lower levels than CD68. PU.1<sup>+</sup> cells in the tumor are most likely macrophages since they show the highest PU.1 expression in general. But PU.1 is not macrophages specific. It is important in hematopoiesis for myeloid and lymphoid precursors.<sup>180</sup> After maturation, it is only expressed in macrophages, dendritic cells and B cells. Peroxisome proliferator-activated receptor gamma (PPARG) is linked to macrophage polarization and plays an important role in regulating responses of macrophages to tumor and infection.<sup>181,182</sup> PPARG is investigated as potential treatment target for cancer.<sup>183</sup> In 3 out of 5 melanoma metastases PPARG was detected, albeit in fewer cells than the other markers.

This data obtained from *ex vivo* samples from melanoma patients led to further development of an animal model to investigate the role of immune cells like macrophages more closely and to establish a nanoparticle based immune therapy. High numbers of macrophages in melanoma biopsies clearly underline their relevance in cancer progression and the need for further studies.

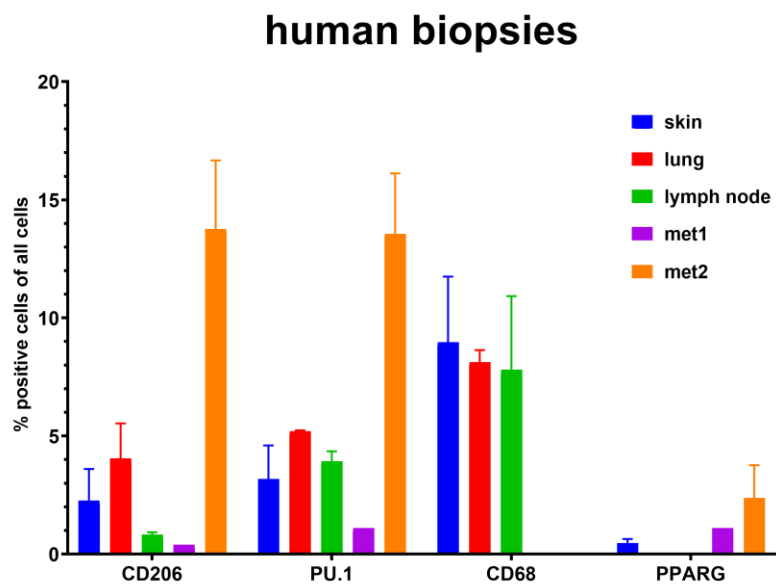


**Figure 15:** Human melanoma biopsies in different tissues showed expression of CD206, PU.1, CD68 and PPARG inside the tumor mass as detected by immunohistochemistry staining (IHC-P). Shown is the percentage of cells inside the tumor expressing the marker. One biopsy per entity (skin, lung, lymph node or metastasis) was analyzed with often more than one distinguishable metastasis (error bar). No bar means no (specific) staining of this marker in the sample.

## Results and Discussion

### 4.5 Development of liposomes as drug carrier<sup>V</sup>

#### 4.5.1 Rationale

As described in 2.1.4 and 2.1.6 liposomal delivery of Doxorubicin was the first application of nanoparticles in clinical routine. Doxorubicin (see **Figure 17**) was chosen as model substance in this project not because of its therapeutic effect but because of its fluorescent properties. Those combined with its affinity for DNA provide the perfect combination for a model system of drug release. Free Doxorubicin (as hydrochloride) is able to penetrate the cell membrane and will accumulate in the cell nucleus when applied to cell culture. Therefore, the fluorescence emitted from the nucleus of free and encapsulated Doxorubicin in equimolar concentrations can be directly compared. Normalization is straightforward, since liposomes can be dissolved using the surfactant Triton™ X-100 and Doxorubicin can be quantified against a standard curve using absorbance or fluorescence measurements. The DNA binding is important because the DNA is mostly confined to nucleus which is a cell organelle large enough to be investigated by confocal fluorescence microscopes without the need for super resolution microscopy. DNA stains like Hoechst 33342 and 33258, which bind the DNA in the minor groove of adenine and thymine rich regions, enable counterstaining of the nucleus to verify its position in case of no or low Doxorubicin signals.<sup>184</sup> Another important fact is that encapsulated Doxorubicin in liposomes is excluded from the nucleus since liposomes (and nanoparticles based on polymers) have never been detected inside the nucleus at least in our hands. By using non-toxic concentrations of Doxorubicin (1 µM) and limiting the experiments to 24 hours, influence on the uptake and processing capacity of liposomes in the cells are prevented. Cell death by using higher Doxorubicin concentrations and longer timespans could also be used as readout, since only Doxorubicin bound to the DNA causes DNA damage. On the other hand, those long-term studies do not provide exact information about release processes happening in hours and degradation or aggregation of liposomes in the cell culture media is likely to happen.

Imaging technologies which illuminate the whole cell, like flow cytometry, cannot discriminate between Doxorubicin still encapsulated in liposomes or already released. Another factor which must be considered always when dealing with fluorophores is quenching and changing fluorescence properties depending on the surrounding media or substances. Doxorubicin content in liposomes was measured for this reason always by absorbance measurement. DNA and histones influence Doxorubicin fluorescence strongly.<sup>185</sup> But if only Doxorubicin inside the nuclei bound to DNA/histone complexes is excited, like in this release experiment, every investigated Doxorubicin molecule behaves in the same way. Only then fluorescence signals can be compared directly and are proportional to the concentration, until quenching appears.

---

<sup>V</sup> The following part was a cooperation project between [REDACTED], research group of [REDACTED] at the Institute of Pharmacy and Biochemistry of the Johannes Gutenberg University Mainz, and I, embedded in the Collaborative Research Center 1066 "Nanodimensional polymer therapeutics for tumor therapy" located in Mainz, Germany. Whereas [REDACTED] focused on the development of the liposomes with special release characteristics, I conducted the biological experiments and analyzed the release of doxorubicin into the cell nucleus. [REDACTED], research group of [REDACTED] at the Dermatology of the University Medical Center Mainz, helped me in conducting the experiments at the Amnis® ImageStream®XMk II and performed the subsequent data analysis. The data shown here is also part of [REDACTED] and [REDACTED] thesis.<sup>187,191</sup>

## Results and Discussion

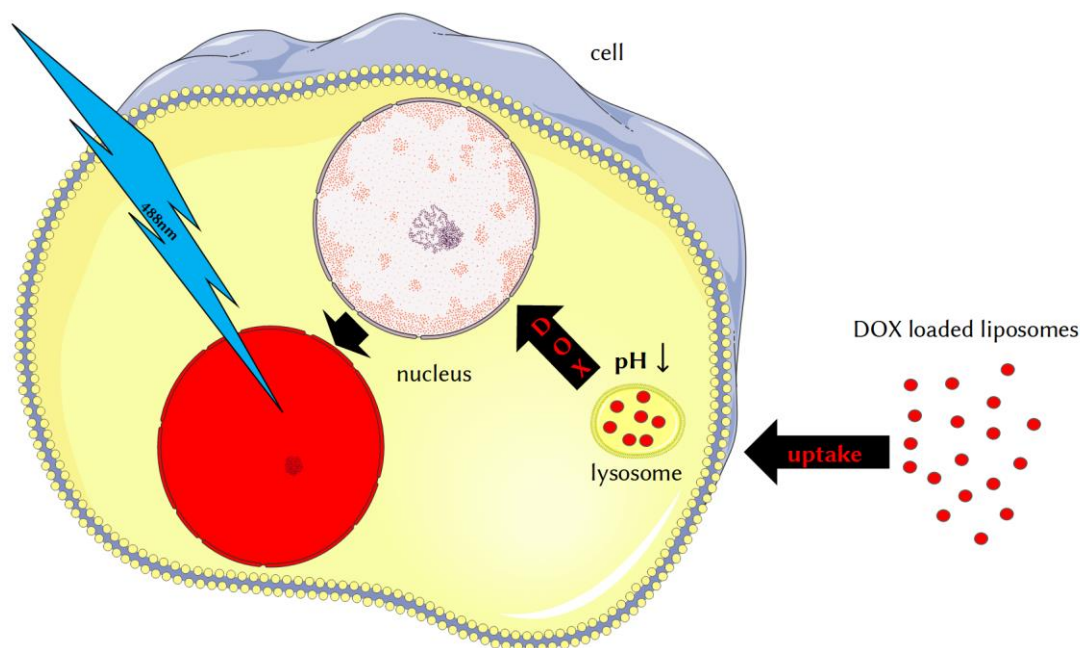


**Figure 16:** Rationale of Doxorubicin release experiments using macrophages and melanoma cells. Liposomes will be taken up by the cell through endocytosis and end up confined in lysosomes inside the cytoplasm.<sup>186</sup> Because of lower pH (5,5) liposomes start to be leaky and will also fuse with the lysosomal membrane, thereby releasing Doxorubicin from their lumen into the cytoplasm. Doxorubicin diffuses freely through the cell and can penetrate the nuclear membrane. Inside the nucleus it binds to DNA. Excited by a 488 nm laser Doxorubicin will emit light with a maximum at 590 nm. By using confocal laser scanning microscopy and counterstaining with Hoechst 33342 or 33258 it is possible to detect fluorescence only in one z-plane of the nucleus. Since every Doxorubicin molecule in the nucleus will be bound to DNA, the signal caused by different liposomal carriers can be compared directly.

All these facts taken together allow to draw the following conclusions (see **Figure 16**): 1.) Every Doxorubicin signal detected in the nuclei arises from released Doxorubicin, since liposomes cannot enter the nuclei. 2.) This system enables direct comparison of different liposome formulations and different surface modification. 3.) Although available Doxorubicin for DNA binding stems from a) liposomes degraded inside the cells, b) liposomes releasing Doxorubicin outside the cell (“leakage”) and c) also depends on uptake of liposomes, drug release is the most important endpoint since only released drug exerts biological effects. Liposome stability was assessed by several assays of [REDACTED] (see 4.5.2) and liposome uptake was monitored by flow cytometry and the *ImageStream* technology. Membrane labeling with lipophilic carbocyanine dye DiD (1,1'-dioctadecyl-3,3,3',3'-tetramethylindodicarbocyanine, 4-chlorobenzenesulfonate salt) enabled tracking of liposomes.

## Results and Discussion

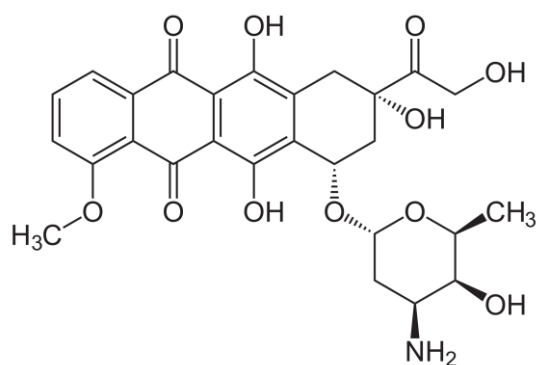


**Figure 17:** Chemical structure of Doxorubicin. In experiments, the water-soluble hydrochloride has been used.

### 4.5.2 Liposomes at the edge of stability

The liposomes C63, C73 and C83, depicted in **Table 3**, were designed by [REDACTED] at the “edge of stability”, meaning that they possess sufficient cargo storage time with minimal leakage at pH 7,2 at 4°C (fridge) and simultaneously enough release at pH 5,5 at 37°C (lysosome).<sup>187</sup> Those three candidates were singled out in a large screening effort with 168 different liposomal formulations. A stabilizing lipid was paired with a modifying lipid in ten different ratios from 100 mol-% to 10 mol-% of the stabilizing lipid. The stability of the liposomes was characterized as the phase transition of the lipid phase from gel to liquid disordered, as this will directly increase the permeability of hydrophilic cargo in the liposome lumen. Hydrophobic defects are precursors of hydrophilic pores and increase strongly near phase transition.<sup>188</sup> This transition is made visible by the fluorophore Laurdan (see **Figure 18**) which experience a shift in fluorescence emission from 440 nm to 490 nm after excitation at 350 nm, since its dipole moment is influenced by water molecules, which are dipoles themselves.<sup>189,190</sup> A more rigid gel like lipid bilayer excludes water molecules better than the liquid disordered phase.

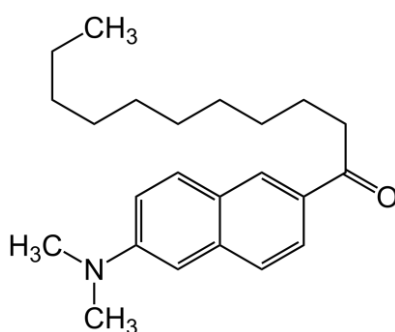


**Figure 18:** Chemical structure of the fluorophore Laurdan used for liposomal stability assays.

Routine characterization of the liposomes included determination of the diameter by light scattering, the polydispersity index (PDI) and the zeta potential (see **Figure 19**) as well as checking those parameters at acidic pH and after 4 months of storage at pH7,2 (see **Figure 20**). Those physicochemical methods provide insights if different liposomal formulations have similar sizes to avoid biases in cellular experiments and to prevent the use of aggregated

## Results and Discussion

samples. Nevertheless, drug release assays based on fluorescence are a better, since leaky liposomes can retain their size but loose cargo.

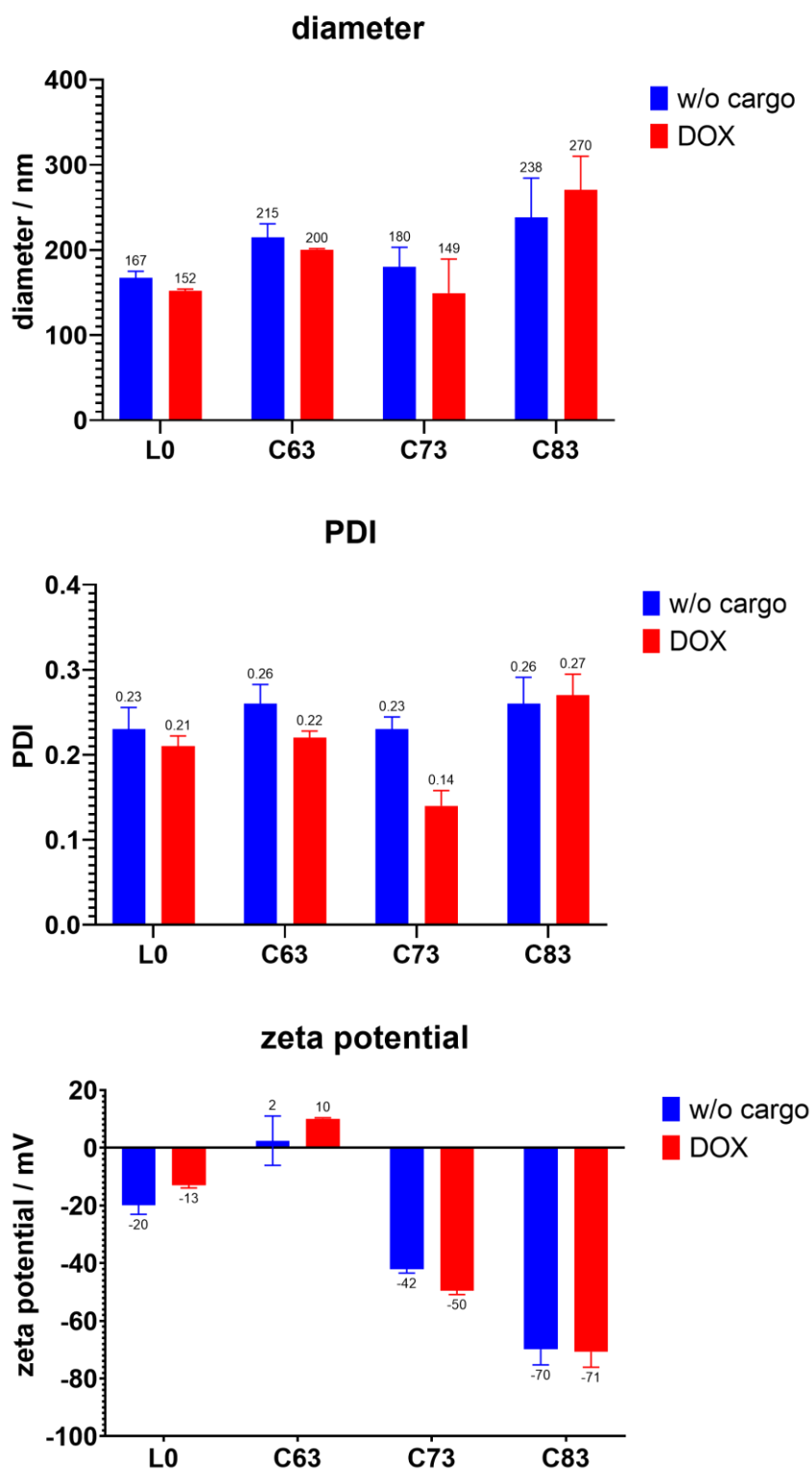


**Figure 19:** Liposome characterization of liposomes shown in Table 4. Each liposomal formulation is shown as “empty” liposome and loaded with Doxorubicin (see 3.12). Data of [REDACTED] 187

## Results and Discussion

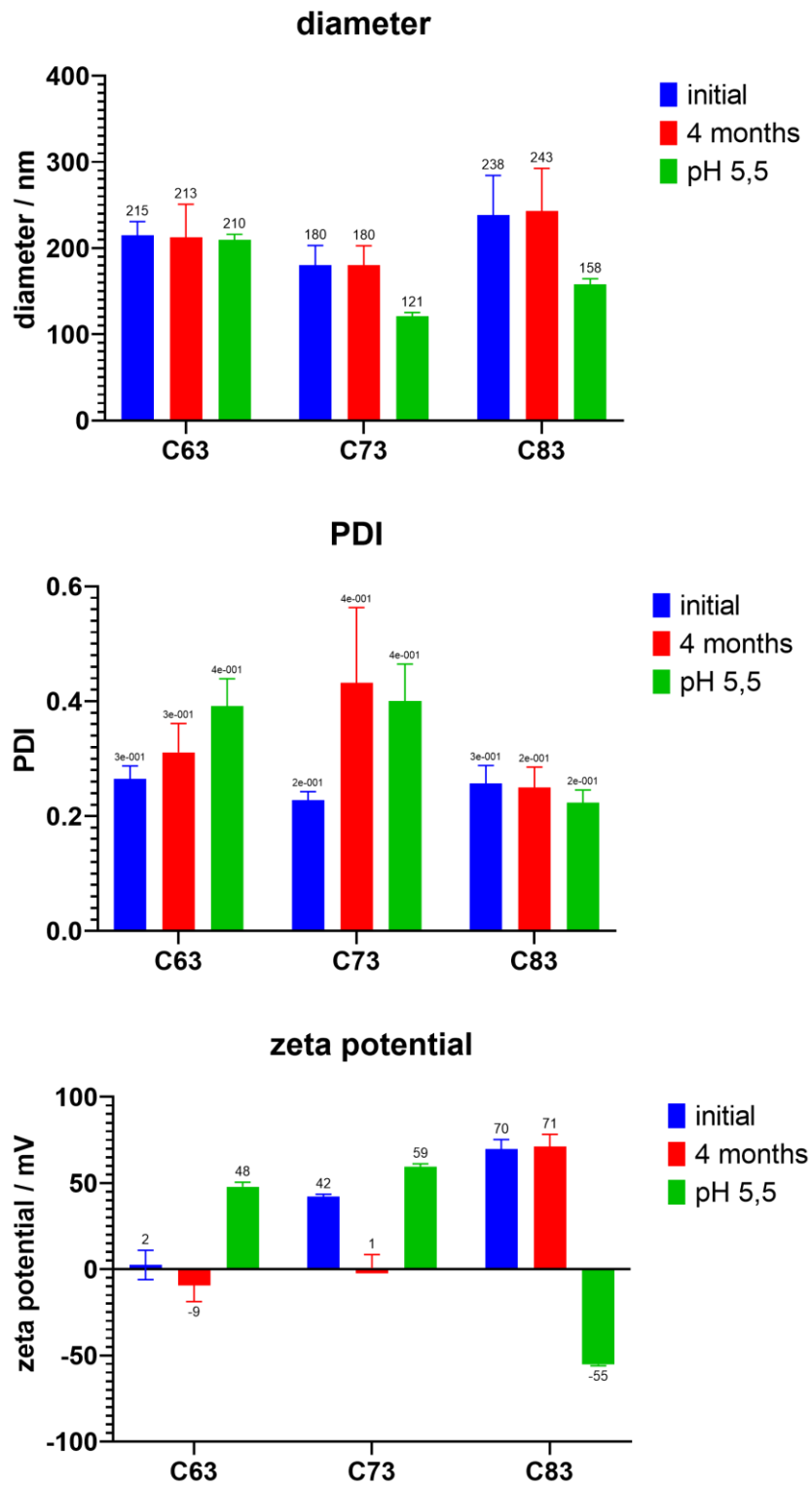


**Figure 20:** Changes in diameter, PDI and zeta potential due to liposome degradation over time and at low pH 5.5. In addition, cargo release was measured. Data of [REDACTED].<sup>187</sup>

## *Results and Discussion*

### **4.5.3 Doxorubicin as model cargo for release assays**

Evaluation of liposomes as Doxorubicin carriers in cell assays was done in four steps. At first Doxorubicin content in liposomes was determined by cracking the liposomes with 5% Triton™ X-100 and measuring the absorbance at 488 nm against a standard curve of free Doxorubicin hydrochloride in a plate reader (see 3.16). Fluorescence measurement was avoided due to quenching effects. The standard curve starting from 1,725 mM as top standard in 10 dilution steps to 6,71  $\mu$ M (dilution factor 2) started at low values to a peak at around 107,81  $\mu$ M and dropped again to lower values at lower Doxorubicin concentrations. In this special situation, one fluorescence value on the y-axis would have two corresponding fluorescence values on the x-axis. To measure absorbance avoided those problems while sacrificing accuracy. In the following experiments where cells were treated with liposomes the added volume of liposome dispersion was adjusted with a factor to have 1  $\mu$ M Doxorubicin concentration in every sample. This procedure ensured equal Doxorubicin concentrations with different liposome batches.

The second step focused on direct toxicity of the Doxorubicin loaded liposomes. Their toxicity at a Doxorubicin concentration of 1  $\mu$ M was compared to three concentrations of free Doxorubicin (1, 2,5 and 10  $\mu$ M; **Figure 23** A, B, E & F). Apoptosis caused by Doxorubicin needs time to unfold. That is why longer time points (24 hours & 48/72 hours) were chosen. It should be stressed that killing the cells was not the aim of this assay. The toxicity assay was done to ensure, that cells are still alive and functional at the used concentration to enable release experiments in intact cells. For up to 24 hours, this was true for both cell types with a Doxorubicin concentration of 1  $\mu$ M. 84% of UKRV-Mel-15a and 78% of macrophages were still alive. But raising the incubation time leads to 37% alive melanoma cells after 72 hours and 58% living macrophages after 48 hours.

The next step was to test delivery of Doxorubicin by liposomes into the nuclei of human monocyte-derived macrophages and human melanoma cells UKRV-Mel-15a *in vitro*. Readout of release was through the developed system of measuring Doxorubicin fluorescence in cell nuclei using confocal microscopy. As backup, cells were also submitted to flow cytometry to get whole-cell fluorescence data from Doxorubicin and the DiD label of the liposomes. Later on, a second method to investigate release was implemented using the Amnis ImageStream technology which provides higher statistical power because more cells (>1000) can be investigated at once.



## Results and Discussion

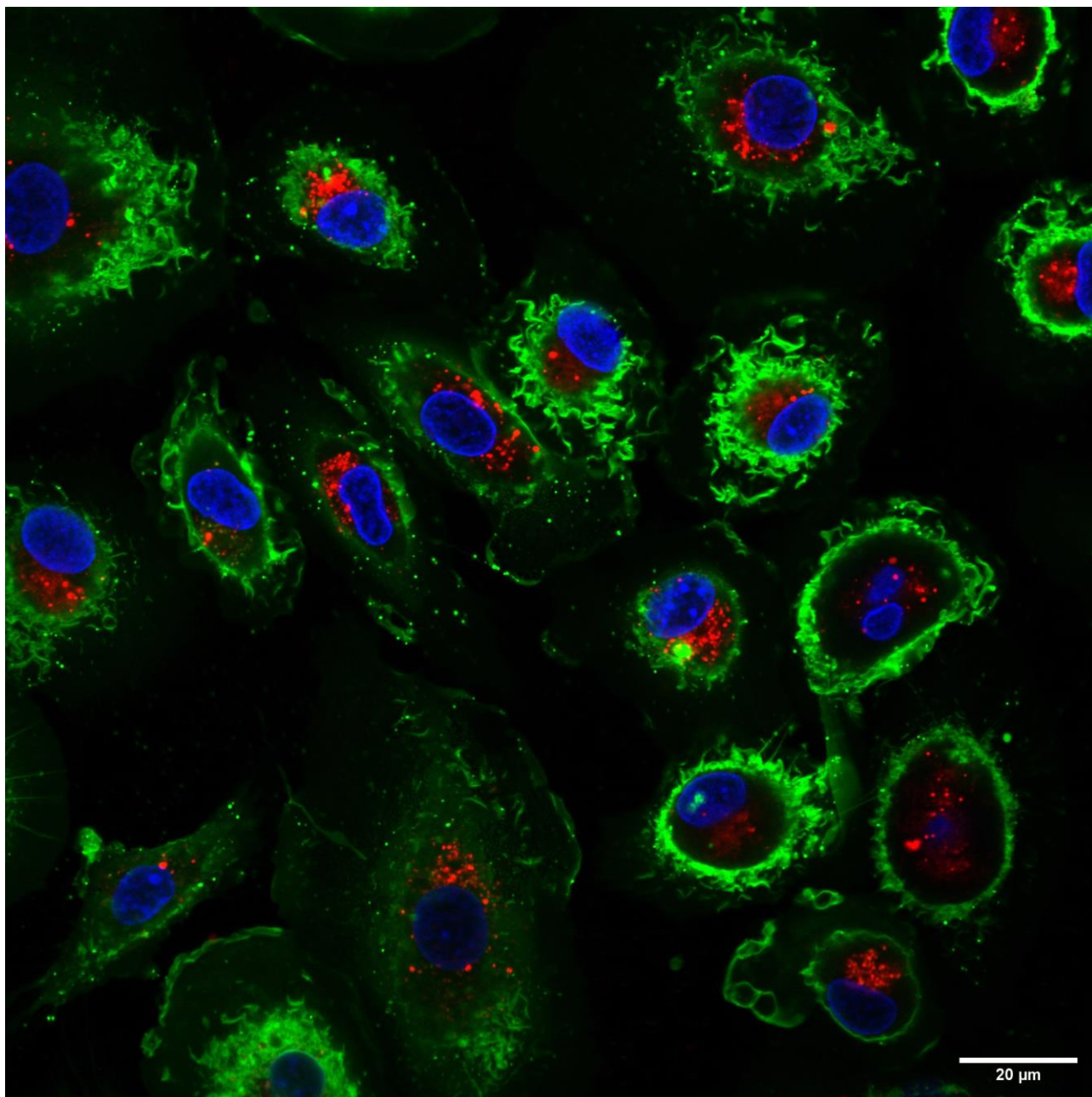


**Figure 21:** As depicted in **Figure 16**, liposomes are taken up by macrophages (shown here) and melanoma cells. Macrophages were incubated for 3 hours with liposomes at cell culture conditions. Nuclei stain with Hoechst 33258 shown in blue, cell membrane stained with NeuroDiO shown in green and liposomal DiD shown in red. Scale bar is 20  $\mu\text{m}$ . The membrane staining was omitted in subsequent release studies, since NeuroDiO interferes with detection of weaker Doxorubicin signals from nuclei. Doxorubicin release studies are shown in **Figure 24** and **Figure 25**.

## Results and Discussion

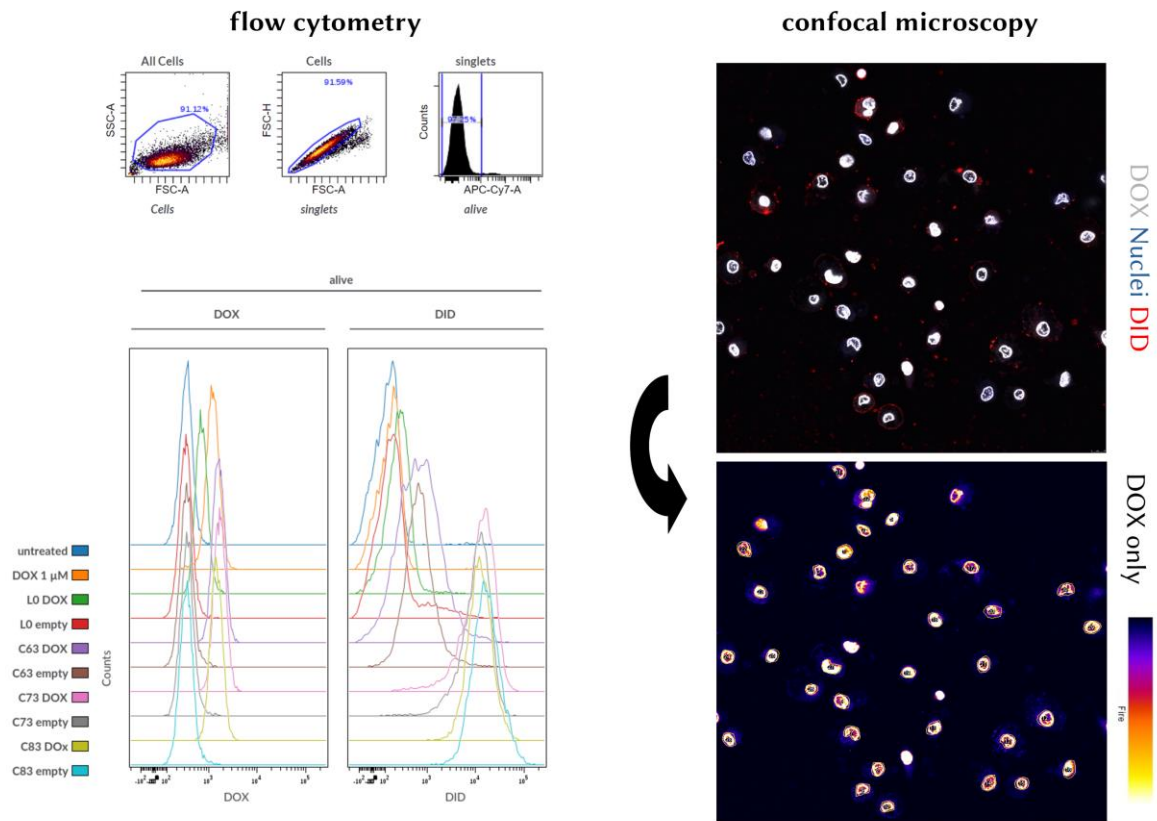
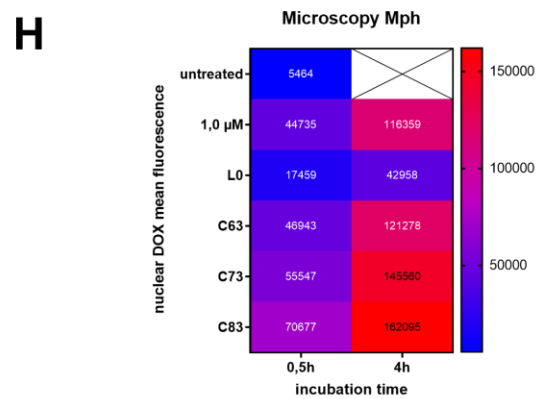
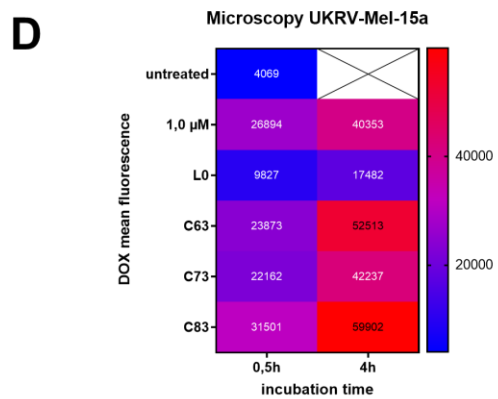
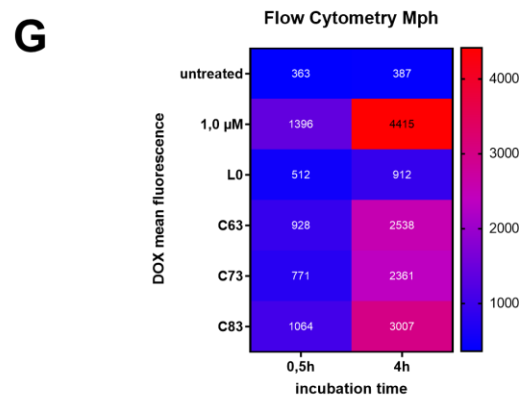
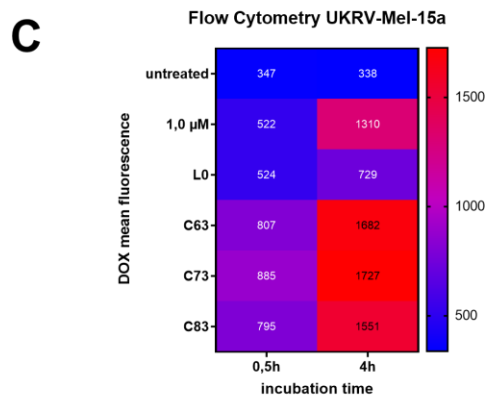
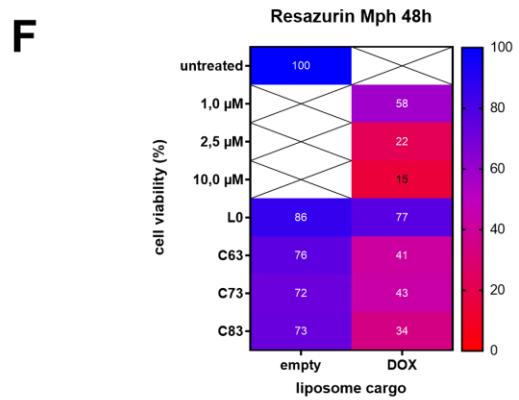
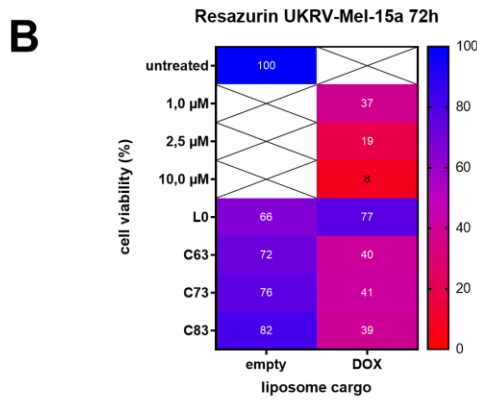
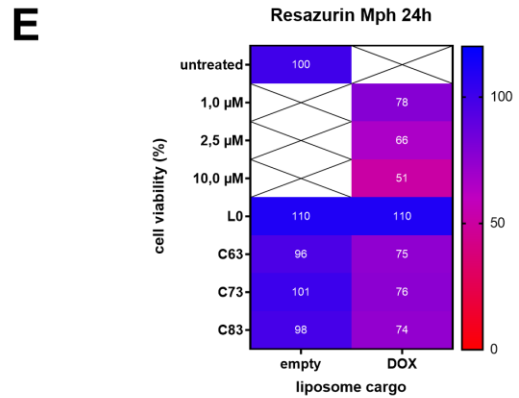
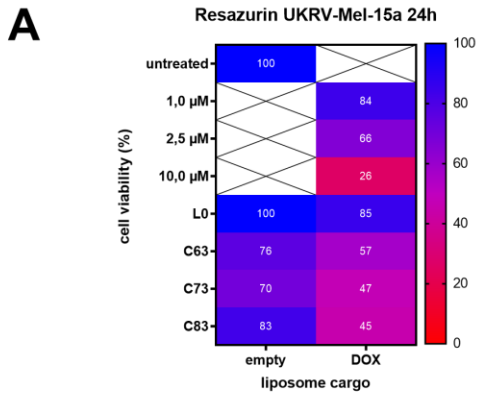


**Figure 22:** Flow cytometry gating strategy to quantify whole cell Doxorubicin signal (left). Debris was excluded by gating on single cells based on their size (FSC-A), signal intensity (FSC-H) and granularity (SSC-A). FVD780 (in APC-Cy7 channel) was used to include only living cells in the analysis which show a lower signal compared to dead cells. In confocal microscopy nuclei were counterstained with Hoechst 33258 (blue). Liposomes were detected by their DiD fluorescence (red). By using the software Fiji, the lookup table “Fire” was applied to detect even very weak Doxorubicin signals (right, lower picture). Nuclei were gated manually.

# Results and Discussion



## Results and Discussion

**Figure 23:** Liposomes with designed fragile stability were tested as Doxorubicin carriers on human melanoma cells (UKRV-Mel-15a) and human monocyte-derived macrophages. The cytotoxicity after 24h and 48h/72h was analyzed via resazurin assay (A, B, E & F). Whole-cell fluorescence caused by liposome uptake was monitored after 30 minutes and 4 hours using flow cytometry (C & G). Doxorubicin release after 30 minutes and 4 hours was detected by measuring Doxorubicin fluorescence exclusively in the cell nuclei using confocal microscopy (D & H). Free Doxorubicin was added as control and for normalization. Doxorubicin content in liposomes was normalized to 1  $\mu\text{M}$  free Doxorubicin. All values are triplicates. Statistic calculations are shown in table S1.

Both cell types were incubated with liposomes at a Doxorubicin concentration of 1  $\mu\text{M}$  for two timepoints. Both timepoints had the same endpoint meaning, that one part of the cells were incubated for 4 hours and 30 minutes before the end of the experiment the other half of cells were incubated. Cells, which were going to be investigated by flow cytometry, were seeded on 24-well cell culture plates. The other cells, designated for microscopy, were seeded on ibidi  $\mu$ -slides (8 well). Since flow cytometry operates with single cell suspensions, cells had to be harvested, stained for live cells and fixed afterwards. ibidi  $\mu$ -slides on the other hand are combined cell culture and microscopy slides. Cells were stained and fixed attached to the slide. Both cell types are adherent.

Whole cell fluorescence of Doxorubicin recorded by flow cytometry caused by destabilized liposomes C63, C732 & C83 exceeded in melanoma cells (**Figure 23 C**) values of 1  $\mu\text{M}$  free Doxorubicin. Only the stable L0 formulation, adapted from Myocet, had the same fluorescence after 30 minutes and was below that value of free Doxorubicin after 4 hours. Higher values than the free substance could hint at higher delivery of Doxorubicin through the cell membrane by liposomes. But quenching effects can also play a role. For macrophages (**Figure 23 G**), although very phagocytotic cells, the liposomes lag behind compared to the free substance at both timepoints. C83 showed the highest values and again L0 the lowest values. In both cell types and in case of every treatment group fluorescence increased from 30 minutes to 4 hours, showing that uptake is an ongoing process between those timepoints. Differences in mean fluorescence values between both cell types might arise from permeability for free Doxorubicin, phagocytic activity, cell density and DNA density/content.

To have a closer look at Doxorubicin release at those early time points cells were imaged using confocal microscope (**Figure 24 & Figure 25**). Cell nuclei were identified using Hoechst dye and gated with the software Fiji. Fluorescence coming from one z-plane was recorded from 20+ nuclei. The membrane staining (**Figure 21**) was omitted, since NeuroDiO interferes with detection of weaker Doxorubicin signals from nuclei. Common findings between flow cytometry and microscopy were the increase in fluorescence between both time points. In melanoma cells (**Figure 23 D**) the liposome C83 had the highest release after 4 hours, although in flow cytometry it had the lowest signal of all destabilized liposomes. In both methods, the stable liposome L0 showed a release far below the destabilized liposomes and the free substance for both cell types. Interestingly, in this method Doxorubicin levels of treatment groups with destabilized liposomes surpassed free Doxorubicin in both cell types at 4 hours. Macrophages (**Figure 23 H**) showed already after 30 minutes higher values than the free substance. Microscopy proved its ability to assess Doxorubicin release into the nuclei and it detected differences between the liposomal formulations. The already mentioned common findings support the microscopic approach.

Time consuming manual gating from a limited number of confocal pictures turned out to be a bottleneck in screening of many liposomal formulations multiplied by surface modifications of those different species. To avoid this bottleneck the ImageStream technology, combining microscopy and flow cytometry, was tested as alternative in pilot experiments.

## Results and Discussion

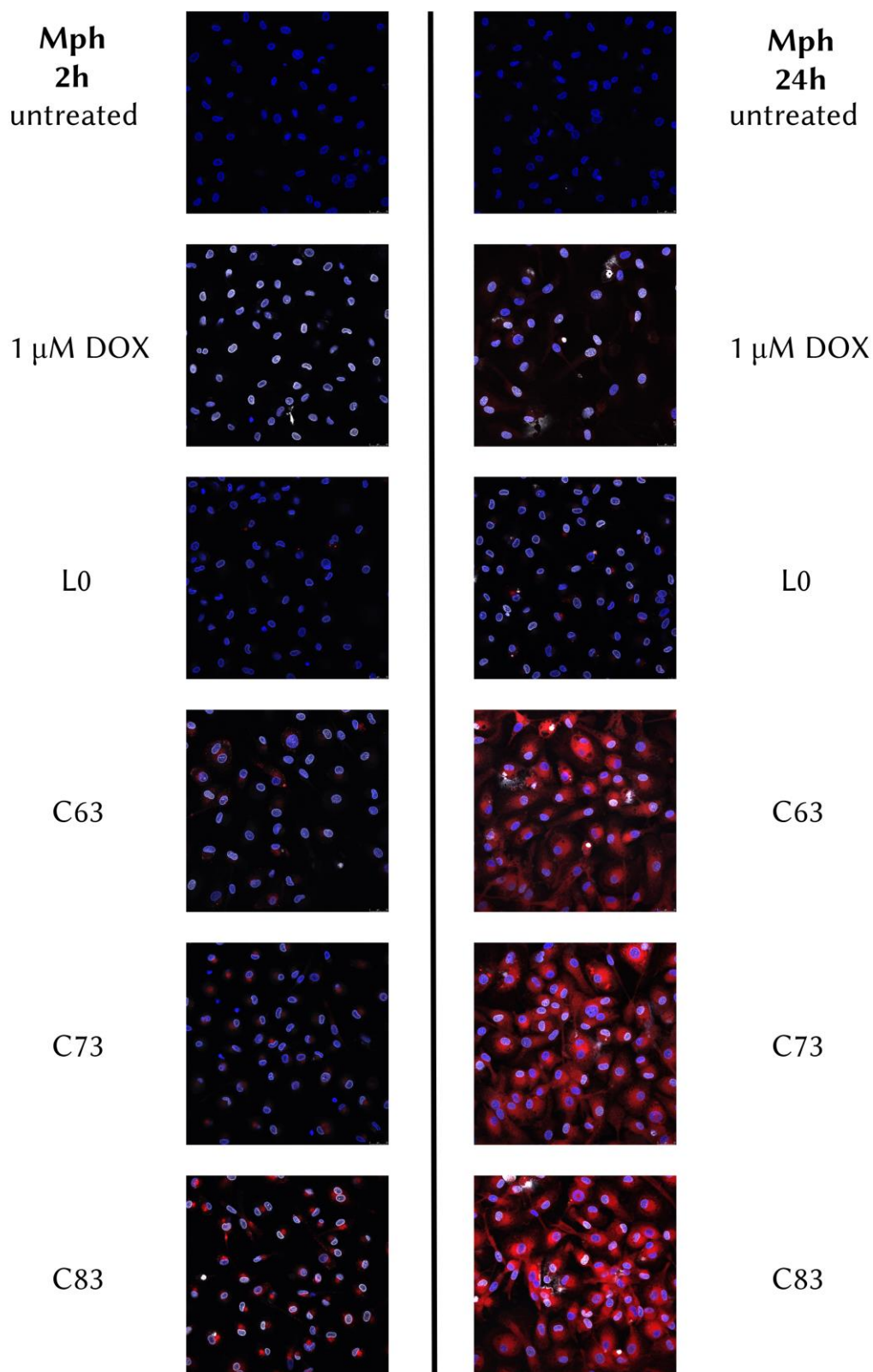


**Figure 24:** Liposomal delivery of Doxorubicin and its accumulation in cell nuclei of human monocyte-derived macrophages after 2 hours and 24 hours of incubation at cell culture conditions (37°C, 5% CO<sub>2</sub>). Untreated cells served as negative control and uptake was compared to 1 μM free Doxorubicin. Nuclei are shown in blue (Hoechst 33258), liposome label in red (DiD) and Doxorubicin in grayscale. Scale bars are 25 μm. Analysis was done by manually gating the nuclei and quantifying fluorescence in the Doxorubicin channel only using the software Fiji.

## Results and Discussion

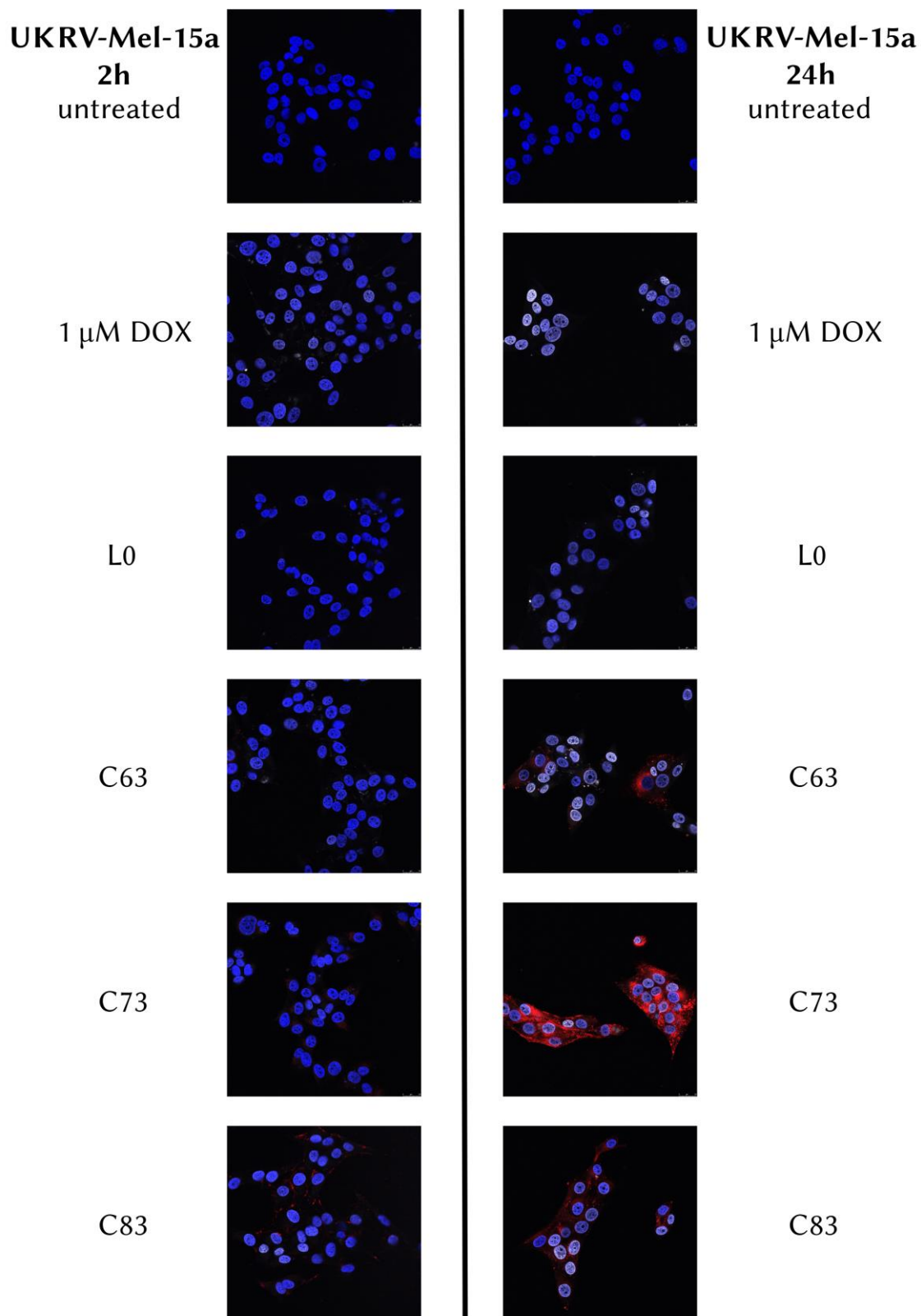


**Figure 25:** This figure shows the same experimental setup as in **Figure 24**. In this case human melanoma cell line UKRV-Mel-15a was incubated with Doxorubicin loaded liposomes.

# Results and Discussion

## 4.5.4 Novel screening method for Doxorubicin release

The ability of the *ImageStream* technology to resolve Doxorubicin uptake into the nuclei like the established method using confocal microscopy was tested as proof-of-concept experiment. The *ImageStream* lacks a confocal microscope and uses widefield fluorescence microscopy instead (see **Figure 26 B**) to record a picture of every single cell, which passes the flow cell. The system is based on fluidics, like conventional flow cytometry. Disadvantages of the image acquisition, low acquisition time and no resolution on the z-axis, should be counterweighted by the possibility to investigate several thousand cells per run offering better statistical power. Cell viability and other markers stained with labeled antibodies have been (viability) or can be (markers) included in the analysis. The method would be verified if it is possible to gate on nuclei only and if the same trends shown in analysis by microscopy could be reproduced.

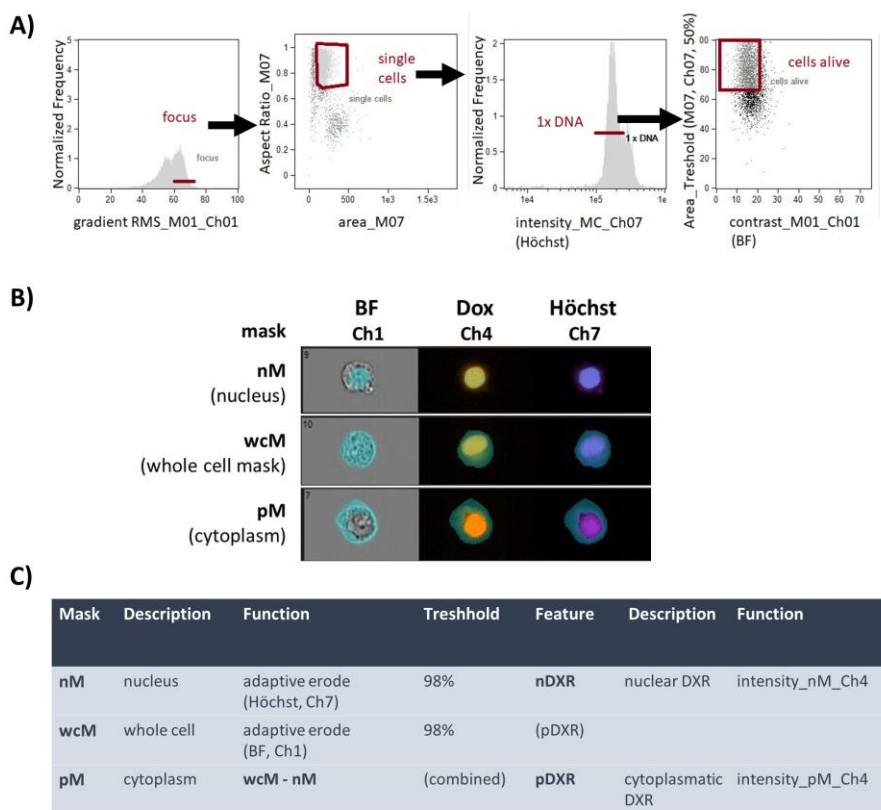


**Figure 26:** Single cell fluorescence data of cells passing the flow cell of the *ImageStream* flow cytometer is recorded by one acquired picture in each channel recorded and for each cell investigated. The *AMNIS IDEAS* Software allows gating on cell populations (A) and cell regions (B). This allows to discriminate Doxorubicin that has traveled to the nuclei and Doxorubicin still located in the cytoplasm (C). Gating and analysis using the *AMNIS IDEAS* software was done by [REDACTED]

## Results and Discussion

It was possible to define cell nuclei of melanoma cells and macrophages as regions of interest, counterstained by Hoechst dye and detached in a single cell suspension. Smaller cells might cause problems, since the nuclei must be large enough and the cell should have a rather large cytoplasm to clearly separate those two areas of the cell. The software based on fluorescence signals created overlaying “masks” by an algorithm. By this way, the signals were split up into signals from the nuclei and cytoplasm (see **Figure 26 B** light blue areas). A cell itself was detected in the brightfield (“BF”) picture automatically by the software. Hoechst bound to nuclear DNA emits a strong fluorescence signal, which is used by the software to define the region “nucleus”. This masks, “whole cell”, “nucleus” and the latter subtracted from the former “cytoplasm”, are used to measure the Doxorubicin fluorescence as “feature” spatially. This software feature, which replaces manual gating in several thousand cells, would be possible to transfer to confocal microscopy but the number of cells investigated would not be transferable.

The quintessence from previous experiments is that the liposomes designed at the edge of stability show higher release into the nucleus when compared to conventional L0. Furthermore, flow cytometry and confocal microscopy indicate ongoing release into the nucleus between the time points 30 minutes and 4 hours. At the later time point, Doxorubicin values of the destabilized liposomes often surpasses free Doxorubicin at 1  $\mu\text{M}$ . All those points mentioned were validated using the new approach (see **Figure 27** & **Figure 28**). While at the early time point of 30 minutes all destabilized liposomes fluctuated around the reference of free substance, at 4 hours cells treated with those liposomes had more Doxorubicin in their nuclei. L0 treated cells lagged at both time points. Obviously, Doxorubicin signals rose between 30 minutes and 4 hours.

Those findings support the new method as valid replacement for the former method based on confocal microscopy, especially in screening approaches.

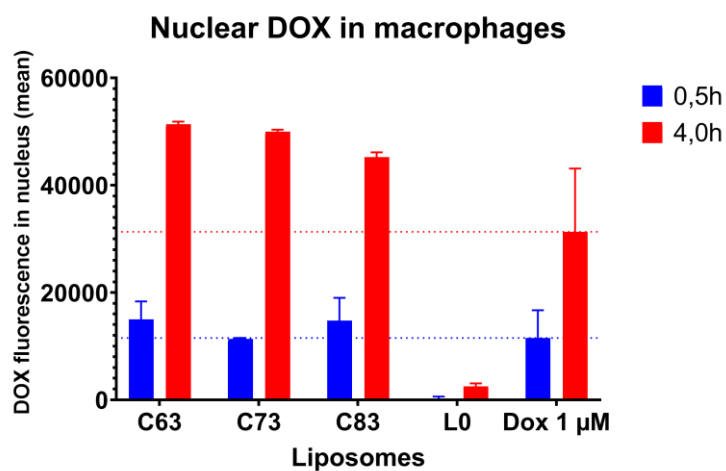


**Figure 27:** Analog to **Figure 23** the release of doxorubicin from liposomal carriers was analyzed using image-based flow cytometry (see 3.10). This method enables to gate and quantify doxorubicin fluorescence exclusively from the cell nuclei. Human monocyte-derived macrophages were incubated with different liposomal species normalized to 1  $\mu\text{M}$  doxorubicin content for 30 minutes and 4 hours. Free doxorubicin (1  $\mu\text{M}$ ) was used as control (dotted lines). All samples are duplicates.



## Results and Discussion

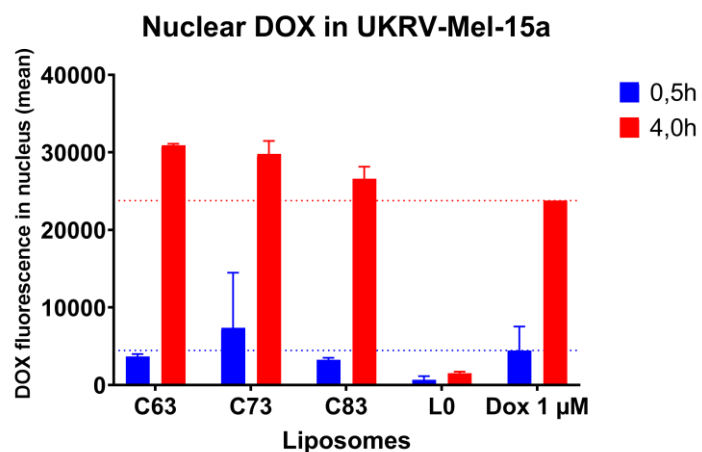


**Figure 28:** Analog to **Figure 23** the release of doxorubicin from liposomal carriers was analyzed using image-based flow cytometry (see 3.10). This method enables to gate and quantify doxorubicin fluorescence exclusively from the cell nuclei. Human melanoma cell line UKRV-Mel-15a was incubated with different liposomal species normalized to 1 µM doxorubicin content for 30 minutes and 4 hours. Free doxorubicin (1 µM) was used as control (dotted lines). All samples are triplicates.

## *Results and Discussion*

### **4.5.5 Screening of liposomes with modifications: biotin and PEG**

Having established the screening method, several liposomal formulations and surface modifications were tested for their potential to alter Doxorubicin release into the nuclei. Focus was not on different uptake behaviors. DiD label might also be influenced by the liposomal formulation and the integration of DiD into the cell membrane after liposome disintegration. Doxorubicin release into the nuclei where it can exert its biological effects is the important therapeutic parameter (bioavailability).

PEGylation is a common technique to reduce unspecific cellular uptake, to prolong circulation times, influencing aggregation/stability and protein corona formation.<sup>192,193</sup> Doxorubicin loaded C83 and stable L0 were modified with linear PEG or hyperbranched PG to investigate its effect on liposome stability and uptake by measuring the release into the nuclei compared to the unmodified liposomes (see **Figure 29**). To see early effects the time points 30 minutes and 4 hours were chosen as in previous experiments. Conventional linear PEG with a molecular weight of 3190 g/mol was compared to hyperbranched PG having a molecular weight of 3084 g/mol. Both modifications were used at 5 mol-%. During synthesis, the modification can face the lumen or the outside of the liposome. Unexpectedly diametral effects of PEG/PG on Doxorubicin were discovered. Whereas destabilized liposome GD20 (a C83 formulation) showed a diminished release of Doxorubicin, the stable liposome GD30 (a L0 formulation) had the opposite effect of enhanced release through PEGylation. Both types of PEG did not differ in their effects, most likely since also linear PEG will form a disordered coil resembling a hyperbranched PG.<sup>194</sup> In this experiment free Doxorubicin was applied in two concentrations: 0,5  $\mu\text{M}$  and 1  $\mu\text{M}$ . At the early time point the Doxorubicin signal in the 0,5  $\mu\text{M}$  group was almost at the baseline, but after 4 hours it was detectable. This shows the resolution of the developed method, as 0,5  $\mu\text{M}$  should be the lowest standard, at least in the *ImageStream* approach. GD30 had the lowest Doxorubicin release which was around that of 0,5  $\mu\text{M}$  free Doxorubicin after 4 hours. After 30 minutes no signal above background could be detected for GD30. PEGylation enhanced the stability of C83 liposomes which lead to reduced release of Doxorubicin.

## Results and Discussion

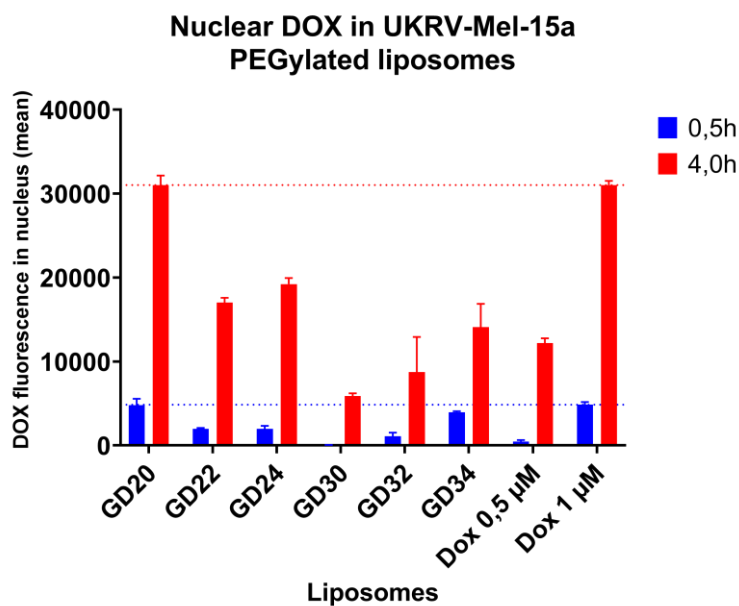


**Figure 29:** Analog to Figure 23 the release of Doxorubicin from liposomal carriers unmodified (X0), modified with linear PEG (X2) or hyperbranched PG (X4) was analyzed using image-based flow cytometry (see 3.10). This method enables to gate and quantify Doxorubicin fluorescence exclusively from the cell nuclei. Human melanoma cell line UKRV-Mel-15a was incubated with different liposomal species normalized to 1  $\mu\text{M}$  Doxorubicin content for 30 minutes and 4 hours. Free Doxorubicin (0,5  $\mu\text{M}$  & 1  $\mu\text{M}$ ) was used as control (dotted lines). All samples are triplicates.

This influence of PEGylation on Doxorubicin was not visible in previous experiments where liposomes were modified with PEG coupled to pH-labile linkers containing a ketal or vinyl ether group (see **Figure 30**). In acidic environments those linkers will be cleaved and the liposomes shed their PEG coating. Since these preliminary experiments were performed before the development of the *ImageStream* method, only whole cell Doxorubicin fluorescence was recorded of human melanoma cells and human macrophages treated with those modified liposomes using flow cytometry. L7 is a PEGylated variant of L0. This stable liposome showed again the lowest Doxorubicin signal. As shown in previous experiments (**Figure 23**), not only release of L0/L7 is low, but also the uptake rate is low. pH sensitive PEG modification did not alter the high Doxorubicin uptake of C63, C73 and C83 liposomes. In comparison to data shown previously in **Figure 29** the liposomes with pH sensitive PEG act like liposomes without modification whereas liposomes with PEG and a stable linker show reduced intracellular Doxorubicin release. This diminished release was verified by [REDACTED] in release experiments with Sulforhodamine B loaded liposomes modified with hyperbranched PG, linear PEG and both pH sensitive variants.<sup>187</sup> The liposomes were incubated in buffer at pH 5,5 for 4 hours and 37°C to simulate cellular uptake into lysosomes in the same time frame as the cell experiments.<sup>195,196</sup> Sulforhodamine B is a hydrophilic fluorescent dye with comparable molecular weight of 581 g/mol (sodium salt) to Doxorubicin with 580 g/mol (hydrochloride salt).

## Results and Discussion

Cleavage of ketal PEG was expected to happen in this time frame of 4 hours based on previous studies.<sup>197,198</sup> Vinylether PEG should have reacted much slower.<sup>199</sup> The comparable behavior of both PEG linkers was therefore unexpected.

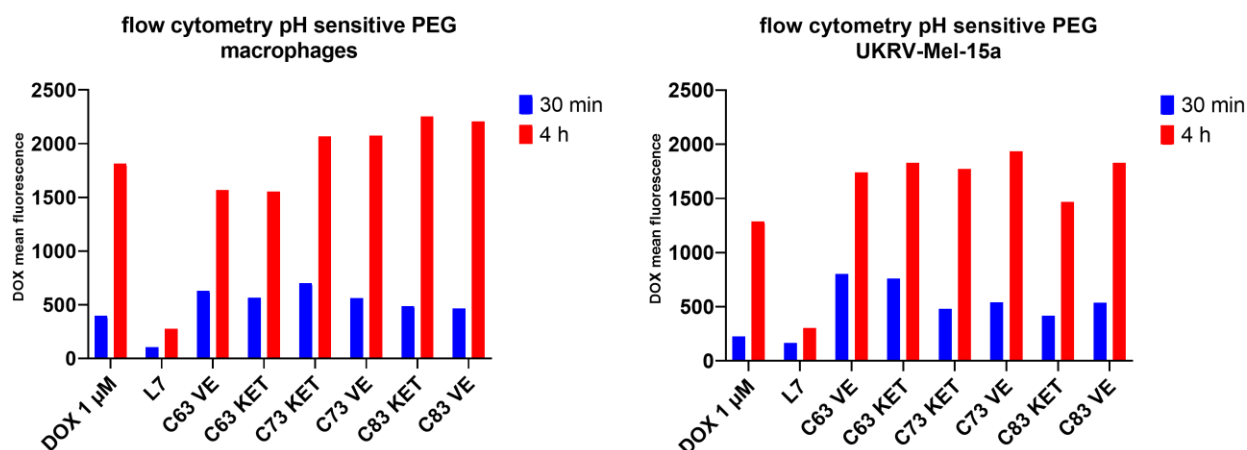


**Figure 30:** Whole cell Doxorubicin fluorescence in human macrophages and human melanoma cell line UKRV-Mel-15a caused by pH sensitive ketal- and vinylether-PEG modified liposomes (5 mol-%) were detected via flow cytometry. Doxorubicin content was normalized to 1 μM and compared to uptake of free Doxorubicin in the same concentration.

Taken together, the *ImageStream* method offers a perfect compromise between spatial resolution and the possible number of cells to investigate in order to have significant results and statistical power.

It is necessary to screen every liposomal formulation and every modification since both can influence the physicochemical properties of liposomes and in the end their release of cargo. It has been shown that PEGylation reduces release of Doxorubicin into the nuclei of cells and that designing fragile liposomes boosts the release of cargo at early time points in comparison to liposomes already used in the clinic (L0). Whether an early release or a high stability is favorable depends on the application *in vivo*. Targeting using antibodies or other small molecules needs a certain circulation time of particles to enable them to reach the target tissue and to avoid premature clearance. This developed Doxorubicin assay is necessary to perform beforehand of *in vivo* experiments to have release characteristics and kinetics *in vitro*. Then it is possible to compare biological effects of stable or instable liposomes and to know effective doses of a drug in a time dependent manner. If used at concentrations not toxic to the animal Doxorubicin is also an ideal model drug for *in vivo* testing since its detection in nuclei can also be done in tissue samples.

## Results and Discussion

### 4.5.6 Stability of liposomal membrane anchors<sup>VI</sup>

Modifications on liposomes, like integrating fluorophores or ligands for receptors on target cells, demand a stable connection to the liposome if applied to complex *in vivo* systems where an abundance of cellular membranes and proteins can interact with the modification and its anchor (see **Figure 31 A**). Hydrophobic modifications can be applied directly during liposomal formulation and will integrate into the hydrophobic phase of the phospholipid bilayer, like the lipid fluorophore DiD often used to trace liposomes in this work. In order to target cells, the modifications should be accessible on the surface of the liposomes and they are often hydrophilic (e.g. proteins like antibodies or biotin). A common strategy is to couple those molecules with or without a spacer molecule (often a PEG chain) to a lipid which inserts itself into the phospholipid bilayer thereby acting as anchor. Mimicking the biological system, diacylglycerides or cholesterol can serve as anchors (see **Figure 31 B**). Phospholipid bilayers are complex dynamic systems, which exist depending on the temperature and their lipid composition in a fluid state.<sup>200</sup> In cellular membranes the high amount of lipid species and the insertion of transmembrane proteins add complexity. In general, for amphiphilic molecules in (aquatic) solution certain forms of aggregation are energetically favorable. Above the critical micelle concentration, they form micelles, where the hydrophobic tails form a hydrophobic core and every polar component is oriented outwards to the polar solvent (water). Another favored structure is the lipid bilayer, where two layers of amphiphiles oriented at 180° form a sandwich with a hydrophobic inner layer (see **Figure 31 A**). Liposomes have this bilayer structure and their inner space of separated solvent (water) is called lumen. Cells are nothing but large liposomes with multiple inner layers of membranes, like organelles and the nucleus. This structure implies, that anchors inserted in the membrane cannot be as stable as covalent bonds. Lipids can move inside the membrane, switch layers or even transfer themselves into another neighboring bilayer, spontaneously or catalyzed by enzymes like scramblase, flippase or floppase.

---

<sup>VI</sup> The following part 4.6 was a cooperation between [REDACTED], research group of [REDACTED] at the Institute of Pharmacy and Biochemistry of the Johannes Gutenberg University Mainz, and I, embedded in the Collaborative Research Center 1066 “*Nanodimensional polymer therapeutics for tumor therapy*” located in Mainz, Germany. [REDACTED] synthesized the modified liposomes. Together we planned and performed the biological experiments and analyzed the data. The study on the stability of alkyl chain lipid anchors in liposomal systems has been published.<sup>146</sup>

## Results and Discussion

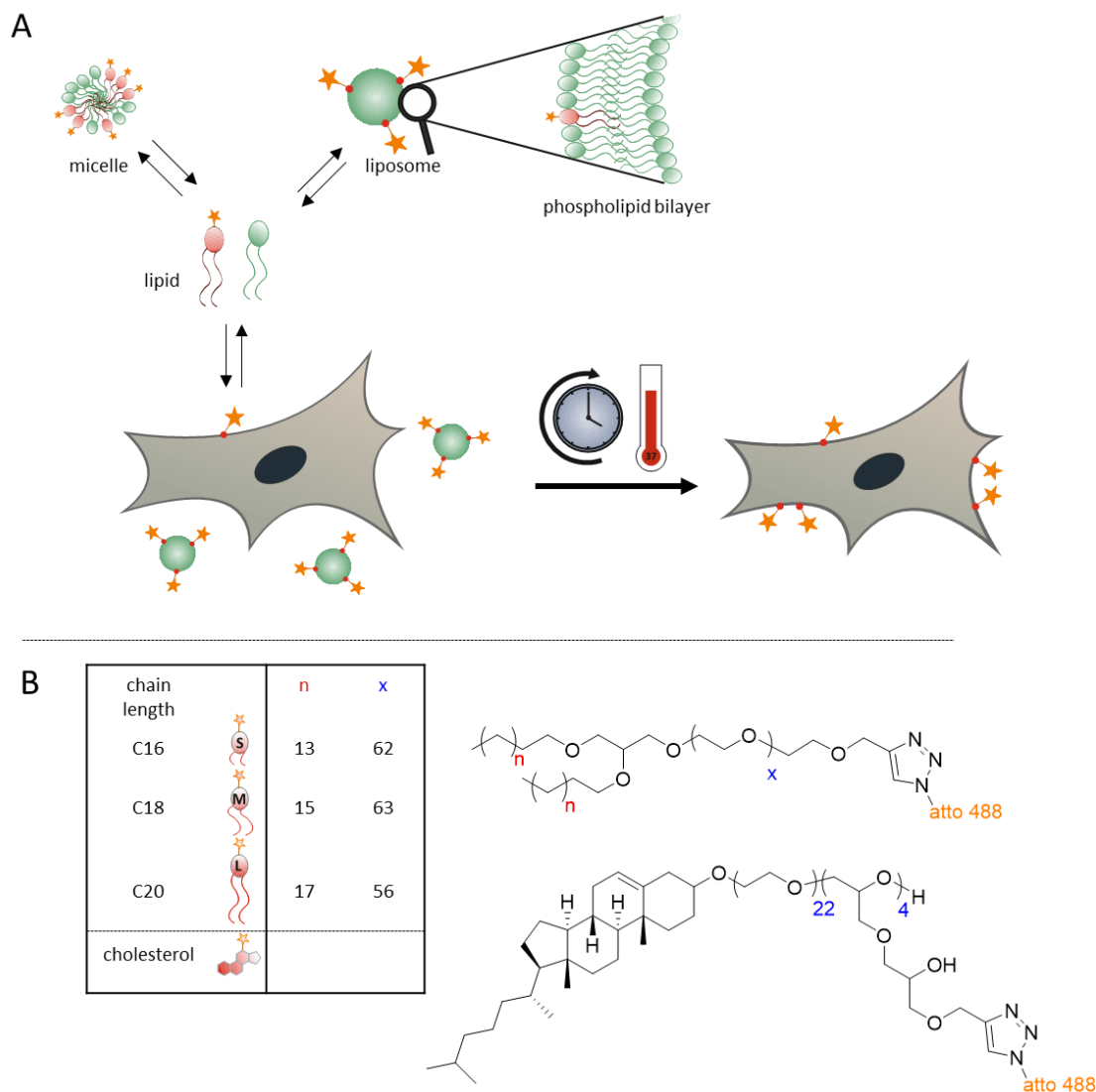


**Figure 31:** Amphiphilic lipids applied to systems containing cells in an aqueous solution are in an equilibrium between micelles, liposomes with a bilayer structure or they integrate into the bilayer system of the cell itself (A). The fluorophore atto 488 was coupled to synthetic polyether lipids tethered to alkyl chains with 16 – 18 carbon atoms or cholesterol (B).  $x$  describes the number of polyethylene glycol units.<sup>146</sup>

Previous studies revealed that cholesterol anchors show rapid lipid exchange with other membranes they encounter.<sup>201</sup> In contrast anchors with C18 chains showed a strongly reduced exchange. These studies were expanded to define the number of carbon atoms necessary for robust anchors. Cholesterol based anchors were used as control in 2 different concentrations of 1% and 5% (v/v), as were the lipids with alkyl chains of 16-20 carbon atoms. To monitor lipid mobility the fluorophore atto 488 was used. Between 22 and 53 polyethylene glycol units served as spacer between fluorophore and the non-polar fatty acid ester groups or in other words, between modification and lipid bilayer. Previously used rat RBE4 cells were exchanged by human melanoma cell line UKRV-Mel-15a, as they represent future target cells in cancer therapy and are large in size. Lipid transfer experiments were carried out by incubation of the adherent cells with liposomal formulation carrying different anchors in normal cell culture medium and conditions for 4 h or 24 (see 3.18). Medium and free liposomes were removed and the remaining cells were detached by trypsin. All cellular processes were stopped by formaldehyde-based fixation. Dead cells were excluded with a live/dead stain. In flow cytometry the whole cell is illuminated by a laser source. Exchange of atto 488 from the liposomes into the cell membrane was quantified. Free liposomes were removed by medium removal and washing steps. Besides, they would

## Results and Discussion

not be detectable as events due to their 100fold smaller size than the tumor cells. Cholesterol based anchors showed their expected behavior of significantly higher transfer rates compared to alkyl anchors (see **Figure 32**) for both timepoints. C18 and C20 alkyl chains show similar stability as anchors in the liposomal membrane. However, C16 alkyl chains show a significant tendency to transfer to the cell membrane shown by the increase in fluorescence especially after 24 hours (see **Figure 33**), although it is not as strong as in the case of cholesterol anchors.

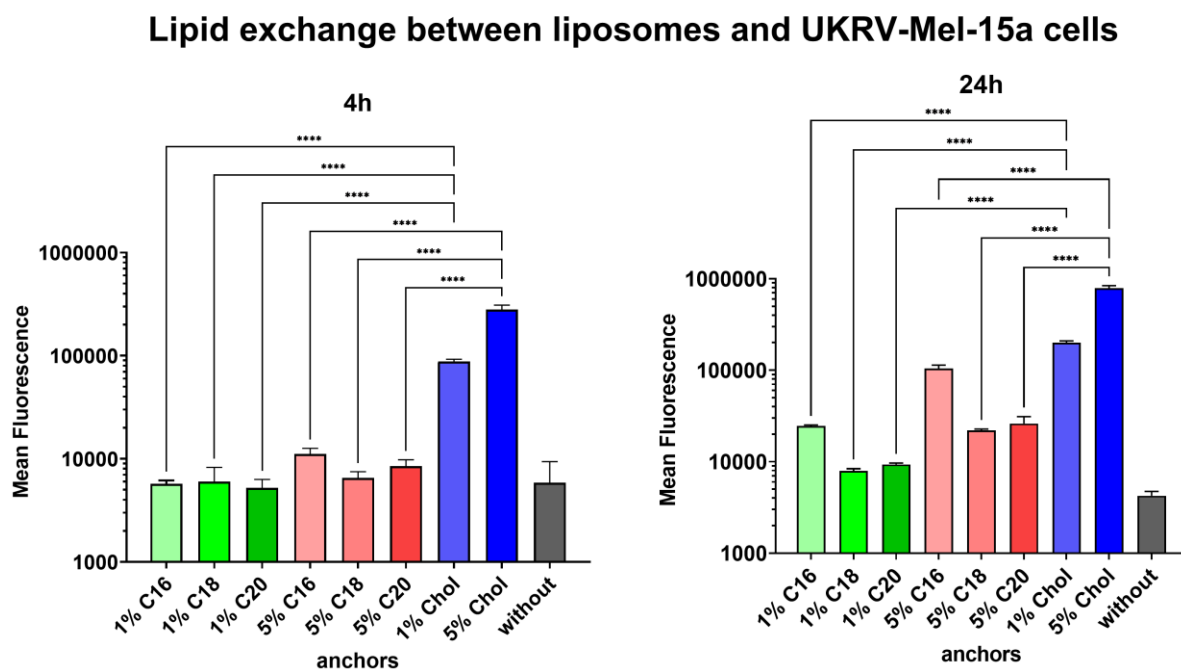


**Figure 32:** Lipid exchange between liposomes carrying a fluorophore atto 488 coupled to different anchors and human melanoma cell line UKRV-Mel-15a after 4 h and 24 h measured by flow cytometry.  $N = 3$ . Statistical significance was determined using the One-Way ANOVA with Fisher's LSD test. Ns = not significant, \*  $p < 0,05$ , \*\*  $p < 0,01$ , \*\*\*  $p < 0,001$ , \*\*\*\*  $p < 0,0001$ .

In flow cytometric measurements it is not possible to distinguish between lipid exchange between liposomes in the extracellular space and the cell membrane or uptake of liposomes in lysosomes inside the cell. To verify our theory of lipid exchange, confocal microscopy was used to show a uniform staining of the cell rather than single vesicles full of liposomes.<sup>146</sup> This indicates, that going below the typical alkyl chain length in biological membranes (C18) results in decreased van der Waals forces and subsequent easier transfer between membranes.<sup>202</sup>

Anchor stability experiments needs to be addressed *in vitro* for every modification because it is almost impossible to resolve *in vivo*. Although these experiments focused only on the role of the anchor, the modification itself and the spacer are expected to also influence how stable the modification of the liposome will be in complex environments.

## Results and Discussion

### Lipid exchange between liposomes and UKRV-Mel-15a cells alkyl chains only

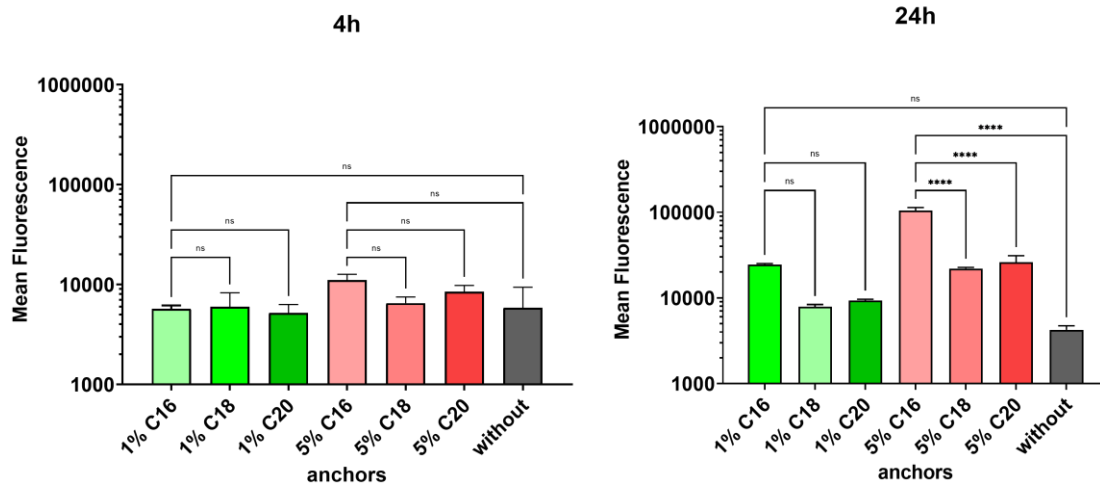


**Figure 33:** Data from **Figure 32** reduced to a statistical comparison of the three tested anchors based on alkyl chains from 16 to 20 carbon atoms length.  $N = 3$ . Statistical significance was determined using the One-Way ANOVA with Fisher's LSD test. *Ns* = not significant, \*  $p < 0,05$ , \*\*  $p < 0,01$ , \*\*\*  $p < 0,001$ , \*\*\*\*  $p < 0,0001$ .



## Results and Discussion

### 4.5.7 Targeting of biotin liposomes<sup>VII</sup>

After testing the effects of PEGylation on Doxorubicin release the next step was to enable surface modifications for targeting cells and/or tissue *in vivo*. A biotin-(neutr)avidin antibody-based approach was chosen. Liposome bound biotin enables, through neutravidin as adapter, the binding of biotinylated antibodies (see **Figure 34**). A linear PEG chain coupled to a distearoylphosphoglycerol served as spacer for biotin. During liposome formulation, both C18 chains of the phospholipid integrate into the lipid bilayer of the liposome, serving as anchor. This commercially available compound was added during synthesis. As biotin is only a small molecule of 244 g/mol and liposome formation with PEG chains was already established, low impact on synthesis was expected. After synthesis and purification of liposomes by HPLC, the liposomes can be incubated with neutravidin (a deglycosylated derivate of avidin) to form a strong non-covalent bond.<sup>203</sup> The biotin-(strept)avidin bond is widely used in life science to facilitate binding of enzymes to antibodies, purification of biotinylated substances and nucleic acid purification. In a second step a biotinylated antibody, or any other biotinylated molecule, can be added to the liposomes. This system is designed to avoid any influence of large proteins during liposome formation and vice versa any denaturation of the proteins during the conditions of the formulation. By choosing freely the ratios of liposomes, neutravidin and antibody this system is very versatile. In this work we focused on the first step of having a biotin label on the liposomes. This was tested with stable (L0) and fragile liposomes (mainly C83). To have a cell free and reliant test system, streptavidin (SA)- and bovine serum albumin (BSA) coated silica particles with a diameter of 5  $\mu\text{m}$  were used as binding substrate for biotin modified liposomes. Every step of this targeting system is planned to be tested separately. The test of the first step, synthesizing biotin labeled liposomes, is the binding of the biotin carrying liposomes to streptavidin labeled silica beads. The bovine serum albumin beads served as negative or background control since unspecific binding cannot be ruled out. Readout is via flow cytometry and the DiD label of the liposomes. The 5  $\mu\text{m}$  beads are in the size range of cells and can be detected in every common flow cytometer. Steps 2 (neutravidin binding) and 3 (antibody binding) are the focus of future work in this cooperation of the CRC1066.

---

<sup>VII</sup> The following part 4.7 was a cooperation project between [REDACTED], research group of [REDACTED] at the Institute of Pharmacy and Biochemistry of the Johannes Gutenberg University Mainz, and I, embedded in the Collaborative Research Center 1066 "Nanodimensional polymer therapeutics for tumor therapy" located in Mainz, Germany. [REDACTED] synthesized the modified liposomes. Together we developed the targeting strategy, planned and performed the biological experiments and analyzed the data.

## Results and Discussion

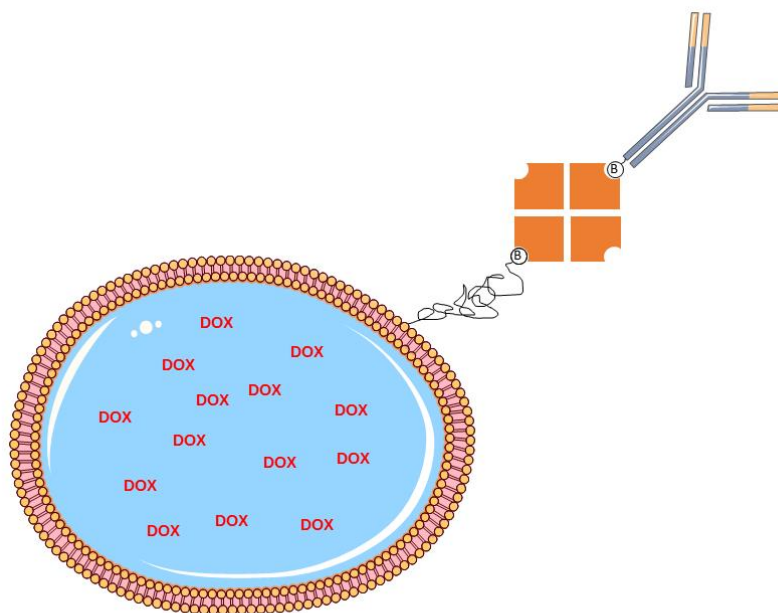


**Figure 34:** Rationale of liposome targeting using antibodies and the biotin-streptavidin (here neutravidin) system. Biotin is included in the lipid formulation as biotin-PEG-phospholipid (see 3.12). After liposome formation via dual centrifugation in a stepwise process first neutravidin and then a biotinylated antibody is added to the liposome dispersion. This strategy enables full flexibility regarding biotin, neutravidin and antibody ratios and it also circumvents the presence of large proteins like neutravidin and immunoglobulins during liposome formation. This sketch is not true to scale and for simplicity only one biotin linked to PEG is shown. Please take note, that the PEG-biotin chain can also be in the lumen.

The first aim was to establish the best molar ratio of biotin, which shows the strongest binding to streptavidin coated silica beads while having low background binding to bovine serum albumin beads. Liposomes were incubated with both silica bead species simultaneously to provide a specific and unspecific binding partner at the same time. Incubation time was limited to 20 minutes to avoid aggregation and absorption on the beads independent of specific biotin-streptavidin binding. The streptavidin beads also carried a fluorescent dye whereas the BSA beads did not which enabled their separation in the measurement. Confocal microscopy images of silica particles with liposomes bound to their surface served as proof of concept (see **Figure 40**). Liposomes (in red) formed an uniform layer on the surface. Clearly, interactions between protein surface coating and liposomes and/or electrostatic interactions lead to absorption of liposomes on the silica beads. BSA silica beads are coated with biotin liposomes, too. For this reason, the experimental setup with exposition of liposomes to both species of silica beads at once was adopted. The DiD signal of both bead populations (see **Figure 35**) was quantified and a ratio of specific signal of SA beads versus unspecific signal of BSA beads was calculated. The greater the value of this ratio, the better the targeting accuracy, since high values of the SA beads can be baffled by high values of the BSA beads for the same liposome.

## Results and Discussion

This experiment was focused on the instable candidate C83 and the “control” liposome L0 (see 3.17). Both species were synthesized with six different molar ratios of biotin: 0,05 mol%, 0,10 mol%, 0,25 mol%, 0,50 mol%, 1,0 mol% and 5 mol% (“PEG-Biotin”). As control liposomes lipids with PEG chains in the same length but without biotin were used (“PEG”). It can be estimated, that at least half of the PEG-lipid is bound in the outer layer of the liposome, reducing the effective biotin molar ratio to half. Both silica beads species were used 1:1 at a concentration of 156,25 µg/mL and liposomes at 2,5 vol%. To remove unbound liposomes the silica beads were briefly centrifuged and the supernatant containing free liposomes was discarded. The silica beads could be sedimented due to their higher density of 1,8 g/cm<sup>3</sup> whereas liposomes have basically the density of water of 1,0 g/cm<sup>3</sup>.

Surprisingly the C83 liposomes bound strongly to both silica bead species (see **Figure 36**) resulting in, albeit significant, low ratios between 1 to 2 (see **Figure 38B**). Every biotin ratio led to slightly higher binding towards SA beads without a difference between the biotin ratios tested. L0 stable on the other hand, showed a low release in every method used so far, showed a high binding to SA beads meanwhile having low background (see **Figure 37**). In this case, a ratio  $\gg 1$  resulted for every biotin ratio tested (see **Figure 38A**). Because DiD signal of SA beads slightly increased with increasing biotin and the DiD signal of BSA slowly decreased with increasing biotin, the ratio became only significant for 1 and 5 mol% biotin. However, with a ratio of 51,33% ( $\pm 15,57$ ) for 5 mol% biotin in L0 liposomes, contrasted to 6,02% ( $\pm 2,59\%$ ) for C83, L0 shows an overwhelming biotin based target capability. Of note, as PEG liposomes showed a preference for BSA beads (C83, ratio  $< 1$ ) or SA beads (L0, ratio  $> 1$ ) it is clear, that other effects than the non-covalent biotin streptavidin binding contribute to the absorption of liposomes on silica beads, too. Such effects can arise from hydrophobic interactions between PEG and SA or BSA. The zeta potential, simplified the surface charge, of the liposomes might cause electrostatic interactions. As C83 has a more negative value than L0 liposomes (see **Figure 19** for unmodified liposomes), this might explain its higher interaction with BSA beads.

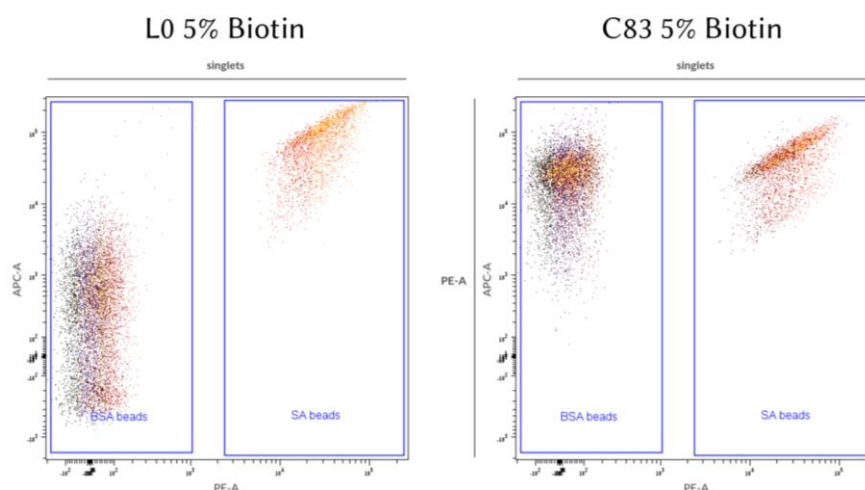


**Figure 35:** Exemplary gating strategy to distinguish between unlabeled BSA silica beads and labeled (redF) SA silica beads based on their fluorescence signal in the “PE” channel. For both bead types (here liposomes with 5% biotin modification) the mean fluorescence of the DiD membrane label in the “APC” channel was quantified and used to calculate the ratio between SA and BSA beads.

## Results and Discussion

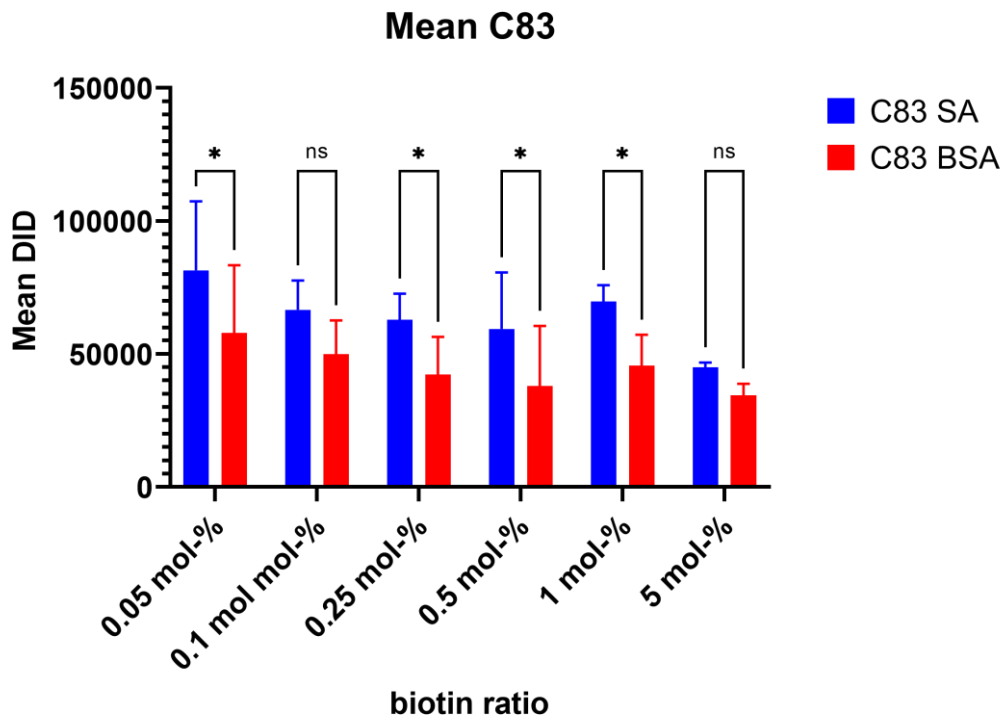


**Figure 36:** Binding of C83 liposomes, labeled with DiD and modified with different molar ratios of Biotin (x axis), to 5  $\mu\text{m}$  Silicabeads coated either with streptavidin (SA) or bovine serum albumin (BSA) was analyzed by flow cytometry (see 3.17).

N = 6.

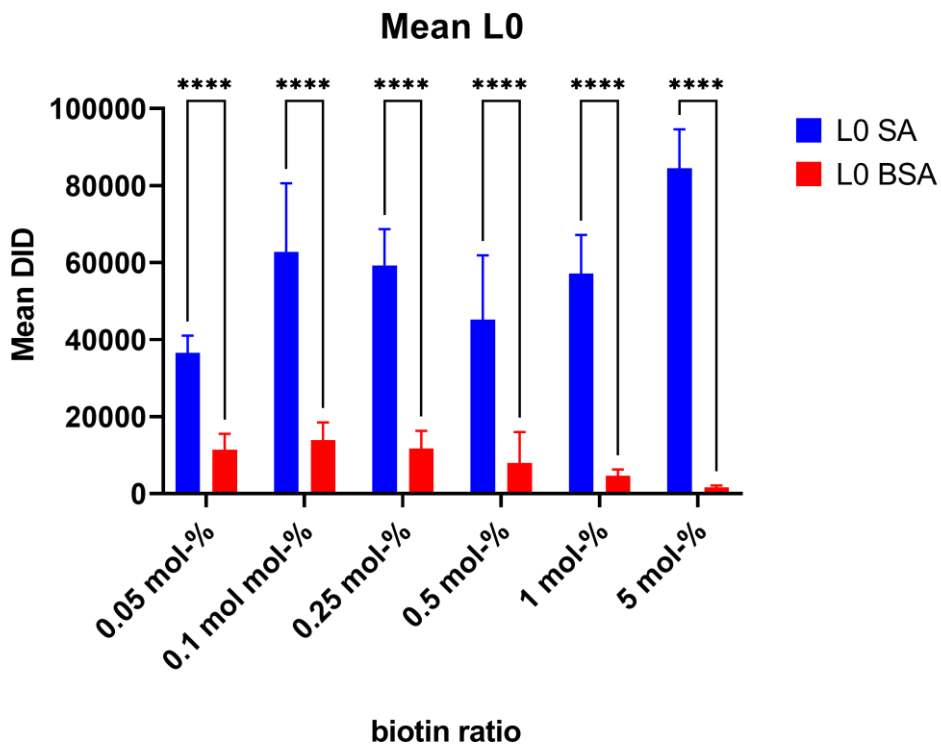


**Figure 37:** Binding of L0 liposomes, labeled with DiD and modified with different molar ratios of Biotin (x axis), to 5  $\mu\text{m}$  Silicabeads coated either with streptavidin (SA) or bovine serum albumin (BSA) was analyzed by flow cytometry (see 3.17).

N = 6.

## Results and Discussion

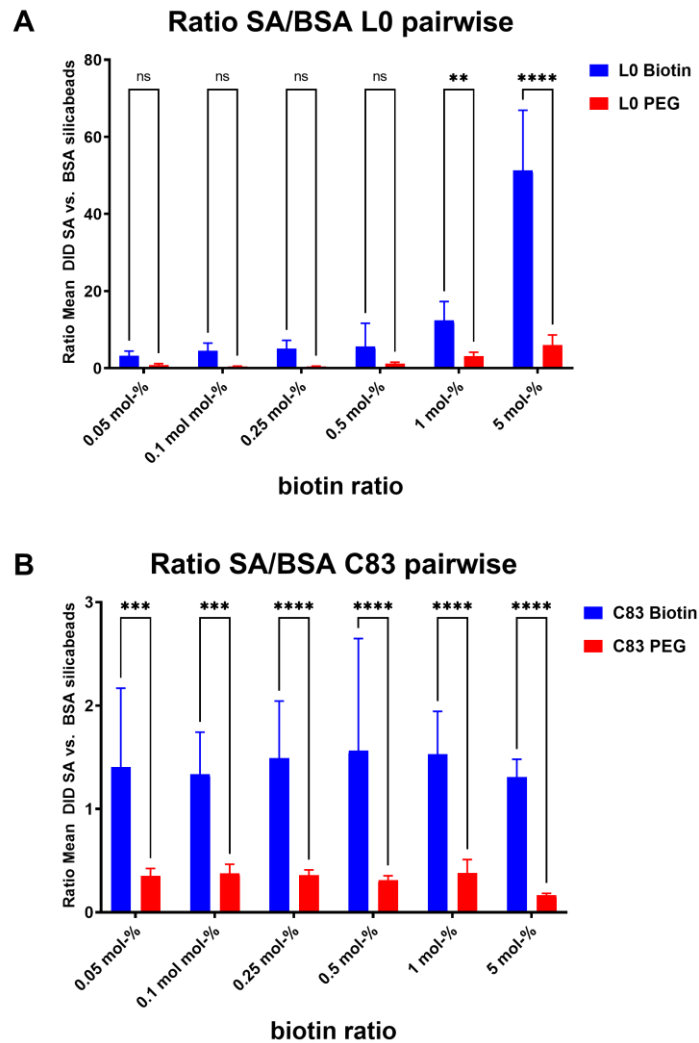


**Figure 38:** Based on fluorescence signals shown in Figure 36 & Figure 37 the ratio between binding of biotin labeled L0 (A) and C83 (B) liposomes to SA or BSA coated silicabeads shows targeting via biotin-streptavidin binding. Ratios above 1 indicate stronger binding of biotin labeled liposomes to SA coated beads compared to BSA beads.  $N = 6$ . Statistical significance was determined using the Two-Way ANOVA with Fisher's LSD test. ns = not significant, \*  $p < 0,05$ , \*\*  $p < 0,01$ , \*\*\*  $p < 0,001$ , \*\*\*\*  $p < 0,0001$ .

To check whether this varying behavior between stable and instable liposomes is true for every instable formulation, C63 and C73 were tested with only one biotin ratio as control (see **Figure 39**). The findings for C83 are replicated for the other two instable liposomes. Even though biotinylated C63 and C73 bind stronger to SA beads, the high background binding to BSA beads resulted in low ratios of 2,81% ( $\pm 1,32$ ) for C63 (significant) and 1,95% ( $\pm 0,33$ ) C73 (not significant). C63 PEG liposomes showed a significant preference for SA beads that might come from previously mentioned effects. C73 PEG liposomes showed equal binding to both silica beads.

## Results and Discussion

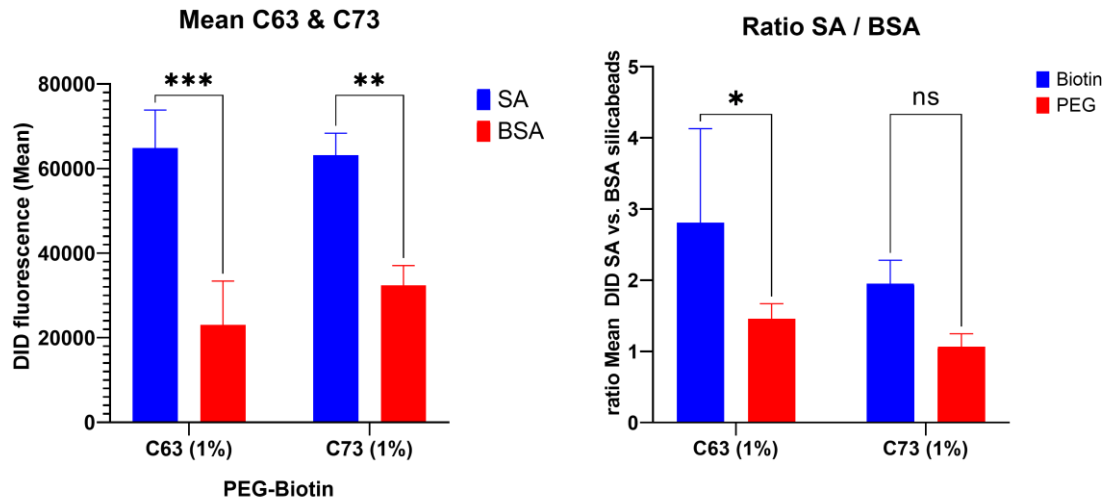


**Figure 39:** With C63 and C73 liposomes biotin targeting was also tested, but only with 1% PEG or PEG-Biotin as modification. Analogue to **Figure 36**, **Figure 37** and **Figure 38** data is displayed as raw DiD mean fluorescence (left) and as ratio between binding to streptavidin or bovine serum albumin coated silica beads (right).  $N = 3$ . Statistical significance was determined using the Two-Way ANOVA with Fisher's LSD test. ns = not significant, \*  $p < 0,05$ , \*\*  $p < 0,01$ , \*\*\*  $p < 0,001$ , \*\*\*\*  $p < 0,0001$ .

## Results and Discussion

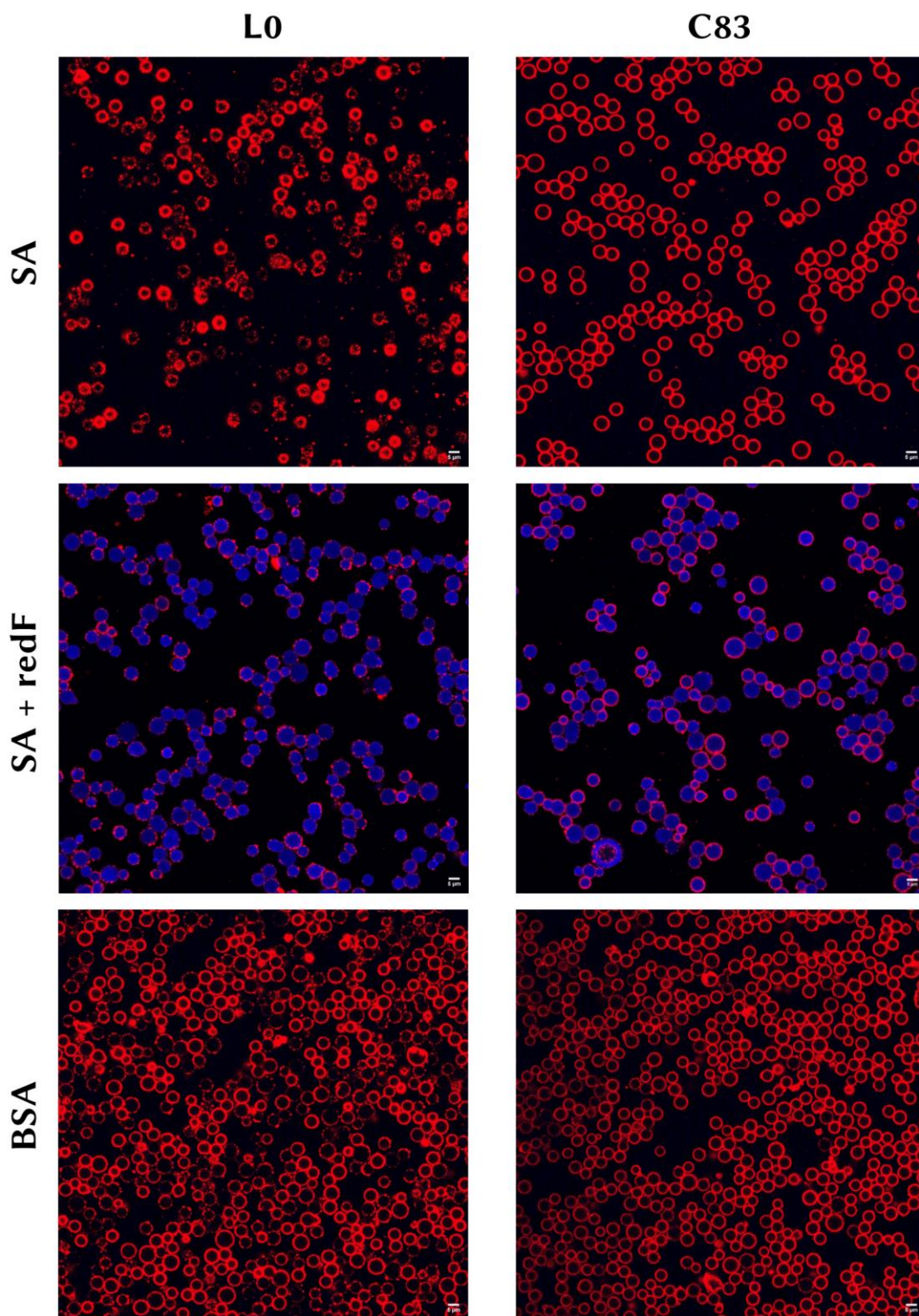


**Figure 40:** Biotinylated stable (L0) and instable (C83) liposomes were incubated with 5 μm silica beads either coated with streptavidin (SA) or bovine serum albumin (BSA) for 30 min at room temperature in a reaction tube, then washed and transferred to an ibidi microscopy slide. SA coated beads were also available with an incorporated fluorescent dye (SA + redF). DiD label of liposomes is shown in red and fluorescence of silica beads in blue. Scale bar is 5 μm.

## ***Results and Discussion***

### **4.6 *In vivo* melanoma model in humanized mice**

#### **4.6.1 Rationale**

Human melanoma cells lines UKRV-Mel-15a (not shown) and Ma-Mel-19 injected s.c. in the back of NOD Scid tgHLA-A2 mice give rise to subcutaneous tumors with a slow growth curve of 1-2 months before the tumors reach a size where the animals have to be euthanized due to animal welfare regulations. This is in contrast to many murine melanoma models where cells lines are also injected s.c., like the often-used B16 model.<sup>204</sup> In the latter tumors reach this size which forces the end of the experiment in a matter of days. This slow growth of human melanoma cells in the humanized mice resembles the physiological development of melanoma in the human body.<sup>205,206</sup> Peritumoral injection of human PBMC as mixed immune cell population is carried out when the tumors reach a measurable size of  $\geq 50 \text{ mm}^3$ . Tumors grow with or without human immune cells present. A population of the tumor mass by immune cells is ensured by applying them in close proximity. To have tumor-naïve immune cells later on, as control cells we also injected immune cells i.p. which do populate mainly the peritoneum and the spleen.<sup>207</sup> Of course, it is possible to use not injected PBMC as control cells, but those cells were not influenced by murine tissue. Therapy with Tasquinimod as free drug or encapsulated in liposomes was also carried out by peritumoral injection. Once weekly, for 3 to 4 weeks in volumes of 100  $\mu\text{L}$  per injection. After sacrifice of the mice, *ex vivo* analysis was carried out by removal of the tumor and the spleen. Further analysis focused on the tumor tissue, but the cellular composition of the spleens and tissue samples fixed in paraffin are kept for further studies. Tumors were first incubated in an enzyme cocktail called Accumax™ followed by manual disruption of the tissue using scissors, forceps and scalpels. Once cut into small pieces, the tissue was forced through 70  $\mu\text{m}$  cell sieves to avoid aggregates or even tissue pieces to hinder downstream processing for flow cytometry. For spleen samples the enzymatic step was not necessary. Routine analysis was staining the tissue samples in IHC-P for CD45, CD3, CD4, CD8 and GARP (not shown) and flow cytometry with two separate marker panels for macrophages and T cells. Since macrophages numbers were generally low after around 4 weeks inside the mice, focus was shifted to T cells and their cellular composition.

In a collaboration, few tumor samples could be investigated using a high plex staining method based on fluorescently labeled antibodies to detect 100+ markers in (frozen) tissue samples called Chipcytometry. This new method was tested if it could be used to investigate the complex tumor microenvironment in humanized mice. Chapter 4.7 deals with this comparison, which was recently published.<sup>208</sup>



## Results and Discussion

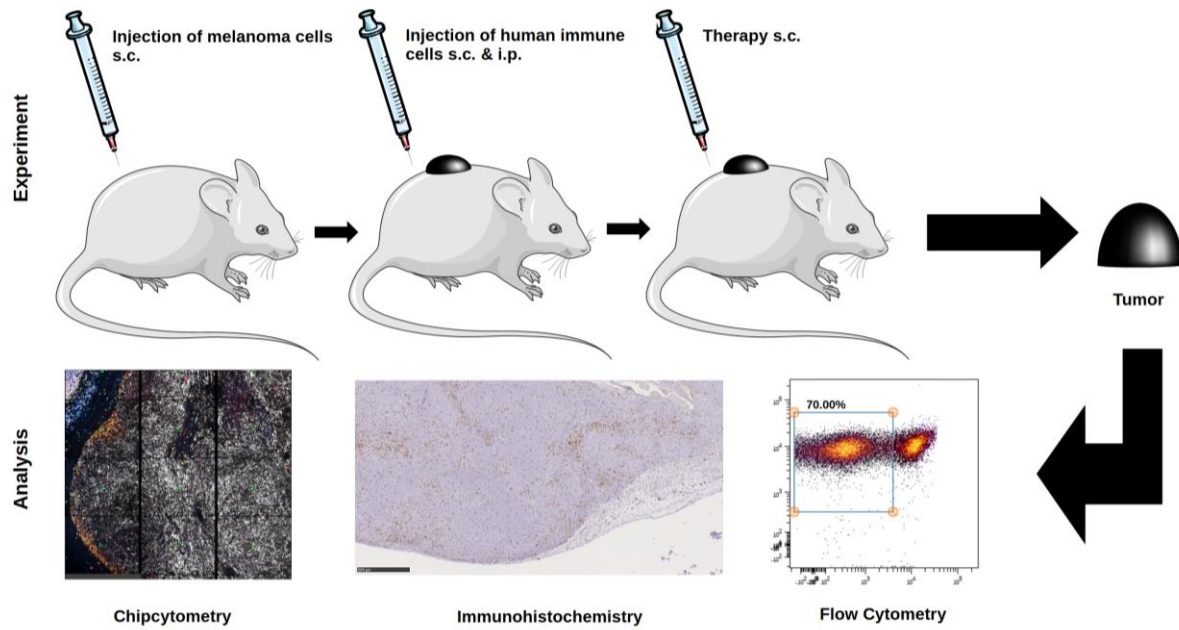


**Figure 41:** Schematic draw of the humanized mouse melanoma model. Human melanoma cells (Ma-Mel-19) are injected s.c. into the back of immunodeficient NOD Scid mice. After development of measurable tumors, human PBMC are injected s.c. peritumoral and i.p. to create a human TME and to have a tumor-naïve immune cell population in the spleen. Immunomodulators to treat tumors are injected s.c. peritumoral. Tumors and spleen (not shown) are extracted for ex vivo analysis by Chipcytometry, IHC-P and flow cytometry.

**Table 5.** Treatment scheme of animal experiments. For details, see 3.13.

| Group | human PBMC | Treatment | Concentration   |
|-------|------------|-----------|-----------------|
| 1     | no         | control   | ---             |
| 2     | yes        | control   | ---             |
| 3     | no         | yes       | low / liposomes |
| 4     | no         | yes       | high            |
| 5     | yes        | yes       | low / liposomes |
| 6     | yes        | yes       | high            |

## Results and Discussion

The experiment to investigate tumor growth of human melanoma cells and subsequent treatment with the immunomodulator was designed in two arms with three groups each. One arm is non-humanized, meaning that those mice receive only human tumor cells but no human immune cells. Tumor cells in this group grow in a fully murine environment. One group remains untreated (1, blue) and receives only the solvent, a mixture of saline and DMSO. Two groups are treated, one with a low concentration of Tasquinimod (3, green) and one with a high concentration (4, purple). In one experiment (V7), the low Tasquinimod concentration was exchanged to Tasquinimod liposomes. The humanized group mirrors this layout, but in this arm human immune cells (PBMC) are present. Tumors grow in a human tumor microenvironment. The humanized arm also had three groups: untreated (2, red), low Tasquinimod (5, orange) and high Tasquinimod (6, black). Experiment duration was comparable among the three experiments with 43, 49 and 42 days (Figure 43 A, B & C). It took 10 to 15 days until the tumors reached a measurable size. Injection of human PBMC occurred on day 23 (V2), 15 (V3) and 18 (V7). Treatment with Tasquinimod was carried out weekly three (V2 & V7) to four times (V3). Tumor size on the last day of the experiment is shown as red dotted line for the non-humanized arm and as blue dotted line for the humanized arm. Since every *in vivo* experiment shows fluctuations based on factors like slight differences in ages of the animals, different sex ratios, small variations in the experiment schedule and – most important – the use of different PBMC donors, values were normalized. Tumor volume of the untreated group on the last day of the experiment in each arm was set to 1 (100%). In each arm separately, both treatment groups were compared to their reference of the untreated sample. This way, it could be shown that only in the presence of human immune cells Tasquinimod is able to suppress tumor growth in both concentrations applied (Figure 43 D & E). In humanized mice the higher Tasquinimod concentration lowered tumor size to 45% ( $\pm 14$ ) and the lower concentration to 55% ( $\pm 19$ ) of the original tumor size, whereas in non-humanized mice a high Tasquinimod concentration led to 77% ( $\pm 28$ ) and a lower to 100% ( $\pm 19$ ). In Tasquinimod treated groups tumors did not vanish, but in the majority tumor growth was in a stalemate. Most animals survived till the endpoint of the experiment since the subcutaneous tumors did not give rise to metastases. Due to the use of HLA-A2.1 positive donors, no signs of Graft versus Host Disease (GvHD) were detected in the time window of up to 49 days. Animals were checked regularly for signs of sickness and their weight was recorded as fitness marker. GvHD relates to a loss of weight, reduced activity and disrupted skin barrier. <sup>128,209,210</sup>

## Results and Discussion

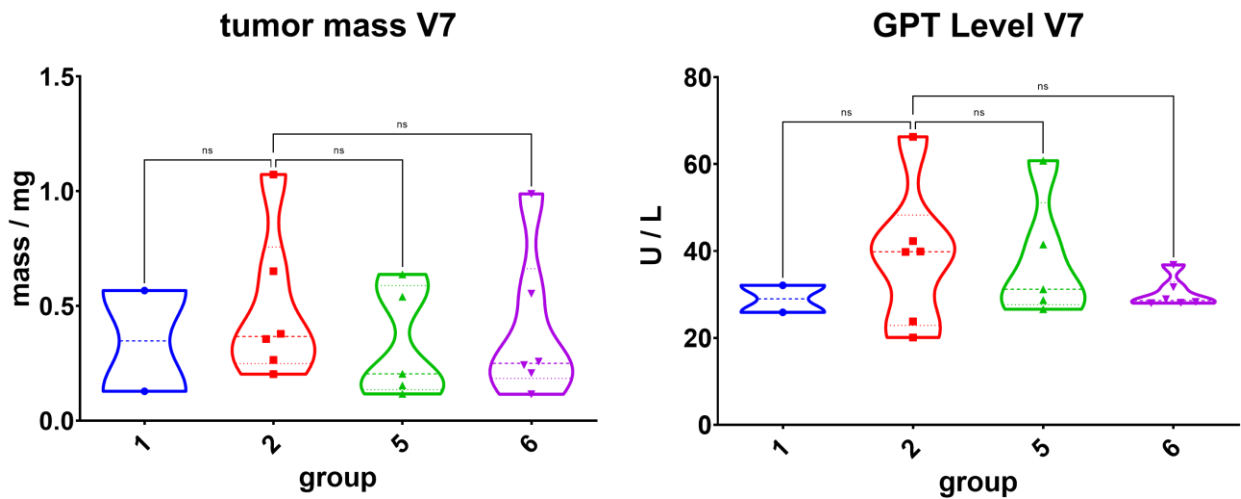


**Figure 42:** Tumor mass of extracted tumors and GPT levels in serum were measured in V7 as further markers for tumor growth and animal fitness.  $N = 2 - 6$  (see data points per group). Statistical significance was determined using the One-Way ANOVA with Fisher's LSD test. ns = not significant, \*  $p < 0,05$ , \*\*  $p < 0,01$ , \*\*\*  $p < 0,001$ , \*\*\*\*  $p < 0,0001$ .

In experiment V7 blood levels of alanine transaminase / glutamate-pyruvate transaminase (ALT / GPT) as inflammation marker and the mass of excised tumors was determined (see **Figure 42**). The tumor mass showed no significant difference between treatment in contrast to the tumor volume. The trend of lighter or smaller tumors in treatment groups can also be seen here. GPT activity in serum was measured to detect signs of GvHD not seen in the animal's behavior or weight. As group 1 has not received human immune cells, there can be no GvHD in those animals. Only two mice were included as internal controls in the investigation of the tumor microenvironment. The remaining animals of the non-humanized arm were not included, as there was no human tumor microenvironment and of course no physiological murine tumor microenvironment due to their immunodeficient status.

## Results and Discussion

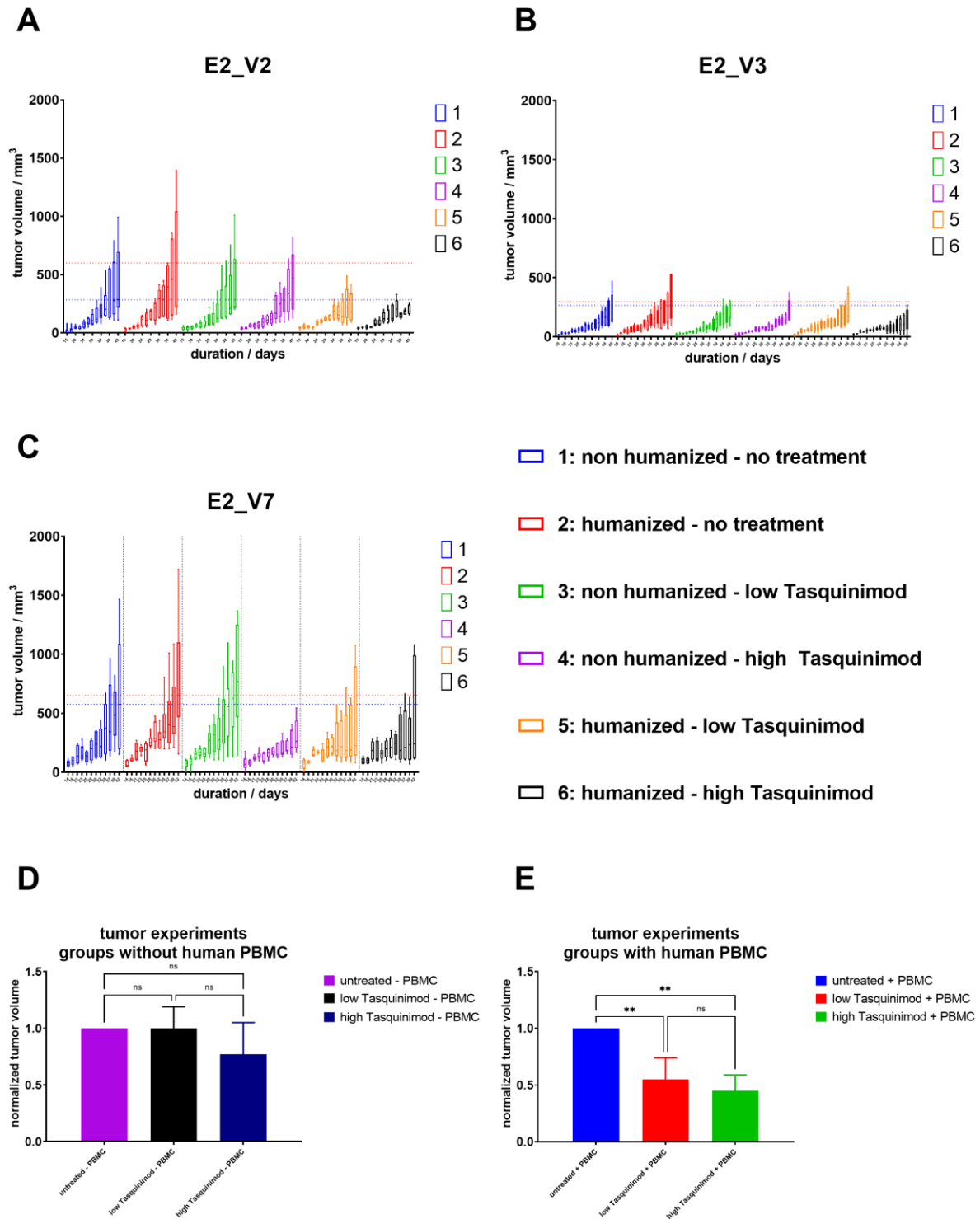


**Figure 43:** Evaluation of Tasquinimod as immune modulator in a melanoma model based on the cell line Ma-Mel-19 in immunodeficient mice with or without human PBMC to reconstitute the immune system (see 3.13). Three independent animal experiments were performed (A, B & C). Tumor volume on the last day of the experiment was normalized to untreated animals, either humanized (E) or non-humanized (D) and compared to treatment groups. Number of animals per treatment group is shown in table S2. D & E: N = 3. Statistical significance was determined using the One-Way ANOVA with Fisher's LSD test. ns = not significant, \*  $p < 0,05$ , \*\*  $p < 0,01$ , \*\*\*  $p < 0,001$ , \*\*\*\*  $p < 0,0001$ .

## Results and Discussion

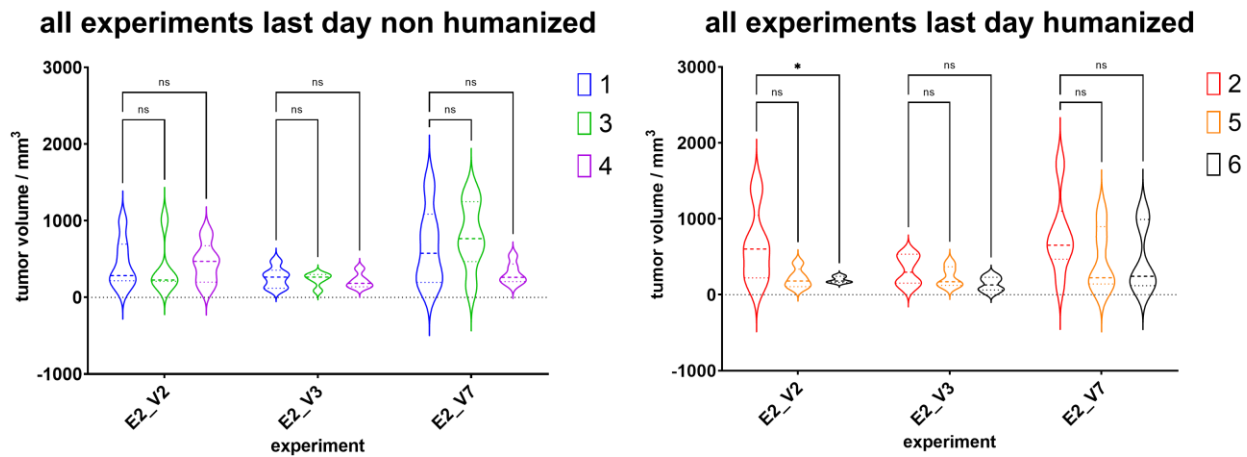


**Figure 44:** Tumor size of melanoma tumors in humanized mice shown in Figure 43 on the last day of the experiment when the animals were sacrificed divided between non-humanized (left) and humanized (right) animals. Experiment runs and treatment groups correspond to those in Figure 43. Statistical significance was determined using the Two-Way ANOVA with Fisher's LSD test. ns = not significant, \*  $p < 0,05$ , \*\*  $p < 0,01$ , \*\*\*  $p < 0,001$ , \*\*\*\*  $p < 0,0001$ .

### 4.6.2 TME analysis by immunohistochemistry and flow cytometry

At the end of the experiments, the tumors were excised and cut in two. One half was fixed and embedded in paraffin for immunohistochemistry staining and the other half was digested to investigate the tumor microenvironment by flow cytometry. Those two methods were used to search for changes in immune cell composition between the groups (see **Figure 45**) and were compared side by side (see **Figure 46**). Immunohistochemistry as single plex method in our case lacks the ability to gate cell types by several markers. For this reason, flow cytometry data is also shown as % of all cells instead of % of population as it is common in flow cytometry. The reduced marker panel of only T cell related markers CD45, CD4 and CD8 is dictated by IHC-P. But as spatial information is retained in IHC-P, it was possible to focus exclusively on immune cells infiltrating the tumor mass. Flow cytometry offers a broader marker panel and the ability to gate on subpopulations. For sample preparation the whole tumor with surrounding tissue was digested. Immune cells located in the surrounding tissue, skin or injection site are included inevitably. First the focus was to find a possible difference in CD45<sup>+</sup>, CD4<sup>+</sup> or CD8<sup>+</sup> cells caused by treatment with Tasquinimod. In two (V2 & V3) out of three experiments only CD45<sup>+</sup> cell numbers were elevated in IHC-P staining when tumors had been treated with the lower concentration of Tasquinimod. In all other cases, investigated by IHC-P or flow cytometry, there are minor differences in the mean values, but none of them are significant.

The next comparison (see **Figure 46**) focuses directly on the performance of both different detection methods. In each single group and in each experiment separately IHC-P is compared to flow cytometry. In experiments V7 and V3, albeit visible trends, there is no significance difference between the two methods in detection of CD45, CD4 and CD8. Only in experiment V2 more CD45<sup>+</sup> and CD8<sup>+</sup> cells were detected in the low Tasquinimod group by IHC-P (see **Figure 46 G & I**), for CD4<sup>+</sup> cells this was true for both Tasquinimod concentrations (see **Figure 46 H**).

## Results and Discussion

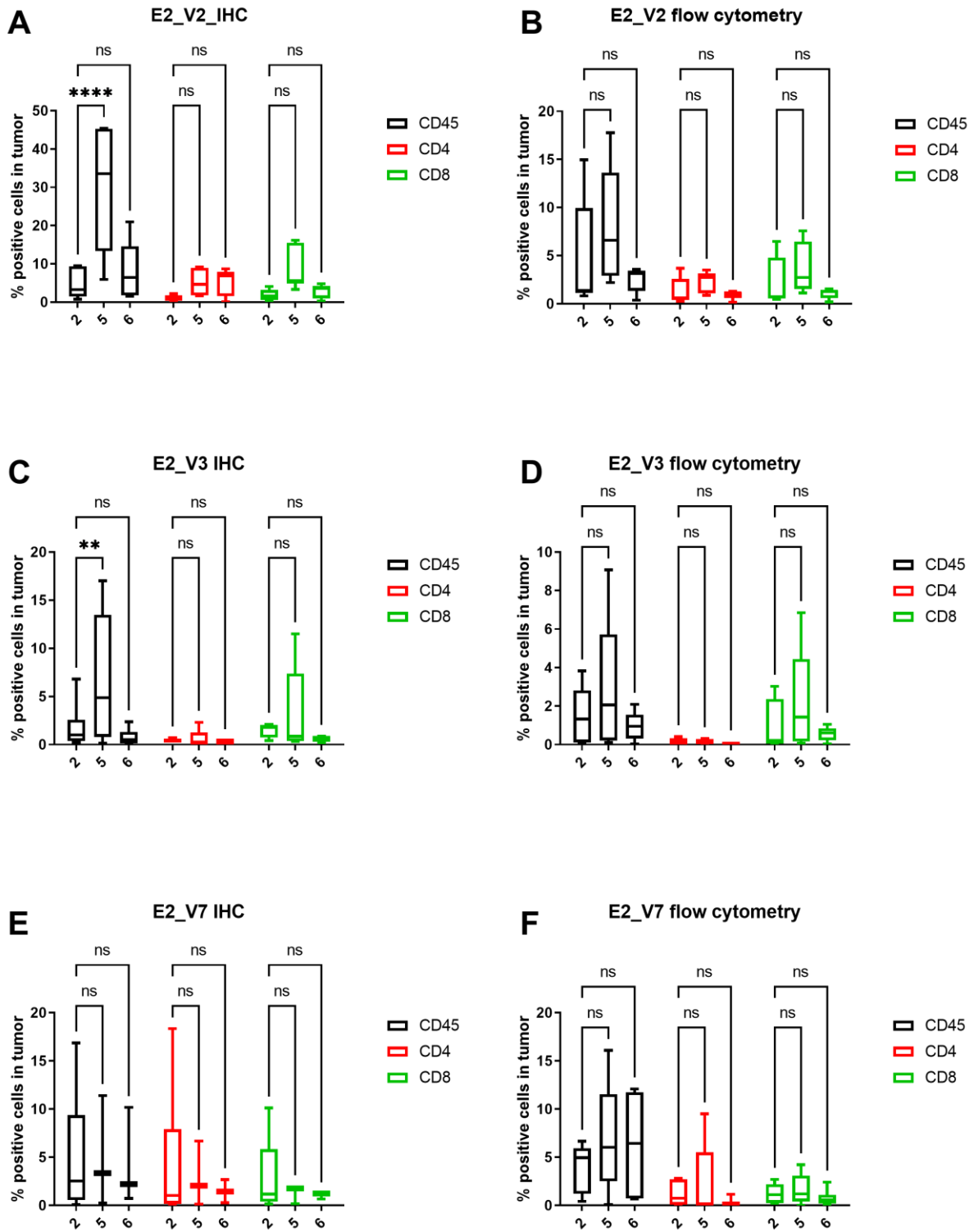


**Figure 45:** Comparison of immunohistochemistry (A, C & E) and flow cytometry (B, D & F) to detect intratumoral human immune cells in the melanoma model in humanized mice (see 3.13). Expression of immune cell markers CD45, CD4 and CD8 is compared in the different treatment groups (untreated – 2, low Tasquinimod or liposomes – 5 and high Tasquinimod – 6) for each animal experiment separately (V2, V3 & V7). Direct comparison between the two detection methods used is shown in Figure 46. Statistical significance was determined using the Two-Way ANOVA with Fisher's LSD test. ns = not significant, \*  $p < 0,05$ , \*\*  $p < 0,01$ , \*\*\*  $p < 0,001$ , \*\*\*\*  $p < 0,0001$ . Number of animals per treatment group is shown in table S2.

# Results and Discussion

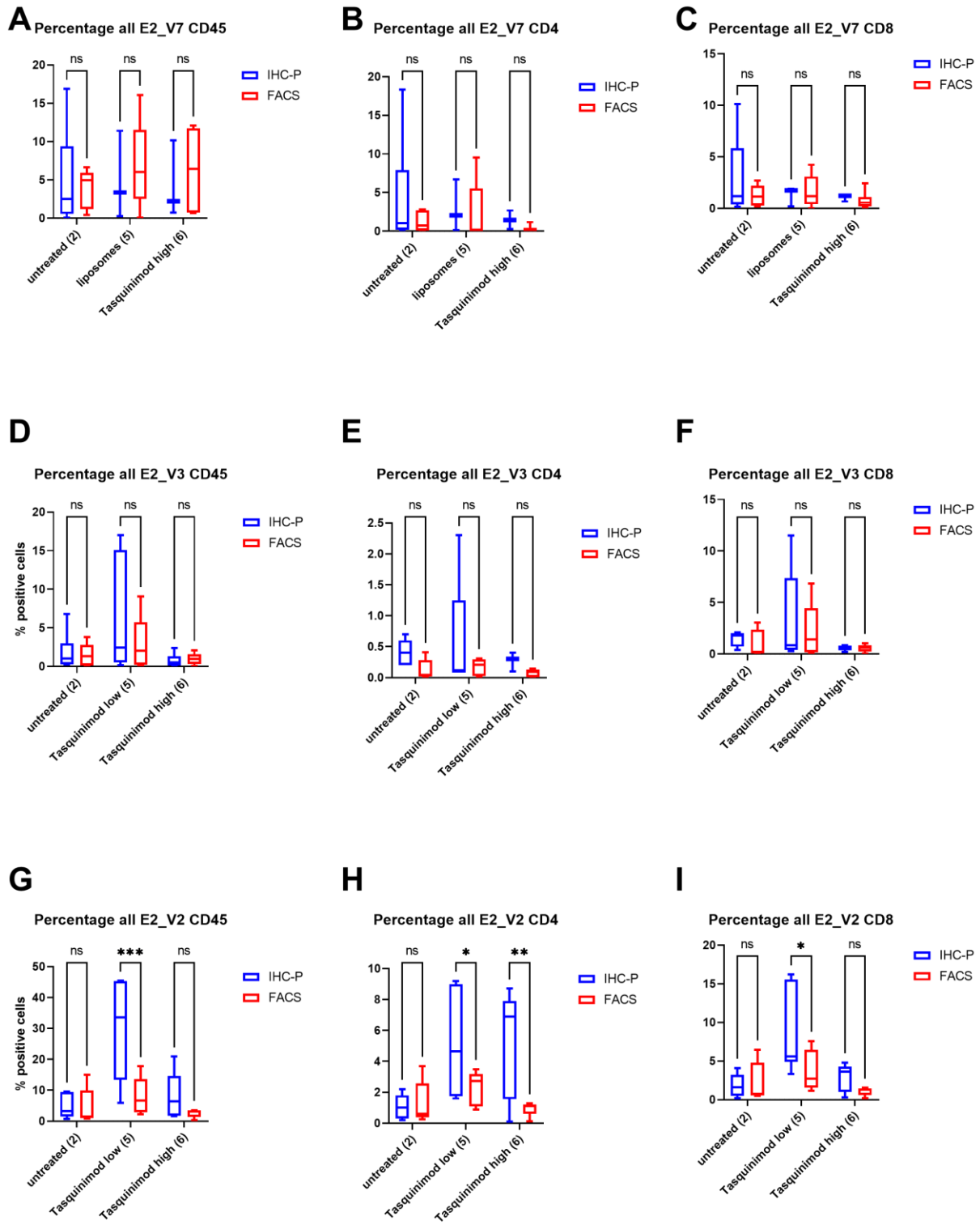


**Figure 46:** Direct comparison of immunohistochemistry and flow cytometry to detect intratumoral human immune cells in the melanoma model in humanized mice (3.13). Expression of immune cell markers CD45, CD4 and CD8 is compared in the different treatment groups (untreated – 2, low Tasquinimod or liposomes – 5 and high Tasquinimod – 6) for each animal experiment and immune cell marker separately (V2, V3 & V7). Direct comparison between the three treatment groups is shown in Figure 45. Statistical significance was determined using the Two-Way ANOVA with Fisher’s LSD test. ns = not significant, \*  $p < 0,05$ , \*\*  $p < 0,01$ , \*\*\*  $p < 0,001$ , \*\*\*\*  $p < 0,0001$ . Number of animals per treatment group is shown in table S2.

## Results and Discussion

### 4.6.3 Transcriptome analysis by NanoString Sprint Profiler

In experiment V7 part of the single cell suspension obtained from digested tumors was subjected to RNA expression analysis by the *NanoString* technology. Cells were lysed by a chaotropic buffer and RNA was extracted by silica columns. The extracted RNA was incubated with a panel of RNA probes. Those probes are labeled with a color barcode of different fluorophores and specific for around 800 targets (PanCancer IO 360 panel) and another set of probes, that are used to immobilize the mRNA/probe complex for detection by an automated fluorescence microscope. In other words, mRNA molecules are directly counted. As in qPCR analysis, a set of household genes are used to compare gene expression between different samples. This differential gene expression as comparison between two groups is shown in **Figure 47** as volcano plots and gene lists sorted by genes that are up- or downregulated. It is easily to see, that the treatment with Tasquinimod liposomes and their relatively low Tasquinimod concentration does not lead to a strong alteration in gene expression, whereas the treatment with Tasquinimod at 5 mg per kg bodyweight leads to the upregulation of the genes *BNIP3*, *FOSL1* and *RPS6KB1* and the downregulation of 23 genes (see left side). Logically, since the liposome treated group does not differ much from the untreated group, there are also strong differences in gene regulations between liposome and Tasquinimod treated group. Since in this comparison the Tasquinimod group serves as reference, the majority (28) of genes is upregulated and 3 genes are downregulated (*FOSL1*, *PGPEP1* and *RPS6KB1*). *FOSL1* and *RPS6KB1* were also detected in the comparison between Tasquinimod treated and untreated group.

BCL2/adenovirus E1B 19 kDa protein-interacting protein 3 (BNIP3) is a pro-apoptotic factor located at the outer mitochondria membrane which is upregulated in hypoxic conditions and its upregulation has been linked to poor prognosis in several cancer types.<sup>211</sup> Fos-related antigen 1 (FRA1) is part of the transcription factor (complex) AP-1 induced by KRAS signaling. In lung adenocarcinoma aberrant mutated KRAS signaling, with AP-1 as effector, is very frequent. FOSL1 regulates tumor cell survival and high FOSL1 expression is associated with a poor prognosis.<sup>212</sup> Another effect of mutant KRAS is the activation of ribosomal protein S6 kinase B1 (RPS6KB1) via aurora kinase A (AURKA) in luminal gastrointestinal cancers.<sup>213</sup> RPS6KB1 is also linked to autophagy, the intracellular recycling process.<sup>214</sup> Taken together, those three upregulated genes could hint at a defensive cellular response to the stress caused by Tasquinimod treatment which is not sufficient to prevent effects of Tasquinimod *in vivo*.

This method served as screening approach to identify targets in immune and cancer cells influenced by Tasquinimod treatment for further studies, since flow cytometry and immunohistochemistry failed to deliver a clear answer to the question why Tasquinimod is able to inhibit tumor growth. Despite CD36, the discovered genes showing significant up- or downregulation during Tasquinimod treatment were not included in qPCR panels yet (see table 6) and will be validated in future approaches.



# Results and Discussion

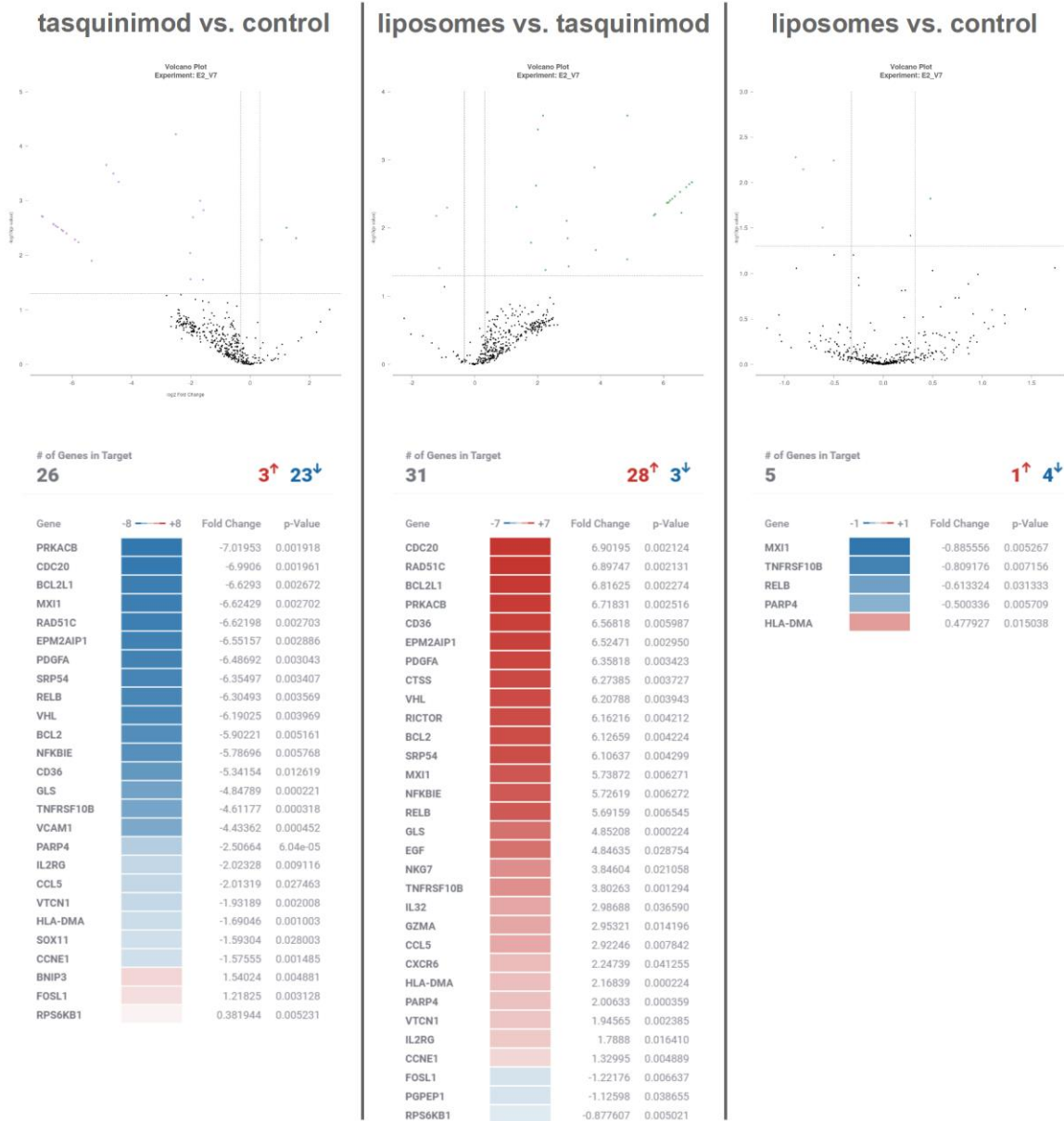


**Figure 47:** Volcano plots visualizing differential gene expression in tumor samples of humanized mice (see 3.11). RNA expression analysis was done using fluorescent RNA probes imaged by the NanoString Sprint Profiler (see 3.11). All three treatment groups with human immune cells present (untreated/control, low Tasquinimod/Tasquinimod and Tasquinimod liposomes/liposomes) were compared pairwise to each other. 5 samples in control group, 3 in liposome group and 4 in Tasquinimod group. Only targets with  $p \leq 0,05$  are displayed (above the dotted lines in the volcano plot).

## Results and Discussion

**Table 6.** List of differentially expressed genes (see **Figure 47** left).

| Gene                            | Up/Downregulation | Full Name   |
|---------------------------------|-------------------|---|
| <b>PRKACB</b> <sup>215</sup>    | ---               | cAMP-dependent protein kinase catalytic subunit beta                                  |
| <b>CDC20</b> <sup>216</sup>     | ---               | cell division cycle protein 20 homolog  |
| <b>BCL2L1</b> <sup>217</sup>    | ---               | Bcl-2-like 1  |
| <b>MXI1</b> <sup>218</sup>      | ---               | MAX-interacting protein 1   |
| <b>RAD51C</b> <sup>219</sup>    | ---               | RAD51 homolog C   |
| <b>EPM2AIP1</b> <sup>220</sup>  | ---               | EPM2A interacting protein 1   |
| <b>PDGFA</b> <sup>221</sup>     | ---               | Platelet-derived growth factor subunit A  |
| <b>SRP54</b> <sup>222</sup>     | ---               | signal recognition particle 54  |
| <b>RELB</b> <sup>223</sup>      | ---               | Transcription factor RelB   |
| <b>VHL</b> <sup>224</sup>       | ---               | Von Hippel–Lindau tumor suppressor  |
| <b>BCL2</b> <sup>217</sup>      | ---               | B-cell lymphoma 2   |
| <b>NFKBIE</b> <sup>225</sup>    | ---               | Nuclear factor of kappa light polypeptide gene enhancer in B-cells inhibitor, epsilon |
| <b>CD36</b> <sup>157,158</sup>  | ---               | platelet glycoprotein 4, fatty acid translocase                                       |
| <b>TNFRSF10B</b> <sup>226</sup> | ---               | tumor necrosis factor receptor superfamily member 10B                                 |
| <b>VCAM1</b> <sup>227</sup>     | ---               | Vascular cell adhesion protein 1  |
| <b>BNIP3</b> <sup>228</sup>     | +                 | BCL2/adenovirus E1B 19 kDa protein-interacting protein 3                              |
| <b>FOSL1</b> <sup>229</sup>     | +                 | Fos-related antigen 1   |
| <b>RPS6KB1</b> <sup>230</sup>   | +                 | Ribosomal protein S6 kinase beta-1  |

## Results and Discussion

### 4.7 Analysis of the tumor microenvironment comparing low- and highplex methods<sup>VIII</sup>

The previous section shows clearly that analysis of the tumor microenvironment by immunohistochemistry staining and flow cytometry is limited and lacks depth in terms of marker quantity while preserving spatial information. Therefore, we partnered with the company Zellkraftwerk (now Bruker Corporation) who developed the Chipcytometry platform. It offers the opportunity to investigate frozen tissue sections fixed on special staining slides in repetitive staining cycles with fluorophore labeled antibodies.

In the pilot study it was investigated if this method is compatible with the mixed human/murine tissue present in the humanized mouse model, which requires antibodies specific to human targets. 17 targets including DNA were stained and acquired in 11 cycles (see 3.14). As described in the methods part images were processed with the proprietary ZellExplorer data analysis software to finally have FCS files as output, where cells can be gated based on their marker expression. **Figure 48** summarizes data obtained by this novel method with markers / cell types comparable to the previous used methods in section 4.6 plus human macrophages as CD45<sup>+</sup>CD68<sup>+</sup> cells. In the three tumors investigated by this method both CD4<sup>+</sup> and CD8<sup>+</sup> T cells could be detected.

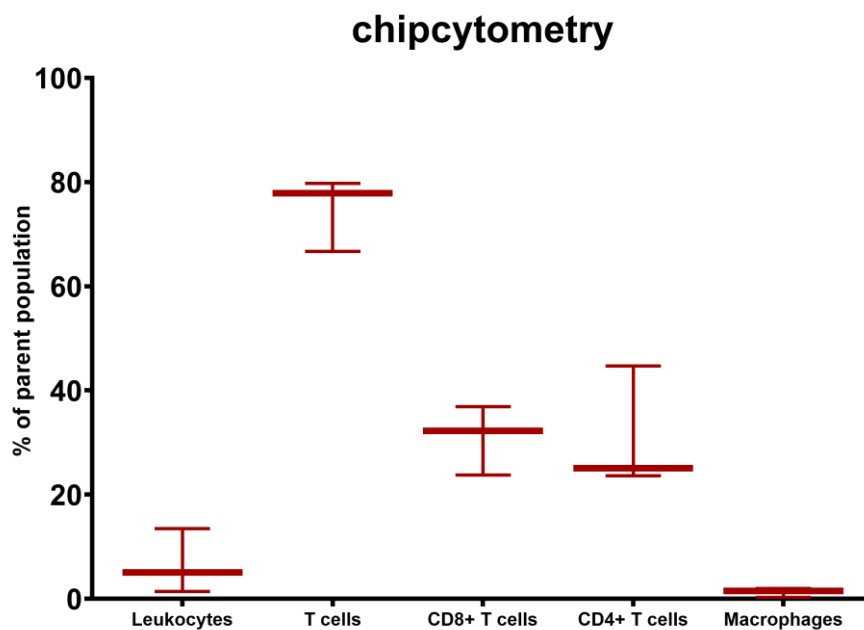


**Figure 48:** Samples of tumor humanized mice were subjected to the novel multiplex staining method Chipcytometry to prove its usability in animal tumor models, especially in humanized mice models with mixed human and murine antigens. Cells were gated according to their marker expression. Leukocytes (CD45<sup>+</sup>), T cells (CD45<sup>+</sup>CD3<sup>+</sup>), CD8<sup>+</sup> T cells (CD45<sup>+</sup>CD3<sup>+</sup>CD8<sup>+</sup>), CD4<sup>+</sup> T cells (CD45<sup>+</sup>CD3<sup>+</sup>CD4<sup>+</sup>) and macrophages (huCD45<sup>+</sup>huCD68<sup>+</sup>). Three untreated animals were analyzed.

<sup>VIII</sup> This work was a cooperation project with the company Zellkraftwerk GmbH (now Bruker Corporation) and has been published. <sup>208</sup> [REDACTED], employee of Zellkraftwerk, was responsible for staining, acquisition and analysis of frozen tumor samples, which originated from animal experiments conducted by the research group of [REDACTED] (University Medical Center Mainz, Germany), using their Chipcytometry technology.

## *Results and Discussion*

**Figure 49** displays the differences in the methods used to investigate the tumor microenvironment in humanized mice. Part A shows a large mosaic picture of 4 x 4 fields of view combined. One single CD4<sup>+</sup> T cell is shown in magnification to display all the fluorescence signals in single color pictures. It is obvious, that overlay pictures do not work with the 15 colors shown on the right of the picture. That is why data analysis by special software that can segment the tissue into single cells is mandatory and the transformation of fluorescence data of each channel for each cell into data point of FCS files as in Part C shown of flow cytometry data. Gating of cell population is from there on analog to flow cytometry. With the add-on that spatial information is still available for spatial analysis of cellular localization of cell neighbor relations. Only a certain marker depth allows for cell identification which is necessary for immune cells. In clinical routine, immunohistochemistry allows for the staining of a single marker which can be identified by a brown stain of the oxidized chromogen 3,3' diamino benzidine (DAB) deposited in the vicinity of a complex of primary antibody, secondary antibody coupled to biotin and the streptavidin-horseradish peroxidase (HRP) conjugate. Cell nuclei are counterstained with a hemalum solution (hematein combined with an aluminium salt, mostly alums) in light blue. Due to the nuclei stain, software like QuPath is able to segment the tissue sample into single cells. After this step cells can be classified as positive or negative by their DAB stain as shown in Part B. Part C shows a classical dot plot of a tumor sample digested and analyzed by flow cytometry. Using a viability stain, which is usually a protein or DNA stain able to penetrate dead cells with their perforated cell membranes faster thereby giving them a higher fluorescence in comparison to living cells, live cells can be separated from dead ones. FVD506 stains proteins and is resistant to fixation protocols using formaldehyde after staining. The dot plot shows gating for live and dead human immune cells positive for CD45. It is important to gate for markers first and then exclude dead cells in this single population since larger cells will give a higher signal anyway due to more stainable proteins present. The pitfall is to confuse large cells with dead cells in a mixed cell population like digested tissue or PBMC. This dead cell exclusion is limited in tissue samples investigated by IHC-P or Chipcytometry. Since dead cells might retain their structure for a certain time until they are fully dissolved into apoptotic bodies or digested by other cells like macrophages.<sup>231</sup> One way to find dead cells is to look at the DNA structure. Since chromatin condensation (pyknosis) and subsequent fragmentation (karyorrhexis) are hallmarks of apoptosis, cells with irregular nuclei shapes or appearance should be excluded.

## Results and Discussion

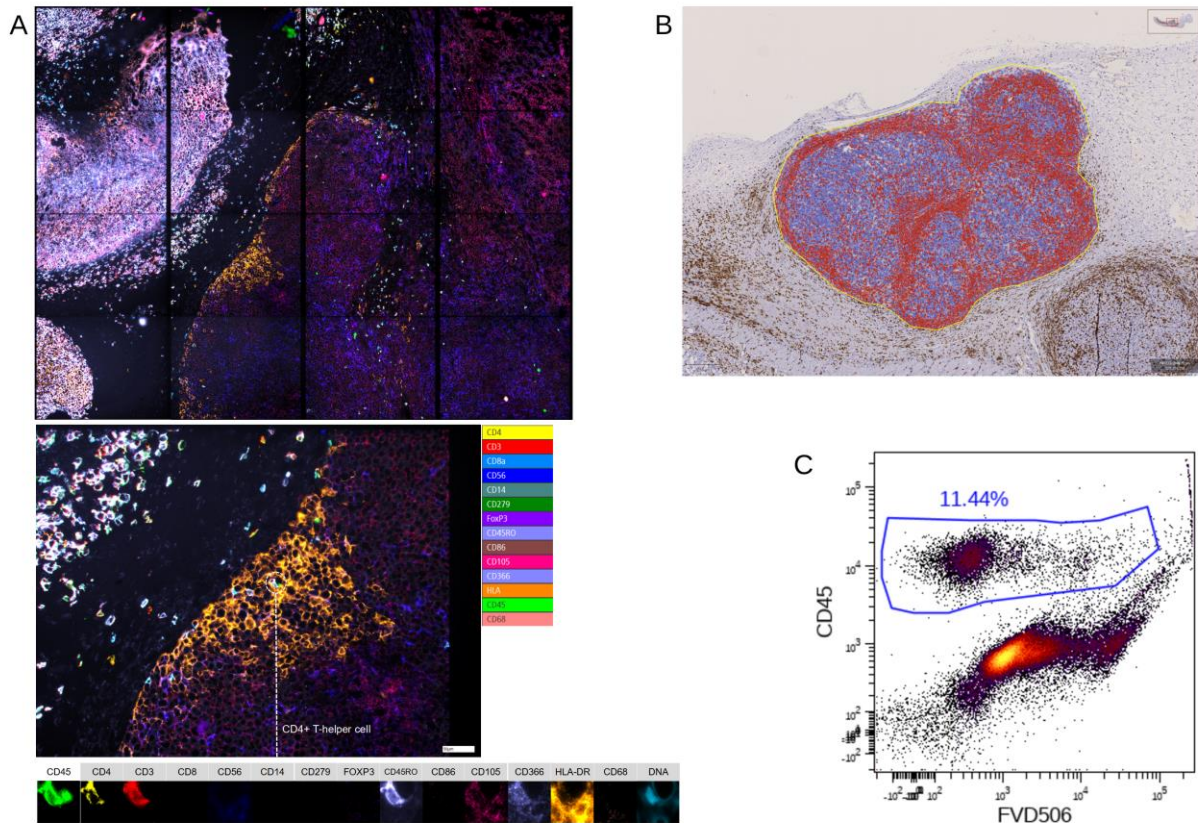


**Figure 49:** Visualization of chipcytometry (A) as highplex method to analyze the tumor microenvironment of tumor bearing humanized mice at single cell level in comparison to classical 1 marker immunohistochemistry staining of CD45 (B, DAB staining and haematoxylin counterstain; CD45<sup>+</sup> cells in red and negative cells in blue within the region of interest gated in yellow) and flow cytometry (C, showing gating for CD45 positive immune cells in a tumor sample) without spatial information. Chipcytometry data is summarized in Figure 48.

A further example of single cell analysis using chipcytometry is shown in **Figure 50**. In part A a close-up of a CD8<sup>+</sup> T cell is shown and its expression of CD45, CD3, CD8, CD45RO, CD279, CD366 and CD25. Not detected were CD4, CD45RA and FOXP3. The CD4<sup>+</sup> T cell in part B is positive for CD45, CD3, CD4, CD45RO, CD279, CD366, CD25 and FOXP3. It is only negative for CD8 and CD45RA. As both cells are positive for CD45RO instead of CD45RA they are activated or memory cells, as can be expected in a xenograft.<sup>232</sup> It also shows the specificity of the antibody staining, as CD4<sup>+</sup> T cells are negative for CD8 and vice versa. The merged picture demonstrates perfectly that highplex staining sophisticated algorithms are absolutely necessary to extract information out of it. Simple direct visualization by colors is no longer possible (for all markers at once).

## Results and Discussion

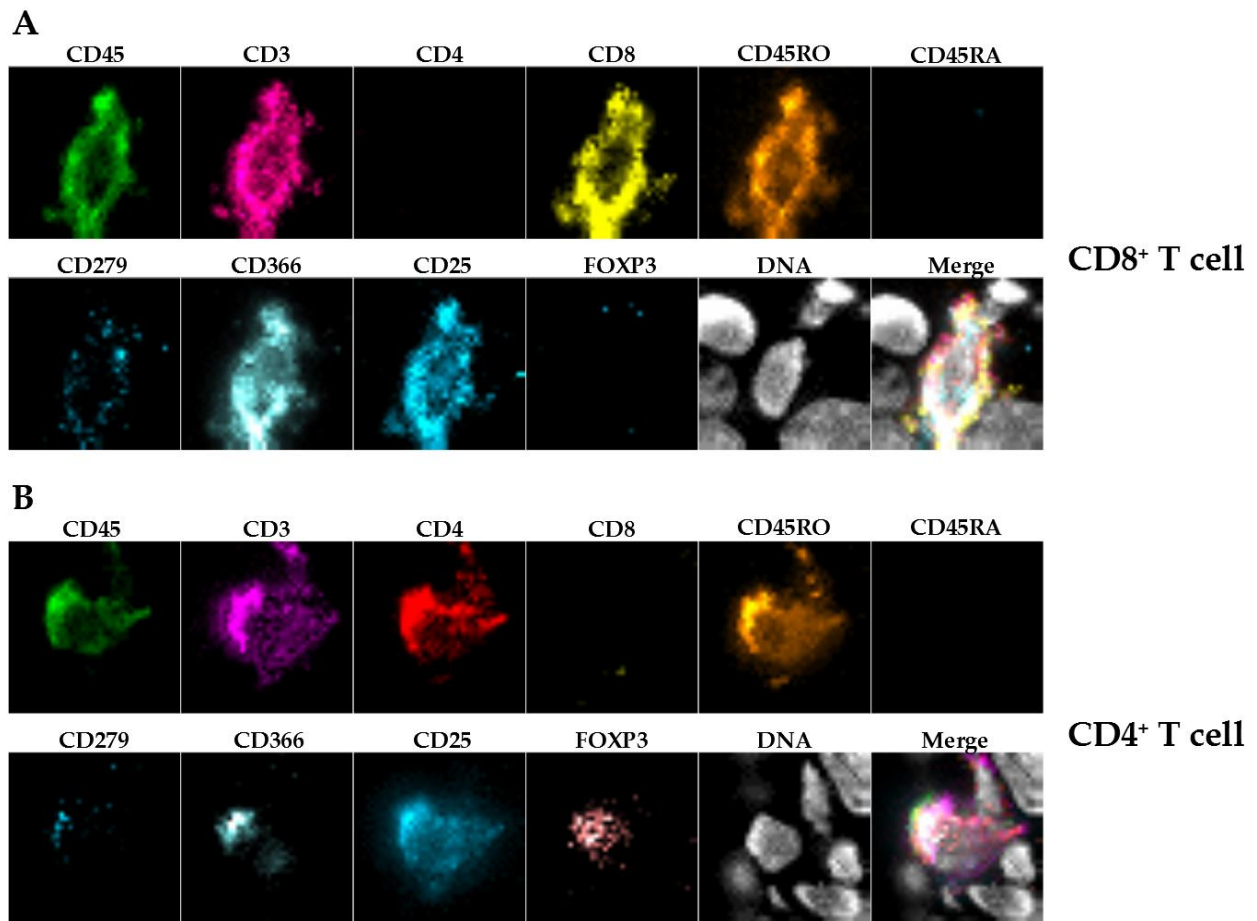


**Figure 50:** Representative single cell analysis within spatial context by chipcytometry. CD8<sup>+</sup> T cells (A) and their CD4<sup>+</sup> counterparts (B) can be identified and further analyzed regarding their sub- and phenotype. Chipcytometry data is summarized in Figure 48.<sup>233</sup>

To clarify the power of Chipcytometry or comparable highplex tissue staining methods, **table 6** displays which cell types were detected using this method in addition to flow cytometry and immunohistochemistry. Especially the further investigation of T cell phenotype is important for biopsies of patients under immunotherapy of cancer by checkpoint inhibitors, where T cells can be crucial for therapy response. PD-1<sup>+</sup> or TIM-3<sup>+</sup> T cells display expression of two markers investigated as target for future immunotherapies and as markers for therapy response of anti-PD-1 or anti-CTLA-4 antibodies.<sup>234–236</sup> Alone 3 markers plus additional markers for tumor cells and a DNA stain are necessary for investigating marker expression of either CD4<sup>+</sup> or CD8<sup>+</sup> T cells. Furthermore, localization of T cells outside or inside the tumor, a so-called hot or cold tumor, is particularly important for therapy outcome.<sup>237</sup> Not only classification of cells in positive or negative is possible, but also different expression levels can be determined, like in flow cytometry.

## Results and Discussion

**Table 7** Immune cell subpopulations in untreated tumor-bearing animals detected by Chipcytometry (n = 3).

| Marker Definition | Parent Population | Cell Type                | % of Parent Population | SD   |
|-------------------|-------------------|--------------------------|------------------------|------|
| CD45+             | All               | immune cells             | 6.7                    | 5.7  |
| CD3+              | CD45+             | T cells                  | 74.8                   | 7.1  |
| CD4+              | CD45+CD3+         | T helper cells           | 31.1                   | 11.7 |
| CD8+              | CD45+CD3+         | cytotoxic T cells        | 30.9                   | 6.7  |
| CD45RO+CD45RA-    | CD45+CD3+CD4+     | activated/memory t cells | 85.2                   | 20.1 |
| CD45RO+CD45RA-    | CD45+CD3+CD8+     | activated/memory t cells | 84.0                   | 24.2 |
| CD4+FOXP3+CD25+   | CD45+CD3+CD4+     | regulatory T cells       | 4.8                    | 3.3  |
| CD279+            | CD45+CD3+CD4+     | PD1+ T cells             | 24.8                   | 10.3 |
| CD366+            | CD45+CD3+CD4+     | TIM-3+ T cells           | 59.2                   | 29.8 |
| CD279+            | CD45+CD3+CD8+     | PD1+ T cells             | 16.5                   | 9.7  |
| CD366+            | CD45+CD3+CD8+     | TIM-3+ T cells           | 54.7                   | 5.1  |
| CD68+             | CD45+             | macrophages              | 1.3                    | 0.9  |

The preliminary analysis demonstrated, that a highplex method, until now designed for investigating only pure human or pure murine samples, is capable of processing samples from the mixed human-murine tissue of humanized mice. The requirement is antibodies with no or low cross-reactivity between the two species. Even if some antibodies from pre-designed human panels fail in this regard, they could be replaced easily.

It was possible to investigate immune cells to a much deeper level than with immunohistochemistry or flow cytometry. T cells expressing markers important for monitoring immune therapies (TIM-3 and PD1) were discovered with using only a small antibody-panel in this proof-of-concept study. Even though on more advanced flow cytometers more markers per panel would be possible, spatial information would be lost inevitable. More analyzed samples would allow for a deeper analysis of immune cell distribution and interaction outside and inside the tumor mass.

## Results and Discussion

### 4.8 GARP (LRRC32) as target molecule

Leucine rich repeat containing 32 (LRRC32 or GARP) is a promising target for lifting the immunosuppression in the tumor microenvironment (see 2.4). It is on the surface of suppressive regulatory T cells, other immune cells and directly on tumor cells.<sup>238</sup> GARP exerts its functions mainly via TGF- $\beta$ 1, a suppressive cytokine. Nevertheless, a soluble form of GARP is able to induce activation of regulatory T cells. Through addressing GARP expressing tumor cells cancer can be fought directly or through targeting suppressive immune cells in combination with checkpoint inhibitors indirectly. Targeting proteins as targets can be achieved using antibody fragments (Fab or Fv) while avoiding the Fc part and its unspecific binding and unwanted immune effects.

First modifications of liposomes to carry antibody(fragments) have been investigated in chapter 4.5.7. To verify the usability of GARP as target, it was mandatory to check the GARP expression in the humanized mouse melanoma model and on the used melanoma cell line Ma-Mel-19. GARP expression is not limited to melanoma but can be found in other tumor entities like glioblastoma, too.<sup>239</sup>

*In vivo* GARP expression in the xenograft melanoma model was checked via IHC-P staining for GARP in the tumor mass (see **Figure 51**). The majority of tumors showed strong GARP staining, mostly inside the nuclei but also to a weaker extent in the cytoplasm. Some tumors are homogeneously stained (upper picture), some tumors show a gradient with high levels at the tumor / tumor microenvironment boundary declining towards the center of the tumor mass. Because of those varying GARP expression patterns, for every sample a H score was calculated, considering weak and strong DAB staining for GARP (see **Figure 53**).<sup>240</sup> Between the treatment groups of every single experiment, no difference compared to the control group (2) could be detected. Experiment V7 showed a higher score compared to V2 and V3. GARP expression varies from extremely high to very low in every treatment group. In every run only one PBMC donor and one batch of tumor cells was used. What does vary is the application site of immune cells and therefore the number of immune cells in the tumor vicinity. This might explain the different expression levels of GARP in human melanoma tumors in the mice.

To provide a second method for detection of GARP an RNA probe panel using the NanoString technology was applied to lysate of tumor samples from xenograft tumors (see **Figure 52**). Human GARP (LRRC32) mRNA was detected in every sample. Treatment with free Tasquinimod at a high dose elevated GARP mRNA levels compared to the control group treated only with the solvent. Tumors treated with Tasquinimod loaded liposomes show a similar trend to higher GARP levels but without significance. Since most of the lysed cells are tumor cells it confirms our *in vitro* findings in flow cytometry and confocal microscopy, that GARP is expressed by Ma-Mel-19 (see **Figure 54**).

GARP expression in human melanoma cell in our humanized mouse model has been detected by four different methods: IHC-P, flow cytometry, immunofluorescence and on mRNA level by the NanoString system. Nonetheless, it remains to be shown in further experiments, that it can be used as target structure despite its non-exclusivity for tumor cells.



## Results and Discussion

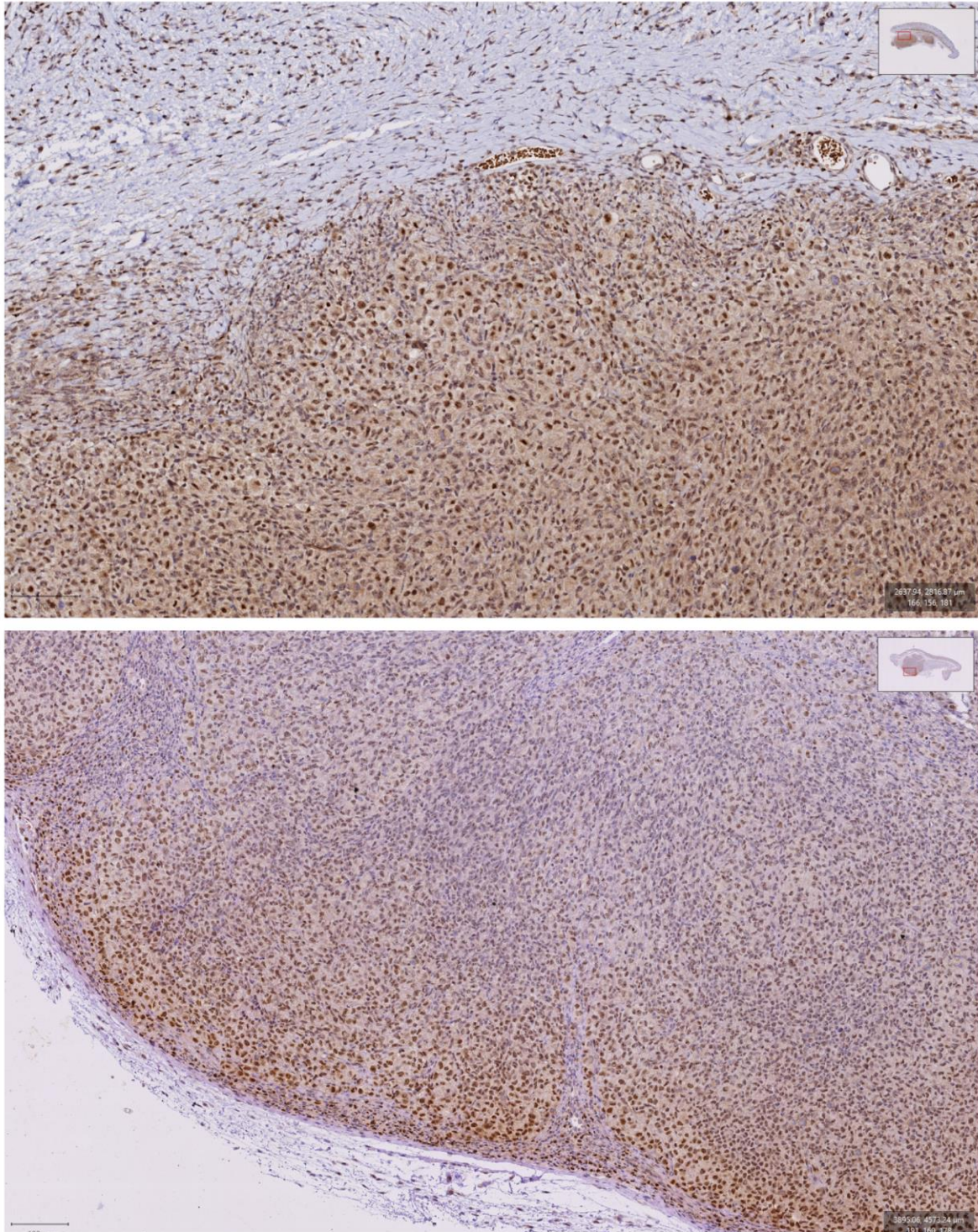


**Figure 51:** Immunohistochemistry staining of GARP (LRRC32) with DAB (brown) in subcutaneous tumors of Ma-Mel-19 cells in humanized mice counterstained with hematoxylin (blue). Tumors show a predominantly nuclear staining either homogeneous in the tumor mass (upper tumor) or as a gradient (lower picture) with high expression at the border between tumor and surrounding tissue. Cytoplasm is also positive for GARP, but at a lower density compared to the nucleus. Scale bar is 100  $\mu\text{m}$ .

## Results and Discussion

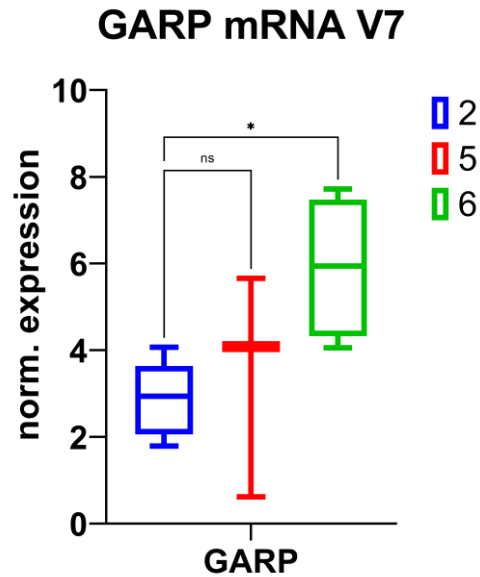


**Figure 52:** GARP mRNA detected in tumor samples of Ma-Mel-19 tumors grown in humanized mice. Statistical significance was determined using the Ordinary one-way ANOVA with Fisher's LSD test. ns = not significant, \*  $p < 0,05$ , \*\*  $p < 0,01$ , \*\*\*  $p < 0,001$ , \*\*\*\*  $p < 0,0001$ . Number of samples per treatment group: group 2 = 5, group 5 = 3 and group 6 = 4.

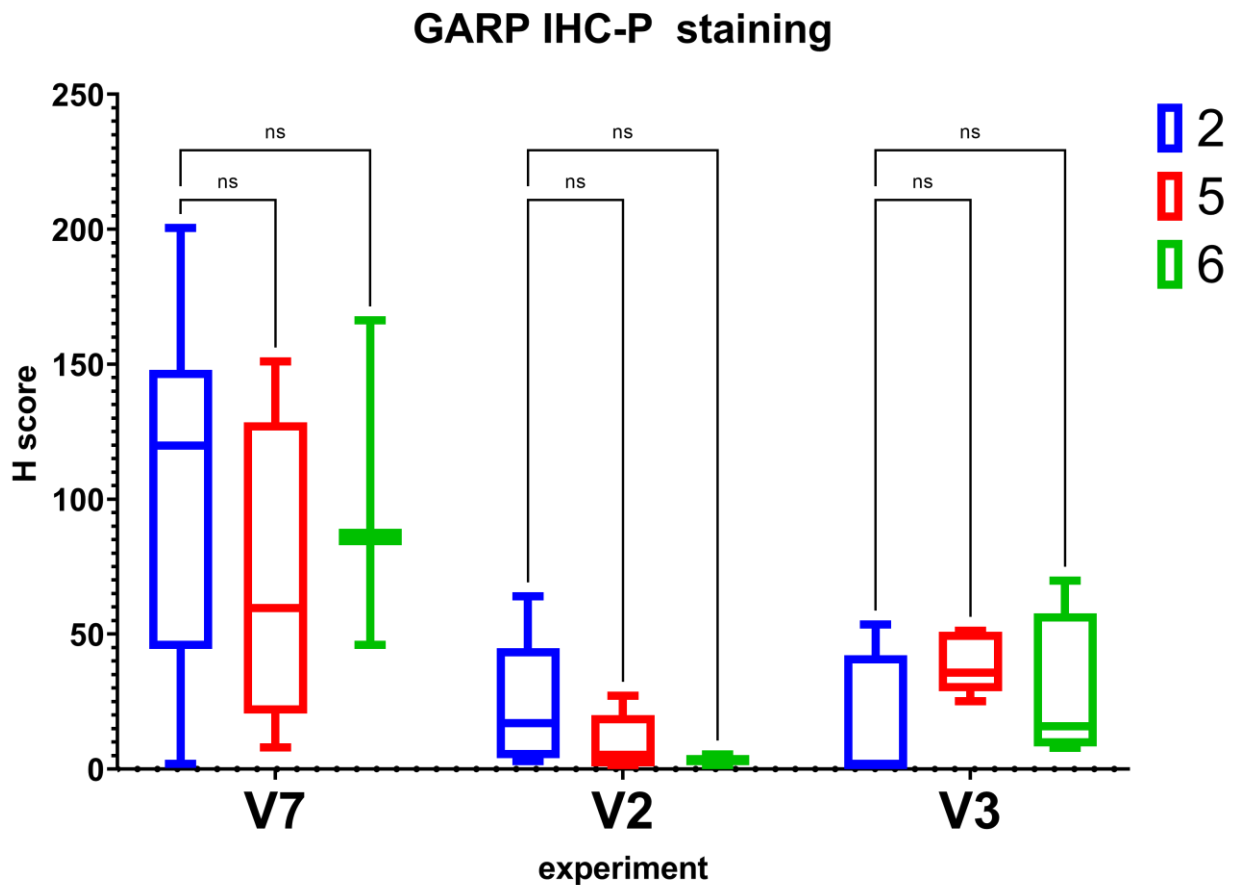


**Figure 53:** GARP protein detection in tumor samples of Ma-Mel-19 tumors grown in humanized mice. Statistical significance was determined using the two-way ANOVA with Fisher's LSD test. ns = not significant, \*  $p < 0,05$ , \*\*  $p < 0,01$ , \*\*\*  $p < 0,001$ , \*\*\*\*  $p < 0,0001$ . Number of samples per treatment group: V7 (group 2 = 9, group 5 = 4 and group 6 = 3), V2 (group 2 = 5, group 5 = 6 and group 6 = 4) and V3 (group 2 = 7, group 5 = 5 and group 6 = 4).

## Results and Discussion

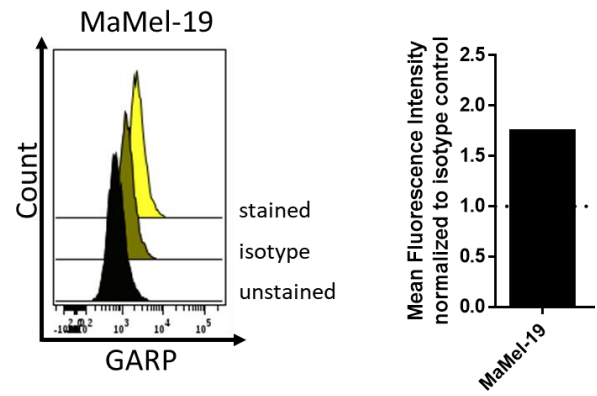
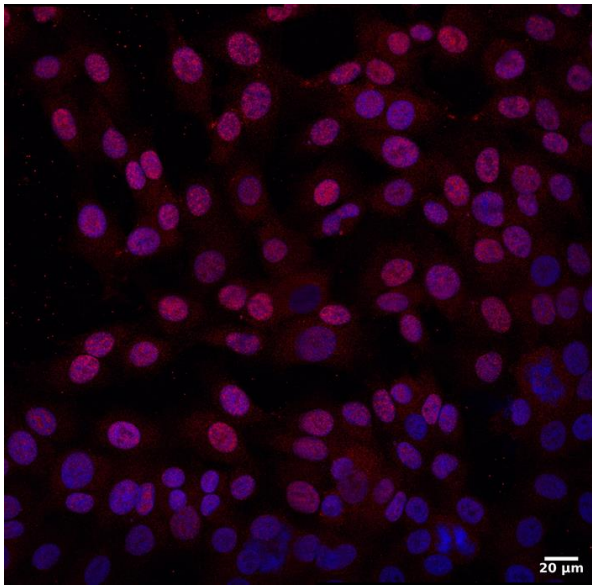


**Figure 54:** Immunofluorescence staining of Ma-Mel-19 *in vitro* in confocal microscopy (see 3.7) (left, GARP, nuclei) and flow cytometry (left). Ma-Mel-19 cells show expression of GARP protein in discrete spots in the nuclei and to a lower extent in the cytoplasm. Staining in flow cytometry was verified by an isotype control.

# 5 Conclusion

This work tries to offer a comprehensive approach in validating and further developing nanocarriers in their role as drug carriers to be used in an *in vivo* system. Starting from particle design of liposomes on the “edge of stability”, quantifying their release characteristics and starting to apply targeting strategies, continued with the first *in vitro* test in established cultures of human melanoma cells and human monocyte-derived macrophages as potential target cells, ending with providing human *in vivo* test conditions in the humanized mouse melanoma model. None of these steps can be skipped, since one would lose invaluable information for a biological system like time resolved dosages in the tissue or the target cells, which is a simple, yet often unanswered, question.

As shown in chapter 4.1 a culture of human monocyte-derived macrophages and marker readout on the mRNA level using qPCR as well as on the protein level using flow cytometry was established. It is clear, that IL-4 polarized M2 macrophages do not resemble TAM in *in vivo* settings. Even *in vivo* TAM signature is strongly patient and cancer type dependent.<sup>23,241</sup> But it is not the aim to validate anti-tumor treatments with drug carriers tested *in vitro* on M2 polarized macrophages. Instead, this *in vitro* system offers the chance to test whether a certain mechanism like siRNA transfection or inhibitors does work like expected and to which extend it does so. This is especially important in cases, where there is no *in vivo* effect observed. Without pre-testing there is no way to blame this on either failing drug release/delivery or on missing effect of the drug.

siRNA was tested as possible agent to knock down genes in TAM to break the suppression of the immune system. Viromer BLUE as commercial transfection reagent was able to knock down genes in human monocyte-derived macrophages as shown with siRNA against *LMNA*, *IL4R*, *NR4A3*, *STAT6* and *PPARG*. For *IL4R* and *PPARG* effects of siRNA mediated knock down were analyzed on mRNA level with qPCR and protein level with flow cytometry. Certain surface markers like M2 marker CD36 and markers important for immune response regulation like PD-L1 and PD-L2 responded to knock down of *IL4R*, *STAT6*, *PPARG* and *NR4A3*. Further biological effects of siRNA knock down should be evaluated *in vivo* as responses in IL-4 polarized M2 macrophages cannot predict outcomes of anti-tumor effects *in vivo*. siRNA in our hands was abandoned so far as possible drug candidate since it was not possible to conduct knock down with liposomes and other available nanocarriers *in vitro*. Nevertheless, in the meantime siRNA therapeutics have been approved as (very expensive) treatment of rare diseases.<sup>242–244</sup> Three new drugs have been developed which deliver siRNA in lipid nanoparticles to the liver. But other encapsulation and delivery strategies are currently investigated.<sup>245</sup> Cancer therapy is still a field where siRNA therapeutics are tested.<sup>246</sup>

Focus was shifted to small molecules which circumvent the many pitfalls siRNA transfection offers. Inhibitors in form of small organic molecules provide more stability and act directly on the target structure/protein without the need for siRNA mediated degradation of mRNA by RNA-induced silencing complex (RISC). Tasquinimod was chosen as first test substance to influence TAM (see chapter 2.1.5). As key players in the tumor microenvironment, macrophages, T cells and melanoma cell lines were chosen to test Tasquinimod effects on. In first preliminary studies no significant effect on surface marker expression of M2 macrophages could be observed *in vitro* when they were incubated for 24 hours with Tasquinimod (see **Figure 10**). Experiments with the Seahorse system revealed that there are differences in the cell metabolism between M1 and M2 macrophages (see **Figure 11** & **Figure 12**). Short time treatment with Tasquinimod at 100  $\mu$ M for 1 hour elevated basal respiration and ATP production very slightly in M1 macrophages with the result of a significant difference towards M2 macrophages either untreated or treated with 100  $\mu$ M

## Conclusion

Tasquinimod. Proliferation of CD4<sup>+</sup> and CD8<sup>+</sup> T cells by polyclonal stimulation with an anti-CD3 antibody was unaltered at 10  $\mu\text{M}$  Tasquinimod. A ten-fold higher Tasquinimod concentration led to a slightly diminished proliferation (see **Figure 13**). Tasquinimod solutions used for weekly injections in animal experiments had concentrations ranging from 600  $\mu\text{M}$  (1 mg/kg bodyweight) to 3100  $\mu\text{M}$  (5 mg/kg bodyweight) or 6200  $\mu\text{M}$  (10 mg/kg bodyweight). But these higher concentrations were diluted rapidly after s.c. injection at the tumor site and over the time till the next injection one week later. Thus, lower concentrations were used for *in vitro* experiments. To influence growth of human melanoma cell lines, even higher concentrations of 200  $\mu\text{M}$  were necessary to reduce proliferation of Ma-Mel-19 cells slightly, whereas UKRV-Mel-15 stays unaltered (see **Figure 14**). In comparison to literature higher concentrations were used due to the application route of s.c. injection at the tumor site, which delivers a more defined drug dose compared to add Tasquinimod to the drinking water of the mice in doses of 1-30 mg/kg/day as in several other studies. This range leads to serum levels of 1-4  $\mu\text{M}$  and tumor (s.c.) tissue levels of 0,4-1,0  $\mu\text{M}$ .<sup>62</sup> In cellular assays concentrations up to 50  $\mu\text{M}$  were used with different tumor cell lines.<sup>71</sup>

Since valid anti-tumor therapies can only be developed *in vivo*, development of suitable nano-scaled drug carriers was the next milestone. Our cooperation partners at the department of pharmacy are specialists in liposome formulation by dual centrifugation, a method which is capable of producing a high number of samples in a short amount of time under sterile conditions with low amounts of raw material. After large scale screening experiments, a group of liposomal formulations with distinct stability and release properties was chosen for further biological experiments. A necessity for biological experiments *in vitro* and *in vivo* is a certain storage time in order to use one batch of liposomes for replicates of biological experiments. If liposomes degrade already at pH7 and 4°C, free drug substance would probably lead to biological effects, but release studies on those liposomes would be biased. Then again, ideal drug carriers need some inherent instability or degradability *in vivo* or, to be more specific, in cells. It is known that pH values drop in lysosomes. Therefore, liposome candidates were screened for stability at pH7,4 / 4°C and release at pH5,5 / 37°C simultaneously. Three formulations possessing those characteristics (C63, C73 and C83) were used for downstream experiments *in vitro* and one formulation even *in vivo* (C83). At first Doxorubicin was used as model drug due to its fluorescence to translate release characteristics from buffers to cells. In a three-fold approach, Doxorubicin loaded liposomes were tested for toxicity after long time spans via Resazurin assay, for liposome uptake via flow cytometry and for intranuclear Doxorubicin accumulation after release from liposomes via confocal microscopy (see **Figure 23**). To have a comparison to conventional liposomes already used in the clinic, L0, a formulation similar to Myocet, was tested alongside the instable liposomes in every experiment. Although the composition of the liposomes is the same, they differ in their loading of Doxorubicin. Myocet liposomes are loaded after formulation in an active approach via a pH gradient, whereas L0 was loaded passively during formulation.<sup>247</sup> Doxorubicin content in liposomes was normalized to 1  $\mu\text{M}$  of free Doxorubicin in order to avoid strong toxicity at least in a time frame of up to 24 hours. Doxorubicin should only act as release marker and not as cytostatic drug. The DNA binding property of Doxorubicin was the key to use this release detection system, as it provides a black and white situation which results in a high sensitivity for release detection. The results state clearly, that the instable C63, C73 and C83 formulations are far superior to the L0 formulation regarding Doxorubicin release as detected by confocal microscopy in the cell nuclei and by the toxicity generated by released Doxorubicin in the Resazurin assay. This test system is applicable in primary immune cells, like the human macrophages, and in cell lines, like the human melanoma cells. Although total uptake, toxicity and release do vary between the cell types overall trends remain unaltered. The early time points of 30 minutes and 4 hours shed light into ongoing uptake and release processes as overall Doxorubicin signal in the cell and in the nucleus increases in this time span and is already detectable at the early time point of 30 minutes. These studies can be extended to at least 24 hours, as shown in **Figure 25**. Later this release quantification strategy was vastly enhanced

## Conclusion

by using the Image Stream technology which is basically a flow cytometer taking several pictures of every cell passing the flow chamber. Those pictures from cells interrogated sequentially with several lasers replace the photomultiplier tubes detecting fluorescence (or light in general) in traditional flow cytometers. Since this spatial information of the cell's fluorescence is retained, it is possible to gate on the cell nucleus in every single cell. The only downside is that this machine does not produce true confocal pictures but only has brightfield microscopes. Previous findings have been reproduced with the new modification and further studies showed effects of different forms of PEGylation (linear or branched) and different forms of PEG attachment (pH sensitive or insensitive).

Just as important as efficient release at the right time point, is the targeting of the drug carriers to the right tissue and the right cell. Consequently, formulation of biotin liposomes was the next step. Biotin serves as adaptor for avidin or its relatives streptavidin (SA) and neutravidin. As small molecule it does not interfere with liposome synthesis, as large proteins like antibodies or avidin would do. Since avidin is a tetramer it can still bind three other biotin molecules and therefore a biotinylated antibody can bind to an avidin coated liposome surface. L0 and C83 liposomes were formulated with different molar ratios of biotin linked to a PEG chain from 0,05 mol% to 5 mol% and their binding to streptavidin coated silica beads with a diameter of 5  $\mu\text{m}$  was evaluated by flow cytometry (see **Figure 38**). To analyze non-specific binding too, liposomes were incubated with two different kinds of silica beads at once and liposomes with the same PEG ratio but without biotin were included as negative control. The streptavidin coated ones and beads coated with bovine serum albumin (BSA). The lipid composition determines binding behavior. Instable biotin liposomes (C83) showed high binding to both silica bead types or in other words no targeting. C83 PEG liposomes without biotin even disfavor binding to streptavidin beads, resulting in a SA/BSA ratio below 1. Those with biotin have a ratio only slightly above one. Contrary, with stable biotin liposomes (L0) less unspecific binding to BSA beads was observed and the highest SA/BSA ratio of those beads was 51,33% ( $\pm 15,57$ ) with 5 mol% biotin. Higher PEGylation favored binding of SA beads to, but to a much lesser extent. For 1 and 5 mol% biotin L0 liposomes showed a significant higher ratio compared to those liposomes with only PEG. C63 and C73 mirrored the behavior of C83 (see **Figure 39**). Actual coating of silica beads by liposomes was visible in confocal microscopy (see **Figure 40**).

After having collected information about drug release, the next logical step to evaluate the possibility to influence the immune system with Tasquinimod is the translation into the humanized mice melanoma model (see 4.6). Weekly Tasquinimod treatment of xenograft melanoma tumors in mice humanized with PBMC led to significantly reduced tumor growth (see **Figure 43**). Treatment groups in non-humanized mice, xenograft tumors in immunodeficient mice without the addition of human immune cells, did not show this effect. This led to the conclusion, that the anti-tumor effects of Tasquinimod must be of immunomodulatory nature. Extensive analysis of the tumor and its environment via immunohistochemistry staining and flow cytometry did not provide a conclusive explanation for the observed anti-tumor effect. Transcriptomic analysis by mRNA panel analysis using the *NanoString* platform revealed downregulation of 23 genes and upregulation of 3 genes (*BNIP3*, *FOSL1* and *RPS6KB1*) in tumor samples treated with Tasquinimod and analyzed *ex vivo* on the end of the experiment (see **Figure 47**). Further experiments will have to verify via different methods and clarify the roles of those genes in the tumor microenvironment.

Overall, this humanized mouse model is rather limited to T cells as predominant cell type present 3 – 4 weeks after transplantation. However, Tasquinimod effects dependent on the presence of immune cells were observable and CD8<sup>+</sup> T cells (CTL) as main effector cells against tumor cells were present. For achieving better macrophage survival and more development of myeloid immune cells newly developed mouse strains should be used for future experiments. SGM3 mice as advancement of the NSG mice have a transgenic expression of human stem cell factor (SCF), granulocyte-macrophage colony-stimulating factor (GM-CSF) and IL-3 as addition to their immunodeficient

## Conclusion

background (see 2.2) to support better development of immune cells from the myeloid lineage.<sup>248</sup> MISTRG mice follow the same strategy with an expression of macrophage colony-stimulating factor (M-CSF), IL-3, GM-CSF, and thrombopoietin in a different mouse strain.<sup>249</sup>

This bulk gene expression analysis lacks spatial information, as the whole tissue of the tumor sample is digested and lysed afterwards. It does offer the analysis of almost 800 targets in one assay. To gain highplex data paired with spatial information, we partnered up with the company Zellkraftwerk, which offers highplex immunofluorescence analysis of frozen tissue samples with their Chipcytometry technology. We provided samples and they used their technology to analyze the expression of 16 (human) protein targets in the xenograft tumor tissue. The marker panel of this pilot study can easily be expanded to more than 100 targets in one sample. This method did offer us more information than flow cytometry and immunohistochemistry combined. Unfortunately, sample number was extremely limited, due to the character of an academic pilot study. Nonetheless, we could verify the detection of mainly T cells exclusively in the tumor tissue coupled with information about their phenotype. Even macrophages were detected in incredibly low numbers. Highplex methods in transcriptomics and proteomics, which several companies have developed, will replace immunohistochemistry and flow cytometry in tissue analysis.

Application of nanoparticles as drug carriers is until now limited to peritumoral injection in our model due to the lack of active targeting strategies. To overcome this burden and enable systemic injection of the drug carriers and tumor therapy in places where direct injection is not possible, Leucine rich repeat containing 32 (LRRC32 or GARP) was evaluated as target structure. GARP expression was detected with the *NanoString* platform and immunohistochemistry staining in xenograft tumors *ex vivo* (see **Figure 52** & **Figure 53**). *In vitro* Ma-Mel-19 cells show GARP expression predominantly in the nucleus (see **Figure 54**). If GARP is suited as target for drug carriers *in vivo* despite its expression by platelets must be still tested in the humanized mice melanoma model. However, an antibody against the GARP:TGF- $\beta$ 1 complex in mice did not cause thrombotic events.<sup>137</sup> Biotinylated liposomes can easily be modified with any biotinylated antibody through avidin as bridge after liposome formulation and drug encapsulation.

# 6 Outlook

The developed test system consisting of cells treated *in vitro* with Doxorubicin loaded liposomes and their readout in the ImageStream system makes it possible to test various modifications of liposomes like PEGylation and coupled antibodies on many different cell types for various time points under controlled conditions. These results about release can be transported to *in vivo* system where quantification of release is rarely possible. Although Doxorubicin is an “old” chemotherapeutic it can be also used to measure drug transport *in vivo*. Doxorubicin fluorescence in cell nuclei of tissue can be detected in cryo stains. Switching from Doxorubicin as model drug to immunomodulatory drugs can of course effect to a certain extent liposomal stability and release rates, but these effects can be minimized if hydrophilic drugs with the same molecular weight are used. Even with Tasquinimod, a rather hydrophobic substance, liposome synthesis was possible. Drugs, without fluorescence or other straightforward methods to detect, do not offer the possibility to monitor release directly. Monitoring only the carrier itself with fluorophores incorporated into the carrier or its membrane in the case of liposomes might lead to misguided conclusions. Therefore, it is mandatory to collect this information beforehand with a model drug like Doxorubicin. Its accumulation inside the nucleus provides a great “resolution” between Doxorubicin still encapsulated and free Doxorubicin. Many other tracers of release do not offer this resolution in reality. DQ™ Ovalbumin would be suitable, but it is a large protein which might not survive liposome synthesis.<sup>250</sup> Fluorescein Di-β-D-Glucopyranoside and calcein AM both are non-fluorescent substances, gaining their fluorescence properties after modification by intracellular enzymes.<sup>251,252</sup> Thus, both substances should display release by arising fluorescence. Both tracers were tested during this study but could not resolve release clearly. Doxorubicin is superior in regard of producing a black and white situation of Doxorubicin in liposomes unable to reach the DNA in the nucleus and free Doxorubicin which is able to do so. This feature in connection with the ability to normalize cracked liposomes to free substance provides an actual quantification which is not possible with non-fluorescent substrates for enzymes.

During this study, liposomes have proved their potential as drug carriers outside the field of cancer in the COVID-19 pandemic. Several companies have developed mRNA vaccines, which all use a liposomal formulation (lipoplexes) to facilitate transfection of human cells.<sup>253,254</sup> One subunit protein vaccine displays the virus spike protein expressed in insect cells on the surface of micelles formed by polysorbate 80.<sup>255</sup> Despite the use of Doxorubicin liposomes in cancer treatment since the 1990s and other liposomal formulations of drugs, this use as vaccine boosted the use of liposomes tremendously. Never before so many people have been treated in so little time with nanoparticles. Even if the pandemic somehow overshadowed the fight against cancer, almost every pharmaceutical company, which is now producing mRNA vaccines, is also committed to fight cancer. In most cases this was the primary aim to employ this technology. For vaccinations, crude liposomal formulations are sufficient, as cationic lipids are long known to transfect cells (polyethylenimine (PEI) for example)<sup>256</sup> and phagocytic cells like macrophages and dendritic cells are the target for a vaccine anyhow.

Spatial information becomes more and more important in understanding the interplay between immune system and cancer cells. This existing interplay seems to play an important role in deciding a tumor’s responsiveness towards modern immunotherapies which was the breakthrough in cancer treatment for certain tumor types. Highplex methods provide the necessary depth to firstly identify immune cell types and secondly to receive information about their phenotype while preserving precious spatial data. Nowadays spatial highplex analysis is divided into proteomics and genomics but certain technologies blur this strict boundary by offering highplex capabilities in both fields or combining



## Outlook

antibodies with nucleotide barcodes to surpass limitations like spillover and necessary lasers and filters for fluorophores. “Spatially resolved transcriptomics” have been voted as method of the year 2020 by *Nature Methods*, underlining the rising importance of this method both in basic research but also in clinical science and routine.<sup>257</sup> Countless numbers of FFPE slides hibernate in research facilities and clinics all over the world containing information for many malignancies and diseases. As this information already exists, state-of-the-art methods are needed to harvest this information and to put it into context. Humanized mice are an important bridge between basic research in cell lines or animal models and translation into the clinic. Although they do not offer a perfect human immune system, at least they offer insight into the interplay between tumor cells and immune cells and might lead to the right prediction for therapy success. By using tumor cells and immune cells from the same patient, it is possible to test personalized therapy approaches. Personalized medicine is another super trend of the century, founded in the knowledge about heterogeneity between patients and even inside the patient in the case of tumors and the new competence to transfer this knowledge about a single patient into therapy.

As first target we evaluated Leucine rich repeat containing 32 (LRRC32 / GARP) in human melanoma cell lines and in tumor samples of xenograft tumors in humanized mice both on protein and mRNA level. GARP expression in patient samples has been described (see 2.4). Future experiments must prove the possibility to target cancer cells *in vivo*. Since GARP is highly expressed on platelets, the injection route plays a pivotal route. It is likely, that i.v. injection would lead to neutralization of the nanocarrier because of its attachment to platelets. Peritumoral injection or injection in tissue can circumvent this neutralization. Toxic cargo of liposomes would lead to an anti-tumor effect regardless of whether regulatory T cells are killed and prevented from shedding TGF- $\beta$  or tumor cells are targeted and killed directly.

## 7 Literature

- (1) Schank, T. E.; Hassel, J. C. Immunotherapies for the Treatment of Uveal Melanoma—History and Future. *Cancers* **2019**, *11* (8), 1–14. <https://doi.org/10.3390/cancers11081048>.
- (2) Yde, S. S.; Sjoegren, P.; Heje, M.; Stolle, L. B. Mucosal Melanoma: A Literature Review. *Current Oncology Reports* **2018**, *20* (3). <https://doi.org/10.1007/s11912-018-0675-0>.
- (3) Peris, K.; Fagnoli, M. C.; Garbe, C.; Kaufmann, R.; Bastholt, L.; Seguin, N. B.; Bataille, V.; Marmol, V. del; Dummer, R.; Harwood, C. A.; Hauschild, A.; Höller, C.; Haedersdal, M.; Malvey, J.; Middleton, M. R.; Morton, C. A.; Nagore, E.; Stratigos, A. J.; Szeimies, R.-M.; Tagliaferri, L.; Trakatelli, M.; Zalaudek, I.; Eggermont, A.; Grob, J. J. Diagnosis and Treatment of Basal Cell Carcinoma: European Consensus–Based Interdisciplinary Guidelines. *European Journal of Cancer* **2019**, *118*. <https://doi.org/10.1016/j.ejca.2019.06.003>.
- (4) Bastian, B. C. *The Molecular Pathology of Melanoma: An Integrated Taxonomy of Melanocytic Neoplasia*; 2014; Vol. 9. <https://doi.org/10.1146/annurev-pathol-012513-104658>.
- (5) Merkel, E. A.; Gerami, P. Malignant Melanoma of Sun-Protected Sites: A Review of Clinical, Histological, and Molecular Features. *Laboratory Investigation* **2017**, *97* (6), 630–635. <https://doi.org/10.1038/labinvest.2016.147>.
- (6) Grob, J. J. The “Ugly Duckling” Sign: Identification of the Common Characteristics of Nevi in an Individual as a Basis for Melanoma Screening. *Archives of Dermatology* **1998**, *134* (1), 103-a-104. <https://doi.org/10.1001/archderm.134.1.103-a>.
- (7) Michielin, O.; van Akkooi, A. C. J.; Ascierto, P. A.; Dummer, R.; Keilholz, U. Cutaneous Melanoma: ESMO Clinical Practice Guidelines for Diagnosis, Treatment and Follow-Up. *Annals of Oncology* **2019**, *30* (12), 1884–1901. <https://doi.org/10.1093/annonc/mdz411>.
- (8) Haenssle, H. A.; Fink, C.; Schneiderbauer, R.; Toberer, F.; Buhl, T.; Blum, A.; Kalloo, A.; ben Hadj Hassen, A.; Thomas, L.; Enk, A.; Uhlmann, L.; Alt, C.; Arenbergerova, M.; Bakos, R.; Baltzer, A.; Bertlich, I.; Blum, A.; Bokor-Billmann, T.; Bowling, J.; Braghiroli, N.; Braun, R.; Buder-Bakhaya, K.; Buhl, T.; Cabo, H.; Cabrijan, L.; Cevic, N.; Classen, A.; Deltgen, D.; Fink, C.; Georgieva, I.; Hakim-Meibodi, L. E.; Hanner, S.; Hartmann, F.; Hartmann, J.; Haus, G.; Hoxha, E.; Karls, R.; Koga, H.; Kreuzsch, J.; Lallas, A.; Majenka, P.; Marghoob, A.; Massone, C.; Mekokishvili, L.; Mestel, D.; Meyer, V.; Neuberger, A.; Nielsen, K.; Oliviero, M.; Pampena, R.; Paoli, J.; Pawlik, E.; Rao, B.; Rendon, A.; Russo, T.; Sadek, A.; Samhaber, K.; Schneiderbauer, R.; Schweizer, A.; Toberer, F.; Trennheuser, L.; Vlahova, L.; Wald, A.; Winkler, J.; Woßling, P.; Zalaudek, I. Man against Machine: Diagnostic Performance of a Deep Learning Convolutional Neural Network for Dermoscopic Melanoma Recognition in Comparison to 58 Dermatologists. *Annals of Oncology* **2018**, *29* (8), 1836–1842. <https://doi.org/10.1093/annonc/mdy166>.
- (9) Salerni, G.; Carrera, C.; Lovatto, L.; Puig-Butille, J. A.; Badenas, C.; Plana, E.; Puig, S.; Malvey, J. Benefits of Total Body Photography and Digital Dermatoscopy (“two-Step Method of Digital Follow-up”) in the Early Diagnosis of Melanoma in Patients at High Risk for Melanoma. *Journal of the American Academy of Dermatology* **2012**, *67* (1), e17–e27. <https://doi.org/10.1016/j.jaad.2011.04.008>.
- (10) Phillips, M.; Marsden, H.; Jaffe, W.; Matin, R. N.; Wali, G. N.; Greenhalgh, J.; McGrath, E.; James, R.; Ladoyanni, E.; Bewley, A.; Argenziano, G.; Palamaras, I. Assessment of Accuracy of an Artificial Intelligence Algorithm to Detect Melanoma in Images of Skin Lesions. *JAMA network open* **2019**, *2* (10), e1913436. <https://doi.org/10.1001/jamanetworkopen.2019.13436>.
- (11) Shain, A. H.; Bastian, B. C. From Melanocytes to Melanomas. *Nature Reviews Cancer* **2016**, *16* (6), 345–358. <https://doi.org/10.1038/nrc.2016.37>.
- (12) Balch, C. M.; Gershenwald, J. E.; Soong, S. J.; Thompson, J. F.; Atkins, M. B.; Byrd, D. R.; Buzaid, A. C.; Cochran, A. J.; Coit, D. G.; Ding, S.; Eggermont, A. M.; Flaherty, K. T.; Gimotty, P. A.; Kirkwood, J. M.; McMasters, K. M.; Mihm, M. C.; Morton, D. L.; Ross, M. I.; Sober, A. J.; Sondak, V. K. Final Version of 2009 AJCC Melanoma Staging and Classification. *Journal of Clinical Oncology* **2009**, *27* (36), 6199–6206. <https://doi.org/10.1200/JCO.2009.23.4799>.
- (13) Leitlinienprogramm Onkologie; Deutsche Krebshilfe; Deutsche Krebsgesellschaft; AWMF. S3-Leitlinie Diagnostik , Therapie Und Nachsorge Des Melanoms Wesentliche Neuerungen Durch Die Aktualisierung. *Leitlinienprogramm Onkologie* **2019**, 1–81.
- (14) Akbani, R.; Akdemir, K. C.; Aksoy, B. A.; Albert, M.; Ally, A.; Amin, S. B.; Arachchi, H.; Arora, A.; Auman, J. T.; Ayala, B.; Baboud, J.; Balasundaram, M.; Balu, S.; Barnabas, N.; Bartlett, J.; Bartlett, P.; Bastian, B. C.; Baylin, S. B.; Behera, M.; Belyaev, D.; Benz, C.; Bernard, B.; Beroukhim, R.; Bir, N.; Black, A. D.; Bodenheimer, T.; Boice, L.; Boland, G. M.; Bono, R.; Bootwalla, M. S.; Bosenberg, M.; Bowen, J.; Bowlby, R.; Bristow, C. A.; Brockway-Lunardi, L.; Brooks, D.; Brzezinski, J.; Bshara, W.; Buda, E.; Burns, W. R.; Butterfield, Y. S. N.; Button, M.; Calderone, T.; Cappellini, G. A.; Carter, C.; Carter, S. L.; Cherney, L.; Cherniack, A. D.; Chevalier, A.; Chin, L.; Cho, J.; Cho, R. J.; Choi, Y. I.; Chu, A.; Chudamani, S.; Cibulskis, K.; Ciriello, G.; Clarke, A.; Coons, S.; Cope, L.; Crain, D.; Curley, E.; Danilova, L.; D’Atri, S.; Davidsen, T.; Davies, M. A.; Delman, K. A.; Demchok, J. A.; Deng, Q. A.; Deribe, Y. L.; Dhalla, N.; Dhir, R.; Dicara, D.; Dinikin, M.; Dubina, M.; Ebrom, J. S.; Egea, S.; Eley, G.; Engel, J.; Eschbacher, J. M.; Fedosenko, K. v.; Felau, I.; Fennell, T.; Ferguson, M. L.; Fisher, S.; Flaherty, K. T.; Frazer, S.;

- Frick, J.; Fulidou, V.; Gabriel, S. B.; Gao, J.; Gardner, J.; Garraway, L. A.; Gastier-Foster, J. M.; Gaudioso, C.; Gehlenborg, N.; Genovese, G.; Gerken, M.; Gershenwald, J. E.; Getz, G.; Gomez-Fernandez, C.; Gribbin, T.; Grimsby, J.; Gross, B.; Guin, R.; Gutschner, T.; Hadjipanayis, A.; Halaban, R.; Hanf, B.; Haussler, D.; Haydu, L. E.; Hayes, D. N.; Hayward, N. K.; Heiman, D. I.; Herbert, L.; Herman, J. G.; Hersey, P.; Hoadley, K. A.; Hodis, E.; Holt, R. A.; Hoon, D. S.; Hoppough, S.; Hoyle, A. P.; Huang, F. W.; Huang, M.; Huang, S.; Hutter, C. M.; Ibbbs, M.; Iype, L.; Jacobsen, A.; Jakrot, V.; Janning, A.; Jeck, W. R.; Jefferys, S. R.; Jensen, M. A.; Jones, C. D.; Jones, S. J. M.; Ju, Z.; Kakavand, H.; Kang, H.; Kefford, R. F.; Khuri, F. R.; Kim, J.; Kirkwood, J. M.; Klode, J.; Korkut, A.; Korski, K.; Krauthammer, M.; Kucherlapati, R.; Kwong, L. N.; Kycler, W.; Ladanyi, M.; Lai, P. H.; Laird, P. W.; Lander, E.; Lawrence, M. S.; Lazar, A. J.; Łażniak, R.; Lee, D.; Lee, J. E.; Lee, J.; Lee, K.; Lee, S.; Lee, W.; Leporowska, E.; Leraas, K. M.; Li, H. I.; Lichtenberg, T. M.; Lichtenstein, L.; Lin, P.; Ling, S.; Liu, J.; Liu, O.; Liu, W.; Long, G. v.; Lu, Y.; Ma, S.; Ma, Y.; Mackiewicz, A.; Mahadeshwar, H. S.; Malke, J.; Mallery, D.; Manikhas, G. M.; Mann, G. J.; Marra, M. A.; Matejka, B.; Mayo, M.; Mehrabi, S.; Meng, S.; Meyerson, M.; Mieczkowski, P. A.; Miller, J. P.; Miller, M. L.; Mills, G. B.; Moiseenko, F.; Moore, R. A.; Morris, S.; Morrison, C.; Morton, D.; Moschos, S.; Mose, L. E.; Muller, F. L.; Mungall, A. J.; Murawa, D.; Murawa, P.; Murray, B. A.; Nezi, L.; Ng, S.; Nicholson, D.; Noble, M. S.; Osunkoya, A.; Owonikoko, T. K.; Ozenberger, B. A.; Pagani, E.; Paklina, O. v.; Pantazi, A.; Parfenov, M.; Parfitt, J.; Park, P. J.; Park, W. Y.; Parker, J. S.; Passarelli, F.; Penny, R.; Perou, C. M.; Pihl, T. D.; Potapova, O.; Prieto, V. G.; Protopopov, A.; Quinn, M. J.; Radenbaugh, A.; Rai, K.; Ramalingam, S. S.; Raman, A. T.; Ramirez, N. C.; Ramirez, R.; Rao, U.; Rathmell, W. K.; Ren, X.; Reynolds, S. M.; Roach, J.; Robertson, A. G.; Ross, M. I.; Roszik, J.; Russo, G.; Saksena, G.; Saller, C.; Samuels, Y.; Sander, C.; Sander, C.; Sandusky, G.; Santoso, N.; Saul, M.; Saw, R. P.; Schadendorf, D.; Schein, J. E.; Schultz, N.; Schumacher, S. E.; Schwallier, C.; Scolyer, R. A.; Seidman, J.; Sekhar, P. C.; Sekhon, H. S.; Senbabaoglu, Y.; Seth, S.; Shannon, K. F.; Sharpe, S.; Sharpless, N. E.; Shaw, K. R. M.; Shelton, C.; Shelton, T.; Shen, R.; Sheth, M.; Shi, Y.; Shiau, C. J.; Shmulevich, I.; Sica, G. L.; Simons, J. v.; Sinha, R.; Sipahimalani, P.; Sofia, H. J.; Soloway, M. G.; Song, X.; Sougnez, C.; Spillane, A. J.; Szycała, A.; Stretch, J. R.; Stuart, J.; Suchorska, W. M.; Sucker, A.; Sumer, S. O.; Sun, Y.; Synott, M.; Tabak, B.; Tabler, T. R.; Tam, A.; Tan, D.; Tang, J.; Tarnuzzer, R.; Tarvin, K.; Tatka, H.; Taylor, B. S.; Teresiak, M.; Thiessen, N.; Thompson, J. F.; Thorne, L.; Thorsson, V.; Trent, J. M.; Triche, T. J.; Tsai, K. Y.; Tsou, P.; van den Berg, D. J.; van Allen, E. M.; Veluvolu, U.; Verhaak, R. G.; Voet, D.; Voronina, O.; Walter, V.; Walton, J. S.; Wan, Y.; Wang, Y.; Wang, Z.; Waring, J. S.; Watson, I. R.; Weinhold, N.; Weinstein, J. N.; Weisenberger, D. J.; White, P.; Wilkerson, M. D.; Wilmott, J. S.; Wise, L.; Wiznerowicz, M.; Woodman, S. E.; Wu, C. J.; Wu, C. C.; Wu, J.; Wu, Y.; Xi, R.; Xu, A. W.; Yang, D.; Yang, L.; Yang, L.; Zack, T. I.; Zenklusen, J. C.; Zhang, H.; Zhang, J.; Zhang, W.; Zhao, X.; Zhu, J.; Zhu, K.; Zimmer, L.; Zmuda, E.; Zou, L. Genomic Classification of Cutaneous Melanoma. *Cell* **2015**, *161* (7), 1681–1696. <https://doi.org/10.1016/j.cell.2015.05.044>.
- (15) Hanahan, D.; Weinberg, R. A. Hallmarks of Cancer: The next Generation. *Cell* Elsevier March 4, 2011, pp 646–674. <https://doi.org/10.1016/j.cell.2011.02.013>.
- (16) Schupp, J.; Krebs, F. K.; Zimmer, N.; Trzeciak, E.; Schuppan, D.; Tuettgenberg, A. Targeting Myeloid Cells in the Tumor Sustaining Microenvironment. *Cellular Immunology* **2019**, *343*, 103713. <https://doi.org/10.1016/j.cellimm.2017.10.013>.
- (17) Hui, L.; Chen, Y. Tumor Microenvironment: Sanctuary of the Devil. *Cancer Letters* **2015**, *368* (1), 7–13. <https://doi.org/10.1016/j.canlet.2015.07.039>.
- (18) Ginhoux, F.; Jung, S. Monocytes and Macrophages: Developmental Pathways and Tissue Homeostasis. *Nat Rev Immunol* **2014**, *14* (6), 392–404. <https://doi.org/10.1038/nri3671>.
- (19) Martinez, F. O.; Gordon, S. The M1 and M2 Paradigm of Macrophage Activation: Time for Reassessment. *F1000Prime Rep* **2014**, *6*. <https://doi.org/10.12703/p6-13>.
- (20) Murray, P. J. Macrophage Polarization. *Annu. Rev. Physiol.* **2017**, *79* (2017), 541–566. <https://doi.org/10.1146/annurev-physiol-022516-034339>.
- (21) Rhee, I. Diverse Macrophages Polarization in Tumor Microenvironment. *Arch Pharm Res* **2016**, *39* (11), 1588–1596. <https://doi.org/10.1007/s12272-016-0820-y>.
- (22) Kaina, B.; Grösch, S.; Decote-Ricardo, D.; Zhou, J.; Tang, Z.; Gao, S.; Li, C.; Feng, Y.; Zhou, X. Tumor-Associated Macrophages: Recent Insights and Therapies. *Frontiers in Oncology | www.frontiersin.org* **2020**, *10*, 188. <https://doi.org/10.3389/fonc.2020.00188>.
- (23) van Ginderachter, J. A.; Yona, S.; Boissonnas, A.; Laviron, M. Ontogeny of Tumor-Associated Macrophages. *Ontogeny of Tumor-Associated Macrophages. Front. Immunol* **2019**, *10*, 1799. <https://doi.org/10.3389/fimmu.2019.01799>.
- (24) Ohradanova-Repic, A.; Ghaemmaghami, A. M.; Carmo, A. M.; Viola, A.; Castegna, A.; Munari, F.; Sánchez-Rodríguez, R.; Scolaro, T. The Metabolic Signature of Macrophage Responses. *Frontiers in Immunology | www.frontiersin.org* **2019**, *1*, 1462. <https://doi.org/10.3389/fimmu.2019.01462>.
- (25) Ryan, D. G.; O'Neill, L. A. J. Krebs Cycle Reborn in Macrophage Immunometabolism. *Annual Review of Immunology* **2020**, *38* (1), 289–316. <https://doi.org/10.1146/annurev-immunol-081619-104850>.
- (26) Togashi, Y.; Shitara, K.; Nishikawa, H. Regulatory T Cells in Cancer Immunosuppression – Implications for Anticancer Therapy. *Nature Reviews Clinical Oncology*. <https://doi.org/10.1038/s41571>.
- (27) Farhood, B.; Najafi, M.; Mortezaee, | Keywan. CD8 + Cytotoxic T Lymphocytes in Cancer Immunotherapy: A Review. **2018**. <https://doi.org/10.1002/jcp.27782>.

## Literature

- (28) Bluestone, J. A.; Anderson, M. Tolerance in the Age of Immunotherapy. *New England Journal of Medicine* **2020**, *383* (12), 1156–1166. <https://doi.org/10.1056/nejmra1911109>.
- (29) Wang, Z.; Wu, X. Study and Analysis of Antitumor Resistance Mechanism of PD1/PD-L1 Immune Checkpoint Blocker. *Cancer Medicine*. Blackwell Publishing Ltd November 1, 2020, pp 8086–8121. <https://doi.org/10.1002/cam4.3410>.
- (30) Bagchi, S.; Yuan, R.; Engleman, E. G. Immune Checkpoint Inhibitors for the Treatment of Cancer: Clinical Impact and Mechanisms of Response and Resistance. **2020**. <https://doi.org/10.1146/annurev-pathol-042020>.
- (31) Galon, J.; Bruni, D. Approaches to Treat Immune Hot, Altered and Cold Tumours with Combination Immunotherapies. *Nature Reviews Drug Discovery*. Nature Publishing Group March 1, 2019, pp 197–218. <https://doi.org/10.1038/s41573-018-0007-y>.
- (32) Xie, G.; Dong, H.; Liang, Y.; Ham, J. D.; Rizwan, R.; Chen, J. CAR-NK Cells: A Promising Cellular Immunotherapy for Cancer. *EBioMedicine*. Elsevier B.V. September 1, 2020. <https://doi.org/10.1016/j.ebiom.2020.102975>.
- (33) Rafiq, S.; Hackett, C. S.; Brentjens, R. J. Engineering Strategies to Overcome the Current Roadblocks in CAR T Cell Therapy. *Nature Reviews* **2020**, *17* (167), 147–167. <https://doi.org/10.1038/s41571-019-0297-y>.
- (34) Park, J. H.; Rivière, I.; Gonen, M.; Wang, X.; Sénéchal, B.; Curran, K. J.; Sauter, C.; Wang, Y.; Santomasso, B.; Mead, E.; Roshal, M.; Maslak, P.; Davila, M.; Brentjens, R. J.; Sadelain, M. Long-Term Follow-up of CD19 CAR Therapy in Acute Lymphoblastic Leukemia. *New England Journal of Medicine* **2018**, *378* (5), 449–459. <https://doi.org/10.1056/nejmoa1709919>.
- (35) Maus, M. v.; Bonini, C.; Moon, E. K.; Martinez, M. CAR T Cells for Solid Tumors: New Strategies for Finding, Infiltrating, and Surviving in the Tumor Microenvironment. *Frontiers in Immunology* | [www.frontiersin.org](http://www.frontiersin.org) **2019**, *10*, 128. <https://doi.org/10.3389/fimmu.2019.00128>.
- (36) Testori, A. A. E.; Ribero, S.; Indini, A.; Mandalà, M. Adjuvant Treatment of Melanoma: Recent Developments and Future Perspectives. *American Journal of Clinical Dermatology* **2019**, *20* (6), 817–827. <https://doi.org/10.1007/s40257-019-00456-4>.
- (37) Weiss, S. A.; Wolchok, J. D.; Sznol, M. Immunotherapy of Melanoma: Facts and Hopes. *Clinical Cancer Research* **2019**, *25* (17), 5191–5201. <https://doi.org/10.1158/1078-0432.CCR-18-1550>.
- (38) Proietti, I.; Skroza, N.; Michelini, S.; Mambrin, A.; Balduzzi, V.; Bernardini, N.; Marchesiello, A.; Tolino, E.; Volpe, S.; Maddalena, P.; di Fraia, M.; Mangino, G.; Romeo, G.; Potenza, C. BRAF Inhibitors: Molecular Targeting and Immunomodulatory Actions. <https://doi.org/10.3390/cancers12071823>.
- (39) Guo, Y.; Pan, W.; Liu, S.; Shen, Z.; Xu, Y.; Hu, L. ERK/MAPK Signalling Pathway and Tumorigenesis (Review). *Experimental and Therapeutic Medicine* **2020**. <https://doi.org/10.3892/etm.2020.8454>.
- (40) Wan, P. T. C.; Garnett, M. J.; Roe, S. M.; Lee, S.; Niculescu-Duvaz, D.; Good, V. M.; Jones, C. M.; Marshall, C. J.; Springer, C. J.; Barford, D. Mechanism of Activation of the RAF-ERK Signaling Pathway by Oncogenic Mutations of B-RAF. *Cell* **2004**, *116*, 855–867.
- (41) Wei, S. C.; Levine, J. H.; Cogdill, A. P.; Zhao, Y.; Anang, N. A. A. S.; Andrews, M. C.; Sharma, P.; Wang, J.; Wargo, J. A.; Pe'er, D.; Allison, J. P. Distinct Cellular Mechanisms Underlie Anti-CTLA-4 and Anti-PD-1 Checkpoint Blockade. *Cell* **2017**, *170* (6), 1120–1133.e17. <https://doi.org/10.1016/j.cell.2017.07.024>.
- (42) Simeone, E.; Grimaldi, A. M.; Festino, L.; Trojaniello, C.; Vitale, M. G.; Vanella, V.; Palla, M.; Ascierto, P. A. Immunotherapy in Metastatic Melanoma: A Novel Scenario of New Toxicities and Their Management. *Melanoma Management* **2019**, *6* (4), MMT30. <https://doi.org/10.2217/mmt-2019-0005>.
- (43) Larkin, J.; Chiarion-Sileni, V.; Gonzalez, R.; Grob, J. J.; Rutkowski, P.; Lao, C. D.; Cowey, C. L.; Schadendorf, D.; Wagstaff, J.; Dummer, R.; Ferrucci, P. F.; Smylie, M.; Hogg, D.; Hill, A.; Márquez-Rodas, I.; Haanen, J.; Guidoboni, M.; Maio, M.; Schöffski, P.; Carlino, M. S.; Lebbé, C.; McArthur, G.; Ascierto, P. A.; Daniels, G. A.; Long, G. v.; Bastholt, L.; Rizzo, J. I.; Balogh, A.; Moshyk, A.; Hodi, F. S.; Wolchok, J. D. Five-Year Survival with Combined Nivolumab and Ipilimumab in Advanced Melanoma. *New England Journal of Medicine* **2019**, *381* (16), 1535–1546. <https://doi.org/10.1056/NEJMoa1910836>.
- (44) Blank, C. U.; Haining, W. N.; Held, W.; et al. Defining ‘T Cell Exhaustion.’ *Nature Reviews Immunology* **2019**, *19*, 665–674. <https://doi.org/10.1038/s41577-019-0221-9>.
- (45) Robert, C.; Ribas, A.; Schachter, J.; Arance, A.; Grob, J. J.; Mortier, L.; Daud, A.; Carlino, M. S.; McNeil, C. M.; Lotem, M.; Larkin, J. M. G.; Lorigan, P.; Neyns, B.; Blank, C. U.; Petrella, T. M.; Hamid, O.; Su, S. C.; Krepler, C.; Ibrahim, N.; Long, G. v. Pembrolizumab versus Ipilimumab in Advanced Melanoma (KEYNOTE-006): Post-Hoc 5-Year Results from an Open-Label, Multicentre, Randomised, Controlled, Phase 3 Study. *The Lancet Oncology* **2019**, *20* (9), 1239–1251. [https://doi.org/10.1016/S1470-2045\(19\)30388-2](https://doi.org/10.1016/S1470-2045(19)30388-2).
- (46) Nowicki, T. S.; Hu-Lieskovan, S.; Ribas, A. Mechanisms of Resistance to PD-1 and PD-L1 Blockade. *The Cancer Journal* **2018**, *24* (1), 47–53. <https://doi.org/10.1097/PPO.0000000000000303>.
- (47) Daud, A. I.; Wolchok, J. D.; Robert, C.; Hwu, W. J.; Weber, J. S.; Ribas, A.; Hodi, F. S.; Joshua, A. M.; Kefford, R.; Hersey, P.; Joseph, R.; Gangadhar, T. C.; Dronca, R.; Patnaik, A.; Zarour, H.; Roach, C.; Toland, G.; Luceford, J. K.; Li, X. N.; Emancipator, K.; Dolled-Filhart, M.; Kang, S. P.; Ebbinghaus, S.; Hamid, O. Programmed Death-Ligand 1 Expression and Response to the Anti-Programmed Death 1 Antibody Pembrolizumab in Melanoma. *Journal of Clinical Oncology* **2016**, *34* (34), 4102–4109. <https://doi.org/10.1200/JCO.2016.67.2477>.
- (48) Carlino, M. S.; Long, G. v.; Schadendorf, D.; Robert, C.; Ribas, A.; Richtig, E.; Nyakas, M.; Caglevic, C.; Tarhini, A.; Blank, C.; Hoeller, C.; Bar-Sela, G.; Barrow, C.; Wolter, P.; Zhou, H.; Emancipator, K.; Jensen, E. H.; Ebbinghaus, S.; Ibrahim, N.; Daud, A. Outcomes by Line of Therapy and Programmed Death Ligand 1

## Literature

- Expression in Patients with Advanced Melanoma Treated with Pembrolizumab or Ipilimumab in KEYNOTE-006: A Randomised Clinical Trial. *European Journal of Cancer* **2018**, *101*, 236–243. <https://doi.org/10.1016/j.ejca.2018.06.034>.
- (49) Ascierto, P. A.; Ferrucci, P. F.; Fisher, R.; del Vecchio, M.; Atkinson, V.; Schmidt, H.; Schachter, J.; Queirolo, P.; Long, G. v.; di Giacomo, A. M.; Svane, I. M.; Lotem, M.; Bar-Sela, G.; Couture, F.; Mookerjee, B.; Ghori, R.; Ibrahim, N.; Moreno, B. H.; Ribas, A. Dabrafenib, Trametinib and Pembrolizumab or Placebo in BRAF-Mutant Melanoma. *Nature Medicine*. Nature Publishing Group June 1, 2019, pp 941–946. <https://doi.org/10.1038/s41591-019-0448-9>.
- (50) Sullivan, R. J.; Hamid, O.; Gonzalez, R.; Infante, J. R.; Patel, M. R.; Hodi, F. S.; Lewis, K. D.; Tawbi, H. A.; Hernandez, G.; Wongchenko, M. J.; Chang, Y. M.; Roberts, L.; Ballinger, M.; Yan, Y.; Cha, E.; Hwu, P. Atezolizumab plus Cobimetinib and Vemurafenib in BRAF-Mutated Melanoma Patients. *Nature Medicine*. Nature Publishing Group June 1, 2019, pp 929–935. <https://doi.org/10.1038/s41591-019-0474-7>.
- (51) Vyas, M.; Müller, R.; Pogge von Strandmann, E. Antigen Loss Variants: Catching Hold of Escaping Foes. *Frontiers in Immunology* **2017**, *8*, 175. <https://doi.org/10.3389/fimmu.2017.00175>.
- (52) Sahin, U.; Türeci, Ö. *Personalized Vaccines for Cancer Immunotherapy*.
- (53) Scheetz, L.; Park, K. S.; Li, Q.; Lowenstein, P. R.; Castro, M. G.; Schwendeman, A.; Moon, J. J. Engineering Patient-Specific Cancer Immunotherapies. *Nature Biomedical Engineering*. Nature Publishing Group October 1, 2019, pp 768–782. <https://doi.org/10.1038/s41551-019-0436-x>.
- (54) Peng, M.; Mo, Y.; Wang, Y.; Wu, P.; Zhang, Y.; Xiong, F.; Guo, C.; Wu, X.; Li, Y.; Li, X.; Li, G.; Xiong, W.; Zeng, Z. Neoantigen Vaccine: An Emerging Tumor Immunotherapy. *Molecular Cancer*. BioMed Central Ltd. August 23, 2019. <https://doi.org/10.1186/s12943-019-1055-6>.
- (55) Sahin, U.; Oehm, P.; Derhovanessian, E.; Jabulowsky, R. A.; Vormehr, M.; Gold, M.; Maurus, D.; Schwarck-Kokarakis, D.; Kuhn, A. N.; Omokoko, T.; Kranz, L. M.; Diken, M.; Kreiter, S.; Haas, H.; Attig, S.; Rae, R.; Cuk, K.; Kemmer-Brück, A.; Breitkreuz, A.; Tolliver, C.; Caspar, J.; Quinkhardt, J.; Hebich, L.; Stein, M.; Hohberger, A.; Vogler, I.; Liebig, I.; Renken, S.; Sikorski, J.; Leierer, M.; Müller, V.; Mitzel-Rink, H.; Miederer, M.; Huber, C.; Grabbe, S.; Utikal, J.; Pinter, A.; Kaufmann, R.; Hassel, J. C.; Loquai, C.; Türeci, Ö. An RNA Vaccine Drives Immunity in Checkpoint-Inhibitor-Treated Melanoma. *Nature* **2020**. <https://doi.org/10.1038/s41586-020-2537-9>.
- (56) Acharya, N.; Sabatos-Peyton, C.; Carrizosa Anderson, A. Tim-3 Finds Its Place in the Cancer Immunotherapy Landscape. *Journal for Immunotherapy of Cancer* **2020**, *8*, 911. <https://doi.org/10.1136/jitc-2020-000911>.
- (57) Harjunpää, H.; Guilleray, C. TIGIT as an Emerging Immune Checkpoint. *Clinical and Experimental Immunology* **2020**, *200* (2), 108–119. <https://doi.org/10.1111/cei.13407>.
- (58) Roma-rodrigues, C.; Rivas-garcía, L.; Baptista, P. v.; Fernandes, A. R. Gene Therapy in Cancer Treatment: Why Go Nano? *Pharmaceutics*. MDPI AG March 1, 2020. <https://doi.org/10.3390/pharmaceutics12030233>.
- (59) Mikelez-alonso, I.; Aires, A.; Cortajarena, A. L. Cancer Nano-Immunotherapy from the Injection to the Target: The Role of Protein Corona. *International Journal of Molecular Sciences*. MDPI AG January 2, 2020. <https://doi.org/10.3390/ijms21020519>.
- (60) Danhier, F. To Exploit the Tumor Microenvironment: Since the EPR Effect Fails in the Clinic, What Is the Future of Nanomedicine? *J Control Release* **2016**, *244* (Pt A), 108–121. <https://doi.org/10.1016/j.jconrel.2016.11.015>.
- (61) Park, J.; Choi, Y.; Chang, H.; Um, W.; Hee Ryu, J.; Chan Kwon, I. Alliance with EPR Effect: Combined Strategies to Improve the EPR Effect in the Tumor Microenvironment. *Issue 26 Theranostics* **2019**, *9* (26), 8073–8090. <https://doi.org/10.7150/thno.37198>.
- (62) Isaacs, J. T.; Pili, R.; Qian, D. Z.; Dalrymple, S. L.; Garrison, J. B.; Kyprianou, N.; Björk, A.; Olsson, A.; Leanderson, T. Identification of ABR-215050 as Lead Second Generation Quinoline-3- Carboxamide Anti-Angiogenic Agent for the Treatment of Prostate Cancer. *Prostate* **2006**, *66* (16), 1768–1778. <https://doi.org/10.1002/pros.20509>.
- (63) Isaacs, J. T.; Pili, R.; Qian, D. Z.; Dalrymple, S. L.; Garrison, J. B.; Kyprianou, N.; Björk, A.; Olsson, A.; Leanderson, T. Identification of ABR-215050 as Lead Second Generation Quinoline-3-Carboxamide Anti-Angiogenic Agent for the Treatment of Prostate Cancer. *The Prostate* **2006**, *66* (16), 1768–1778. <https://doi.org/10.1002/pros.20509>.
- (64) Escudier, B.; Faivre, S.; van Cutsem, E.; Germann, N.; Pouget, J. C.; Plummer, R.; Vergote, I.; Thistlethwaite, F.; Bjarnason, G. A.; Jones, R.; Mackay, H.; Edeline, J.; Fartoux, L.; Hirte, H.; Oza, A. A Phase II Multicentre, Open-Label, Proof-of-Concept Study of Tasquinimod in Hepatocellular, Ovarian, Renal Cell, and Gastric Cancers. *Targeted Oncology* **2017**, *12* (5), 655–661. <https://doi.org/10.1007/s11523-017-0525-2>.
- (65) Gong, P.; Liu, H.; Liu, X.; Zhou, G.; Liu, M.; Yang, X.; Xiong, W.; Wang, Q.; Ma, J.; Ren, Z.; He, M.; Zhang, X. Efficacy of Tasquinimod in Men with Metastatic Castration-Resistant Prostate Cancer. *Medicine* **2018**, *97* (46), e13204. <https://doi.org/10.1097/md.00000000000013204>.
- (66) Shen, L.; Pili, R. Tasquinimod Targets Suppressive Myeloid Cells in the Tumor Microenvironment. *Oncol Immunology* **2019**, *8* (10), 1–3. <https://doi.org/10.1080/2162402X.2015.1072672>.
- (67) Vogl, T.; Tenbrock, K.; Ludwig, S.; Leukert, N.; Ehrhardt, C.; van Zoelen, M. A. D.; Nacken, W.; Foell, D.; van der Poll, T.; Sorg, C.; Roth, J. Mrp8 and Mrp14 Are Endogenous Activators of Toll-like Receptor 4, Promoting Lethal, Endotoxin-Induced Shock. **2007**. <https://doi.org/10.1038/nm1638>.
- (68) Olsson, A.; Nakhle, J.; Sundstedt, A.; Plas, P.; Bauchet, A. L.; Pierron, V.; Bruetschy, L.; Deric, A.; Torngren, M.; Liberg, D.; Schmidlin, F.; Leanderson, T. Tasquinimod Triggers an Early Change in the Polarization of Tumor Associated Macrophages in the Tumor Microenvironment. *J Immunother Cancer* **2015**, *3*, 53. <https://doi.org/10.1186/s40425-015-0098-5>.

## Literature

- (69) Pelletier, M.; Simard, J. C.; Girard, D.; Tessier, P. A. Quinoline-3-Carboxamides Such as Tasquinimod Are Not Specific Inhibitors of S100A9. *Blood Advances* **2018**, *2* (10), 1170–1171. <https://doi.org/10.1182/bloodadvances.2018016667>.
- (70) Nakhlé, J.; Pierron, V.; Bauchet, A. L.; Plas, P.; Thiongane, A.; Meyer-Losic, F.; Schmidlin, F. Tasquinimod Modulates Tumor-Infiltrating Myeloid Cells and Improves the Antitumor Immune Response to PD-L1 Blockade in Bladder Cancer. *Oncotarget* **2016**, *5* (6), 1–15. <https://doi.org/10.1080/2162402X.2016.1145333>.
- (71) Isaacs, J. T.; Antony, L.; Dalrymple, S. L.; Brennen, W. N.; Gerber, S.; Hammers, H.; Wissing, M.; Kachhap, S.; Luo, J.; Xing, L.; Bjork, P.; Olsson, A.; Bjork, A.; Leanderson, T. Tasquinimod Is an Allosteric Modulator of HDAC4 Survival Signaling within the Compromised Cancer Microenvironment. *Cancer Research* **2013**, *73* (4), 1386–1399. <https://doi.org/10.1158/0008-5472.CAN-12-2730>.
- (72) Cheng, C.; Yang, J.; Li, S.-W.; Huang, G.; Li, C.; Min, W.-P.; Sang, Y. HDAC4 Promotes Nasopharyngeal Carcinoma Progression and Serves as a Therapeutic Target. <https://doi.org/10.1038/s41419-021-03417-0>.
- (73) Gupta, S.; Krug, S.; Pokkali, S.; Leanderson, T.; Isaacs, J. T.; Srikrishna, G.; Bishai, W. R. Pharmacologic Exhaustion of Suppressor Cells with Tasquinimod Enhances Bacterial Clearance during Tuberculosis. *American Journal of Respiratory and Critical Care Medicine* **2019**, *199* (3), 386–389. <https://doi.org/10.1164/rccm.201805-0820LE>.
- (74) Organización Mundial de la Salud (OMS). World Health Organization Model List of Essential Medicines. *Mental and Holistic Health: Some International Perspectives* **2019**, *21*, 119–134.
- (75) Gabizon, A. A.; Patil, Y.; La-Beck, N. M. New Insights and Evolving Role of Pegylated Liposomal Doxorubicin in Cancer Therapy. *Drug Resistance Updates*. Churchill Livingstone November 1, 2016, pp 90–106. <https://doi.org/10.1016/j.drug.2016.10.003>.
- (76) Cagel, M.; Grotz, E.; Bernabeu, E.; Moreton, M. A.; Chiappetta, D. A. Doxorubicin: Nanotechnological Overviews from Bench to Bedside. *Drug Discovery Today* **2017**, *22* (2), 270–281. <https://doi.org/10.1016/j.drudis.2016.11.005>.
- (77) Barenholz, Y. Doxil® - The First FDA-Approved Nano-Drug: Lessons Learned. *Journal of Controlled Release* **2012**, *160* (2), 117–134. <https://doi.org/10.1016/j.jconrel.2012.03.020>.
- (78) Pang, B.; Qiao, X.; Janssen, L.; Velds, A.; Groothuis, T.; Kerkhoven, R.; Nieuwland, M.; Ovaa, H.; Rottenberg, S.; van Tellingen, O.; Janssen, J.; Huijgens, P.; Zwart, W.; Neefjes, J. Drug-Induced Histone Eviction from Open Chromatin Contributes to the Chemotherapeutic Effects of Doxorubicin. *Nature Communications* **2013**, *4*. <https://doi.org/10.1038/ncomms2921>.
- (79) Prathumsap, N.; Shinlapawittayatorn, K.; Chattipakorn, S. C.; Chattipakorn, N. Effects of Doxorubicin on the Heart: From Molecular Mechanisms to Intervention Strategies. *European Journal of Pharmacology* **2020**, *866* (November 2019), 172818. <https://doi.org/10.1016/j.ejphar.2019.172818>.
- (80) Lucas, A.; Lam, D.; Cabrales, P. Doxorubicin-Loaded Red Blood Cells Reduced Cardiac Toxicity and Preserved Anticancer Activity. *Drug Delivery* **2019**, *26* (1), 433–442. <https://doi.org/10.1080/10717544.2019.1591544>.
- (81) Molinaro, R.; Martinez, J. O.; Zinger, A.; de Vita, A.; Storci, G.; Arrighetti, N.; de Rosa, E.; Hartman, K. A.; Basu, N.; Taghipour, N.; Corbo, C.; Tasciotti, E. Leukocyte-Mimicking Nanovesicles for Effective Doxorubicin Delivery to Treat Breast Cancer and Melanoma. *Biomaterials Science* **2020**, *8* (1), 333–341. <https://doi.org/10.1039/c9bm01766f>.
- (82) Gao, F.; Zhang, C.; Qiu, W. X.; Dong, X.; Zheng, D. W.; Wu, W.; Zhang, X. Z. PD-1 Blockade for Improving the Antitumor Efficiency of Polymer–Doxorubicin Nanoprodug. *Small* **2018**, *14* (37), 1–12. <https://doi.org/10.1002/smll.201802403>.
- (83) Bao, Y.; Hu, Q.; Wang, X.; Feng, X.; He, Y.; Guo, Y.; Fu, D. Chemo-Immunotherapy with Doxorubicin Prodrug and Erythrocyte Membrane-Enveloped Polymer Nano-Vaccine Enhances Antitumor Activity. *Biomedicine and Pharmacotherapy* **2020**, *129*. <https://doi.org/10.1016/j.biopha.2020.110377>.
- (84) Chen, L.; Alrbyawi, H.; Poudel, I.; Arnold, R. D.; Babu, R. J. Co-Delivery of Doxorubicin and Ceramide in a Liposomal Formulation Enhances Cytotoxicity in Murine B16BL6 Melanoma Cell Lines. *AAPS PharmSciTech* **2019**, *20* (3). <https://doi.org/10.1208/s12249-019-1316-0>.
- (85) Mestas, J.; Hughes, C. C. W. Of Mice and Not Men: Differences between Mouse and Human Immunology. *The Journal of Immunology* **2004**, *172* (5), 2731–2738. <https://doi.org/10.4049/jimmunol.172.5.2731>.
- (86) Masopust, D.; Sivula, C. P.; Jameson, S. C. Of Mice, Dirty Mice, and Men: Using Mice To Understand Human Immunology. *The Journal of Immunology* **2017**, *199* (2), 383–388. <https://doi.org/10.4049/jimmunol.1700453>.
- (87) Wing, J. B.; Tanaka, A.; Sakaguchi, S. Human FOXP3 + Regulatory T Cell Heterogeneity and Function in Autoimmunity and Cancer. *Immunity*. Cell Press February 19, 2019, pp 302–316. <https://doi.org/10.1016/j.immuni.2019.01.020>.
- (88) Wege, A. K. Humanized Mouse Models for the Preclinical Assessment of Cancer Immunotherapy. *BioDrugs* **2018**, *32* (3), 245–266. <https://doi.org/10.1007/s40259-018-0275-4>.
- (89) Ito, R.; Takahashi, T.; Ito, M. Humanized Mouse Models: Application to Human Diseases. *Journal of Cellular Physiology* **2018**, *233* (5), 3723–3728. <https://doi.org/10.1002/jcp.26045>.
- (90) Yong, K. S. M.; Her, Z.; Chen, Q. Humanized Mice as Unique Tools for Human-Specific Studies. *Archivum Immunologiae et Therapiae Experimentalis*. Birkhauser Verlag AG August 1, 2018, pp 245–266. <https://doi.org/10.1007/s00005-018-0506-x>.

## Literature

- (91) Choi, Y.; Lee, S.; Kim, K.; Kim, S. H.; Chung, Y. J.; Lee, C. Studying Cancer Immunotherapy Using Patient-Derived Xenografts (PDXs) in Humanized Mice. *Experimental and Molecular Medicine*. Nature Publishing Group August 1, 2018, p 99. <https://doi.org/10.1038/s12276-018-0115-0>.
- (92) Bosma, G. C.; Custer, R. P.; Bosma, M. J. A Severe Combined Immunodeficiency Mutation in the Mouse. *Nature* **1983**, *301* (5900), 527–530. <https://doi.org/10.1038/301527a0>.
- (93) Mombaerts, P.; Iacomini, J.; Johnson, R. S.; Herrup, K.; Tonegawa, S.; Papaioannou, V. E. RAG-1-Deficient Mice Have No Mature B and T Lymphocytes. *Cell* **1992**, *68* (5), 869–877. [https://doi.org/10.1016/0092-8674\(92\)90030-G](https://doi.org/10.1016/0092-8674(92)90030-G).
- (94) Hao, Z.; Rajewsky, K. Homeostasis of Peripheral B Cells in the Absence of B Cell Influx from the Bone Marrow. *Journal of Experimental Medicine* **2001**, *194* (8), 1151–1163. <https://doi.org/10.1084/jem.194.8.1151>.
- (95) van der Loo, J. C. M.; Hanenberg, H.; Cooper, R. J.; Luo, F.-Y.; Lazaridis, E. N.; Williams, D. A. Nonobese Diabetic/Severe Combined Immunodeficiency (NOD/SCID) Mouse as a Model System to Study the Engraftment and Mobilization of Human Peripheral Blood Stem Cells. *Blood* **1998**, *92* (7), 2556–2570. <https://doi.org/10.1182/blood.v92.7.2556>.
- (96) Shultz, L. D.; Lyons, B. L.; Burzenski, L. M.; Gott, B.; Chen, X.; Chaleff, S.; Kotb, M.; Gillies, S. D.; King, M.; Mangada, J.; Greiner, D. L.; Handgretinger, R. Human Lymphoid and Myeloid Cell Development in NOD/LtSz-Scid IL2R  $\gamma$  Null Mice Engrafted with Mobilized Human Hemopoietic Stem Cells. *The Journal of Immunology* **2005**, *174* (10), 6477–6489. <https://doi.org/10.4049/jimmunol.174.10.6477>.
- (97) Ito, M.; Hiramatsu, H.; Kobayashi, K.; Suzue, K.; Kawahata, M.; Hioki, K.; Ueyama, Y.; Koyanagi, Y.; Sugamura, K.; Tsuji, K.; Heike, T.; Nakahata, T. NOD/SCID/ $\gamma$  null Mouse: An Excellent Recipient Mouse Model for Engraftment of Human Cells. *Blood* **2002**, *100* (9), 3175–3182. <https://doi.org/10.1182/blood-2001-12-0207>.
- (98) Wunderlich, M.; Chou, F. S.; Link, K. A.; Mizukawa, B.; Perry, R. L.; Carroll, M.; Mulloy, J. C. AML Xenograft Efficiency Is Significantly Improved in NOD/SCID-IL2RG Mice Constitutively Expressing Human SCF, GM-CSF and IL-3. *Leukemia*. Nature Publishing Group August 5, 2010, pp 1785–1788. <https://doi.org/10.1038/leu.2010.158>.
- (99) Rongvaux, A.; Willinger, T.; Martinek, J.; Strowig, T.; Gearty, S. v.; Teichmann, L. L.; Saito, Y.; Marches, F.; Halene, S.; Palucka, A. K.; Manz, M. G.; Flavell, R. A. Development and Function of Human Innate Immune Cells in a Humanized Mouse Model. *Nature Biotechnology* **2014**, *32* (4), 364–372. <https://doi.org/10.1038/nbt.2858>.
- (100) Shultz, L. D.; Brehm, M. A.; Victor Garcia-Martinez, J.; Greiner, D. L. Humanized Mice for Immune System Investigation: Progress, Promise and Challenges. *Nature Reviews Immunology*. NIH Public Access November 2012, pp 786–798. <https://doi.org/10.1038/nri3311>.
- (101) Hu, Z.; Xia, J.; Fan, W.; Wargo, J.; Yang, Y. G. Human Melanoma Immunotherapy Using Tumor Antigen-Specific T Cells Generated in Humanized Mice. *Oncotarget* **2016**, *7* (6), 6448–6459. <https://doi.org/10.18632/oncotarget.7044>.
- (102) Forsberg, E. M. V.; Lindberg, M. F.; Jespersen, H.; Alsen, S.; Bagge, R. O.; Donia, M.; Svane, I. M.; Nilsson, O.; Ny, L.; Nilsson, L. M.; Nilsson, J. A. HER2 CAR-T Cells Eradicate Uveal Melanoma and T-Cell Therapy-Resistant Human Melanoma in IL2 Transgenic NOD/SCID IL2 Receptor Knockout Mice. *Cancer Research* **2019**, *79* (5), 899–904. <https://doi.org/10.1158/0008-5472.CAN-18-3158>.
- (103) Morton, J. J.; Bird, G.; Refaeli, Y.; Jimeno, A. Humanized Mouse Xenograft Models: Narrowing the Tumor-Microenvironment Gap. *Cancer Research* **2016**, *76* (21), 6153–6158. <https://doi.org/10.1158/0008-5472.CAN-16-1260>.
- (104) Tsujikawa, T.; Mitsuda, J.; Ogi, H.; Miyagawa-Hayashino, A.; Konishi, E.; Itoh, K.; Hirano, S. Prognostic Significance of Spatial Immune Profiles in Human Solid Cancers. *Cancer Science*. Blackwell Publishing Ltd October 1, 2020, pp 3426–3434. <https://doi.org/10.1111/cas.14591>.
- (105) Brady, L.; Kriner, M.; Coleman, I.; Morrissey, C.; Roudier, M.; True, L. D.; Gulati, R.; Plymate, S. R.; Zhou, Z.; Birditt, B.; Meredith, R.; Geiss, G.; Hoang, M.; Beechem, J.; Nelson, P. S. Inter- and Intra-Tumor Heterogeneity of Metastatic Prostate Cancer Determined by Digital Spatial Gene Expression Profiling. *Nature Communications* **2021**, *12* (1). <https://doi.org/10.1038/s41467-021-21615-4>.
- (106) McKinnon, K. M. Flow Cytometry: An Overview. *Current Protocols in Immunology* **2018**, *2018* (February), 5.1.1-5.1.11. <https://doi.org/10.1002/cpim.40>.
- (107) Bonilla, D. L.; Reinin, G.; Chua, E. Full Spectrum Flow Cytometry as a Powerful Technology for Cancer Immunotherapy Research. <https://doi.org/10.3389/fmolb.2020.612801>.
- (108) Stack, E. C.; Wang, C.; Roman, K. A.; Hoyt, C. C. Multiplexed Immunohistochemistry, Imaging, and Quantitation: A Review, with an Assessment of Tyramide Signal Amplification, Multispectral Imaging and Multiplex Analysis. *Methods* **2014**, *70* (1), 46–58. <https://doi.org/10.1016/j.ymeth.2014.08.016>.
- (109) McLaughlin, K. Multiplexing Immunohistochemistry. *Materials and Methods* **2019**, *9*, 2846. <https://doi.org/10.13070/mm.en.9.2846>.
- (110) Tan, W. C. C.; Nerurkar, S. N.; Cai, H. Y.; Ng, H. H. M.; Wu, D.; Wee, Y. T. F.; Lim, J. C. T.; Yeong, J.; Lim, T. K. H. Overview of Multiplex Immunohistochemistry/Immunofluorescence Techniques in the Era of Cancer Immunotherapy. *Cancer Communications* **2020**, No. February, 135–153. <https://doi.org/10.1002/cac2.12023>.
- (111) Hennig, C.; Adams, N.; Hansen, G. A Versatile Platform for Comprehensive Chip-Based Explorative Cytometry. *Cytometry Part A* **2009**, *75* (4), 362–370. <https://doi.org/10.1002/cyto.a.20668>.

## Literature

- (112) Teo, J.; Mirenska, A.; Tan, M.; Lee, Y.; Oh, J.; Hong, L. Z.; Wnek, R.; Yap, Y. S.; Shih, S. J.; S Bhagat, A. A.; Chin, C. L.; Skibinski, D. A. A Preliminary Study for the Assessment of PD-L1 and PD-L2 on Circulating Tumor Cells by Microfluidic-Based Chipcytometry. *Future Science OA* **2017**, *3* (4). <https://doi.org/10.4155/fsoa-2017-0079>.
- (113) Hümmert, M. W.; Alvermann, S.; Gingele, S.; Gross, C. C.; Wiendl, H.; Mirenska, A.; Hennig, C.; Stangel, M. Immunophenotyping of Cerebrospinal Fluid Cells by Chipcytometry. *Journal of Neuroinflammation* **2018**, *15* (1), 1–11. <https://doi.org/10.1186/s12974-018-1176-7>.
- (114) Consentius, C.; Mirenska, A.; Jurisch, A.; Reinke, S.; Scharm, M.; Zenclussen, A. C.; Hennig, C.; Volk, H. D. In Situ Detection of CD73+ CD90+ CD105+ Lineage: Mesenchymal Stromal Cells in Human Placenta and Bone Marrow Specimens by Chipcytometry. *Cytometry Part A* **2018**, *93* (9), 889–893. <https://doi.org/10.1002/cyto.a.23509>.
- (115) Leng, T.; Akther, H. D.; Hackstein, C. P.; Powell, K.; King, T.; Friedrich, M.; Christoforidou, Z.; McCuaig, S.; Neyazi, M.; Arancibia-Cárcamo, C. v.; Hagel, J.; Powrie, F.; Peres, R. S.; Millar, V.; Ebner, D.; Lamichhane, R.; Ussher, J.; Hinks, T. S. C.; Marchi, E.; Willberg, C.; Klenerman, P. TCR and Inflammatory Signals Tune Human MAIT Cells to Exert Specific Tissue Repair and Effector Functions. *Cell Reports* **2019**, *28* (12), 3077–3091.e5. <https://doi.org/10.1016/j.celrep.2019.08.050>.
- (116) Happle, C.; Lachmann, N.; Škuljec, J.; Wetzke, M.; Ackermann, M.; Brenning, S.; Mucci, A.; Jirmo, A. C.; Groos, S.; Mirenska, A.; Hennig, C.; Rodt, T.; Bankstahl, J. P.; Schwerk, N.; Moritz, T.; Hansen, G. *Pulmonary Transplantation of Macrophage Progenitors as Effective and Long-Lasting Therapy for Hereditary Pulmonary Alveolar Proteinosis*.
- (117) Mulazzani, M.; Fräßle, S. P.; von Mücke-Heim, I.; Langer, S.; Zhou, X.; Ishikawa-Ankerhold, H.; Leube, J.; Zhang, W.; Dötsch, S.; Svec, M.; Rudelius, M.; Dreyling, M.; von Bergwelt-Baildon, M.; Straube, A.; Buchholz, V. R.; Busch, D. H.; von Baumgarten, L. Long-Term in Vivo Microscopy of CAR T Cell Dynamics during Eradication of CNS Lymphoma in Mice. <https://doi.org/10.1073/pnas.1903854116>.
- (118) Weenink, B.; French, P. J.; Sillevs Smitt, P. A. E.; Debets, R.; Geurts, M. Cancers Immunotherapy in Glioblastoma: Current Shortcomings and Future Perspectives. <https://doi.org/10.3390/cancers12030751>.
- (119) David, J. M.; Dominguez, C.; Mccampbell, K. K.; Gulley, J. L.; Schlom, J.; Palena, C. A Novel Bifunctional Anti-PD-L1/TGF- $\beta$  Trap Fusion Protein (M7824) Efficiently Reverts Mesenchymalization of Human Lung Cancer Cells. **2017**. <https://doi.org/10.1080/2162402X.2017.1349589>.
- (120) Ravi, R.; Noonan, K. A.; Pham, V.; Bedi, R.; Zhavoronkov, A.; Ozerov, I. v.; Makarev, E.; Artemov, A. v.; Wysocki, P. T.; Mehra, R.; Nimmagadda, S.; Marchionni, L.; Sidransky, D.; Borrello, I. M.; Izumchenko, E.; Bedi, A. Bifunctional Immune Checkpoint-Targeted Antibody-Ligand Traps That Simultaneously Disable TGF $\beta$  Enhance the Efficacy of Cancer Immunotherapy. <https://doi.org/10.1038/s41467-017-02696-6>.
- (121) Tzavlaki, K.; Moustakas, A. TGF- $\beta$  Signaling. *Biomolecules* **2020**, *10* (487). <https://doi.org/10.3390/biom10030487>.
- (122) Zhang, C.; Zhang, X.; Xu, R.; Huang, B.; Chen, A.-J.; Li, C.; Wang, J.; Li, X.-G. TGF-B2 Initiates Autophagy via Smad and Non-Smad Pathway to Promote Glioma Cells' Invasion. <https://doi.org/10.1186/s13046-017-0628-8>.
- (123) Tu, Y.; Han, J.; Dong, Q.; Chai, R.; Li, N.; Lu, Q.; Xiao, Z.; Guo, Y.; Wan, Z.; Xu, Q. TGF-B2 Is a Prognostic Biomarker Correlated with Immune Cell Infiltration in Colorectal Cancer. **2020**. <https://doi.org/10.1097/MD.00000000000023024>.
- (124) Takahashi, H.; R Alves, C. R.; Stanford, K. I.; W Middelbeek, R. J.; Nigro, P.; Ryan, R. E.; Xue, R.; Sakaguchi, M.; Lynes, M. D.; So, K.; Mul, J. D.; Lee, M.-Y.; Balan, E.; Pan, H.; Dreyfuss, J. M.; Hirshman, M. F.; Azhar, M.; Hannukainen, J. C.; Nuutila, P.; Kalliokoski, K. K.; Nielsen, S.; Pedersen, B. K.; Ronald Kahn, C.; Tseng, Y.-H.; Goodyear, L. J. TGF-B2 Is an Exercise-Induced Adipokine That Regulates Glucose and Fatty Acid Metabolism. *Nature Metabolism*. <https://doi.org/10.1038/s42255-018-0030-7>.
- (125) Bandyopadhyay, B.; Fan, J.; Guan, S.; Li, Y.; Chen, M.; Woodley, D. T.; Li, W. A “Traffic Control” Role for TGF $\beta$ 3: Orchestrating Dermal and Epidermal Cell Motility during Wound Healing. *The Journal of Cell Biology* **2006**, *172* (7), 1093–1105. <https://doi.org/10.1083/jcb.200507111>.
- (126) Liénart, S.; Merceron, R.; Vanderaa, C.; Lambert, F.; Colau, D.; Stockis, J.; van der Woning, B.; de Haard, H.; Saunders, M.; Coulie, P. G.; Savvides, S. N.; Lucas, S. Structural Basis of Latent TGF-B1 Presentation and Activation by GARP on Human Regulatory T Cells. *Science* **2018**, *362*, 952–956.
- (127) Fridrich, S.; Hahn, S. A.; Linzmaier, M.; Felten, M.; Zwarg, J.; Lennerz, V.; Tuettenberg, A.; Stöcker, W. How Soluble GARP Enhances TGF  $\beta$  Activation. *PLoS ONE* **2016**, *11* (4). <https://doi.org/10.1371/journal.pone.0153290>.
- (128) Hahn, S. A.; Stahl, H. F.; Becker, C.; Correll, A.; Schneider, F. J.; Tuettenberg, A.; Jonuleit, H. Soluble GARP Has Potent Antiinflammatory and Immunomodulatory Impact on Human CD4+ T Cells. *Blood* **2013**, *122* (7), 1182–1191. <https://doi.org/10.1182/blood-2012-12-474478>.
- (129) Carrillo-Gálvez, A. B.; Quintero, J. E.; Rodríguez, R.; Menéndez, S. T.; Victoria González, M.; Blanco-Lorenzo, V.; Allonca, E.; de Araújo Farias, V.; González-Correa, J. E.; Erill-Sagalés, N.; Martínez-Zubiaurre, I.; Hellevik, T.; Sánchez-Hernández, S.; Muñoz, P.; Zurita, F.; Martín, F.; Rodríguez-Manzaneque, J. C.; Anderson, P. GARP Promotes the Proliferation and Therapeutic Resistance of Bone Sarcoma Cancer Cells through the Activation of TGF- $\beta$ . *Cell Death & Disease* **2020**, *11* (11), 985. <https://doi.org/10.1038/s41419-020-03197-z>.
- (130) Zhang, X.; Guo, M.; Yang, J.; Zheng, Y.; Xiao, Y.; Liu, W.; Ren, F. Increased Expression of GARP in Papillary Thyroid Carcinoma. **2022**. <https://doi.org/10.1007/s12022-018-9557-0>.
- (131) Salem, M.; Wallace, C.; Velegriaki, M.; Li, A.; Ansa-Addo, E.; Metelli, A.; Kwon, H.; Riesenberger, B.; Wu, B.; Zhang, Y.; Guglietta, S.; Sun, S.; Liu, B.; Li, Z. Tumor Biology and Immunology GARP Dampens Cancer Immunity by



## Literature

- Sustaining Function and Accumulation of Regulatory T Cells in the Colon. **2019**. <https://doi.org/10.1158/0008-5472.CAN-18-2623>.
- (132) Metelli, A.; Salem, M.; Wallace, C. H.; Wu, B. X.; Li, A.; Li, X.; Li, Z. Immunoregulatory Functions and the Therapeutic Implications of GARP-TGF- $\beta$  in Inflammation and Cancer. *Journal of Hematology & Oncology* **2018**, *11* (24). <https://doi.org/10.1186/s13045-018-0570-z>.
- (133) Hahn, S. A.; Neuhoff, A.; Landsberg, J.; Schupp, J.; Eberts, D.; Leukel, P.; Bros, M.; Weilbaecher, M.; Schuppan, D.; Grabbe, S.; Tueting, T.; Lennerz, V.; Sommer, C.; Jonuleit, H.; Tuettenberg, A. A Key Role of GARP in the Immune Suppressive Tumor Microenvironment. *Oncotarget* **2016**, *7* (28). <https://doi.org/10.18632/oncotarget.9598>.
- (134) Seoane, J.; Gomis, R. R. TGF- $\beta$  Family Signaling in Tumor Suppression and Cancer Progression. *Cold Spring Harbor Perspectives in Biology*. Cold Spring Harbor Laboratory Press December 1, 2017. <https://doi.org/10.1101/cshperspect.a022277>.
- (135) de Streel, G.; Bertrand, C.; Chalon, N.; Liénart, S.; Bricard, O.; Lecomte, S.; Devreux, J.; Gaignage, M.; de Boeck, G.; Mariën, L.; van de Walle, I.; van der Woning, B.; Saunders, M.; de Haard, H.; Vermeersch, E.; Maes, W.; Deckmyn, H.; Coulie, P. G.; van Baren, N.; Lucas, S. Selective Inhibition of TGF-B1 Produced by GARP-Expressing Tregs Overcomes Resistance to PD-1/PD-L1 Blockade in Cancer. <https://doi.org/10.1038/s41467-020-17811-3>.
- (136) Metelli, A.; Wu, B. X.; Riesenberger, B.; Guglietta, S.; Huck, J. D.; Mills, C.; Li, A.; Rachidi, S.; Krieg, C.; Rubinstein, M. P.; Gewirth, D. T.; Sun, S.; Lilly, M. B.; Wahlquist, A. H.; Carbone, D. P.; Yang, Y.; Liu, B.; Li, Z. *Thrombin Contributes to Cancer Immune Evasion via Proteolysis of Platelet-Bound GARP to Activate LTGF- $\beta$* ; 2020; Vol. 12.
- (137) de Streel, G.; Bertrand, C.; Chalon, N.; Liénart, S.; Bricard, O.; Lecomte, S.; Devreux, J.; Gaignage, M.; de Boeck, G.; Mariën, L.; van de Walle, I.; van der Woning, B.; Saunders, M.; de Haard, H.; Vermeersch, E.; Maes, W.; Deckmyn, H.; Coulie, P. G.; van Baren, N.; Lucas, S. Selective Inhibition of TGF-B1 Produced by GARP-Expressing Tregs Overcomes Resistance to PD-1/PD-L1 Blockade in Cancer. *Nature Communications* **2020**, *11* (1). <https://doi.org/10.1038/s41467-020-17811-3>.
- (138) Campbell, M. G.; Cormier, A.; Ito, S.; Seed, R. I.; Bondesson, A. J.; Lou, J.; Marks, J. D.; Baron, J. L.; Cheng, Y.; Nishimura, S. L. Cryo-EM Reveals Integrin-Mediated TGF- $\beta$  Activation without Release from Latent TGF- $\beta$ . *Cell* **2020**, *180* (3), 490-501.e16. <https://doi.org/10.1016/j.cell.2019.12.030>.
- (139) Coulie, P. G.; Lucas, S.; Dedobbeleer, O.; Stockis, J.; van der Woning, B. Of IgA Class-Switch Recombination and Production Stimulated Human B Lymphocytes Increases 1 Complexes on the Surface of  $\beta$  GARP/TGF-1 Released from  $\beta$  Cutting Edge: Active TGF. **2021**. <https://doi.org/10.4049/jimmunol.1601882>.
- (140) Wallace, C. H.; Wu, B. X.; Salem, M.; Ansa-Addo, E. A.; Metelli, A.; Sun, S.; Gilkeson, G.; Shlomchik, M. J.; Liu, B.; Li, Z. B Lymphocytes Confer Immune Tolerance via Cell Surface GARP-TGF- $\beta$  Complex. *JCI Insight* **2018**, *3* (7). <https://doi.org/10.1172/jci.insight.99863>.
- (141) Kubach, J.; Hubo, M.; Amendt, C.; Stroh, C.; Jonuleit, H. IgG1 Anti-Epidermal Growth Factor Receptor Antibodies Induce CD8-Dependent Antitumor Activity. *International Journal of Cancer* **2015**, *136* (4), 821-830. <https://doi.org/10.1002/ijc.29037>.
- (142) Ugurel, S.; Thirumaran, R. K.; Bloethner, S.; Gast, A.; Sucker, A.; Mueller-Berghaus, J.; Rittgen, W.; Hemminki, K.; Becker, J. C.; Kumar, R.; Schadendorf, D. B-RAF and N-RAS Mutations Are Preserved during Short Time in Vitro Propagation and Differentially Impact Prognosis. *PLoS ONE* **2007**, *2* (2). <https://doi.org/10.1371/journal.pone.0000236>.
- (143) Dahl, C.; Christensen, C.; Göran, J.; Lorentzen, A.; Skjødt, M. L.; Borg, Å.; Pawelec, G.; Guldborg, P. Mutual Exclusivity Analysis of Genetic and Epigenetic Drivers in Melanoma Identifies a Link Between P14ARF and RAR $\beta$  Signaling. **2013**. <https://doi.org/10.1158/1541-7786.MCR-13-0006>.
- (144) Kotecha, N.; Krutzik, P. O.; Irish, J. M. Web-Based Analysis and Publication of Flow Cytometry Experiments. *Current Protocols in Cytometry* **2010**, *53* (1), 10.17.1-10.17.24. <https://doi.org/10.1002/0471142956.cy1017s53>.
- (145) Schindelin, J.; Arganda-Carreras, I.; Frise, E.; Kaynig, V.; Longair, M.; Pietzsch, T.; Preibisch, S.; Rueden, C.; Saalfeld, S.; Schmid, B.; Tinevez, J. Y.; White, D. J.; Hartenstein, V.; Eliceiri, K.; Tomancak, P.; Cardona, A. Fiji: An Open-Source Platform for Biological-Image Analysis. *Nat Methods* **2012**, *9* (7), 676-682. <https://doi.org/10.1038/nmeth.2019>.
- (146) Gleue, L.; Schupp, J.; Zimmer, N.; Becker, E.; Frey, H.; Tuettenberg, A.; Helm, M. Stability of Alkyl Chain-Mediated Lipid Anchoring in Liposomal Membranes. *Cells* **2020**, *9* (10), 2213. <https://doi.org/10.3390/cells9102213>.
- (147) Bankhead, P.; Loughrey, M. B.; Fernández, J. A.; Dombrowski, Y.; McArt, D. G.; Dunne, P. D.; McQuaid, S.; Gray, R. T.; Murray, L. J.; Coleman, H. G.; James, J. A.; Salto-Tellez, M.; Hamilton, P. W. QuPath: Open Source Software for Digital Pathology Image Analysis. *Scientific Reports* **2017**, *7* (1), 1-7. <https://doi.org/10.1038/s41598-017-17204-5>.
- (148) Hamilton, T. A.; Zhao, C.; Pavicic Jr, P. G.; Datta, S.; Adam Harris, R.; Institutet, K.; Cordula Stover, S. M. Myeloid Colony-Stimulating Factors as Regulators of Macrophage Polarization. **2014**. <https://doi.org/10.3389/fimmu.2014.00554>.
- (149) Ushach, I.; Zlotnik, A. Biological Role of Granulocyte Macrophage Colony-Stimulating Factor (GM-CSF) and Macrophage Colony-Stimulating Factor (M-CSF) on Cells of the Myeloid Lineage. <https://doi.org/10.1189/jlb.3RU0316-144R>.

## Literature

- (150) Chanput, W.; Peters, V.; Wichers, H. THP-1 and U937 Cells. [https://doi.org/10.1007/978-3-319-16104-4\\_14](https://doi.org/10.1007/978-3-319-16104-4_14).
- (151) Liu, Y.; Beyer, A.; Aebersold, R. On the Dependency of Cellular Protein Levels on mRNA Abundance. *Cell*. Cell Press April 21, 2016, pp 535–550. <https://doi.org/10.1016/j.cell.2016.03.014>.
- (152) Larionova, I.; Tuguzbaeva, G.; Ponomaryova, A.; Stakheyeva, M.; Cherdyntseva, N.; Pavlov, V.; Choinzonov, E.; Kzhyskowska, J.; Karagiannis, G. S.; Etzerodt, A.; Jalkanen, S. Tumor-Associated Macrophages in Human Breast, Colorectal, Lung, Ovarian and Prostate Cancers. *Article* **2020**, *10*, 1. <https://doi.org/10.3389/fonc.2020.566511>.
- (153) Jaynes, J. M.; Sable, R.; Ronzetti, M.; Bautista, W.; Knotts, Z.; Abisoye-Ogunniyan, A.; Li, D.; Calvo, R.; Dashnyam, M.; Singh, A.; Guerin, T.; White, J.; Ravichandran, S.; Kumar, P.; Talsania, K.; Chen, V.; Ghebremedhin, A.; Karanam, B.; bin Salam, A.; Amin, R.; Odzorig, T.; Aiken, T.; Nguyen, V.; Bian, Y.; Zarif, J. C.; de Groot, A. E.; Mehta, M.; Fan, L.; Hu, X.; Simeonov, A.; Pate, N.; Abu-Asab, M.; Ferrer, M.; Southall, N.; Ock, C.-Y.; Zhao, Y.; Lopez, H.; Kozlov, S.; de Val, N.; Yates, C. C.; Baljinnyam, B.; Marugan, J.; Rudloff, U. *Mannose Receptor (CD206) Activation in Tumor-Associated Macrophages Enhances Adaptive and Innate Antitumor Immune Responses*; 2020; Vol. 12.
- (154) Sanyal, R.; Polyak, M. J.; Zuccolo, J.; Puri, M.; Deng, L.; Roberts, L.; Zuba, A.; Storek, J.; Luider, J. M.; Sundberg, E. M.; Mansoor, A.; Baigorri, E.; Chu, M. P.; Belch, A. R.; Pilarski, L. M.; Deans, J. P. MS4A4A: A Novel Cell Surface Marker for M2 Macrophages and Plasma Cells. *Immunology & Cell Biology* **2017**, *95* (7), 611–619. <https://doi.org/10.1038/icb.2017.18>.
- (155) Kuek, L. E.; Leffler, M.; Mackay, G. A.; Hulet, M. D. The MS4A Family: Counting Past 1, 2 and 3. *Immunology and Cell Biology*. Nature Publishing Group January 1, 2016, pp 11–23. <https://doi.org/10.1038/icb.2015.48>.
- (156) Mattioli, I.; Tomay, F.; de Pizzol, M.; Silva-Gomes, R.; Savino, B.; Gulic, T.; Doni, A.; Lonardi, S.; Astrid Boutet, M.; Nerviani, A.; Carriero, R.; Molgora, M.; Stravalaci, M.; Morone, D.; Shalova, I. N.; Lee, Y.; Biswas, S. K.; Mantovani, G.; Sironi, M.; Pitzalis, C.; Vermi, W.; Bottazzi, B.; Mantovani, A.; Locati, M. The Macrophage Tetraspan MS4A4A Enhances Dectin-1-Dependent NK Cell-Mediated Resistance to Metastasis. *Nature Immunology* **2019**, *20* (8), 1012–1022. <https://doi.org/10.1038/s41590-019-0417-y>.
- (157) Wang, J.; Li, Y. CD36 Tango in Cancer: Signaling Pathways and Functions. *Theranostics* **2019**, *9*, 17. <https://doi.org/10.7150/thno.36037>.
- (158) Pfeiler, S.; Thakur, M.; Grünauer, P.; Megens, R. T. A.; Joshi, U.; Coletti, R.; Samara, V.; Müller-Stoy, G.; Ishikawa-Ankerhold, H.; Stark, K.; Klingl, A.; Fröhlich, T.; Arnold, G. J.; Wörmann, S.; Bruns, C. J.; Algül, H.; Weber, C.; Massberg, S.; Engelmann, B. CD36-Triggered Cell Invasion and Persistent Tissue Colonization by Tumor Microvesicles during Metastasis. *FASEB Journal* **2019**, *33* (2), 1860–1872. <https://doi.org/10.1096/fj.201800985R>.
- (159) Su, P.; Wang, Q.; Bi, E.; Ma, X.; Liu, L.; Yang, M.; Qian, J.; Yi, Q. Enhanced Lipid Accumulation and Metabolism Are Required for the Differentiation and Activation of Tumor-Associated Macrophages. **2020**. <https://doi.org/10.1158/0008-5472.CAN-19-2994>.
- (160) Miura, T.; Yoshizawa, T.; Hirai, H.; Seino, H.; Morohashi, S.; Wu, Y.; Wakiya, T.; Kimura, N.; Kudo, D.; Ishido, K.; Toyoki, Y.; Kijima, H.; Hakamada, K. Prognostic Impact of CD163+ Macrophages in Tumor Stroma and CD8+ T-Cells in Cancer Cell Nests in Invasive Extrahepatic Bile Duct Cancer. *Anticancer Res* **2017**, *37* (1), 183–190. <https://doi.org/10.21873/anticancer.11304>.
- (161) Jamiyan, T.; Kuroda, H.; Yamaguchi, R.; Abe, A.; Hayashi, M. CD68- and CD163-Positive Tumor-Associated Macrophages in Triple Negative Cancer of the Breast. *Virchows Arch* **2020**, *477*, 767–775. <https://doi.org/10.1007/s00428-020-02855-z/Published>.
- (162) Guo, F.; Feng, Y.; Zhao, G.; Zhang, R.; Cheng, Z.; Kong, W.; Wu, H.; Xu, B.; Lv, X.; Ma, X. Tumor-Associated CD163+ M2 Macrophage Infiltration Is Highly Associated with PD-L1 Expression in Cervical Cancer. *Cancer Management and Research* **2020**, *Volume 12*, 5831–5843. <https://doi.org/10.2147/CMAR.S257692>.
- (163) Huang, Y.-K.; Wang, M.; Sun, Y.; di Costanzo, N.; Mitchell, C.; Achuthan, A.; Hamilton, J. A.; Busuttill, R. A.; Boussioutas, A. Macrophage Spatial Heterogeneity in Gastric Cancer Defined by Multiplex Immunohistochemistry. *Nature Communications* **2019**, *10* (1), 3928. <https://doi.org/10.1038/s41467-019-11788-4>.
- (164) Shiraishi, D.; Fujiwara, Y.; Horlad, H.; Saito, Y.; Iriki, T.; Tsuboki, J.; Cheng, P.; Nakagata, N.; Mizuta, H.; Bekki, H.; Nakashima, Y.; Oda, Y.; Takeya, M.; Komohara, Y. CD163 Is Required for Protumoral Activation of Macrophages in Human and Murine Sarcoma. *Cancer Research* **2018**, *78* (12), 3255–3266. <https://doi.org/10.1158/0008-5472.CAN-17-2011>.
- (165) Nielsen, M. C.; Hvidbjerg Gantzel, R.; Clària, J.; Trebicka, J.; Møller, H. J.; Grønbaek, H. Macrophage Activation Markers, CD163 and CD206, in Acute-on-Chronic Liver Failure. *Cells* **2020**, *9* (5), 1175. <https://doi.org/10.3390/cells9051175>.
- (166) Roslind, A.; Johansen, J. S. Chapter 7 YKL-40: A Novel Marker Shared by Chronic Inflammation and Oncogenic Transformation. In *Inflammation and Cancer, Methods in Molecular Biology*; 2009; Vol. 511, pp 159–184. [https://doi.org/10.1007/978-1-59745-447-6\\_7](https://doi.org/10.1007/978-1-59745-447-6_7).
- (167) Bian, B.; Li, L.; Yang, J.; Liu, Y.; Xie, G.; Zheng, Y.; Zeng, L.; Zeng, J.; Shen, L. Prognostic Value of YKL-40 in Solid Tumors: A Meta-Analysis of 41 Cohort Studies. *Cancer Cell International* **2019**, *19* (1), 259. <https://doi.org/10.1186/s12935-019-0983-y>.
- (168) Gudmundsdottir, S.; Lieder, R.; Sigurjonsson, O. E.; Petersen, P. H. Chitosan Leads to Downregulation of YKL-40 and Inflammasome Activation in Human Macrophages. *Journal of Biomedical Materials Research - Part A* **2015**, *103* (8), 2778–2785. <https://doi.org/10.1002/jbm.a.35417>.

## Literature

- (169) Tang, K.; Wu, Y.-H.; Song, Y.; Yu, B. Indoleamine 2,3-Dioxygenase 1 (IDO1) Inhibitors in Clinical Trials for Cancer Immunotherapy. *J Hematol Oncol* **2020**, *14*, 68. <https://doi.org/10.1186/s13045-021-01080-8>.
- (170) Schramme, F.; Crosignani, S.; Frederix, K.; Hoffmann, D.; Pilotte, L.; Stroobant, V.; Preillon, J.; Driessens, G.; van den Eynde, B. J. Inhibition of Tryptophan-Dioxygenase Activity Increases the Antitumor Efficacy of Immune Checkpoint Inhibitors. **2020**. <https://doi.org/10.1158/2326-6066.CIR-19-0041>.
- (171) Li, P.; Xu, W.; Liu, F.; Zhu, H.; Zhang, L.; Ding, Z.; Liang, H.; Song, J. The Emerging Roles of IDO2 in Cancer and Its Potential as a Therapeutic Target. *Biomedicine & Pharmacotherapy* **2021**, *137*, 111295. <https://doi.org/10.1016/j.biopha.2021.111295>.
- (172) Long, G. v.; Dummer, R.; Hamid, O.; Gajewski, T. F.; Caglevic, C.; Dalle, S.; Arance, A.; Carlino, M. S.; Grob, J.-J.; Kim, T. M.; Demidov, L.; Robert, C.; Larkin, J.; Anderson, J. R.; Maleski, J.; Jones, M.; Diede, S. J.; Mitchell, T. C. Epcadostat plus Pembrolizumab versus Placebo plus Pembrolizumab in Patients with Unresectable or Metastatic Melanoma (ECHO-301/KEYNOTE-252): A Phase 3, Randomised, Double-Blind Study. *The Lancet Oncology* **2019**, *20* (8). [https://doi.org/10.1016/S1470-2045\(19\)30274-8](https://doi.org/10.1016/S1470-2045(19)30274-8).
- (173) Moore, G. E. Culture of Normal Human Leukocytes. *JAMA: The Journal of the American Medical Association* **1967**, *199* (8), 519. <https://doi.org/10.1001/jama.1967.03120080053007>.
- (174) Geisler, S.; Mayersbach, P.; Becker, K.; Schennach, H.; Fuchs, D.; Gostner, J. M. Serum Tryptophan, Kynurenine, Phenylalanine, Tyrosine and Neopterin Concentrations in 100 Healthy Blood Donors. *Pteridines* **2015**, *26* (1), 31–36. <https://doi.org/10.1515/pterid-2014-0015>.
- (175) Han, H. Chapter 16 RNA Interference to Knock Down Gene Expression. [https://doi.org/10.1007/978-1-4939-7471-9\\_16](https://doi.org/10.1007/978-1-4939-7471-9_16).
- (176) Zins, K.; Abraham, D. Chapter 17 Cancer Immunotherapy: Targeting Tumor-Associated Macrophages by Gene Silencing. [https://doi.org/10.1007/978-1-0716-0290-4\\_17](https://doi.org/10.1007/978-1-0716-0290-4_17).
- (177) de Paoli, F.; Eeckhoutte, J.; Copin, C.; Vanhoutte, J.; Duhem, C.; Derudas, B.; Dubois-Chevalier, J.; Colin, S.; Zawadzki, C.; Jude, B.; Haulon, S.; Lefebvre, P.; Staels, B.; Chinetti-Gbaguidi, G. The Neuron-Derived Orphan Receptor 1 (NOR1) Is Induced upon Human Alternative Macrophage Polarization and Stimulates the Expression of Markers of the M2 Phenotype. *Atherosclerosis* **2015**, *241* (1), 18–26. <https://doi.org/10.1016/j.atherosclerosis.2015.04.798>.
- (178) Rahal, O. M.; Wolfe, A. R.; Mandal, P. K.; Larson, R.; Tin, S.; Jimenez, C.; Zhang, D.; Horton, J.; Reuben, J. M.; McMurray, J. S.; Woodward, W. A. Blocking Interleukin (IL)4- and IL13-Mediated Phosphorylation of STAT6 (Tyr641) Decreases M2 Polarization of Macrophages and Protects Against Macrophage-Mediated Radioresistance of Inflammatory Breast Cancer. *International Journal of Radiation Oncology Biology Physics* **2018**, *100* (4), 1034–1043. <https://doi.org/10.1016/j.ijrobp.2017.11.043>.
- (179) Kishton, R. J.; Sukumar, M.; Restifo, N. P. Metabolic Regulation of T Cell Longevity and Function in Tumor Immunotherapy. *Cell Metabolism*. Cell Press July 5, 2017, pp 94–109. <https://doi.org/10.1016/j.cmet.2017.06.016>.
- (180) Rothenberg, E. v.; Hosokawa, H.; Ungerback, J. Mechanisms of Action of Hematopoietic Transcription Factor PU.1 in Initiation of T-Cell Development. *Frontiers in Immunology* **2019**, *10* (FEB). <https://doi.org/10.3389/fimmu.2019.00228>.
- (181) Zhou, D.; Ji, L.; Chen, Y. TSP0 Modulates IL-4-Induced Microglia/Macrophage M2 Polarization via PPAR-γ Pathway. *Journal of Molecular Neuroscience* **2020**, *70* (4), 542–549. <https://doi.org/10.1007/s12031-019-01454-1>.
- (182) Leopold Wager, C. M.; Arnett, E.; Schlesinger, L. S. Mycobacterium Tuberculosis and Macrophage Nuclear Receptors: What We Do and Don't Know. *Tuberculosis* **2019**, *116*, S98–S106. <https://doi.org/10.1016/j.tube.2019.04.016>.
- (183) Gionfriddo, G.; Plastina, P.; Augimeri, G.; Catalano, S.; Giordano, C.; Barone, I.; Morelli, C.; Giordano, F.; Gelsomino, L.; Sisci, D.; Witkamp, R.; Andò, S.; van Norren, K.; Bonofiglio, D. Modulating Tumor-Associated Macrophage Polarization by Synthetic and Natural PPARγ Ligands as a Potential Target in Breast Cancer. *Cells* **2020**, *9* (1). <https://doi.org/10.3390/cells9010174>.
- (184) Portugal, J.; Waring, M. J. *Assignment of DNA Binding Sites for 4',6-Diamidine-2-Phenylindole and Bisbenzimidazole (Hoechst 33258). A Comparative Footprinting Study*; 1988; Vol. 949.
- (185) Mohan, P.; Rapoport, N. Doxorubicin as a Molecular Nanotheranostic Agent: Effect of Doxorubicin Encapsulation in Micelles or Nanoemulsions on the Ultrasound-Mediated Intracellular Delivery and Nuclear Trafficking. *Molecular Pharmaceutics* **2010**, *7* (6), 1959–1973. <https://doi.org/10.1021/mp100269f>.
- (186) Takikawa, M.; Fujisawa, M.; Yoshino, K.; Takeoka, S. Intracellular Distribution of Lipids and Encapsulated Model Drugs from Cationic Liposomes with Different Uptake Pathways. *International Journal of Nanomedicine* **2020**, *15*, 8401–8409. <https://doi.org/10.2147/IJN.S267638>.
- (187) Voigt, M. LIPOSOMES FOR DRUG DELIVERY, Mainz, 2019.
- (188) Anosov, A. A.; Smirnova, E. Y.; Sharakshane, A. A.; Nikolayeva, E. A.; Zhdankina, Y. S. Increase in the Current Variance in Bilayer Lipid Membranes near Phase Transition as a Result of the Occurrence of Hydrophobic Defects. *Biochimica et Biophysica Acta - Biomembranes* **2020**, *1862* (2). <https://doi.org/10.1016/j.bbamem.2019.183147>.
- (189) Hennig, R.; Heidrich, J.; Saur, M.; Schmäser, L.; Roeters, S. J.; Hellmann, N.; Woutersen, S.; Bonn, M.; Weidner, T.; Markl, J.; Schneider, D. IM30 Triggers Membrane Fusion in Cyanobacteria and Chloroplasts. *Nature Communications* **2015**, *6* (1), 7018. <https://doi.org/10.1038/ncomms8018>.

## Literature

- (190) Wasif Baig, M.; Pederzoli, M.; Jurkiewicz, P.; Cwiklik, L.; Pittner, J. Orientation of Laurdan in Phospholipid Bilayers Influences Its Fluorescence: Quantum Mechanics and Classical Molecular Dynamics Study. *Molecules* **2018**, *23* (7), 1707. <https://doi.org/10.3390/molecules23071707>.
- (191) Haller, A. Modulation of Pharmacokinetics of Nanodimensional Drug Carriers, Mainz, 2021.
- (192) D'souza, A. A.; Shegokar, R. Polyethylene Glycol (PEG): A Versatile Polymer for Pharmaceutical Applications. *Expert Opinion on Drug Delivery* **2016**, *13* (9), 1257–1275. <https://doi.org/10.1080/17425247.2016.1182485>.
- (193) Bros, M.; Nuhn, L.; Simon, J.; Moll, L.; Mailänder, V.; Landfester, K.; Grabbe, S. The Protein Corona as a Confounding Variable of Nanoparticle-Mediated Targeted Vaccine Delivery. *Frontiers in Immunology* **2018**, *9* (1760), 1760. <https://doi.org/10.3389/fimmu.2018.01760>.
- (194) Alessi, M. L.; Norman, A. I.; Knowlton, S. E.; Ho, D. L.; Greer, S. C. Helical and Coil Conformations of Poly(Ethylene Glycol) in Isobutyric Acid and Water. *Macromolecules* **2005**, *38* (22), 9333–9340. <https://doi.org/10.1021/ma051339e>.
- (195) Pang, C.; Song, C.; Li, Y.; Wang, Q.; Zhu, X.; Wu, J.; Tian, Y.; Fan, H.; Hu, J.; Li, C.; Wang, B.; Li, X.; Liu, W.; Fan, L. The Establishment and Application Studies on Precise Lysosome PH Indicator Based on Self-Decomposable Nanoparticles. <https://doi.org/10.1186/s11671-020-03367-0>.
- (196) Tantama, M.; Hung, Y. P.; Yellen, G. Imaging Intracellular PH in Live Cells with a Genetically Encoded Red Fluorescent Protein Sensor. *J. Am. Chem. Soc* **2011**, *133*. <https://doi.org/10.1021/ja202902d>.
- (197) Worm, M. PH-Cleavable and Hyperbranched Polyether Architectures: From Novel Synthesis Strategies to Applications in Nanotechnology and Biomedicine, Mainz, 2016.
- (198) Fritz, T. Multifunctional Liposomes: Microscale Formulation, Modification and in Vitro Interaction, Mainz, 2016.
- (199) Danner, A.-K. Multifunctional Amphiphilic Polyethers: From Polyether Lipids to Tapered Structures, Mainz, 2018.
- (200) Yang, Y.; Lee, M.; Fairn, G. D. Phospholipid Subcellular Localization and Dynamics. *Journal of Biological Chemistry* **2018**, *293* (17), 6230–6240. <https://doi.org/10.1074/jbc.R117.000582>.
- (201) Fritz, T.; Voigt, M.; Worm, M.; Negwer, I.; Müller, S. S.; Kettenbach, K.; Ross, T. L.; Roesch, F.; Koynov, K.; Frey, H.; Helm, M. Orthogonal Click Conjugation to the Liposomal Surface Reveals the Stability of the Lipid Anchorage as Crucial for Targeting. *Chemistry - A European Journal* **2016**, *22* (33), 11578–11582. <https://doi.org/10.1002/chem.201602758>.
- (202) Casares, D.; Escribá, P. v.; Rosselló, C. A. Membrane Lipid Composition: Effect on Membrane and Organelle Structure, Function and Compartmentalization and Therapeutic Avenues. *International Journal of Molecular Sciences* **2019**, *20* (9), 2167. <https://doi.org/10.3390/ijms20092167>.
- (203) Le, Q.; Nguyen, V.; Park, S. Recent Advances in the Engineering and Application of Streptavidin-like Molecules. <https://doi.org/10.1007/s00253-019-10036-5>.
- (204) Giavazzi Raffaella and Decio, A. Syngeneic Murine Metastasis Models: B16 Melanoma. In *Metastasis Research Protocols*; Dwek Miriam and Schumacher, U. and B. S. A., Ed.; Springer New York: New York, NY, 2014; pp 131–140. [https://doi.org/10.1007/978-1-4614-8244-4\\_10](https://doi.org/10.1007/978-1-4614-8244-4_10).
- (205) Sikora, M.; Rudnicka, L.; Borkowska, B.; Kardynal, A.; Słowińska, M.; Rakowska, A.; Warszawik-Hendzel, O.; Wiergowska, A.; Ługowska, I.; Rutkowski, P.; Debniak, T.; Lubiński, J.; Olszewska, M. Genetic Polymorphisms May Influence the Vertical Growth Rate of Melanoma. *Journal of Cancer* **2018**, *9* (17), 3078–3083. <https://doi.org/10.7150/jca.26404>.
- (206) Tartari, F.; Guglielmo, A.; Fuligni, F.; Pileri, A. Changes in Emergency Service Access after Spread of COVID-19 across Italy. *Journal of the European Academy of Dermatology and Venereology*. Blackwell Publishing Ltd August 1, 2020, pp e350–e351. <https://doi.org/10.1111/jdv.16553>.
- (207) Jarman, E. R.; Perschke, K.; Montermann, E.; Herz, U.; Renz, H.; Knop, J.; Reske-Kunz, A. B. Deficient Cytokine Response of Human Allergen-Specific T Lymphocytes from Humanized SCID Mice and Reconstitution by Professional Antigen- Presenting Cells. *Journal of Allergy and Clinical Immunology* **2000**, *105* (5), 967–974. <https://doi.org/10.1067/mai.2000.105320>.
- (208) Schupp, J.; Christians, A.; Zimmer, N.; Gleue, L.; Jonuleit, H.; Helm, M.; Tuettenberg, A. In-Depth Immune-Oncology Studies of the Tumor Microenvironment in a Humanized Melanoma Mouse Model. *International Journal of Molecular Sciences* **2021**, *22* (3), 1011. <https://doi.org/10.3390/ijms22031011>.
- (209) Huang, F.; Cao, F. L.; Zheng, S. G. Update of Humanized Animal Disease Models in Studying Graft-versus-Host Disease. *Human Vaccines and Immunotherapeutics*. Taylor and Francis Inc. November 2, 2018, pp 2618–2623. <https://doi.org/10.1080/21645515.2018.1512454>.
- (210) Pektor, S.; Schlöder, J.; Klasen, B.; Bausbacher, N.; Wagner, D. C.; Schreckenberger, M.; Grabbe, S.; Jonuleit, H.; Miederer, M. Using Immuno-PET Imaging to Monitor Kinetics of T Cell-Mediated Inflammation and Treatment Efficiency in a Humanized Mouse Model for GvHD. *European Journal of Nuclear Medicine and Molecular Imaging* **2020**, *47* (5), 1314–1325. <https://doi.org/10.1007/s00259-019-04507-0>.
- (211) Gorbunova, A. S.; Yapyrintseva, M. A.; Denisenko, T. v.; Zhivotovsky, B. BNIP3 in Lung Cancer: To Kill or Rescue? *Cancers* **2020**, *12* (11), 3390. <https://doi.org/10.3390/cancers12113390>.
- (212) Elangovan, I. M.; Vaz, M.; Tamatam, C. R.; Potteti, H. R.; Reddy, N. M.; Reddy, S. P. FOSL1 Promotes Kras-Induced Lung Cancer through Amphiregulin and Cell Survival Gene Regulation. *American Journal of Respiratory Cell and Molecular Biology* **2018**, *58* (5), 625–635. <https://doi.org/10.1165/rcmb.2017-0164OC>.

## Literature

- (213) Wang-Bishop, L.; Chen, Z.; Gomaa, A.; Lockhart, A. C.; Salaria, S.; Wang, J.; Lewis, K. B.; Ecsedy, J.; Washington, K.; Beauchamp, R. D.; El-Rifai, W. Inhibition of AURKA Reduces Proliferation and Survival of Gastrointestinal Cancer Cells With Activated KRAS by Preventing Activation of RPS6KB1. *Gastroenterology* **2019**, *156* (3), 662–675.e7. <https://doi.org/10.1053/j.gastro.2018.10.030>.
- (214) Devis-Jauregui, L.; Eritja, N.; Davis, M. L.; Matias-Guiu, X.; Llobet-Navàs, D. Autophagy in the Physiological Endometrium and Cancer. *Autophagy*. Bellwether Publishing, Ltd. 2021, pp 1077–1095. <https://doi.org/10.1080/15548627.2020.1752548>.
- (215) Yao, X.; Hu, W.; Zhang, J.; Huang, C.; Zhao, H.; Yao, X. Application of CAMP-Dependent Catalytic Subunit  $\beta$  (PRKACB) Low Expression in Predicting Worse Overall Survival: A Potential Therapeutic Target for Colorectal Carcinoma. *Journal of Cancer* **2020**, *11* (16), 4841–4850. <https://doi.org/10.7150/jca.46156>.
- (216) Cheng, S.; Castillo, V.; Sliva, D. CDC20 Associated with Cancer Metastasis and Novel mushroom-derived CDC20 Inhibitors with Antimetastatic Activity. *INTERNATIONAL JOURNAL OF ONCOLOGY* **2019**, *54*, 2250–2256. <https://doi.org/10.3892/ijo.2019.4791>.
- (217) Warren, C. F. A.; Wong-Brown, M. W.; Bowden, N. A. BCL-2 Family Isoforms in Apoptosis and Cancer. *Cell Death and Disease* **2019**, *10* (177). <https://doi.org/10.1038/s41419-019-1407-6>.
- (218) Huang, Y.; Yang, • Xijie; Lu, Y.; Zhao, Y.; Meng, R.; Zhang, • Sheng; Dong, • Xiaorong; Xu, S.; Wu, G. UBE2O Targets Mxi1 for Ubiquitination and Degradation to Promote Lung Cancer Progression and Radioresistance. *Cell Death & Differentiation* **2021**, *28*, 671–684. <https://doi.org/10.1038/s41418-020-00616-8>.
- (219) Sullivan, M. R.; Bernstein, K. A. RAD-1cal New Insights into RAD51 Regulation. *Genes* **2018**, *9* (629). <https://doi.org/10.3390/genes9120629>.
- (220) Liu, C.; Fennell, L. J.; Bettington, M. L.; Walker, N. I.; Dwine, J.; Leggett, B. A.; Whitehall, V. L. J. DNA Methylation Changes That Precede Onset of Dysplasia in Advanced Sessile Serrated Adenomas. *Clinical Epigenetics* **2019**, *11* (90). <https://doi.org/10.1186/s13148-019-0691-4>.
- (221) Xu, R.; Ji, J.; Zhang, X.; Han, M.; Zhang, C.; Xu, Y.; Wei, Y.; Wang, S.; Huang, B.; Chen, A.; Zhang, D.; Zhang, Q.; Li, W.; Jiang, Z.; Wang, J.; Li, X. PDGFA/PDGFR $\alpha$ -Regulated GOLM1 Promotes Human Glioma Progression through Activation of AKT. *Journal of Experimental and Clinical Cancer Research* **2017**, *36* (1). <https://doi.org/10.1186/s13046-017-0665-3>.
- (222) Bellanné, C.; Bellanné-Chantelot, B.; Schmaltz-Panneau, B.; Marty, C.; Fenneteau, O.; Callebaut, I.; Clauin, S. ´ E.; Aur´, A.; Docet, A.; Damaj, G.-L.; Leblanc, T.; Pellier, I.; Ecile Stoven, C. ´ ; Souquere, S.; Eana, I.; Debr´debré, A.-D.; Beaupain, B.; Aladjidi, N.; Barlogis, V.; Fr´, F.; Fréd´, F.; Bauduer, F.; Bensaid, P.; Boespflug-Tanguy, O.; Berger, C.; Bertrand, Y.; Carausu, L.; Fieschi, C.; Galambrun, C.; Schmidt, A.; Journal, H.; Vainchenker, W.; Plo, I.; Donadieu, J. Mutations in the SRP54 Gene Cause Severe Congenital neutropenia as Well as Shwachman-Diamond-like Syndrome. *Blood* **2018**, *132* (12), 1318–1331.
- (223) Yang, M.; Sun, L.; Han, J.; Zheng, C.; Liang, H.; Zhu, J.; Jin, T. Biological Characteristics of Transcription Factor RelB in Different Immune Cell Types: Implications for the Treatment of Multiple Sclerosis. *Molecular Brain* **2019**, *12* (115). <https://doi.org/10.1186/s13041-019-0532-6>.
- (224) Zhang, J.; Zhang, Q. VHL and Hypoxia Signaling: Beyond HIF in Cancer. *Biomedicines* **2018**, *6* (35). <https://doi.org/10.3390/biomedicines6010035>.
- (225) Della-Valle, V.; Roos-Weil, D.; Scourzic, L.; Mouly, E.; Aid, Z.; Darwiche, W.; Lecluse, Y.; Damm, F.; Mémet, S.; Mercher, T.; Aoufouchi, S.; Nguyen-Khac, F.; Bernard, O. A.; Ghamlouch, H. Nfkbie-Deficiency Leads to Increased Susceptibility to Develop B-Cell Lymphoproliferative Disorders in Aged Mice. *Blood Cancer Journal* **2020**, *10*, 38. <https://doi.org/10.1038/s41408-020-0305-6>.
- (226) Qu, Y.; Liao, Z.; Wang, X.; Zhang, J.; Liu, C. EFLDO Sensitizes Liver Cancer Cells to TNFSF10-induced Apoptosis in a P53-dependent Manner. *Molecular Medicine Reports* **2019**, *49* (5), 3799–3806. <https://doi.org/10.3892/mmr.2019.10046>.
- (227) Dai, Y.; Hawinkels, L.; Jiao, H.; Zhang, D.; Bi, J.; Liang, Q.; Wang, S.; Zhang, L.; Han, F.; Li, S.; Qiu, B.; Fan, X.; Chen, W.; Ye, Y.; Ding, Y. VCAM1 Promotes Tumor Cell Invasion and Metastasis by Inducing EMT and Transendothelial Migration in Colorectal Cancer. *Frontiers in Oncology* | [www.frontiersin.org](http://www.frontiersin.org) **2020**, *1*, 1066. <https://doi.org/10.3389/fonc.2020.01066>.
- (228) Gorbunova, A. S.; Yapyrintseva, M. A.; Denisenko, T. v.; Zhivotovsky, B. BNIP3 in Lung Cancer: To Kill or Rescue? *Cancers* **2020**, *12* (3390). <https://doi.org/10.3390/cancers12113390>.
- (229) Vallejo, A.; Perurena, N.; Guruceaga, E.; Mazur, P. K.; Martinez-Canarias, S.; Zandueta, C.; Valencia, K.; Arricibita, A.; Gwinn, D.; Sayles, L. C.; Chuang, C. H.; Guembe, L.; Bailey, P.; Chang, D. K.; Biankin, A.; Ponz-Sarvisé, M.; Andersen, J. B.; Khatri, P.; Bozec, A.; Sweet-Cordero, E. A.; Sage, J.; Lecanda, F.; Vicent, S. An Integrative Approach Unveils FOSL1 as an Oncogene Vulnerability in KRAS-Driven Lung and Pancreatic Cancer. *Nature Communications* **2017**, *8*. <https://doi.org/10.1038/ncomms14294>.
- (230) Chen, B.; Yang, L.; Zhang, R.; Gan, Y.; Zhang, W.; Liu, D.; Chen, H.; Tang, H. Hyperphosphorylation of RPS6KB1, Rather than Overexpression, Predicts Worse Prognosis in Non-Small Cell Lung Cancer Patients. *PLoS ONE* **2017**, *12* (8). <https://doi.org/10.1371/journal.pone.0182891>.
- (231) Xu, X.; Lai, Y.; Hua, Z. C. Apoptosis and Apoptotic Body: Disease Message and Therapeutic Target Potentials. *Bioscience Reports* **2019**, *39* (1). <https://doi.org/10.1042/BSR20180992>.
- (232) Golubovskaya, V.; Wu, L. Different Subsets of T Cells, Memory, Effector Functions, and CAR-T Immunotherapy. *Cancers* **2016**, *8* (3), 36. <https://doi.org/10.3390/cancers8030036>.

## Literature

- (233) Schupp, J.; Christians, A.; Zimmer, N.; Gleue, L.; Jonuleit, H.; Helm, M.; Tuettenberg, A. In-Depth Immune-Oncology Studies of the Tumor Microenvironment in a Humanized Melanoma Mouse Model. *International Journal of Molecular Sciences* **2021**, *22* (3). <https://doi.org/10.3390/ijms22031011>.
- (234) Kumagai, S.; Togashi, Y.; Kamada, T.; Sugiyama, E.; Nishinakamura, H.; Takeuchi, Y.; Vitaly, K.; Itahashi, K.; Maeda, Y.; Matsui, S.; Shibahara, T.; Yamashita, Y.; Irie, T.; Tsuge, A.; Fukuoka, S.; Kawazoe, A.; Udagawa, H.; Kirita, K.; Aokage, K.; Ishii, G.; Kuwata, T.; Nakama, K.; Kawazu, M.; Ueno, T.; Yamazaki, N.; Goto, K.; Tsuboi, M.; Mano, H.; Doi, T.; Shitara, K.; Nishikawa, H. The PD-1 Expression Balance between Effector and Regulatory T Cells Predicts the Clinical Efficacy of PD-1 Blockade Therapies. *Nature Immunology*. <https://doi.org/10.1038/s41590-020-0769-3>.
- (235) Wolf, Y.; Anderson, A. C.; Kuchroo, V. K. TIM3 Comes of Age as an Inhibitory Receptor. *Nature Reviews Immunology*. <https://doi.org/10.1038/s41577-019-0224-6>.
- (236) Oweida, A.; Hararah, M. K.; Phan, A.; Binder, D.; Bhatia, S.; Lennon, S.; Bukkapatnam, S.; van Court, B.; Uyanga, N.; Darragh, L.; Kim, H. M.; Raben, D.; Tan, A. C.; Heasley, L.; Clambey, E.; Nemenoff, R.; Karam, S. D. Resistance to Radiotherapy and PD-L1 Blockade Is Mediated by TIM-3 Upregulation and Regulatory T-Cell Infiltration. *Clin Cancer Res* **2018**, *24* (21). <https://doi.org/10.1158/1078-0432.CCR-18-1038>.
- (237) Umansky, V.; Bonaventura, P.; Shekarian, T.; Alcazer, V.; Valladeau-Guilemond, J.; Valsesia-Wittmann, S.; Amigorena, S.; Caux, C.; Depil, S. Cold Tumors: A Therapeutic Challenge for Immunotherapy. *Frontiers in Immunology* | [www.frontiersin.org](http://www.frontiersin.org) **2019**, *10*, 168. <https://doi.org/10.3389/fimmu.2019.00168>.
- (238) Metelli, A.; Wu, B. X.; Fugle, C. W.; Rachidi, S.; Sun, S.; Zhang, Y.; Wu, J.; Tomlinson, S.; Howe, P. H.; Yang, Y.; Garrett-Mayer, E.; Liu, B.; Li, Z. Surface Expression of TGF $\beta$  Docking Receptor GARP Promotes Oncogenesis and Immune Tolerance in Breast Cancer. *Cancer Research* **2016**, *76* (24), 7106–7117. <https://doi.org/10.1158/0008-5472.CAN-16-1456>.
- (239) Zimmer, N.; Kim, E.; Sprang, B.; Leukel, P.; Khafaji, F.; Ringel, F.; Sommer, C.; Tuettenberg, J.; Tuettenberg, A. GARP as an Immune Regulatory Molecule in the Tumor Microenvironment of Glioblastoma Multiforme. *International journal of molecular sciences* **2019**, *20* (15). <https://doi.org/10.3390/ijms20153676>.
- (240) John, T.; Liu, G.; Tsao, M. S. Overview of Molecular Testing in Non-Small-Cell Lung Cancer: Mutational Analysis, Gene Copy Number, Protein Expression and Other Biomarkers of EGFR for the Prediction of Response to Tyrosine Kinase Inhibitors. *Oncogene* **2009**, *28* (SUPPL. 1). <https://doi.org/10.1038/ONC.2009.197>.
- (241) Petty AJ; Yang Y. Tumor-Associated Macrophages: Implications in Cancer Immunotherapy. **2017**. <https://doi.org/10.2217/imt-2016-0135>.
- (242) FDA Approves First Drug to Treat Rare Metabolic Disorder <https://www.fda.gov/news-events/press-announcements/fda-approves-first-drug-treat-rare-metabolic-disorder> (accessed 2021 -05 -24).
- (243) FDA approves first-of-its kind targeted RNA-based therapy to treat a rare disease <https://www.fda.gov/news-events/press-announcements/fda-approves-first-its-kind-targeted-rna-based-therapy-treat-rare-disease> (accessed 2021 -05 -24).
- (244) FDA approves first treatment for inherited rare disease <https://www.fda.gov/news-events/press-announcements/fda-approves-first-treatment-inherited-rare-disease> (accessed 2021 -05 -24).
- (245) Saw, P. E.; Song, E. W. SiRNA Therapeutics: A Clinical Reality. *Science China Life Sciences*. Science in China Press April 1, 2020, pp 485–500. <https://doi.org/10.1007/s11427-018-9438-y>.
- (246) Mainini, F.; Eccles, M. R. Lipid and Polymer-Based Nanoparticle SiRNA Delivery Systems for Cancer Therapy. *Molecules* **2020**, *25* (11), 2692. <https://doi.org/10.3390/molecules25112692>.
- (247) Batist, G.; Barton, J.; Chaikin, P.; Swenson, C.; Welles, L. Myocet (Liposome-Encapsulated Doxorubicin Citrate): A New Approach in Breast Cancer Therapy. *Expert Opinion on Pharmacotherapy* **2002**, *3* (12), 1739–1751. <https://doi.org/10.1517/14656566.3.12.1739>.
- (248) Sippel, T. R.; Radtke, S.; Olsen, T. M.; Kiem, H.-P.; Rongvaux, A. Human Hematopoietic Stem Cell Maintenance and Myeloid Cell Development in Next-Generation Humanized Mouse Models. *Blood Advances* **2019**, *3* (3), 268–274. <https://doi.org/10.1182/bloodadvances.2018023887>.
- (249) Song, Y.; Rongvaux, A.; Taylor, A.; Jiang, T.; Tebaldi, T.; Balasubramanian, K.; Bagale, A.; Kasim Terzi, Y.; Gbyli, R.; Wang, X.; Fu, X.; Gao, Y.; Zhao, J.; Podoltsev, N.; Xu, M.; Neparidze, N.; Wong, E.; Torres, R.; Bruscia, E. M.; Kluger, Y.; Manz, M. G.; Flavell, R. A.; Halene, S. A Highly Efficient and Faithful MDS Patient-Derived Xenotransplantation Model for Pre-Clinical Studies. *Nature Communications* **2019**, *10* (366). <https://doi.org/10.1038/s41467-018-08166-x>.
- (250) Lewis, C. J.; Cobb, B. A. Carbohydrate Oxidation Acidifies Endosomes, Regulating Antigen Processing and TLR9 Signaling. *The Journal of Immunology* **2010**, *184* (7), 3789–3800. <https://doi.org/10.4049/jimmunol.0903168>.
- (251) Mironov, S. L.; Ivannikov, M. v.; Johansson, M. [Ca<sup>2+</sup>]<sub>i</sub> Signaling between Mitochondria and Endoplasmic Reticulum in Neurons Is Regulated by Microtubules: From Mitochondrial Permeability Transition Pore to Ca<sup>2+</sup>-Induced Ca<sup>2+</sup> Release. *Journal of Biological Chemistry* **2005**, *280* (1), 715–721. <https://doi.org/10.1074/jbc.M409819200>.
- (252) Hardiman, E.; Gibbs, M.; Reeves, R.; Bergquist, P. Directed Evolution of a Thermophilic  $\beta$ -Glucosidase for Cellulosic Bioethanol Production. *Applied Biochemistry and Biotechnology* **2010**, *161* (1–8), 301–312. <https://doi.org/10.1007/s12010-009-8794-6>.
- (253) Polack, F. P.; Thomas, S. J.; Kitchin, N.; Absalon, J.; Gurtman, A.; Lockhart, S.; Perez, J. L.; Pérez Marc, G.; Moreira, E. D.; Zerbini, C.; Bailey, R.; Swanson, K. A.; Roychoudhury, S.; Koury, K.; Li, P.; Kalina, W. v.; Cooper, D.; Frenck,

## Literature

- R. W.; Hammitt, L. L.; Türeci, Ö.; Nell, H.; Schaefer, A.; Ünal, S.; Tresnan, D. B.; Mather, S.; Dormitzer, P. R.; Şahin, U.; Jansen, K. U.; Gruber, W. C. Safety and Efficacy of the BNT162b2 mRNA Covid-19 Vaccine. *New England Journal of Medicine* **2020**, *383* (27), 2603–2615. <https://doi.org/10.1056/nejmoa2034577>.
- (254) Baden, L. R.; el Sahly, H. M.; Essink, B.; Kotloff, K.; Frey, S.; Novak, R.; Diemert, D.; Spector, S. A.; Rouphael, N.; Creech, C. B.; McGettigan, J.; Khetan, S.; Segall, N.; Solis, J.; Brosz, A.; Fierro, C.; Schwartz, H.; Neuzil, K.; Corey, L.; Gilbert, P.; Janes, H.; Follmann, D.; Marovich, M.; Mascola, J.; Polakowski, L.; Ledgerwood, J.; Graham, B. S.; Bennett, H.; Pajon, R.; Knightly, C.; Leav, B.; Deng, W.; Zhou, H.; Han, S.; Ivarsson, M.; Miller, J.; Zaks, T. Efficacy and Safety of the mRNA-1273 SARS-CoV-2 Vaccine. *New England Journal of Medicine* **2021**, *384* (5), 403–416. <https://doi.org/10.1056/nejmoa2035389>.
- (255) Tian, J.-H.; Patel, N.; Haupt, R.; Zhou, H.; Weston, S.; Hammond, H.; Logue, J.; Portnoff, A. D.; Norton, J.; Guebre-Xabier, M.; Zhou, B.; Jacobson, K.; Maciejewski, S.; Khatoon, R.; Wisniewska, M.; Moffitt, W.; Kluepfel-Stahl, S.; Ekechukwu, B.; Papin, J.; Boddapati, S.; Jason Wong, C.; Piedra, P. A.; Frieman, M. B.; Massare, M. J.; Fries, L.; Bengtsson, K. L.; Stertman, L.; Ellingsworth, L.; Glenn, G.; Smith, G. SARS-CoV-2 Spike Glycoprotein Vaccine Candidate NVX-CoV2373 Immunogenicity in Baboons and Protection in Mice. *Nature Communications* **2021**, *12* (1), 372. <https://doi.org/10.1038/s41467-020-20653-8>.
- (256) Hao, F.; Li, Y.; Zhu, J.; Sun, J.; Marshall, B.; Lee, R. J.; Teng, L.; Yang, Z.; Xie, J. Polyethylenimine-Based Formulations for Delivery of Oligonucleotides. *Current Medicinal Chemistry* **2018**, *26* (13), 2264–2284. <https://doi.org/10.2174/0929867325666181031094759>.
- (257) Method of the Year 2020: Spatially Resolved Transcriptomics. *Nature Methods* **2021**, *18* (1), 1–1. <https://doi.org/10.1038/s41592-020-01042-x>.

# 8 Supplemental

**Table S1:** Statistical data for Figure 23.

| <b>A</b> | <b>sample</b> | <b>Mean</b> | <b>SD</b>  | <b>N</b> | <b>Mean</b> | <b>SD</b>  | <b>N</b> | <b>E</b> | <b>sample</b> | <b>Mean</b> | <b>SD</b>  | <b>N</b> | <b>Mean</b> | <b>SD</b>  | <b>N</b> |
|----------|---------------|-------------|------------|----------|-------------|------------|----------|----------|---------------|-------------|------------|----------|-------------|------------|----------|
|          |               | empty       |            |          | DOX         |            |          |          |               | empty       |            |          | DOX         |            |          |
|          | untreated     | 100         | 3          | 3        |             |            |          |          | untreated     | 100         | 3          | 3        |             |            |          |
|          | 1,0 $\mu$ M   |             |            |          | 84          | 17         | 3        |          | 1,0 $\mu$ M   |             |            |          | 78          | 16         | 3        |
|          | 2,5 $\mu$ M   |             |            |          | 66          | 3          | 3        |          | 2,5 $\mu$ M   |             |            |          | 66          | 2          | 3        |
|          | 10,0 $\mu$ M  |             |            |          | 26          | 2          | 3        |          | 10,0 $\mu$ M  |             |            |          | 51          | 5          | 3        |
|          | L0            | 100         | 6          | 3        | 85          | 1          | 3        |          | L0            | 110         | 8          | 3        | 110         | 5          | 3        |
|          | C63           | 76          | 9          | 3        | 57          | 7          | 3        |          | C63           | 96          | 7          | 3        | 75          | 3          | 3        |
|          | C73           | 70          | 7          | 3        | 47          | 6          | 3        |          | C73           | 101         | 8          | 3        | 76          | 9          | 3        |
|          | C83           | 83          | 7          | 3        | 45          | 8          | 3        |          | C83           | 98          | 2          | 3        | 74          | 13         | 3        |
| <b>B</b> | <b>sample</b> | <b>Mean</b> | <b>SD</b>  | <b>N</b> | <b>Mean</b> | <b>SD</b>  | <b>N</b> | <b>F</b> | <b>sample</b> | <b>Mean</b> | <b>SD</b>  | <b>N</b> | <b>Mean</b> | <b>SD</b>  | <b>N</b> |
|          |               | empty       |            |          | DOX         |            |          |          |               | empty       |            |          | DOX         |            |          |
|          | untreated     | 100         | 15         | 3        |             |            |          |          | untreated     | 100         | 15         | 3        |             |            |          |
|          | 1,0 $\mu$ M   |             |            |          | 37          | 2          | 3        |          | 1,0 $\mu$ M   |             |            |          | 58          | 2          | 3        |
|          | 2,5 $\mu$ M   |             |            |          | 19          | 0          | 3        |          | 2,5 $\mu$ M   |             |            |          | 22          | 0          | 3        |
|          | 10,0 $\mu$ M  |             |            |          | 8           | 1          | 3        |          | 10,0 $\mu$ M  |             |            |          | 15          | 2          | 3        |
|          | L0            | 66          | 7          | 3        | 77          | 5          | 3        |          | L0            | 86          | 9          | 3        | 77          | 5          | 3        |
|          | C63           | 72          | 4          | 3        | 40          | 3          | 3        |          | C63           | 76          | 4          | 3        | 41          | 3          | 3        |
|          | C73           | 76          | 6          | 3        | 41          | 3          | 3        |          | C73           | 72          | 6          | 3        | 43          | 3          | 3        |
|          | C83           | 82          | 8          | 3        | 39          | 1          | 3        |          | C83           | 73          | 7          | 3        | 34          | 1          | 3        |
| <b>C</b> | <b>sample</b> | <b>Mean</b> | <b>SD</b>  | <b>N</b> | <b>Mean</b> | <b>SD</b>  | <b>N</b> | <b>G</b> | <b>sample</b> | <b>Mean</b> | <b>SD</b>  | <b>N</b> | <b>Mean</b> | <b>SD</b>  | <b>N</b> |
|          |               | 0,5h        |            |          | 4h          |            |          |          |               | 0,5h        |            |          | 4h          |            |          |
|          | untreated     | 347         | 8          | 3        | 338         | 12         | 3        |          | untreated     | 363         | 40         | 3        | 387         | 20         | 3        |
|          | 1,0 $\mu$ M   | 522         | 29         | 3        | 1310        | 49         | 3        |          | 1,0 $\mu$ M   | 1396        | 45         | 3        | 4415        | 396        | 3        |
|          | L0            | 524         | 16         | 3        | 729         | 15         | 3        |          | L0            | 512         | 73         | 3        | 912         | 55         | 3        |
|          | C63           | 807         | 23         | 3        | 1682        | 18         | 3        |          | C63           | 928         | 58         | 3        | 2538        | 303        | 3        |
|          | C73           | 885         | 55         | 3        | 1727        | 78         | 3        |          | C73           | 771         | 36         | 3        | 2361        | 236        | 3        |
|          | C83           | 795         | 56         | 3        | 1551        | 63         | 3        |          | C83           | 1064        | 35         | 3        | 3007        | 369        | 3        |
| <b>D</b> | <b>sample</b> | <b>Mean</b> | <b>SD</b>  | <b>N</b> | <b>Mean</b> | <b>SD</b>  | <b>N</b> | <b>H</b> | <b>sample</b> | <b>Mean</b> | <b>SD</b>  | <b>N</b> | <b>Mean</b> | <b>SD</b>  | <b>N</b> |
|          |               | 0,5h        |            |          | 4h          |            |          |          |               | 0,5h        |            |          | 4h          |            |          |
|          | untreated     | 4069        | 171,358376 | 3        |             |            | 3        |          | untreated     | 5464        | 320,906808 | 3        |             |            | 3        |
|          | 1,0 $\mu$ M   | 26894       | 2262,46968 | 3        | 40353       | 2879,39151 | 3        |          | 1,0 $\mu$ M   | 44735       | 5574,98792 | 3        | 116359      | 11393,6378 | 3        |
|          | L0            | 9827        | 714,681135 | 3        | 17482       | 998,964534 | 3        |          | L0            | 17459       | 2554,28983 | 3        | 42958       | 4757,10249 | 3        |
|          | C63           | 23873       | 4945,76824 | 3        | 52513       | 10453,9189 | 3        |          | C63           | 46943       | 7009,4828  | 3        | 121278      | 13102,0451 | 3        |
|          | C73           | 22162       | 2765,08227 | 3        | 42237       | 8190,2607  | 3        |          | C73           | 55547       | 12688,1097 | 3        | 145560      | 33150,1227 | 3        |
|          | C83           | 31501       | 3802,21863 | 3        | 59902       | 9342,86111 | 3        |          | C83           | 70677       | 13657,8732 | 3        | 162095      | 26030,2396 | 3        |



## *Supplemental*

**Table S2:** Number of animals per treatment group (see **Figure 43**).

| <b>experiment / group</b> | <b>1</b> | <b>2</b> | <b>3</b> | <b>4</b> | <b>5</b> | <b>6</b> |
|---------------------------|----------|----------|----------|----------|----------|----------|
| <b>V2</b>                 | 7        | 5        | 5        | 5        | 5        | 5        |
| <b>V3</b>                 | 6        | 6        | 5        | 5        | 5        | 6        |
| <b>V7</b>                 | 6        | 6        | 6        | 6        | 5        | 6        |

## *Acknowledgments*

# 9 Acknowledgments

Many thanks to:

[Redacted names]

Tissue bank of the University Medical Center Mainz

German Research Foundation (DFG) for funding Collaborative Research Center (SFB) 1066.

## 10 List of figures

|  |    |
|--|----|
| <b>Figure 1:</b> Myeloid cells of the tumor microenvironment, their key effector functions and strategies to target them. <sup>16</sup>  | 7  |
| <b>Figure 2:</b> Proposed model for TGF- $\beta$ 1 in a complex with two LAP and GARP in its inactive form. Physical pulling force exerted by integrins ( $\alpha$ V $\beta$ 8) on a second cell might change conformation of both LAPs and the subsequent release of active TGF- $\beta$ 1. GARP is depicted as mere cell membrane anchor and chaperone for the protein. The monoclonal antibody MHG-8 stabilizes this conformation and thereby prevents TGF- $\beta$ 1 release. <sup>126</sup>   | 17 |
| <b>Figure 3:</b> Human monocyte-derived macrophages (M-CSF) were polarized for 48h towards M1 (IFN- $\gamma$ & LPS) and M2 (IL-4) phenotype and their gene expression was analyzed by qPCR with GAPDH as the housekeeping gene. Genes higher expressed in M2 macrophages are shown in green (values > 1), those lower expressed in M2 are shown in red (values < 1). Data is displayed as fold change and normalized to M1 macrophages. N = 9. Statistical significance was determined using the two tailed t-test.  | 35 |
| <b>Figure 4:</b> Human monocyte-derived macrophages (M-CSF) were polarized for 48h towards M1 (IFN- $\gamma$ & LPS) and M2 (IL-4) phenotype and their surface marker expression was analyzed by flow cytometry. Markers higher expressed in M2 macrophages are shown in green (values > 1), those lower expressed in M2 are shown in red (values < 1). Data is displayed as fold change of mean fluorescence intensity of the stained antigen and normalized to M1 macrophages. N = 9. Statistical significance was determined using the two tailed t-test.  | 36 |
| <b>Figure 5:</b> siRNA mediated knockdown of LMNA, IL4R, NR4A3, STAT6 and PPARG in human monocyte-derived macrophages using Viromer BLUE as transfection reagent for 48h. Transfection efficacy was determined using qPCR to measure gene expression. Data is shown as relative expression normalized to untreated samples and the housekeeping gene SNRPD3. N = 3. Statistical significance was determined using the Two-Way ANOVA with Fisher's LSD test. Ns = not significant, * p < 0,05, ** p < 0,01, *** p < 0,001, **** p < 0,0001.   | 39 |
| <b>Figure 6:</b> Human monocyte-derived and M2 polarized macrophages were transfected with siRNA against IL4R (upper chart) and PPARG (lower chart) and gene expression after 48h was analyzed using qPCR. Data is shown as relative expression normalized to samples transfected with negative control siRNA and the housekeeping gene GAPDH. N = 3. Statistical significance was determined using the Two-Way ANOVA with Fisher's LSD test. Ns = not significant, * p < 0,05, ** p < 0,01, *** p < 0,001, **** p < 0,0001.   | 41 |
| <b>Figure 7:</b> Human monocyte-derived and M2 polarized macrophages were transfected with siRNA against IL4R (A), PPARG (B), STAT6 (C) and NR4A3 (D) and surface marker expression after 48h was analyzed using flow cytometry. Data is shown as relative expression normalized to untreated (M2) samples. N = 3. Statistical significance was determined using the Two-Way ANOVA with Fisher's Uncorrected LSD test. Ns = not significant, * p < 0,05, ** p < 0,01, *** p < 0,001, **** p < 0,0001.  | 42 |
| <b>Figure 8:</b> siRNA mediated knockdown of PPARG in human monocyte-derived macrophages using siRNA loaded L0 and C83 liposomes as transfection reagent for 48h. Transfection efficacy was determined using qPCR to measure gene expression. Data is shown as relative expression normalized to untreated samples and the housekeeping gene SNRPD3. N = 3. Statistical significance was determined using the Ordinary One-Way ANOVA with Fisher's LSD test. Ns = not significant, * p < 0,05, ** p < 0,01, *** p < 0,001, **** p < 0,0001.  | 43 |
| <b>Figure 9:</b> Chemical structure of Tasquinimod.  | 44 |
| <b>Figure 10:</b> Human monocyte-derived macrophages were pre-polarized for 24h and incubated afterwards for 24h with Tasquinimod in two different concentrations (10 $\mu$ M & 100 $\mu$ M). Marker expression was analyzed via flow cytometry. N = 5. Statistical significance was determined using the Two-Way ANOVA with Fisher's Uncorrected LSD test. Ns = not significant, * p < 0,05, ** p < 0,01, *** p < 0,001, **** p < 0,0001.   | 45 |
| <b>Figure 11:</b> The effects of Tasquinimod on the energy metabolism of polarized human monocyte-derived macrophages has been investigated by measuring the oxygen consumption rate (OCR) and extracellular acidification rate (ECAR) with an Agilent Seahorse XFp Analyzer. Because of donor variations the first value was normalized to 1. Due to the addition of oligomycin (between data point 3-4), FCCP (between data point 6-7) and rotenone/antimycin A (between data point 9-10), basal, maximum and spare capacity respiration as well as proton leakage and ATP production can be calculated (see <b>Figure 12</b> ). Macrophages were polarized for 24h and Tasquinimod was added at 100 $\mu$ M after polarization but 1h before the assay. | 47 |
| <b>Figure 12:</b> The effects of Tasquinimod on the energy metabolism of polarized human monocyte-derived macrophages has been investigated by measuring the oxygen consumption rate (OCR) and extracellular acidification rate (ECAR) with an Agilent Seahorse XFp Analyzer (see also <b>Figure 11</b> ). Statistical significance was determined using the Ordinary One-Way ANOVA with Fisher's LSD test. N = 6. Ns = not significant (not shown), * p < 0,05, ** p < 0,01, *** p < 0,001, **** p < 0,0001.  | 48 |
| <b>Figure 13:</b> Human peripheral blood mononuclear cells were labeled with CFSE and cultured for 3 days in wells coated with anti-CD3 antibody in the presence of Tasquinimod at two different concentrations (10 $\mu$ M & 100 $\mu$ M). Afterwards their proliferation was measured using flow cytometry. Shown is the percentage of living proliferated CD4 <sup>+</sup> and CD8 <sup>+</sup> T cells normalized to untreated. N = 5. Statistical significance was determined using the Two-Way ANOVA with Fisher's LSD test. Ns = not significant, * p < 0,05, ** p < 0,01, *** p < 0,001, **** p < 0,0001.  | 49 |

## List of figures

- Figure 14:** Human melanoma cell lines Ma-Mel-19 and UKRV-Mel-15 were labeled with CFSE and cultured for 3 days in the presence of Tasquinimod at three different concentrations (10  $\mu$ M, 100  $\mu$ M & 200  $\mu$ M). Afterwards their proliferation was measured using flow cytometry. Shown is the percentage of living proliferated CD4<sup>+</sup> and CD8<sup>+</sup> T cells. N = 3. Statistical significance was determined using the Two-Way ANOVA with Fisher's LSD test. Ns = not significant, \* p < 0,05, \*\* p < 0,01, \*\*\* p < 0,001, \*\*\*\* p < 0,0001. .... 50
- Figure 15:** Human melanoma biopsies in different tissues showed expression of CD206, PU.1, CD68 and PPARG inside the tumor mass as detected by immunohistochemistry staining (IHC-P). Shown is the percentage of cells inside the tumor expressing the marker. One biopsy per entity (skin, lung, lymph node or metastasis) was analyzed with often more than one distinguishable metastasis (error bar). No bar means no (specific) staining of this marker in the sample. .... 52
- Figure 16:** Rationale of Doxorubicin release experiments using macrophages and melanoma cells. Liposomes will be taken up by the cell through endocytosis and end up confined in lysosomes inside the cytoplasm. <sup>186</sup> Because of lower pH (5,5) liposomes start to be leaky and will also fuse with the lysosomal membrane, thereby releasing Doxorubicin from their lumen into the cytoplasm. Doxorubicin diffuses freely through the cell and can penetrate the nuclear membrane. Inside the nucleus it binds to DNA. Excited by a 488 nm laser Doxorubicin will emit light with a maximum at 590 nm. By using confocal laser scanning microscopy and counterstaining with Hoechst 33342 or 33258 it is possible to detect fluorescence only in one z-plane of the nucleus. Since every Doxorubicin molecule in the nucleus will be bound to DNA, the signal caused by different liposomal carriers can be compared directly. .... 54
- Figure 17:** Chemical structure of Doxorubicin. In experiments, the water-soluble hydrochloride has been used. .... 55
- Figure 18:** Chemical structure of the fluorophore Laurdan used for liposomal stability assays. .... 55
- Figure 19:** Liposome characterization of liposomes shown in Table 4. Each liposomal formulation is shown as "empty" liposome and loaded with Doxorubicin (see 3.12). Data of [REDACTED]. <sup>187</sup> .... 56
- Figure 20:** Changes in diameter, PDI and zeta potential due to liposome degradation over time and at low pH 5,5. In addition, cargo release was measured. Data of [REDACTED]. <sup>187</sup> .... 57
- Figure 21:** As depicted in **Figure 16**, liposomes are taken up by macrophages (shown here) and melanoma cells. Macrophages were incubated for 3 hours with liposomes at cell culture conditions. Nuclei stain with Hoechst 33258 shown in blue, cell membrane stained with NeuroDiO shown in green and liposomal DiD shown in red. Scale bar is 20  $\mu$ m. The membrane staining was omitted in subsequent release studies, since NeuroDiO interferes with detection of weaker Doxorubicin signals from nuclei. Doxorubicin release studies are shown in **Figure 24** and **Figure 25**. .... 59
- Figure 22:** Flow cytometry gating strategy to quantify whole cell Doxorubicin signal (left). Debris was excluded by gating on single cells based on their size (FSC-A), signal intensity (FSC-H) and granularity (SSC-A). FVD780 (in APC-Cy7 channel) was used to include only living cells in the analysis which show a lower signal compared to dead cells. In confocal microscopy nuclei were counterstained with Hoechst 33258 (blue). Liposomes were detected by their DiD fluorescence (red). By using the software Fiji, the lookup table "Fire" was applied to detect even very weak Doxorubicin signals (right, lower picture). Nuclei were gated manually. .... 60
- Figure 23:** Liposomes with designed fragile stability were tested as Doxorubicin carriers on human melanoma cells (UKRV-Mel-15a) and human monocyte-derived macrophages. The cytotoxicity after 24h and 48h/72h was analyzed via resazurin assay (A, B, E & F). Whole-cell fluorescence caused by liposome uptake was monitored after 30 minutes and 4 hours using flow cytometry (C & G). Doxorubicin release after 30 minutes and 4 hours was detected by measuring Doxorubicin fluorescence exclusively in the cell nuclei using confocal microscopy (D & H). Free Doxorubicin was added as control and for normalization. Doxorubicin content in liposomes was normalized to 1  $\mu$ M free Doxorubicin. All values are triplicates. Statistic calculations are shown in table S1. .... 62
- Figure 24:** Liposomal delivery of Doxorubicin and its accumulation in cell nuclei of human monocyte-derived macrophages after 2 hours and 24 hour of incubation at cell culture conditions (37°C, 5% CO<sub>2</sub>). Untreated cells served as negative control and uptake was compared to 1  $\mu$ M free Doxorubicin. Nuclei are shown in blue (Hoechst 33258), liposome label in red (DiD) and Doxorubicin in grayscale. Scale bars are 25  $\mu$ m. Analysis was done by manually gating the nuclei and quantifying fluorescence in the Doxorubicin channel only using the software Fiji. .... 63
- Figure 25:** This figure shows the same experimental setup as in **Figure 24**. In this case human melanoma cell line UKRV-Mel-15a was incubated with Doxorubicin loaded liposomes. .... 64
- Figure 26:** Single cell fluorescence data of cells passing the flow cell of the ImageStream flow cytometer is recorded by one acquired picture in each channel recorded and for each cell investigated. The AMNIS IDEAS Software allows gating on cell populations (A) and cell regions (B). This allows to discriminate Doxorubicin that has traveled to the nuclei and Doxorubicin still located in the cytoplasm (C). Gating and analysis using the AMNIS IDEAS software was done by [REDACTED]. <sup>191</sup> .... 65
- Figure 27:** Analog to **Figure 23** the release of doxorubicin from liposomal carriers was analyzed using image-based flow cytometry (see 3.10). This method enables to gate and quantify doxorubicin fluorescence exclusively from the cell nuclei. Human monocyte-derived macrophages were incubated with different liposomal species normalized to 1  $\mu$ M doxorubicin content for 30 minutes and 4 hours. Free doxorubicin (1  $\mu$ M) was used as control (dotted lines). All samples are duplicates. .... 66
- Figure 28:** Analog to **Figure 23** the release of doxorubicin from liposomal carriers was analyzed using image-based flow cytometry (see 3.10). This method enables to gate and quantify doxorubicin fluorescence exclusively from the cell nuclei. Human melanoma cell line UKRV-Mel-15a was incubated with different liposomal species normalized to 1  $\mu$ M

## List of figures

- doxorubicin content for 30 minutes and 4 hours. Free doxorubicin (1  $\mu\text{M}$ ) was used as control (dotted lines). All samples are triplicates. .... 67
- Figure 29:** Analog to Figure 23 the release of Doxorubicin from liposomal carriers unmodified (X0), modified with linear PEG (X2) or hyperbranched PG (X4) was analyzed using image-based flow cytometry (see 3.10). This method enables to gate and quantify Doxorubicin fluorescence exclusively from the cell nuclei. Human melanoma cell line UKRV-Mel-15a was incubated with different liposomal species normalized to 1  $\mu\text{M}$  Doxorubicin content for 30 minutes and 4 hours. Free Doxorubicin (0,5  $\mu\text{M}$  & 1  $\mu\text{M}$ ) was used as control (dotted lines). All samples are triplicates. .... 69
- Figure 30:** Whole cell Doxorubicin fluorescence in human macrophages and human melanoma cell line UKRV-Mel-15a caused by pH sensitive ketal- and vinyl ether-PEG modified liposomes (5 mol-%) were detected via flow cytometry. Doxorubicin content was normalized to 1  $\mu\text{M}$  and compared to uptake of free Doxorubicin in the same concentration. .... 70
- Figure 31:** Amphiphilic lipids applied to systems containing cells in an aqueous solution are in an equilibrium between micelles, liposomes with a bilayer structure or they integrate into the bilayer system of the cell itself (A). The fluorophore atto 488 was coupled to synthetic polyether lipids tethered to alkyl chains with 16 – 18 carbon atoms or cholesterol (B). x describes the number of polyethylene glycol units. <sup>146</sup> ..... 72
- Figure 32:** Lipid exchange between liposomes carrying a fluorophore atto 488 coupled to different anchors and human melanoma cell line UKRV-Mel-15a after 4 h and 24 h measured by flow cytometry. N = 3. Statistical significance was determined using the One-Way ANOVA with Fisher's LSD test. Ns = not significant, \*  $p < 0,05$ , \*\*  $p < 0,01$ , \*\*\*  $p < 0,001$ , \*\*\*\*  $p < 0,0001$ . .... 73
- Figure 33:** Data from Figure 32 reduced to a statistical comparison of the three tested anchors based on alkyl chains from 16 to 20 carbon atoms length. N = 3. Statistical significance was determined using the One-Way ANOVA with Fisher's LSD test. Ns = not significant, \*  $p < 0,05$ , \*\*  $p < 0,01$ , \*\*\*  $p < 0,001$ , \*\*\*\*  $p < 0,0001$ . .... 74
- Figure 34:** Rationale of liposome targeting using antibodies and the biotin-streptavidin (here neutravidin) system. Biotin is included in the lipid formulation as biotin-PEG-phospholipid (see 3.12). After liposome formation via dual centrifugation in a stepwise process first neutravidin and then a biotinylated antibody is added to the liposome dispersion. This strategy enables full flexibility regarding biotin, neutravidin and antibody ratios and it also circumvents the presence of large proteins like neutravidin and immunoglobulins during liposome formation. This sketch is not true to scale and for simplicity only one biotin linked to PEG is shown. Please take note, that the PEG-biotin chain can also be in the lumen. .... 76
- Figure 35:** Exemplary gating strategy to distinguish between unlabeled BSA silica beads and labeled (redF) SA silica beads based on their fluorescence signal in the "PE" channel. For both bead types (here liposomes with 5% biotin modification) the mean fluorescence of the DiD membrane label in the "APC" channel was quantified and used to calculate the ratio between SA and BSA beads. .... 77
- Figure 36:** Binding of C83 liposomes, labeled with DiD and modified with different molar ratios of Biotin (x axis), to 5  $\mu\text{m}$  Silicabeads coated either with streptavidin (SA) or bovine serum albumin (BSA) was analyzed by flow cytometry (see 3.17). N = 6. .... 78
- Figure 37:** Binding of L0 liposomes, labeled with DiD and modified with different molar ratios of Biotin (x axis), to 5  $\mu\text{m}$  Silicabeads coated either with streptavidin (SA) or bovine serum albumin (BSA) was analyzed by flow cytometry (see 3.17). N = 6. .... 78
- Figure 38:** Based on fluorescence signals shown in Figure 36 & Figure 37 the ratio between binding of biotin labeled L0 (A) and C83 (B) liposomes to SA or BSA coated silicabeads shows targeting via biotin-streptavidin binding. Ratios above 1 indicate stronger binding of biotin labeled liposomes to SA coated beads compared to BSA beads. N = 6. Statistical significance was determined using the Two-Way ANOVA with Fisher's LSD test. ns = not significant, \*  $p < 0,05$ , \*\*  $p < 0,01$ , \*\*\*  $p < 0,001$ , \*\*\*\*  $p < 0,0001$ . .... 79
- Figure 39:** With C63 and C73 liposomes biotin targeting was also tested, but only with 1% PEG or PEG-Biotin as modification. Analogue to Figure 36, Figure 37 and Figure 38 data is displayed as raw DiD mean fluorescence (left) and as ratio between binding to streptavidin or bovine serum albumin coated silica beads (right). N = 3. Statistical significance was determined using the Two-Way ANOVA with Fisher's LSD test. ns = not significant, \*  $p < 0,05$ , \*\*  $p < 0,01$ , \*\*\*  $p < 0,001$ , \*\*\*\*  $p < 0,0001$ . .... 80
- Figure 40:** Biotinylated stable (L0) and instable (C83) liposomes were incubated with 5  $\mu\text{m}$  silica beads either coated with streptavidin (SA) or bovine serum albumin (BSA) for 30 min at room temperature in a reaction tube, then washed and transferred to an ibidi microscopy slide. SA coated beads were also available with an incorporated fluorescent dye (SA + redF). DiD label of liposomes is shown in red and fluorescence of silica beads in blue. Scale bar is 5  $\mu\text{m}$ . .... 81
- Figure 41:** Schematic draw of the humanized mouse melanoma model. Human melanoma cells (Ma-Mel-19) are injected s.c. into the back of immunodeficient NOD Scid mice. After development of measurable tumors, human PBMC are injected s.c. peritumoral and i.p. to create a human TME and to have a tumor-naïve immune cell population in the spleen. Immunomodulators to treat tumors are injected s.c. peritumoral. Tumors and spleen (not shown) are extracted for ex vivo analysis by Chipyctometry, IHC-P and flow cytometry. .... 83
- Figure 42:** Tumor mass of extracted tumors and GPT levels in serum were measured in V7 as further markers for tumor growth and animal fitness. N = 2 – 6 (see data points per group). Statistical significance was determined using the One-Way ANOVA with Fisher's LSD test. ns = not significant, \*  $p < 0,05$ , \*\*  $p < 0,01$ , \*\*\*  $p < 0,001$ , \*\*\*\*  $p < 0,0001$ . .... 85
- Figure 43:** Evaluation of Tasquinimod as immune modulator in a melanoma model based on the cell line Ma-Mel-19 in immunodeficient mice with or without human PBMC to reconstitute the immune system (see 3.13). Three

## List of figures

- independent animal experiments were performed (A, B & C). Tumor volume on the last day of the experiment was normalized to untreated animals, either humanized (E) or non-humanized (D) and compared to treatment groups. Number of animals per treatment group is shown in table S2. D & E: N = 3. Statistical significance was determined using the One-Way ANOVA with Fisher's LSD test. ns = not significant, \*  $p < 0,05$ , \*\*  $p < 0,01$ , \*\*\*  $p < 0,001$ , \*\*\*\*  $p < 0,0001$ ..... 86
- Figure 44:** Tumor size of melanoma tumors in humanized mice shown in Figure 43 on the last day of the experiment when the animals were sacrificed divided between non-humanized (left) and humanized (right) animals. Experiment runs and treatment groups correspond to those in Figure 43. Statistical significance was determined using the Two-Way ANOVA with Fisher's LSD test. ns = not significant, \*  $p < 0,05$ , \*\*  $p < 0,01$ , \*\*\*  $p < 0,001$ , \*\*\*\*  $p < 0,0001$ ..... 87
- Figure 45:** Comparison of immunohistochemistry (A, C & E) and flow cytometry (B, D & F) to detect intratumoral human immune cells in the melanoma model in humanized mice (see 3.13). Expression of immune cell markers CD45, CD4 and CD8 is compared in the different treatment groups (untreated – 2, low Tasquinimod or liposomes – 5 and high Tasquinimod – 6) for each animal experiment separately (V2, V3 & V7). Direct comparison between the two detection methods used is shown in Figure 46. Statistical significance was determined using the Two-Way ANOVA with Fisher's LSD test. ns = not significant, \*  $p < 0,05$ , \*\*  $p < 0,01$ , \*\*\*  $p < 0,001$ , \*\*\*\*  $p < 0,0001$ . Number of animals per treatment group is shown in table S2. .... 88
- Figure 46:** Direct comparison of immunohistochemistry and flow cytometry to detect intratumoral human immune cells in the melanoma model in humanized mice (3.13). Expression of immune cell markers CD45, CD4 and CD8 is compared in the different treatment groups (untreated – 2, low Tasquinimod or liposomes – 5 and high Tasquinimod – 6) for each animal experiment and immune cell marker separately (V2, V3 & V7). Direct comparison between the three treatment groups is shown in Figure 45. Statistical significance was determined using the Two-Way ANOVA with Fisher's LSD test. ns = not significant, \*  $p < 0,05$ , \*\*  $p < 0,01$ , \*\*\*  $p < 0,001$ , \*\*\*\*  $p < 0,0001$ . Number of animals per treatment group is shown in table S2..... 89
- Figure 47:** Volcano plots visualizing differential gene expression in tumor samples of humanized mice (see 3.11). RNA expression analysis was done using fluorescent RNA probes imaged by the NanoString Sprint Profiler (see 3.11). All three treatment groups with human immune cells present (untreated/control, low Tasquinimod/Tasquinimod and Tasquinimod liposomes/liposomes) were compared pairwise to each other. 5 samples in control group, 3 in liposome group and 4 in Tasquinimod group. Only targets with  $p \leq 0,05$  are displayed (above the dotted lines in the volcano plot). .... 91
- Figure 48:** Samples of tumor humanized mice were subjected to the novel multiplex staining method Chipcytometry to prove its usability in animal tumor models, especially in humanized mice models with mixed human and murine antigens. Cells were gated according to their marker expression. Leukocytes (CD45<sup>+</sup>), T cells (CD45<sup>+</sup>CD3<sup>+</sup>), CD8<sup>+</sup> T cells (CD45<sup>+</sup>CD3<sup>+</sup>CD8<sup>+</sup>), CD4<sup>+</sup> T cells (CD45<sup>+</sup>CD3<sup>+</sup>CD4<sup>+</sup>) and macrophages (huCD45<sup>+</sup>huCD68<sup>+</sup>). Three untreated animals were analyzed. .... 93
- Figure 49:** Visualization of chipcytometry (A) as highplex method to analyze the tumor microenvironment of tumor bearing humanized mice at single cell level in comparison to classical 1 marker immunohistochemistry staining of CD45 (B, DAB staining and haematoxylin counterstain; CD45<sup>+</sup> cells in red and negative cells in blue within the region of interest gated in yellow) and flow cytometry (C, showing gating for CD45 positive immune cells in a tumor sample) without spatial information. Chipcytometry data is summarized in Figure 48..... 95
- Figure 50:** Representative single cell analysis within spatial context by chipcytometry. CD8<sup>+</sup> T cells (A) and their CD4<sup>+</sup> counterparts (B) can be identified and further analyzed regarding their sub- and phenotype. Chipcytometry data is summarized in Figure 48.<sup>233</sup> ..... 96
- Figure 51:** Immunohistochemistry staining of GARP (LRRC32) with DAB (brown) in subcutaneous tumors of Ma-Mel-19 cells in humanized mice counterstained with hematoxylin (blue). Tumors show a predominantly nuclear staining either homogeneous in the tumor mass (upper tumor) or as a gradient (lower picture) with high expression at the border between tumor and surrounding tissue. Cytoplasm is also positive for GARP, but at a lower density compared to the nucleus. Scale bar is 100  $\mu\text{m}$ . .... 99
- Figure 52:** GARP mRNA detected in tumor samples of Ma-Mel-19 tumors grown in humanized mice. Statistical significance was determined using the Ordinary one-way ANOVA with Fisher's LSD test. ns = not significant, \*  $p < 0,05$ , \*\*  $p < 0,01$ , \*\*\*  $p < 0,001$ , \*\*\*\*  $p < 0,0001$ . Number of samples per treatment group: group 2 = 5, group 5 = 3 and group 6 = 4. .... 100
- Figure 53:** GARP protein detection in tumor samples of Ma-Mel-19 tumors grown in humanized mice. Statistical significance was determined using the two-way ANOVA with Fisher's LSD test. ns = not significant, \*  $p < 0,05$ , \*\*  $p < 0,01$ , \*\*\*  $p < 0,001$ , \*\*\*\*  $p < 0,0001$ . Number of samples per treatment group: V7 (group 2 = 9, group 5 = 4 and group 6 = 3), V2 (group 2 = 5, group 5 = 6 and group 6 = 4) and V3 (group 2 = 7, group 5 = 5 and group 6 = 4)..... 100
- Figure 54:** Immunofluorescence staining of Ma-Mel-19 in vitro in confocal microscopy (see 3.7) (left, GARP, nuclei) and flow cytometry (left). Ma-Mel-19 cells show expression of GARP protein in discrete spots in the nuclei and to a lower extend in the cytoplasm. Staining in flow cytometry was verified by an isotype control. .... 101

# 11 Curriculum Vitae

JONATHAN SCHUPP

[REDACTED]  
[REDACTED]  
[REDACTED]  
[REDACTED]  
[REDACTED]  
[REDACTED]  
[REDACTED]

## AUSBILDUNG

[REDACTED] [REDACTED]  
[REDACTED] [REDACTED]  
[REDACTED] [REDACTED]

## ARBEITSERFAHRUNG

|            |            |
|------------|------------|
| [REDACTED] | [REDACTED] |
| [REDACTED] | [REDACTED] |
| [REDACTED] | [REDACTED] |
| [REDACTED] | [REDACTED] |

## 12 List of publications

December 2021

- [1] **Schupp, J.**; Christians, A.; Zimmer, N.; Gleue, L.; Jonuleit, H.; Helm, M.; Tuettenberg, A. In-Depth Immuno-Oncology Studies of the Tumor Microenvironment in a Humanized Melanoma Mouse Model. *Int. J. Mol. Sci.* 2021, 22, 1011. <https://doi.org/10.3390/ijms22031011>
- [2] Gleue, L.; **Schupp, J.**; Zimmer, N.; Becker, E.; Frey, H.; Tuettenberg, A.; Helm, M. Stability of Alkyl Chain-Mediated Lipid Anchoring in Liposomal Membranes. *Cells* 2020, 9, 2213. <https://doi.org/10.3390/cells9102213>
- [3] N. Zimmer, E. Kim, **J. Schupp**, B. Sprang, P. Leukel, F. Khafaji, F. Ringel, C. Sommer, J. Tuettenberg, A. Tuettenberg. GARP as an Immune Regulatory Molecule in the Tumor Microenvironment of Glioblastoma Multiforme. *Int. J. Mol. Sci.*, 20 (2019), doi:10.3390/ijms20153676.
- [4] M. Bros, M. Youns, V. Kollek, D. Buchmüller, F. Bollmann, E. J. Seo, **J. Schupp**, E. Montermann, S. Usanova, H. Kleinert, T. Efferth, A. B. Reske-Kunz. Differentially Tolerized Mouse Antigen Presenting Cells Share a Common miRNA Signature Including Enhanced mmu-miR-223-3p Expression Which Is Sufficient to Imprint a Protolerogenic State. *Front Pharmacol.* (2018), doi: 10.3389/fphar.2018.00915.
- [5] **J. Schupp**, F. K. Krebs, N. Zimmer, E. Trzeciak, D. Schuppan, A. Tuettenberg. Targeting myeloid cells in the tumor sustaining microenvironment. *Cell Immunol.* (2017), doi: 10.1016/j.cellimm.2017.10.013.
- [6] A. Kienzle, S. Kurch, J. Schloeder, C. Berges, R. Ose, **J. Schupp**, A. Tuettenberg, H. Weiss, J. Schultze, S. Winzen, M. Schinnerer, K. Koynov, M. Mezger, N.K. Haass, W. Tremel, H. Jonuleit. Dendritic Mesoporous Silica Nanoparticles for pH-Stimuli-Responsive Drug Delivery of TNF-Alpha. *Advanced healthcare materials*, (2017).
- [7] N. Leber, L. Kaps, M. Aslam, **J. Schupp**, A. Brose, D. Schaffel, K. Fischer, M. Diken, D. Strand, K. Koynov, A. Tuettenberg, L. Nuhn, R. Zentel, D. Schuppan. SiRNA-mediated in vivo gene knockdown by acid-degradable cationic nanohydrogel particles. *Journal of controlled release: official journal of the Controlled Release Society*, 248 (2017) 10-23.
- [8] F. Foerster, D. Bamberger, **J. Schupp**, M. Weilbacher, L. Kaps, S. Strobl, L. Radi, M. Diken, D. Strand, A. Tuettenberg, P.R. Wich, D. Schuppan. Dextran-based therapeutic nanoparticles for hepatic drug delivery. *Nanomedicine* (London, England), 11 (2016) 2663-2677.
- [9] S.A. Hahn, A. Neuhoff, J. Landsberg, **J. Schupp**, D. Eberts, P. Leukel, M. Bros, M. Weilbaecher, D. Schuppan, S. Grabbe, T. Tueting, V. Lennerz, C. Sommer, H. Jonuleit, A. Tuettenberg. A key role of GARP in the immune suppressive tumor microenvironment. *Oncotarget*, 7 (2016) 42996-43009.